

**Kirigami-Based Approaches to the Development of Highly Tunable Mechanical, Electrical, and Optical Systems and Devices**

by

Erin Eda Evke

A dissertation submitted in partial fulfillment  
of the requirements for the degree of  
Doctor of Philosophy  
(Materials Science and Engineering)  
in the University of Michigan  
2021

Doctoral Committee:

Professor Max Shtein, Chair  
Professor Anthony Grbic  
Professor Jinsang Kim  
Professor Alan Taub

Erin Evke

[evkee@umich.edu](mailto:evkee@umich.edu)

ORCID iD: 0000-0002-1812-2829

© Erin Evke 2021



## **Dedication**

I dedicate this thesis to my beloved family who have given me endless love and support throughout my journey.

## Acknowledgements

There are many people I want to thank for helping me along the way. Prof. Shtein, you have been an incredible advisor, and I am so grateful to have studied under your tutelage. You always encouraged me not only to be the best researcher I can be but also the best communicator. Thank you for your unwavering support and guidance, thoughtful discussions, and enabling me to explore unconventional ideas.

Thank you to all the faculty at Michigan who shared their insights, resources, and facilities—Professors Alan Taub, Anthony Grbic, Jinsang Kim, Deanna Gates, Alanson Sample, Stephen Forrest, John Shaw, Henry Sodano, as well as Anthony Palazotto from the Air Force Institute of Technology.

I also want to thank my department's staff—Renee Hilgendorf, Debbie Johnson, Shelley Fellers, Todd Richardson, Amy Holihan, Patti Vogel, Chris Cristian, and Kristen Freshley—for all your help. Tim Chambers, thank you for training me on various equipment in Van Vlack and organizing the department outreach events. Keith McIntyre, thank you for helping me with various tasks especially when we moved our lab from Dow to the North Campus Research Complex.

From all the different projects I have worked on, there have been many grad students helping me along the way. Susannah Engdahl and Christina Lee, thank you so much for your help with the sensor project and allowing me to collect data with your camera motion tracking system. Kanat Anurakparadorn and Jiwon Lim, thanks for being great collaborators on the EMI project. Chao Huang, Yu-Wei (Tommy) Wu, Byungjun Lee, and Michael Arwashwan, thank you for all

your help with the solar tracking project. Thank you to Rahul Gangwani and Rachel Menge for your help with the circuit design of the joint motion tracker.

And of course, many thanks to my lab group—old and new members. Chao Huang, I hand off my kirigami wisdom to you. You have been such a great help this past year. Dilara Meli and Katie Wei, you have been extraordinary undergrads. Thanks for everything you've done and for being so dependable. Steve Morris, thanks for your tremendous help in all areas from teaching me how to make an OLED, to designing a circuit over the weekend, to fixing my bike, to really anything. I can always count on you to know something on any topic. Aaron Lamoureux and Lydia Mensah, thanks for welcoming me into the lab and for all your help starting off. Sid Borsadia and Brian Iezzi, though a small group, we were a force not to be reckoned with. I appreciate all the times we brainstormed ways to bring together our seemingly different projects and for all your input. We've had a lot of fun together in and out of lab. To the newer additions to the lab group—Cecelia Kinane, Shea Sanvordenker, Binyu Wang, and Ikenna Ozofofor thanks for all your insights and help as I wrapped up my final year. Thanks for being such a wonderful lab group. It's been such a pleasure working with you.

To the people I've met while in Michigan, thank you for making my time here so special; our shared moments and experiences will be held on to forever. To my close friend, Merjem Mededovic, thanks for all the amazing times together and for being my quarantine buddy. Also, thanks to my GradSWE family for being such an incredible support group. Without GradSWE, I would have never gotten to know so many amazing people. My graduate career also wouldn't be the same without my amazing teammates. Winning back-to-back intramural championship t-shirts have been some of the highlights of my time here. It's too bad our seasons were cut short because of the pandemic, but it has only made me appreciate playing with you guys all the more.

Wes Chapkin, from the moment you came to my old office in Dow to recruit me to join your winning IM soccer and frisbee teams, you have challenged me to be the best version of myself. Your vivacious energy is infectious, and you have never failed to uplift me even in the most challenging times. Thank you for always being there for me—for driving the many weekends to and from Ohio only to find yourself back in lab keeping me company at odd hours of the day.

Finally, I want to thank my parents for their unconditional love and guidance. Thank you for giving me so many opportunities to learn new skills, supporting my endeavors, and doing whatever you can to enable me to be successful. Sara and Meral, thank you for motivating me and challenging me in so many ways. The strides I have made would not be possible without you. Lastly, I want to thank both my grandmas for supporting me. Their courageousness and experiences are a constant reminder to do whatever I can to make the world a better place and to “don’t worry, be happy.”

# Table of Contents

Dedication	ii
Acknowledgements	iii
List of Tables	ix
List of Figures	x
Abstract	xxiii
Chapter 1 Introduction	1
1.1 Overview of kirigami uses in engineering	1
1.2 Prior implementations of linear kirigami-based solutions	3
1.3 Overview and organization of this dissertation	4
Chapter 2 Mechanical Properties of Rotationally Symmetric Kirigami Structure	6
2.1 Prior mathematical implementations of origami and kirigami to conform to curved surfaces	6
2.2 Order of rotational symmetry in kirigami structures	8
2.3 Design parameters influencing the mechanical properties of RSK springs	10
2.3.1 Experimental and FEA results	10
2.3.2 Cantilever beam theory	18
2.4 Finite-element modeling setup of RSK springs	21
2.4.1 Fabrication and testing of stiffer materials	24
2.5 Summary	33
Chapter 3 Kirigami-Based Sensor Platform for Joint Motion Tracking	34
3.1 Introduction	34
3.2 RSK structure as platform for sensing	37
3.3 Summary	45
3.4 Need for a fully wireless device	45
3.4.1 Circuit design	46
3.4.2 Fabrication method	47
3.4.3 Further work	48
Chapter 4 Multi-Axis Optical Tracking System	53

4.1 Overview	53
4.2 Introduction	54
4.2.1 Previous kirigami solar tracker designs	54
4.3 Kirigami design, fabrication, and testing of the compliant mechanism	62
4.3.1 Baseline hexagonal kirigami spring	62
4.3.2 Mechanical testing setup	66
4.3.3 Influence of varying cut parameters	67
4.3.4 Assembly of kirigami tracking system and methods	69
4.3.5 Electrode pattern and physical demonstration of kirigami solar tracking array	77
4.4 Thermal considerations and impact on efficiency of a unit cell	78
4.5 Shadowing effects in the kirigami tracking array	80
4.5.1 Shadowing of nearby concentrators calculations	82
4.5.2 Calculating the total rooftop area for a silicon stationary panel to meet the daily energy requirement	89
4.6 Summary and conclusions	92
4.7 Future work on modifying system design to reduce thermal effects	93
Chapter 5 Tunable Periodic Arrays for High Electromagnetic Absorption	98
5.1 Overview	98
5.2 Introduction	99
5.2.1 Shielding efficiency and reflection loss	100
5.2.2 Prior implementations for modulating internal reflections	105
5.2.3 Applying kirigami for EM absorption	106
5.3 Modeling the kirigami-based polymer composites	107
5.3.1 COMSOL setup	107
5.3.2 Modeling results	109
5.4 Methods	111
5.4.1 Fabrication of solution	111
5.4.2 Fabrication of film	111
5.4.3 Measurement setup	113
5.5 Experimental results	113
5.6 Summary and conclusions	114
5.7 Future work	115
Chapter 6 Additional Applications and Future Work	116
6.1 Design space of kirigami-based shape memory materials	116

6.1.1 Shape memory polymers	117
6.1.2 Shape memory alloys	121
6.2 Mechanotransduction platform to promote cardiomyocyte maturation	125
6.3 Redesigning N95 masks	132
6.4 Additional applications	134
Appendix	135
Bibliography	137

## List of Tables

<b>Table 2.1</b> Design parameters associated with Figure 2.5. <sup>29</sup> .....	12
<b>Table 2.2</b> Material properties used for FEA models and reference for input stress-strain data... 27	
<b>Table 4.1</b> Example displacement coordinates corresponding to Figure 4.9i. ....	68
<b>Table 4.2</b> Breakdown of calculating the energy density and rooftop area for two scenarios. <sup>68</sup> ... 87	
<b>Table 4.3</b> Numerical values corresponding to Figure 4.24. ....	96
<b>Table 6.1</b> Variables for kirigami-based SMP design and testing, including cut parameters and material properties.....	118
<b>Table A.1</b> Database of kirigami-based engineering solutions, sorted by application.....	135



## List of Figures

**Figure 1.1** Examples of origami<sup>2</sup> (left) and kirigami<sup>3</sup> (right). ..... 1

**Figure 1.2** Origami engineering applications. (a) architectural buildings,<sup>4</sup> (b) shock absorbers,<sup>5</sup> (c) deployable solar panels in space,<sup>6</sup> and (d) stents.<sup>5</sup>..... 2

**Figure 1.3** Linear kirigami pattern applied in a variety of applications. From left to right: solar tracking,<sup>9</sup> tunable diffraction gratings,<sup>15</sup> triboelectric nanogenerators,<sup>12</sup> health-monitoring applications.<sup>25</sup> ..... 4

**Figure 2.1** Experimental representation of conformation to curved surface using fractal cutting with example cut patterns.<sup>26</sup> ..... 7

**Figure 2.2** “Design of developable surfaces using kirigami tessellations: (a) the target cylindrical surface and (b) the kirigami array approximating the surface (front view). A piecewise-linear curve passes through  $P_i$  ( $i=1, 2; 3\dots$ ): (c) the kirigami array before bending (front view), which is the last configuration of step 1 and (d)–(g) folding process of the kirigami array. (d)  $\rightarrow$  (e)  $\rightarrow$ (f): step 1, shrinkage of the array. (f)  $\rightarrow$  (g): step 2, bending of the array, (h)–(k) kinematics of eight quadrilaterals surrounding one rhombus cut during folding, corresponding to (d)–(g), rectangular plates labeled by I are kept coplanar during step 1, whereas plates labeled by II and III inclined. The four sides of the rhombus coincide into one line after folding.”<sup>28</sup> ... 8

**Figure 2.3** Rotating linear axis along the central axis to generate new patterns. Symmetry groups are given based on the outer perimeter’s shape, with the understanding that the interior cut pattern may belong to a lower order rotational symmetry group. .... 9

**Figure 2.4** Classification system used to define the order of rotational symmetry..... 10

**Figure 2.5** Comparison of experimental and FEA models of PET at a displacement of 50 mm, having the same thickness ( $t = 0.09$  mm). (a-e) represents symmetric cuts that vary in the radial spacing ( $w$ ), angular spacing ( $\phi$ ), and number of cuts along the perimeter ( $N_{pc}$ ). (f) depicts the kirigami structure having unequal radial spacings. (g) is a normal helical conical spring, having one continuous cut.<sup>29</sup> ..... 11

**Figure 2.6** Experimental and FEA force-displacement curve for baseline pattern. Overlaid images above the curve show experimental and FEA samples deflected at 29 mm. Insets to the right and below depicts FEA results at a large displacement of 152 mm and closeup image of local strain, at a concentrated force of 5 N; color bar represents logarithmic strain potential (%).<sup>29</sup> ..... 13

**Figure 2.7** Experimental setup for uniaxial tensile testing.<sup>29</sup> ..... 14

**Figure 2.8** RSK spring modelled as a combination of rings. .... 15

**Figure 2.9** Logarithmic force versus displacement curves depicting the mechanical properties of various cut patterns. Varying (a) number of cuts along the perimeter, (b) angular spacings, and (c) radial spacings.<sup>29</sup> ..... 17

**Figure 2.10** Segments of the deformed ring represented as beams in bending modeled based on the cantilever beam theory. (a) For two cuts along the perimeter, part of the ring having a positive slope is represented as two beams and the entire ring is broken into eight beams, so the force applied to one beam is one eighth the total force applied to the entire ring. The experimental results and analytical model are shown (b)-(d) based on the number of cuts along the perimeter where  $\Delta R = 3\text{mm}$  and  $\phi = 10^\circ$  with overlaid FEA models displaced by 50 mm.<sup>29</sup> ..... 18

**Figure 2.11** (a) and (b) optical microscope images of the cut width, scale bars indicate 500  $\mu\text{m}$ .  
(c) Scanning electron microscope image of the RSK spring, scale bar indicates 500  $\mu\text{m}$ ..... 21

**Figure 2.12** Physical model and schematic representing the load and boundary conditions for the single ring model, as well as the FEA model showing the concentrating point load and pinned boundary condition for the single ring and full kirigami model.<sup>29</sup> ..... 22

**Figure 2.13** Stress and displacement of FEA simulations. (a) Top view of deformed spring depicting the distribution of stress across the spring, based on Von Mises Criterion, where the scale bar is in GPa. The close-up is of the concentration of stress at the cut ends. (b) Side view of deformed spring, where the color bar indicates displacement in mm.<sup>29</sup> ..... 23

**Figure 2.14** Exploded isometric (a) and side view (b) of a CAD model of the steel parts to clamp the kirigami samples for tensile testing..... 25

**Figure 2.15** Uniaxial tensile tests results of RSK springs made of (a) steel, (b) aluminum, and (c) kapton. (d) Log force versus displacement of steel, aluminum, and kapton at a displacement rate of 0.25 mm/s. .... 26

**Figure 2.16** FEA setup. (a) Mesh and (b) boundary conditions and applied load. .... 28

**Figure 2.17** Experimental and FEA results of kapton RSK spring. (a) Force versus displacement plot at 0.25 and 5 mm/s, as well as FEA results. Inset shows experimental and FEA models at a displacement of 81 mm. The color legend represents displacement in mm. (b) Corresponding FEA model representing the stress distribution with zoomed-in figure of cut ends. The color legend represents Von Mises Stress in MPa..... 29

**Figure 2.18** Force vs. displacement of an aluminum RSK spring loaded to different displacements to examine the hysteresis. (a) shows overlaid images post testing on

the top and during testing below at 60, 40, and 20 mm. (b) is a close-up indicated by the dash box in (a). ..... 31

**Figure 2.19** Uniaxial tensile and compression tests performed on steel RSK springs, as well as FEA results (a) and experimental results at lower displacements (b). ..... 32

**Figure 3.1** RSK structures approximating different curved surfaces. a) RSK springs assume the shape of an orange and (b) an acorn squash; schematic of cut pattern on left and physical model on right. c) Baseline cut pattern delineating the cut parameters and deformation states of the physical and FEA model displaced to 50mm (color bar indicates displacement in mm).<sup>29</sup> ..... 36

**Figure 3.2** Placement of strain sensors on RSK platform. a) top view of cut kirigami spring based on geometry of shoulder. b) Cross-sectional view of RSK-based device depicting the locations of sensing elements with respect to the kirigami platform, flexible adhesive, and skin. c) Sub-unit ring deformed shows the placement of strain sensors placed at the maximum degrees of curvature, which is at the start and ends of the cuts. d) Top and front view of device with bonded strain gauges placed on subject's shoulder without adhesive tape.<sup>29</sup> ..... 39

**Figure 3.3** Tracking motion of raising and lowering arm. a) Skeleton representation of body at neutral position and skeleton with arm raised up to 140o with coordinate system used by the image processing software and elevation angle,  $\theta$ . b) 3D plot representing elevation angle as a function of change of resistance and time in seconds. c) Kirigami sensing device at 0°, 79°, and 120°, represented in (i), (ii), and (iii), respectively.<sup>29</sup> ..... 40

**Figure 3.4** Schematic of the planes of motion (a) humeral elevation angle, (b) humeral plane of elevation, and (c) neutral position of body.<sup>29</sup> ..... 41

**Figure 3.5** Changes in resistance and corresponding angular positions as various motions are performed. From left to right: schematic of motion performed, plot of change of

resistance versus time for two linear strain gauges placed on the RSK substrate, and a plot of the angular positions as a function of time. The three defining planes and axis of motion is plane of elevation angle, elevation angle, and rotation. a) Arm circle backwards, (b) running, (c) arm rotation, (d) shrugging shoulders, and (e) arm across body parallel to ground.<sup>29</sup> ..... 44

**Figure 3.6** Schematic of circuit design for embedding integrated circuit (IC) components to the kirigami sensor platform. .... 46

**Figure 3.7** Diagram of wireless kirigami device (not to scale)..... 47

**Figure 3.8** Top (left) and iso view (right) of kirigami flex pcb after laser-cutting and bonding strain gauges..... 48

**Figure 3.9** Application requirements and additional capabilities of the device..... 49

**Figure 3.10** Integration of kirigami platform with augmented reality used to track joint positions. .... 51

**Figure 3.11** Modification of RSK pattern to conform to foot and back. (a) CAD pattern and laser-cut substrate (b) to fit the shape of the foot. (c) Laser-cut plastic sheet designed to conform to the lower back. .... 52

**Figure 4.1** Basic principle of how kirigami can be used as a solar-tracker. a Relaxed substrate (left) and b stretched substrate (right). b Planar tracker laid flat with sun directly above (left) and tracker tilted to track the position of the sun.<sup>9</sup> ..... 56

**Figure 4.2** Low-profile solar tracking system based on kirigami design principles. (a) represents a top view schematic of the tracking array module. (b) shows a side view of the tracker under different axial strains. (c) shows physical models of the Au interconnects (top view), location of the GaAs PV cell and concentrator arms that define the angle of rotation (side view) and the tracker under axial strain. .... 58

**Figure 4.3** Actuation energy of the concentrator every 125 cycles. Discontinuities are due to instrument limitations, which re-quired the resetting of the tracking mechanism after reaching 875 repeat cycles. .... 59

**Figure 4.4** Limitations of single-axis kirigami solar tracker. (a) Delamination of top and bottom sheets and limited angle of rotation. (b) Difference between fill factor with and without cooling, showing performance depends on temperature of the cell.<sup>64</sup> ..... 60

**Figure 4.5** Progression of kirigami-based solar tracking system designs. .... 61

**Figure 4.6** Tilting mechanism of a hexagonal kirigami spring. a) Left: side view of FE model of a deformed spring displaced 45 mm in the z-direction, middle: side view and right: top view of model displaced 25 mm in the x-direction and 45 mm in the z-direction; color bar indicates normalized stress. b) Experimental measurement of tilt angle based on displacement in the x-direction maintaining a height of 35 mm with linear fit. c) Work required to shear the spring in the x-direction by 25 mm for up to 20,000 cycles, maintaining a height of 35 mm. d) FE model of deformed array arranged in a honeycomb pattern in the x-direction at  $\delta=0$  mm (left) and  $\delta=25$  mm (right) where  $z=35$  mm. e) Side view of deformed physical array arranged in a rectangular pattern for visual clarity at  $\delta=0$  mm (top) and  $\delta=25$  mm (bottom) in the x-direction where  $z=35$  mm.<sup>68</sup> ..... 63

**Figure 4.7** Uniaxial and shear tests of unit cell. a) Force vs displacement plot of unit cell undergoing uniaxial tensile test and (b) undergoing shear test along the x-direction.<sup>68</sup> ..... 65

**Figure 4.8** CAD model of cyclic tester, consisting of DC steppers powering lead screws, aluminum frames to hold unit cells and stage connected to motors.<sup>68</sup> ..... 67

**Figure 4.9** Key cut parameters dictating cut pattern: radial spacing ( $w$ ), the cut phase angle ( $\Phi$ ), the cut phase shift ( $\gamma$ ), and number of cuts along the perimeter. (a) Represents the baseline pattern having a radial spacing of 0.75 mm, cut phase angle of  $6^\circ$ , and cut

phase shift of  $0^\circ$ . (b) Differs from the baseline pattern by decreasing the radial spacing to 0.5 mm. (c) Decreased cut phase angle by  $3^\circ$ , and (d) cut phase shift of  $12^\circ$ . The shape of the pattern can also be altered to form shapes other than a hexagon, such as a rectangle or circle.  $\theta$  as a function of  $\delta$  varying  $w$  (e),  $\phi$  (f), and  $\gamma$  (g) when displaced in the  $x$ - and  $y$ -directions.  $\theta_{\max}$  as a function of  $z$  (h) in the  $x$ -direction and  $\theta_{\max}$  as a function of  $\delta$  of the base along the polar coordinate direction (i). The legend refers to the amount of displacement (mm).<sup>68</sup> ..... 69

**Figure 4.10** Assembly of kirigami tracking system. (a) Laser-cutting sheet to kirigami pattern. (b) Fabricate concentrator array via vacuum thermoforming where a plastic sheet is placed on mold and then a metal coating is deposited, and the concentrators are laser-cut into the individual concentrator. (c) Top view of kirigami cut pattern with outline showing location of concentrator and insert, and side view of FE model depicting the assembly of the tracker with a concentrator.<sup>68</sup> ..... 70

**Figure 4.11** Tilting mechanism of a kirigami hexagonal spring with concentrators embedded in the middle ring. (a) Top view and side view of the tracker with kirigami cut pattern and locations of the concentrator, photodiode or photovoltaic cell, and electrodes. (b) Images of kirigami spring deformed at  $z = 45$  mm with concentrator placed in middle ring (left) and displaced  $\delta = 25$  mm in the  $y$ -direction, prompting the concentrator to tilt  $\theta = 37^\circ$  (right). A and B represent pivot points at the edge and corner of the pattern, respectively. (c) Experimental measurements of the tracker displaced in the  $x$ - or  $y$ -direction at deformed lengths of 33 and 45 mm. Inset represents cut pattern.<sup>68</sup> ..... 72

**Figure 4.12** Tilt angle vs displacement of concentrator facing up or down. (a) Solid symbols represent the concentrator facing down and the open points represent the concentrator facing up ( $z = 35$  mm). The circle symbol represents translation in the  $x$ -direction and the triangular symbol represents translation in the  $y$ -direction. (b)  $\delta = 0$  (c)  $\delta = 25$  mm in  $x$ -direction, resulting in tilt angle of  $40^\circ$ .<sup>68</sup> ..... 73

**Figure 4.13** Varying cut parameters affect maximum tilt angle and shift. (a) Schematics of cut pattern 1 (P1) and cut pattern 2 (P2). (b) Experimental measurements of the tilt angle as a function of displacement for P1 (solid symbols) and P2 (open symbols) and the shift from the median on the right y-axis in red. Inset of the spring with concentrator facing down, showing shift  $\mu = 15$  mm and tilt angle  $\theta = 47^\circ$  in the y-direction at  $z = 35$  mm.<sup>68</sup> ..... 74

**Figure 4.14** Tracking performance of the kirigami spring integrated with mini concentrators in x-direction. (a) Top view of tracker, depicting cut pattern of kirigami spring; the concentrator, photodiode, and electrodes locations; and placement of probes for measuring the electrical current. (b) Side view of electrical measurement setup, in which the spring tilts to maintain its position with the light source at various angles. (c) Experimental measurements of the short circuit current to the initial short circuit current at various tilt angles of the tracker and stationary systems. Blue circles with error bars represent tracking system, and red diamonds represent stationary system with schematics represent  $\theta=0^\circ$  and  $\theta=\pm 22^\circ$ .<sup>68</sup> ..... 75

**Figure 4.15** Tracking performance of the kirigami spring integrated with mini concentrators in y-direction. (a) Top view of tracker depicting cut pattern of kirigami spring, concentrator, photodiode, and electrodes, as well as placement of probes for measuring the electrical current. (b) Side view of electrical measurement setup, in which the spring tilts to maintain its position with the light source at various angles. (c) Experimental measurements of the short circuit current to the initial short circuit current at various tilt angles of the tracker and stationary systems. Green squares with error bars represent tracking system, and red diamonds represent stationary system with schematics represent  $\theta = 0^\circ$  and  $\theta = \pm 22^\circ$ . Deviations from 100% normalized current density are attributed to PV cell misalignment with the focal spot of the concentrator due to manual assembly for the test.<sup>68</sup> ..... 76



**Figure 4.16** Example honeycomb arrangement of cells with embedded electrodes. (a) CAD drawing of electrode pattern within the hexagonal cells and (b) physical model of one-unit cell..... 78

**Figure 4.17** Theoretical thermal effects of the cell on conversion efficiency and energy. (a) Schematic illustration of the types of heat dissipation in the solar cell. (b) Respective thermal circuit diagram with radiation, convection and conduction load. (c) Temperature and efficiency as a function of concentration factor where  $R_{cool} = 10^{-1} \text{ K}\cdot\text{m}^2/\text{W}$ . (d) Temperature and (e) daily accumulated energy versus logarithmic CF with cooling resistance equal to  $10^{-1}, 10^{-2}, 10^{-3} \text{ K}\cdot\text{m}^2/\text{W}$ .<sup>68</sup> ..... 79

**Figure 4.18** Effect of shadowing on the performance of solar trackers. (a) Schematic of solar array on the roof of a house and close-up of the cut pattern array with shaded area representing the area extent of displacing the tracker by 25 mm;  $L$  represents the length and  $W$  represents the width between concentrators. (b) Side view of packed neighbor concentrators, where  $\theta$  is the tilt angle and  $d$  is the shadowing area. (c) Total instantaneous power output produced by average  $180 \text{ m}^2$  rooftop area versus time of a day. Assuming 30% conversion efficiency and cooling resistance equal to  $10^{-3} \text{ K}\cdot\text{m}^2/\text{W}$ . Inset: energy accumulated over the day. d) Comparison of materials consumption and rooftop area needed to meet daily energy requirement at  $CF = 182$  with different  $W$ , assuming daily energy requirement equal to 30 kWh.<sup>68</sup> ..... 81

**Figure 4.19** Schematics showing shadowing of nearby concentrators. (a) Cut pattern array with shaded area representing the area extent of displacing the tracker by 25 mm;  $L$  represents the length,  $W$  represents the width between concentrators,  $D$  represents the length of the array, and  $a$  represents the edge length of the concentrator.  $A_{unit}$ ,  $A_{cell}$ , and  $A_{conc}$  represent the area of the unit, the photovoltaic cell, and concentrator, respectively. (b) Side view of packed neighbor concentrators, where  $\theta$  is the tilt angle and  $d$  is the shadowing area. (c) Side view of two nearby concentrators represented as rectangles, where  $\theta_o$  represents the critical angle when a shadow appears.<sup>68</sup> ..... 83

**Figure 4.20** Shadowing of concentrators and cell temperature influences on energy density, area, and cost, having a maximum tilt angle  $\theta=55^\circ$ . (a) Energy density as a function of CF with varying W. (b) Total rooftop area and (c) materials consumption ratio needed to meet daily average energy requirement. (d) Comparison of energy density, required rooftop area, and materials consumption ratio as a function of CF when  $W = L$ .<sup>68</sup> . 90

**Figure 4.21** Comparison of energy harvesting between four systems: GaAs dual axis trackers, GaAs single axis trackers, GaAs stationary system and Silicon stationary system. (a) Energy accumulated by per area of unit cell on four typical days in one year where the inset depicts the energy density produced over the year. Assuming energy conversion efficiency of GaAs and Si equal to 30% and 20%, respectively. (b) Energy accumulated per area of 1 m<sup>2</sup> panel where the inset depicts the energy density produced over the year.<sup>68</sup> ..... 91

**Figure 4.22** List of key design parameters used for modifying the kirigami tracking mechanism. This includes variations in the cut pattern, height of the deformed spring, material, and device application. .... 92

**Figure 4.23** CAD model (a) and FEA results (b) of the kirigami spring-fresnel lens assembly.. 94

**Figure 4.24** Schematics of heat transfer when PV cell is placed on a heat sink. (a) Diagram of the components of heat transfer between GaAs and Al. Side (b) and top (c) views of an FEA model of the RSK spring with embedded Fresnel lens and GaAs PV cell on an Al heat sink..... 95

**Figure 4.25** Heat dissipation surface effects of a kirigami spring with lens insert. (a) Cell temperature with no heat dissipation surface and (b) heat sink with a thickness of 1 mm..... 97

**Figure 5.1** Electromagnetic spectrum representing a broad frequency range including examples of applications in each range.<sup>72</sup> ..... 100

<b>Figure 5.2</b> Schematic of EM wave components interacting with a material. ....	101
<b>Figure 5.3</b> EM wave interactions with EMI shielding material and skin depth representation as a function of distance from the edge of the shielding material. <sup>79</sup> .....	103
<b>Figure 5.4</b> Example reflection loss broad and peak curves, as well as key factors influencing shielding performance. ....	104
<b>Figure 5.5</b> Linear kirigami pattern unstretched (a), stretched top view (b), and stretched side view (c). ....	107
<b>Figure 5.6</b> Electrical permittivity (a) and magnetic permeability (b) used to carry out the electromagnetic wave simulations. ....	108
<b>Figure 5.7</b> Diagram of COMSOL setup for simulating EM waves through a multi-layer stack. ....	109
<b>Figure 5.8</b> Comsol results of kirigami-based graphene composite. (a) Reflection loss as a function of frequency varying pore geometry. (b) Top and iso view of kirigami honeycomb unit cell. 3D visualization of the electric (c) and magnetic (d) fields at 6.7 GHz corresponding to the geometry in (b). ....	110
<b>Figure 5.9</b> Fabrication method of a thin, kirigami-based carbon composite film using a drop-cast, doctor-blade method. ....	112
<b>Figure 5.10</b> GNP/PDA-PVA film after drop-cast, doctor-blade method. (a) solid film, (b) laser-cut film unstretched, and (c) laser-cut film stretched. ....	113
<b>Figure 5.11</b> Shielding efficiency of the kirigami-based GnP/PDA-PVA composite normalized with the neat shielding efficiency. The inset shows a schematic of the kirigami cut pattern and its dimensions are shown in mm. ....	114

<b>Figure 6.1</b> Storage modulus and tan delta as a function of temperature of epoxy-based shape memory polymer obtained via DMA. ....	118
<b>Figure 6.2</b> Linear kirigami pattern schematic, in which the dimensions are in mm. ....	119
<b>Figure 6.3</b> Thermomechanical test results of kirigami SMPs. (a) Varying temperature, (b) varying displacement rate where the inset shows the stretched SMP, and (c) varying dwell temperatures. ....	120
<b>Figure 6.4</b> Heat flow as a function of temperature of nitinol obtained via DSC. ....	121
<b>Figure 6.5</b> SEM images of micromachined NiTi at (a) 40x, (b) 230x, and (c) 1,500x. Scale bars represent 200 $\mu\text{m}$ , 100 $\mu\text{m}$ , and 10 $\mu\text{m}$ , respectively. ....	122
<b>Figure 6.6</b> Uniaxial tensile test results of kirigami-based NiTi samples at a displacement rate of 0.1 mm/s. (a) Tensile tests to failure; inset shows a kirigami SMA sample deformed to around 3 mm. (b) Thermomechanical test after two cycles to 1 mm at 25°C, 45°C, and 60°C. The inset is a schematic of the cut pattern in mm. ....	124
<b>Figure 6.7</b> Top and iso exploded view of CAD models of the kirigami substrate between a puncher and alignment tool. ....	126
<b>Figure 6.8</b> Experimental and FEA models of kirigami platform. Iso view (a) and side view (c) of 96-well plate platform. (b) FEA model top and side view of a single unit cell. The color legend refers to the Von Mises stress in GPa. ....	127
<b>Figure 6.9</b> Uniaxial force versus displacement plot of 96-well plate substrates experiencing different pre-stress treatments. ....	128
<b>Figure 6.10</b> Uniaxial force versus displacement plot of 18-well plate substrates experiencing different pre-stress treatments and the inset is a close up showing multi-stable states. ....	129

**Figure 6.11** Full and mini arrays with and without an initial bias before testing. Inset is a close-up of the force versus displacement without bias and with bias 2. .... 130

**Figure 6.12** Bending stiffness of one post for the kirigami pattern with two posts per well (a) and one post per well (b). .... 131

**Figure 6.13** RSK-based mask. (a) N95 mask CAD model, (b) knitted fabric mask, (c) CAD pattern of RSK-based mask, (d) top view and (e) iso view of pattern cut out of Al, as well as FEA model (f). The color legend indicates displacement in mm. .... 133

**Figure 6.14** Kirigami springs applications. .... 134

## Abstract

I use kirigami techniques to create high performance, 3-dimensional structures, mechanisms, and multi-functional devices with applications in wearable electronics, optomechanical systems, solar energy harvesting, and electromagnetic wave propagation. *Kirigami* refers to cutting or creating negative space in a material. This design technique is used to create sophisticated 3D structures and devices starting from flat sheets to achieve unprecedented capabilities and performance that would be difficult to achieve using conventional fabrication approaches.

I first explore novel rotationally symmetric kirigami (RSK) structures and their mechanical properties using a combination of experiments, analytical, and finite element modeling. I also show and analyze how the cut pattern influences the structure's cross-plane deformation, enabling the shape to assume globally curved surface contours without wrinkling or buckling the material. This analysis enables a number of different applications, which are discussed below.

I then study the stress and strain distribution across the kirigami structure conforming to a curved surface envelope, where the localization of stress at the saddle-points in the kirigami structure relates to the degree of curvature upon deformation. Rigid electronic components can be integrated with the shape in its flat state without stressing the components upon deformation, making it compatible with mass-manufacturing processes. I also show how other components – i.e., strain gauges – can be placed in regions of substantial strain to measure small deformations. These effects are leveraged to create an inexpensive wearable sensor platform that conforms to the shoulder joint to monitor complex motion and muscle behavior, which are notoriously challenging

to track. This may help facilitate rehabilitation, athletic training, feedback control for augmented mobility, robotics, and other applications.

Using the concept of a closed shape and rotational symmetry of cuts, I demonstrate a multi-axis optical tracking system. Here, out-of-plane deformation and linear translation induces simultaneous tilting of a subset of beams enabling its use as a tracking mechanism. One application of this mechanism is for daily and seasonal tracking of the sun, which I demonstrate by integrating thermoformed concentrators and high efficiency photovoltaic cells with the kirigami structure. Over  $110^\circ$  tracking range and an 80x concentration factor can be achieved while maintaining the height of the tracking array to less than 4 cm. The array is actuated by a finite (e.g., 2.5 cm) lateral displacement irrespective of array size. This work potentially opens the path to substantially lowering the cost of electricity from photovoltaic panels in space-limited areas.

In addition, I explore the use of other materials in kirigami structures to achieve emergent properties for other applications. The use of polymer composites to enhance the absorption of electromagnetic waves for EMI shielding is demonstrated. Other examples include shape memory alloys and polymers to enable reconfigurable structures for aerospace, automotive, medical, robotics, or flexible electronic applications, as well as a dynamic 3D platform designed to promote cardiomyocyte maturation.

# Chapter 1 Introduction

## 1.1 Overview of kirigami uses in engineering

For centuries, people have taken pieces of paper and folded them to create intricate artistic objects, known today as origami. While it is speculated to have originated in China 2,000 years ago, presumably the first documented use of origami dates back to 1680 in Japan. It is in Ihara Saikaku's short poem that origami was described as a way to wrap sake bottles at wedding ceremonies.<sup>1</sup> A similar art form known as *kirigami* involves the use of both folding and cutting. The terms origami and kirigami share the same root *kami* meaning “paper”, and their prefixes *ori* and *kiri* refer to the act of “folding” and “cutting”, respectively. Examples of the two types of ancient arts are demonstrated in **Figure 1.1**.



**Figure 1.1** Examples of origami<sup>2</sup> (left) and kirigami<sup>3</sup> (right).

Recently, many engineering disciplines have begun to leverage sole art forms, *origami* and *kirigami*, as design tools to solve a variety of technical challenges. In the past decade, origami has been used to design new architectural buildings,<sup>4</sup> shock absorbers,<sup>5</sup> deployable solar panels in



space,<sup>6</sup> and stents that snap open inside an artery<sup>5</sup> (**Figure 1.2**). More recently, kirigami has been utilized in engineering solutions. The addition of cutting allows for even greater control over the geometric design and system behavior. Because technologies to generate patterns and functional coatings in two dimensions are now highly evolved, it is believed that unprecedented (meta)material properties and device performance can be obtained by combining them with 2D-to-3D transformations enabled by kirigami techniques.

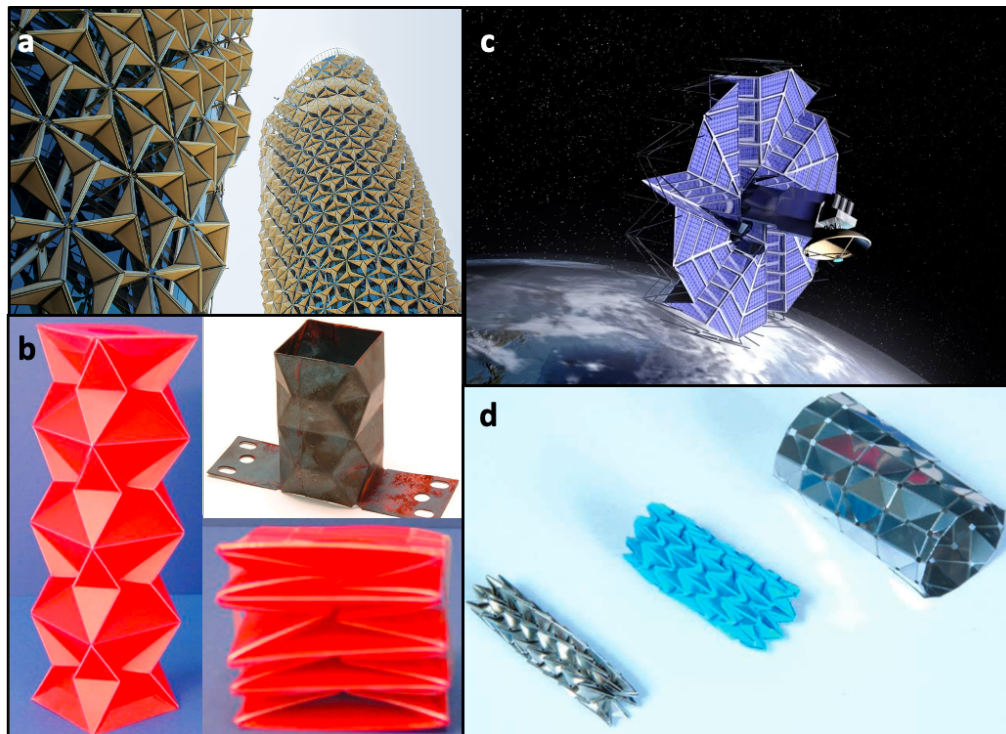


**Figure 1.2** Origami engineering applications. (a) architectural buildings,<sup>4</sup> (b) shock absorbers,<sup>5</sup> (c) deployable solar panels in space,<sup>6</sup> and (d) stents.<sup>5</sup>

Kirigami design principles are effective tools for obtaining highly tunable and flexible structures. Mathematicians, scientists, and engineers across diverse disciplines have proposed ways of predicting new, functional properties and applications of traditional materials,<sup>7,8</sup> including in energy harvesting and optical tracking,<sup>9-13</sup> tunable photonics,<sup>14,15</sup> antennas,<sup>16,17</sup> and soft

robotics.<sup>18,19</sup> Other researchers have also studied origami/kirigami structures as programmable, reconfigurable, and self-actuating metamaterials.<sup>20–22</sup>

Furthermore, generating intricate patterns offers a promising way to scale devices. Through subtractive manufacturing, there have been a variety of ways researchers have introduced cuts into a material. The specific method used corresponds to the length scale and resolution required for the application. The most commonly employed fabrication technique on the macro-scale is laser cutting. The speed and customizability of this technique make it a scalable and cost-effective method for fabricating kirigami patterns. For smaller scale structures, standard lithography techniques can be used to create complex 3D structures ranging from the mesoscale to microscale to nanoscale.<sup>16,17,23</sup> For instance, kirigami-patterned graphene sheets developed using lithography can be strained by over 240% without attenuating electrical conductivity and can potentially be used as sensitive force sensors to study interfacial effects and biological phenomena.<sup>24</sup>

## **1.2 Prior implementations of linear kirigami-based solutions**

The simplest linear kirigami pattern consisting of alternating lines has been one of the most commonly explored structures. Its applications beyond structural and decorative include flexible electronics (e.g. sun-tracking solar cells)<sup>9</sup> and other energy-harvesting (e.g. triboelectric nanogenerator),<sup>12</sup> photonic structures (e.g. tunable gratings),<sup>15</sup> and health-monitoring devices (e.g. electrocardiogram and temperature sensors).<sup>25</sup> The variety of kirigami-based engineering solutions attempted by researchers can be categorized by material, scale, kirigami pattern, application, and year. **Appendix Table A.1** shows a breakdown of published kirigami-based solutions sorted by application.

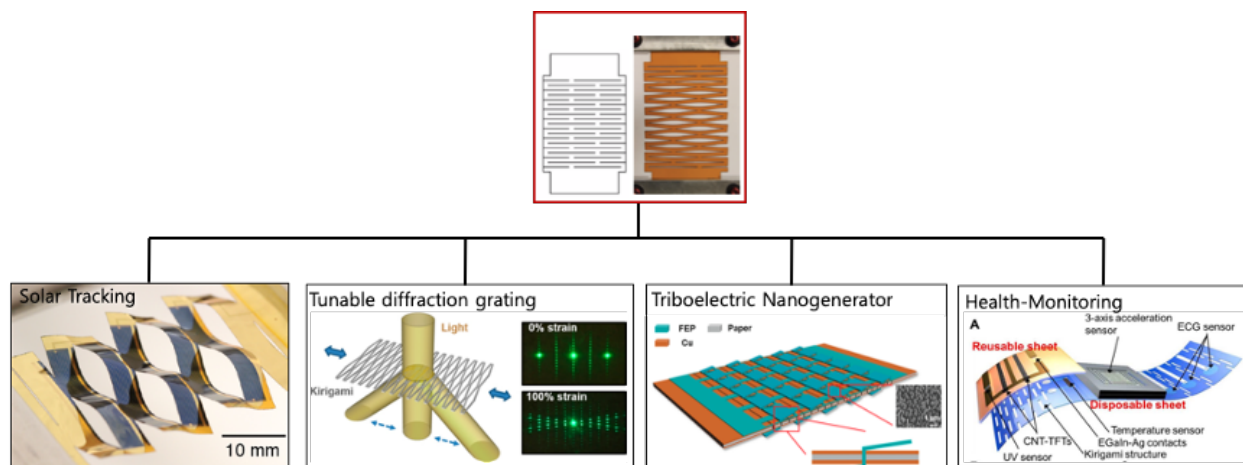


**Figure 1.3** Linear kirigami pattern applied in a variety of applications. From left to right: solar tracking,<sup>9</sup> tunable diffraction gratings,<sup>15</sup> triboelectric nanogenerators,<sup>12</sup> health-monitoring applications.<sup>25</sup>

### 1.3 Overview and organization of this dissertation

This dissertation details the development of kirigami (Japanese art of cutting) approaches to creating sophisticated 3-dimensional structures and devices starting from flat sheets. While the manufacturing of 2-dimensional patterns of functional films and components is well-established in research and industry, many useful structures and applications require 3-dimensional shapes. Integrating flat and rigid electronics with curved topologies is typically very challenging. Herein, kirigami structures are designed, predicted, and analyzed to create devices for wearable sensing, energy-harvesting, and optical tracking devices. In **Chapter 2**, the mechanics and design tools of rotationally symmetric kirigami (RSK) structures are explained, along with the structures' ability to maintain desired electrical properties while undergoing curved surface approximations and large deflections. After understanding the fundamental structure and behavior of RSK springs, this method of geometric manipulation will be implemented to develop a wearable motion tracking device (**Chapter 3**) and then a multi-axis optical tracking system (**Chapter 4**).

While the previous chapters focused on the electrical and optical applications of rotationally symmetric kirigami structures, in **Chapter 5**, a different kirigami pattern is used

leveraging those basic principles. Here, the kirigami substrate is surrounded by two solid polymer composites to achieve higher electromagnetic absorption in the X-band (8-12 GHz) than bulk composites. When the thin kirigami-based film is stretched, it creates a periodic array of pores that act as internal reflectors resulting in high absolute reflection loss.

This dissertation concludes with **Chapter 6**, in which other applications for kirigami are explored. One application considers a redesign of N95 respirators/masks. The COVID-19 pandemic created an unprecedented demand for N95 class respirators, which are desperately needed to help protect against the life-threatening virus. Here, kirigami is applied as a structural element, as well as a carrier for embedded electronics, inside of a knitted, multi-layered fabric. The kirigami interlayer improves conformation to the face's contours allowing for a more comfortable fit and enables smart monitoring of fit and face-touching detection. Additionally, in this Chapter, the use of shape memory alloys and shape memory polymers in the kirigami structure is explored, with thermomechanical tests showing that cuts affect the actuation stress and strain behavior of the material. Shape memory alloys are useful for their high actuation stress and fatigue life but are limited by their low actuation strains. The use of kirigami can potentially break this trade-off and enable new opportunities. Lastly, a scalable, kirigami-based array consisting of rectangular posts is built to fit inside of a standard 96-well assay plate used in biological and pharmacological research and development, with the goal of developing platforms to aid in the maturation of artificial heart tissues used in cardiotoxicity testing. Cyclical stretching and relaxing of the sheet induces a corresponding response to individual posts that are used to mimic the pulsing behavior of cardiomyocytes. A mind map of other potential applications that may benefit from the use of kirigami structures is included.

## Chapter 2 Mechanical Properties of Rotationally Symmetric Kirigami Structure

### 2.1 Prior mathematical implementations of origami and kirigami to conform to curved surfaces

The linear kirigami pattern was shown to impart elasticity to otherwise rigid sheets, enabling several applications, but in applications that require conformation to curved surfaces, the linear cut pattern is unsuitable. For this purpose, fractal cuts and tessellations have been applied. Fractal, derived from the Latin word *fractus* meaning “fragmented”, is an infinitely complex pattern that is self-similar at different levels of magnification, and thus has scaling symmetry. A commonly used example is a snowflake, while others include the Sierpinski gasket or triangle, DNA, trees, and Romanesco broccoli. Tessellations, on the other hand, are repeating geometric shapes, in which no gaps exist between them.

Fractal and tessellation cutting techniques are applied to determine the cuts' arrangement on a planar sheet that is then transformed into a 3D complex shape. Researchers have developed a mathematical foundation for fractal cutting by creating an algorithm that automatically generates a 2D pattern that, when deformed, matches the target 3D shape.<sup>26</sup> In one application, a stretchable electrode fractal pattern was created using silicone rubber coated with an electrically conductive film, wrapped around a spherical baseball without wrinkling, as shown in **Figure 2.1**.<sup>26</sup> The base pattern is shown to have rotating units when a force is applied until moment equilibrium is reached. The final morphology is dependent on the degrees of freedom of the living hinges.

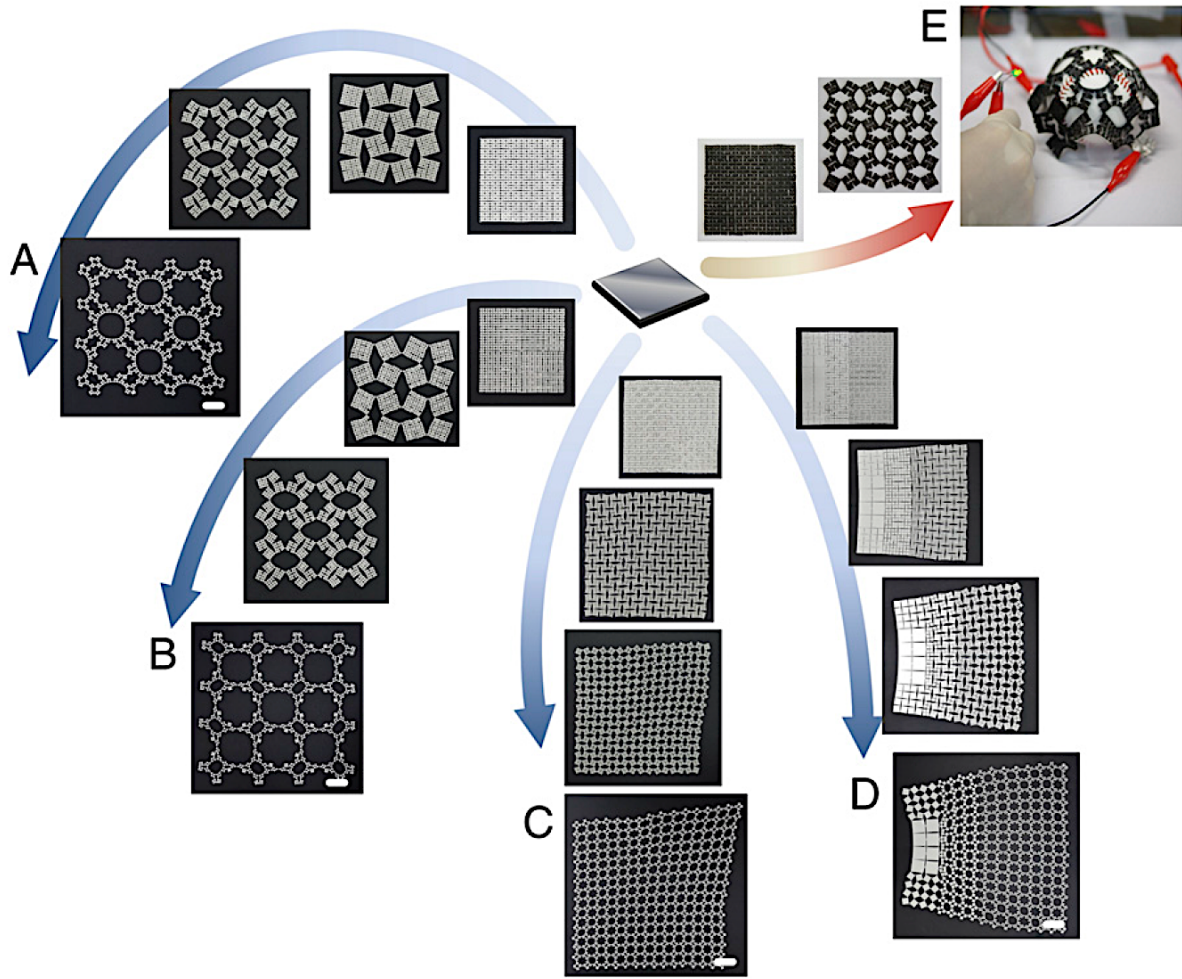


**Figure 2.1** Experimental representation of conformation to curved surface using fractal cutting with example cut patterns.<sup>26</sup>

Similarly, kirigami tessellations have been shown as a way to prescribe a target shape in two or three dimensions.<sup>27,28</sup> The kirigami tessellations have a unique 2D pattern with precisely defined spaces that when activated closes the gaps and creates a repetitive tessellation (e.g. **Figure 2.2** shows a kirigami tessellation conforming to a cylindrical surface).<sup>28</sup> However, this method often requires precise folding to activate the pattern to its final structure, and thus is more time-consuming and less scalable than cuts alone. Furthermore, the surface area of the non-cut area is rather small and could be limiting in some applications.

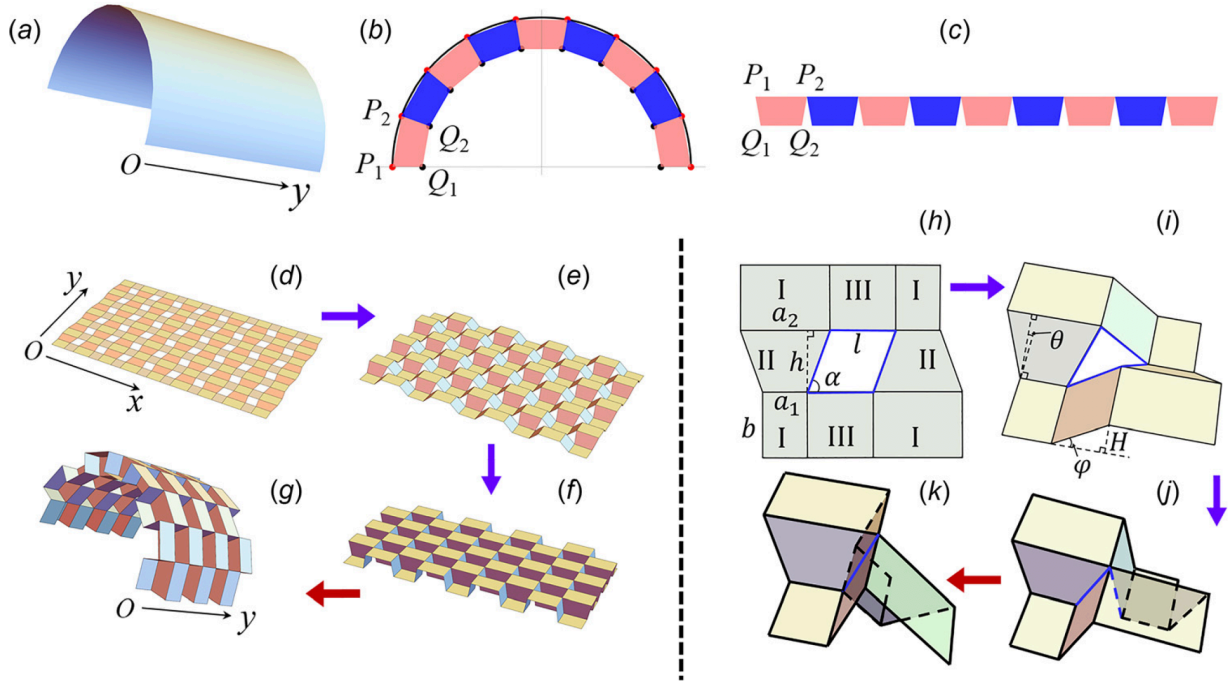


**Figure 2.2** “Design of developable surfaces using kirigami tessellations: (a) the target cylindrical surface and (b) the kirigami array approximating the surface (front view). A piecewise-linear curve passes through  $P_i$  ( $i=1, 2, 3, \dots$ ): (c) the kirigami array before bending (front view), which is the last configuration of step 1 and (d)–(g) folding process of the kirigami array. (d)  $\rightarrow$  (e)  $\rightarrow$  (f): step 1, shrinkage of the array. (f)  $\rightarrow$  (g): step 2, bending of the array, (h)–(k) kinematics of eight quadrilaterals surrounding one rhombus cut during folding, corresponding to (d)–(g), rectangular plates labeled by I are kept coplanar during step 1, whereas plates labeled by II and III inclined. The four sides of the rhombus coincide into one line after folding.”<sup>28</sup>

This chapter focuses on a new method of generating patterns and how variations in the cut parameters influence their mechanical properties. A thin sheet having ordered concentric cuts exhibits an ability to undergo macroscopic stretching to conform to surface envelopes having global Gaussian curvature. A robust way of simulating these structures is shown, using experimentally validated finite-element analysis (FEA) models for different materials.

## 2.2 Order of rotational symmetry in kirigami structures

Novel rotationally symmetric kirigami (RSK) structures are obtained through rotation of the linear kirigami pattern around the central axis, as depicted in **Figure 2.3**. Depending on the number of cuts per side, the order of symmetry can correspond to the symmetry of the overall shape, however the true order of symmetry can be considerably lower if taking the cut pattern into account. For



example, a triangular pattern could be considered to have third order rotational symmetry, albeit this symmetry is not strictly upheld, as not all of the cuts will line up upon a  $120^\circ$  rotation. Patterns having circular outer perimeters thus do not have  $C_\infty$  rotational symmetry with regard to the cut pattern. All shapes exhibit reflection symmetry about their plane, until they are deformed in the cross-plane direction, the mechanics of which produces a spring-like behavior, which for the circular patterns is explored in detail in this chapter.

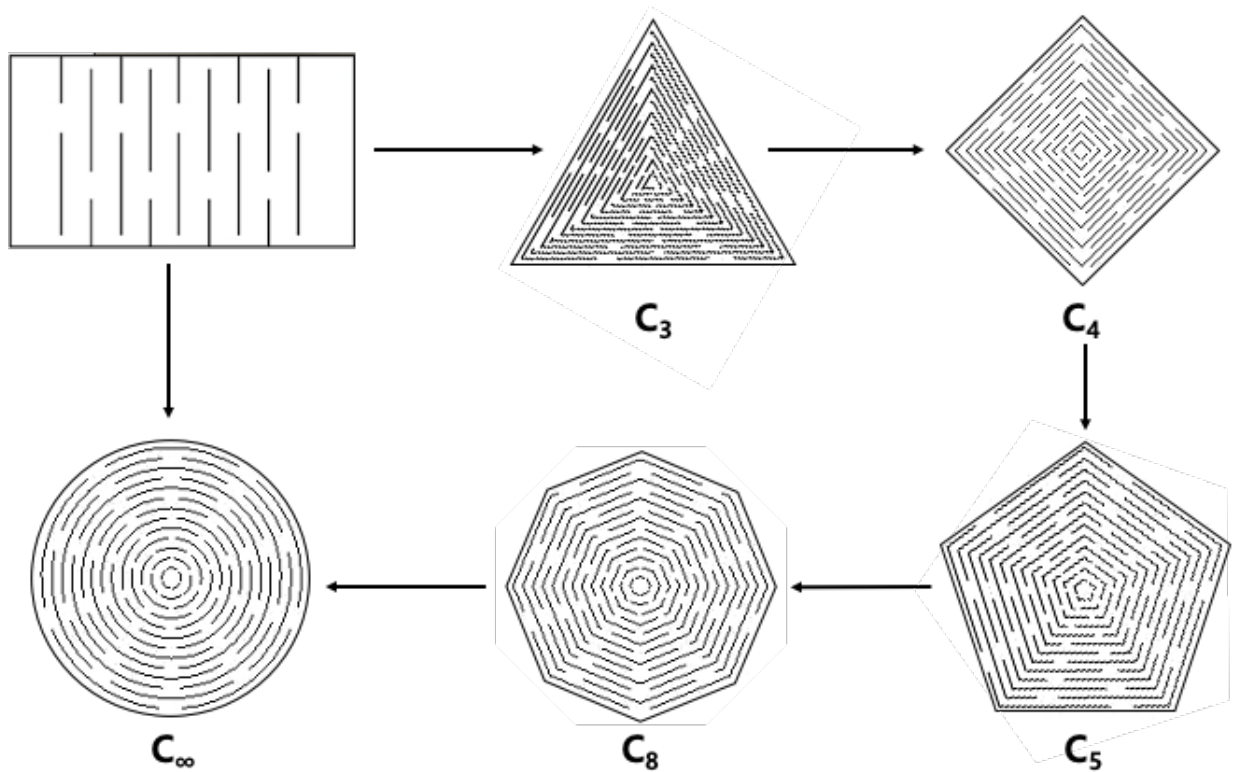


**Figure 2.3** Rotating linear axis along the central axis to generate new patterns. Symmetry groups are given based on the outer perimeter's shape, with the understanding that the interior cut pattern may belong to a lower order rotational symmetry group.

A sub-classification system used to define the circular RSK springs is based on the number of cuts along the perimeter, given the cuts are concentric. As the number of cuts increase, so too does the order of rotational symmetry. For instance, two cuts along the perimeter correspond to second order of symmetry, three cuts correspond to third order, four cuts correspond to fourth



order, and so on (**Figure 2.4**). Later, it will be discussed how the order of symmetry breaks when examining the 3D architecture upon cross-plane deformation.

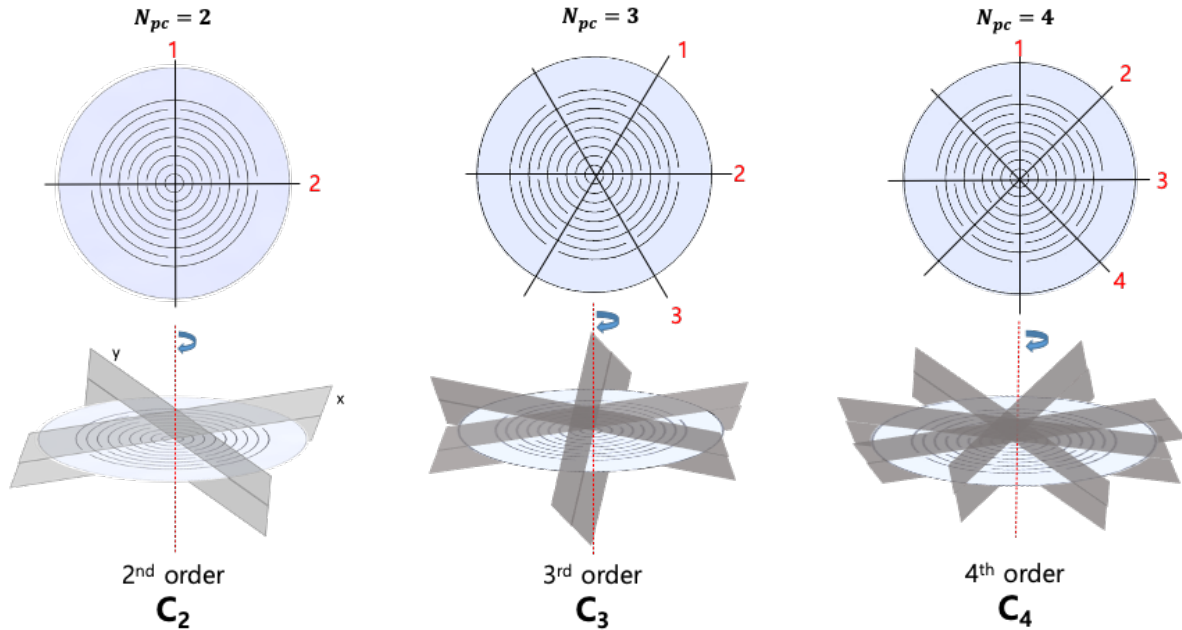


**Figure 2.4** Classification system used to define the order of rotational symmetry.

## 2.3 Design parameters influencing the mechanical properties of RSK springs

### 2.3.1 Experimental and FEA results

Upon cross-plane deformation of the circular kirigami pattern, a RSK spring can conform to a globally curved surface with a shape that can be tailored by changing the cut geometry. **Figure 2.5** illustrates how different cut patterns influence the stretched state where each column represents a specific cut pattern starting with a schematic, followed by physical, and then FEA models. **Figure 2.5a-f** depict RSK springs, while **(g)** shows a normal conical helix spring. The physical models were created by applying a cross-plane displacement of 50 mm to laser-cut polyethylene terephthalate (PET) sheets. The color legends in the last row of panels correspond to the displacement obtained using FEA. More information on the FEA models will be discussed in **Section 2.4**.

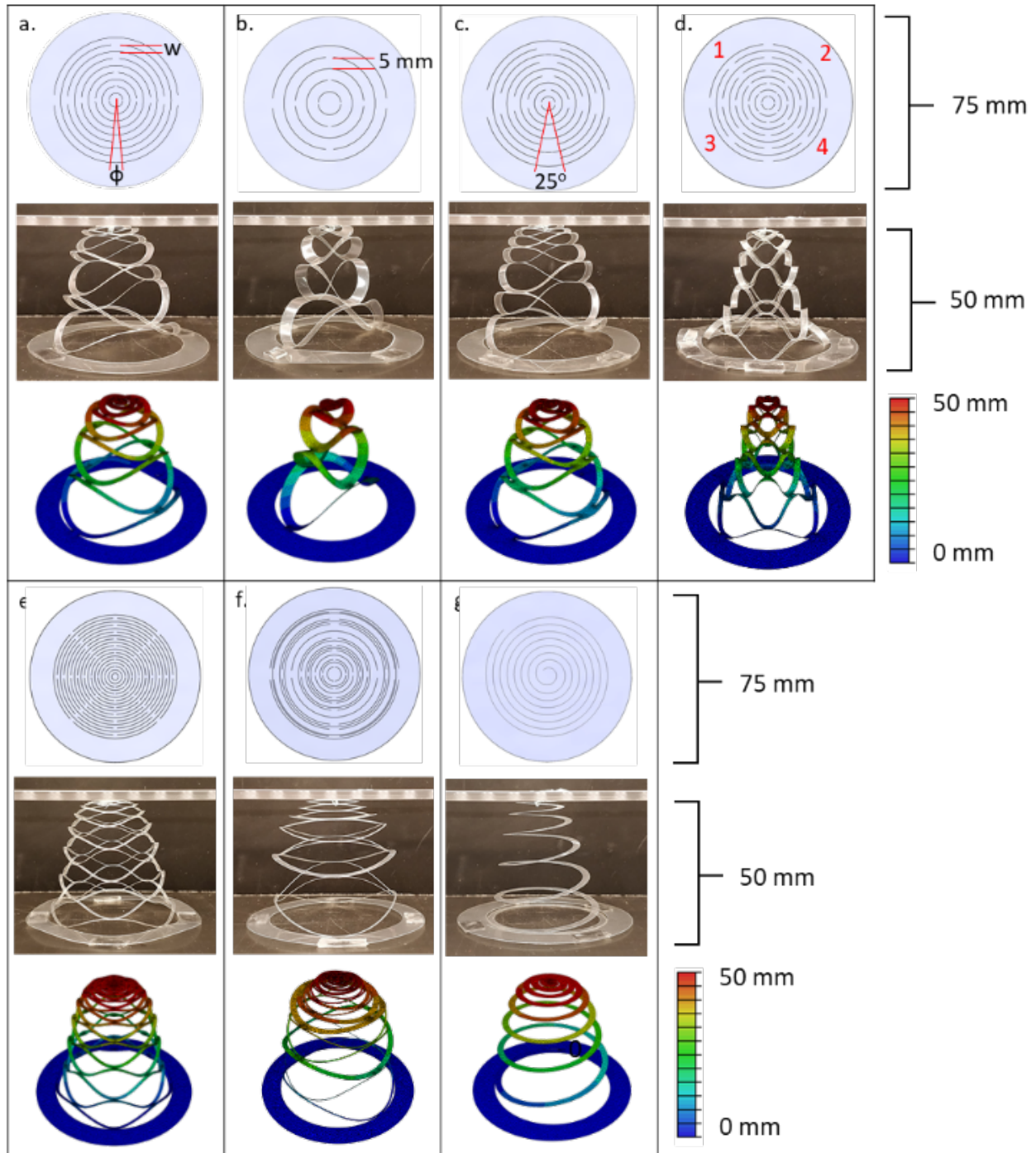


**Figure 2.5** Comparison of experimental and FEA models of PET at a displacement of 50 mm, having the same thickness ( $t = 0.09$  mm). (a-e) represents symmetric cuts that vary in the radial spacing ( $w$ ), angular spacing ( $\phi$ ), and number of cuts along the perimeter ( $N_{pc}$ ). (f) depicts the kirigami structure having unequal radial spacings. (g) is a normal helical conical spring, having one continuous cut.<sup>29</sup>

**Table 2.1** Design parameters associated with Figure 2.5.<sup>29</sup>

	Radial Spacing ( $w$ ) [mm]	Angular Spacing ( $\phi$ ) [°]	Number of cuts ( $N_{pc}$ )
<b>a</b>	3	10	2
<b>b</b>	5	10	2
<b>c</b>	3	25	2
<b>d</b>	3	10	4
<b>e</b>	1	5	4
<b>f</b>	Varies	10	2
<b>g</b>	3	-	1

For a given material comprising the starting sheet, the resulting kirigami springs' shape and mechanical behavior are governed by radial spacing ( $w$ ), angular spacing ( $\phi$ ), the number of cuts along the perimeter of each concentric circle ( $N_{pc}$ ), as well as the thickness ( $t$ ) and inner and outer diameters ( $D_i$  and  $D_o$ ). **Table 2.1** shows the geometric parameters associated with the cut patterns illustrated in **Figure 2.5**. The difference between the baseline pattern and **Figure 2.5b-d** is  $w$ ,  $\phi$ , and  $N_{pc}$ , respectively. The cut pattern of differs **Figure 2.5e** differs from the baseline pattern in  $w$ ,  $\phi$ , and  $N_{pc}$ . **Figure 2.5f** is comprised of nonequal radial spacings to demonstrate how different curvatures can be accommodated within the spring. **Figure 2.5g** is a helical conical spring with one continuous cut, which does not exhibit local saddles. The extent to which each of the individual rings deflect within the kirigami structure is visually dissimilar especially when compared to the normal helical conical shape. One notable difference between the kirigami springs and that of the helical spring is that as the kirigami spring deflects, there is no torsional moment around the central axis.

The basic element of RSK structures can be discretized by a series of beams. The segments between the cuts act as hinges, creating saddle points, as shown in **Figure 2.5**, where the color bar represents displacement in millimeters. Test specimens were made here using laser-cut PET sheets

for convenience and cost-effectiveness. It also sufficiently represents the behavior of other polymeric materials, such as polyimide used for flexible printed circuit boards. The circular kirigami patterns were fabricated by cutting 8.5" x 11" sheets of PET, 901 Highland Laser Printer Film (3M, 90  $\mu\text{m}$ ) with a 50 W Universal Laser Systems CO<sub>2</sub> laser cutter (5% power, 10% speed, 1.5" optics). The Young's Modulus and Poisson's ratio of the film are 2.2 GPa and 0.33, respectively. The overall diameters of the patterns are 75 mm with the largest cut radius at 27 mm.

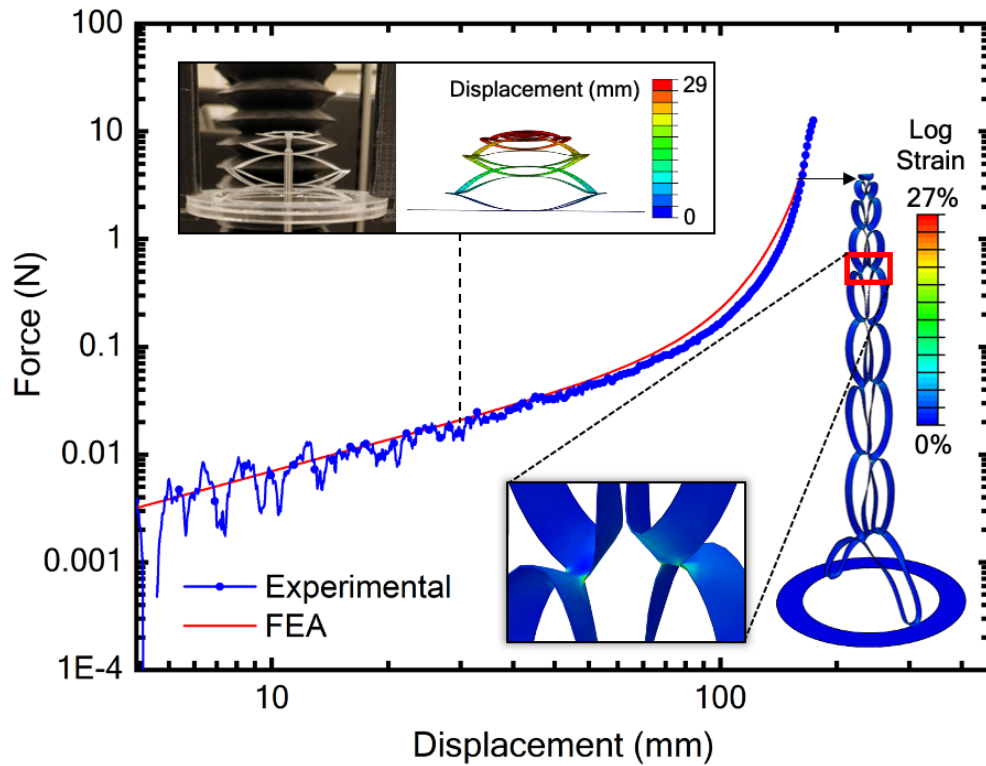


**Figure 2.6** Experimental and FEA force-displacement curve for baseline pattern. Overlaid images above the curve show experimental and FEA samples deflected at 29 mm. Insets to the right and below depicts FEA results at a large displacement of 152 mm and closeup image of local strain, at a concentrated force of 5 N; color bar represents logarithmic strain potential (%).<sup>29</sup>

The mechanical response of the RSK platform was modeled using FEA in which cross-plane, uniaxial forces were applied. The logarithmic force versus displacement is then plotted along with experimental results (**Figure 2.6**). The PET substrate was sandwiched between two acrylic rings to ensure the outer boundary was fully constrained and then clamped into tensile grips via a 3D

printed specimen holder as shown in **Figure 2.7**. The two rings were cut from Optically Clear Cast Acrylic Sheets (McMaster-Carr, 7/64” thick) with the laser cutter (100% power, 5% speed, 2.0” optics). A probe was used to apply a uniaxial force at the center of the spring at a rate of 5 mm/s.

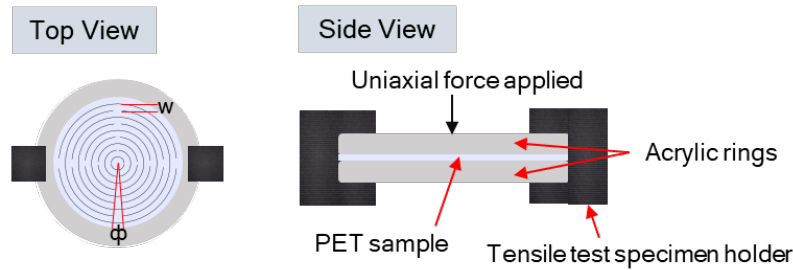


**Figure 2.7** Experimental setup for uniaxial tensile testing.<sup>29</sup>

The FEA models match well with experimental results in the linear elastic regime, as the comparison of out-of-plane behavior in the inset images of **Figure 2.6** shows. The RSK structure can undergo large global displacements to beyond 1,500x its original profile, as shown in the second inset of **Figure 2.6**. Note that while the regimes in the force *versus* displacement plots are designated as linear or nonlinear, from close examination of the deformation, it’s clear that most of the strain is localized to the cut ends, which are thus more prone to plastic deformation. Beyond displacements of approximately 90 mm for the structure in **Figure 2.6**, slight deviations between the FEA and experiment begins, which can be attributed to the FEA models’ assumption of purely elastic behavior, which has neglected plastic strain or strain-hardening that may occur at large displacements.

To further illustrate the deformation behavior of a kirigami spring, a simplified model of the structure’s behavior assumes segments of rings in which the total displacement of the structure is the summation of the displacement of each ring as represented in the model in **Figure 2.8**. Rings in series are defined by their outer and inner radii ( $R_o$  and  $R_i$ ) where the difference is the radial spacing. The applied concentrated force and pinned boundary conditions correspond to the uncut

arc length designated by the cut pattern. The outer edges of the uncut regions of each ring are bounded by the previous ring while the inner edges experience the load. Concentrated point loads are applied at the ends of each of the cuts, so for the baseline pattern that has two cuts along the circumference there are a total of four concentrated load points, assuming the forces are distributed

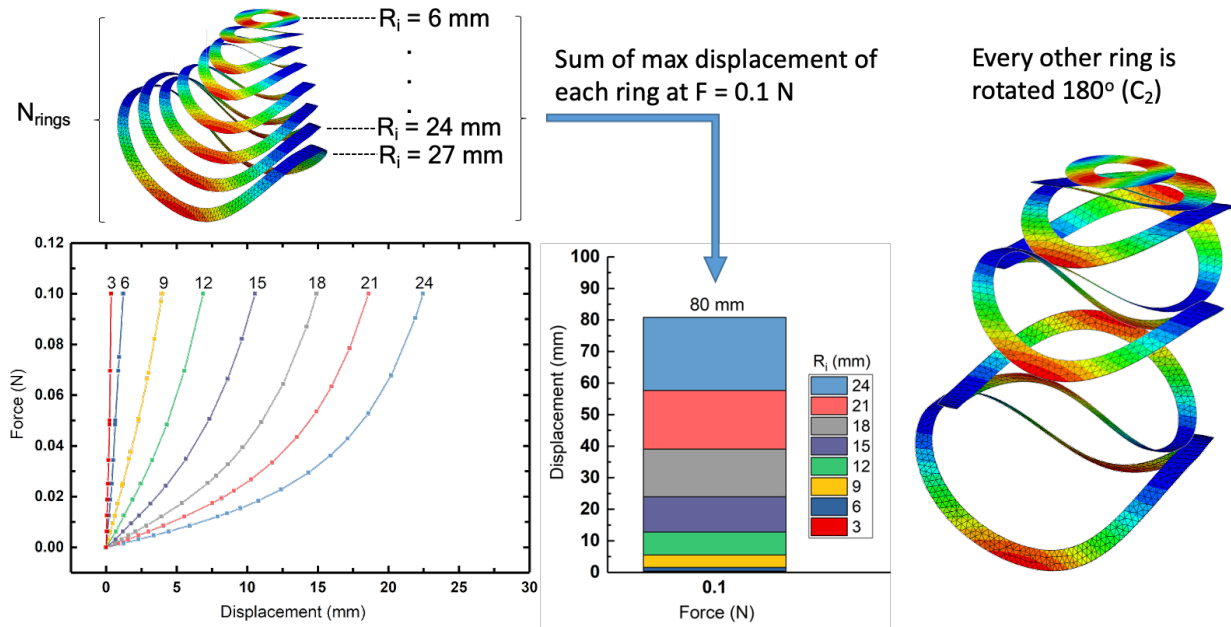
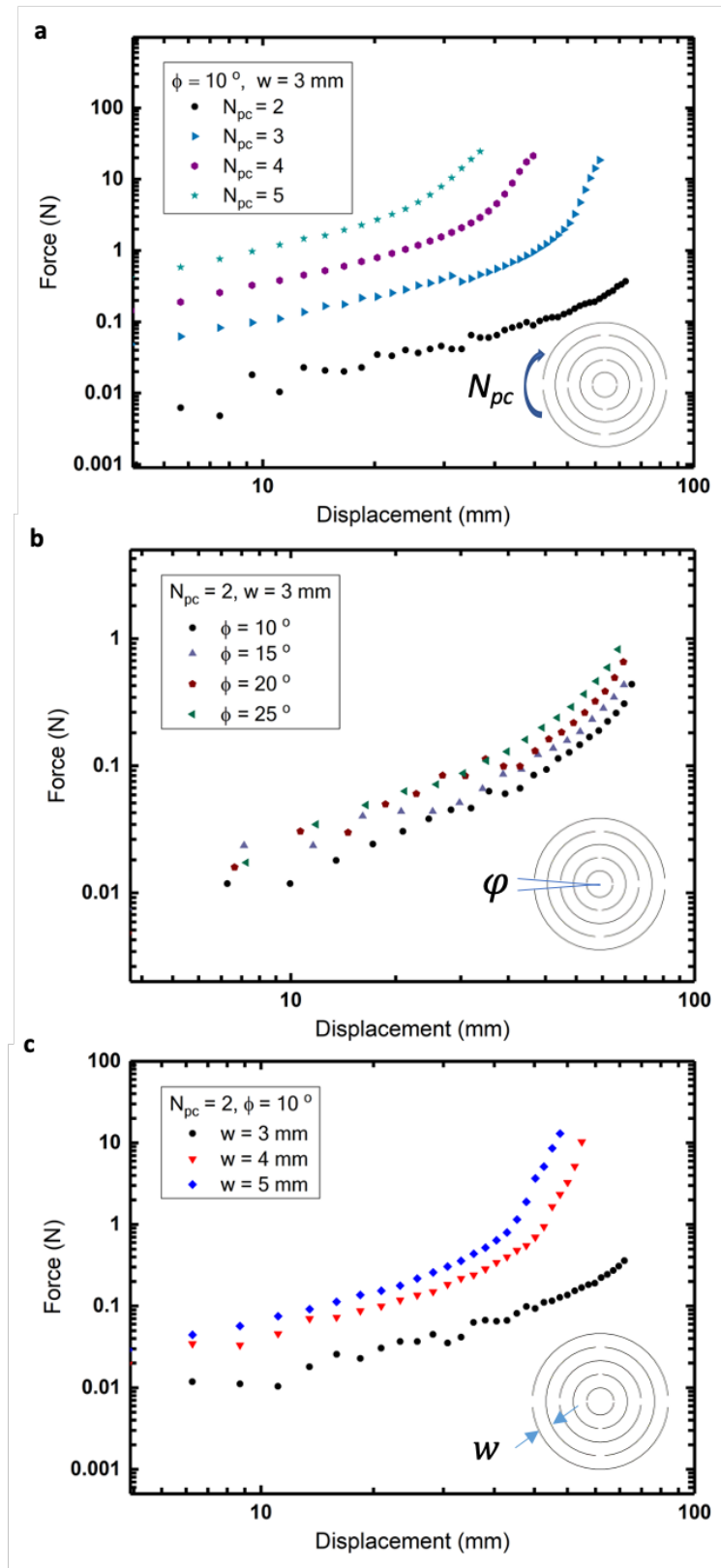


Figure 2.8 RSK spring modelled as a combination of rings.

equally. Therefore, the total force the ring experiences is the sum of the concentrated point loads where the force versus displacement plot represents the concentrated force at one of the cuts as seen in Figure 2.8. As an example, Figure 2.8 corresponds to the ring model when the displacement is equal to 80 mm. Assuming each ring experiences the same applied load, the total displacement of the kirigami spring is a sum of the individual displacements of each ring, where  $\delta$  represents the displacement,  $N_{rings}$  is the number of rings, and  $R$  represents the outer radius. To summarize, the more rings within a given area and perimeter, the larger the linear displacement limit of the spring.

$$\delta_{total} = \sum_i^{N_{rings}} \delta_{R_i} \quad (2.1)$$

**Figure 2.9** shows how variations in the key cut parameters  $w$ ,  $\phi$ , and  $N_{pc}$  affect the force versus displacement behavior. For constant angular and radial spacing, as the number of cuts along the perimeter increases, so too does the force required to displace the structure (**Figure 2.9a**). Similarly, increasing  $\phi$  (**Figure 2.9b**) or increasing  $w$  (**Figure 2.9c**) requires more force to deflect the spring. This is analogous to having a greater number of weaker and series-connected springs (or cantilevered beams) spanning two receding force nodes, as will be discussed further below.



**Figure 2.9** Logarithmic force versus displacement curves depicting the mechanical properties of various cut patterns. Varying (a) number of cuts along the perimeter, (b) angular spacings, and (c) radial spacings.<sup>29</sup>



### 2.3.2 Cantilever beam theory

Cantilever beam theory can be used to gain a better understanding of how the spaces between cuts act as beams and how beam geometry influences the mechanical properties such as yield displacement, albeit occurring in the elastic regime in the strict sense. The beam stiffness scales proportionally to the  $w$ ,  $\phi$ , and  $N_{pc}$ . In other words, the smaller the number of cuts in the radial direction, or the larger the number of azimuthal cuts, the stiffer the beams and thus the higher the overall stiffness of the RSK structure in cross-plane deformation.

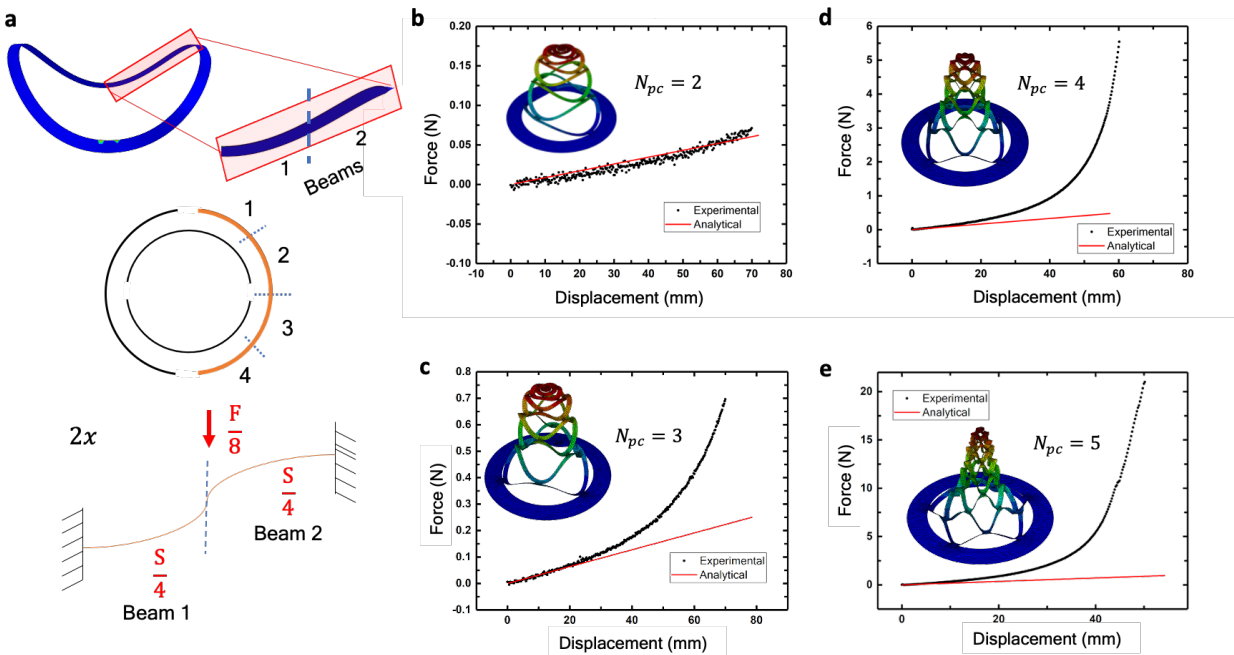


**Figure 2.10** Segments of the deformed ring represented as beams in bending modeled based on the cantilever beam theory. (a) For two cuts along the perimeter, part of the ring having a positive slope is represented as two beams and the entire ring is broken into eight beams, so the force applied to one beam is one eighth the total force applied to the entire ring. The experimental results and analytical model are shown (b)-(d) based on the number of cuts along the perimeter where  $\Delta R = 3\text{mm}$  and  $\phi = 10^\circ$  with overlaid FEA models displaced by 50 mm.<sup>29</sup>

For a cut pattern having two cuts along the perimeter, the saddle-shaped rings can be further partitioned into eight beams based on the curvature of the ring (see **Figure 2.10a**). In other words, one cut segment can be decomposed to four beams where the force applied to one beam is one eighth the total force. The variables used for the derivation are the following:

$\delta$ : Deflection (mm)

F: Force (N)

R: Outer Radius (mm)

$N_{pc}$ : Number of cuts along the perimeter

$\varphi$ : Angular spacing ( $^{\circ}$ )

S: Arc length (mm)

E: Young's modulus (N/mm<sup>2</sup>)

w: Radial spacing (mm)

t: Thickness (mm)

E: Young's modulus (N/mm<sup>2</sup>)

I: Area moment of inertia (mm<sup>4</sup>)

$N_{rings}$ : Number of active rings

x: Hinge length (mm)

Displacement of beam in bending fixed to one end:

$$\delta = \frac{FL^3}{3EI} \quad (2.2)$$

Where the area moment of inertia (I):

$$I = \frac{wt^3}{3} \quad (2.3)$$

The length of the beam corresponds to the arc length of the cut. The arc length based on the angular spacing:

$$S = 2\pi R \left( \frac{\theta}{360} \right) \quad (2.4)$$

$$\theta = \frac{360}{N_{pc}} - \varphi \quad (2.5)$$

$$L \equiv S = \pi R \left( \frac{2}{N_{pc}} - \frac{\varphi}{180} \right) \quad (2.6)$$

Therefore, the displacement of one beam:

$$\delta_{\text{beam}} = \frac{\left(\frac{F}{8}\right) \left(\frac{S}{4}\right)^3}{Ewt^3} \quad (2.7)$$

$$\delta_{\text{total}(i)} = 2\delta_{\text{beam}} \quad (2.8)$$

$$\delta_i = \frac{FS^3}{256Ewt^3} \quad (2.9)$$

The total displacement is the summation of each individual ring's displacement:

$$\delta_{\text{total}} = \sum_i^{N_{rings}} \delta_i \quad (2.10)$$

Depending on the substrate material, the cut width formed by the laser-cutter varies. In addition, the cut parameters (i.e., power, speed, and parts per inch, PPI) affect the cut width. **Figure 2.11** shows optical microscope and scanning electron microscope (SEM) images of PET after it has been laser cut using the parameters mentioned earlier (5% power, 10% speed, 1000 ppi).

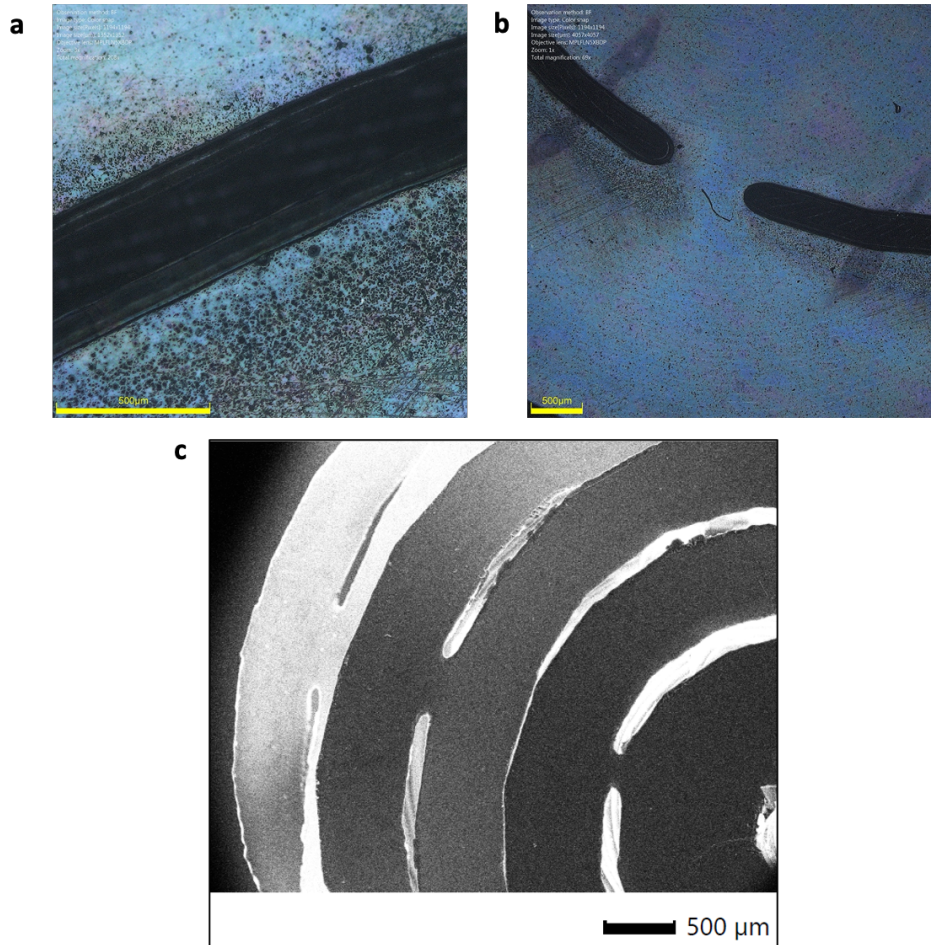


**Figure 2.11** (a) and (b) optical microscope images of the cut width, scale bars indicate 500 μm. (c) Scanning electron microscope image of the RSK spring, scale bar indicates 500 μm.

## 2.4 Finite-element modeling setup of RSK springs

The software package ABAQUS was used to model the elastic behavior of the RSK springs, based on the static, general method with a 6-node linear triangular prism element (C3D6) mesh construction, using the non-linear geometry option. Automatic stabilization and the default dissipated energy fraction is used. The matrix storage is unsymmetric and the time incrementation step is 0.001 to 1 with a step size of  $1 \times 10^{-36}$ , and the analysis is Full Newton. Pinned boundary conditions are used along the outer circular ring and the concentrated point loads are applied to the

springs, as demonstrated in **Figure 2.12**. Certain parameters are modified from the default in the general solutions control found under the other tab > edit> step. Specify in the time incrementation tab the discontinuous analysis  $I_0=8$  and  $I_R=10$ . Under “more,”  $I_A=20$ ,  $D_f=0.5$  and then under line search control,  $N_{1s}=10$ ,  $\eta_{1s}=0.01$ . This allows the solid object to act as a membrane under a transfer load.

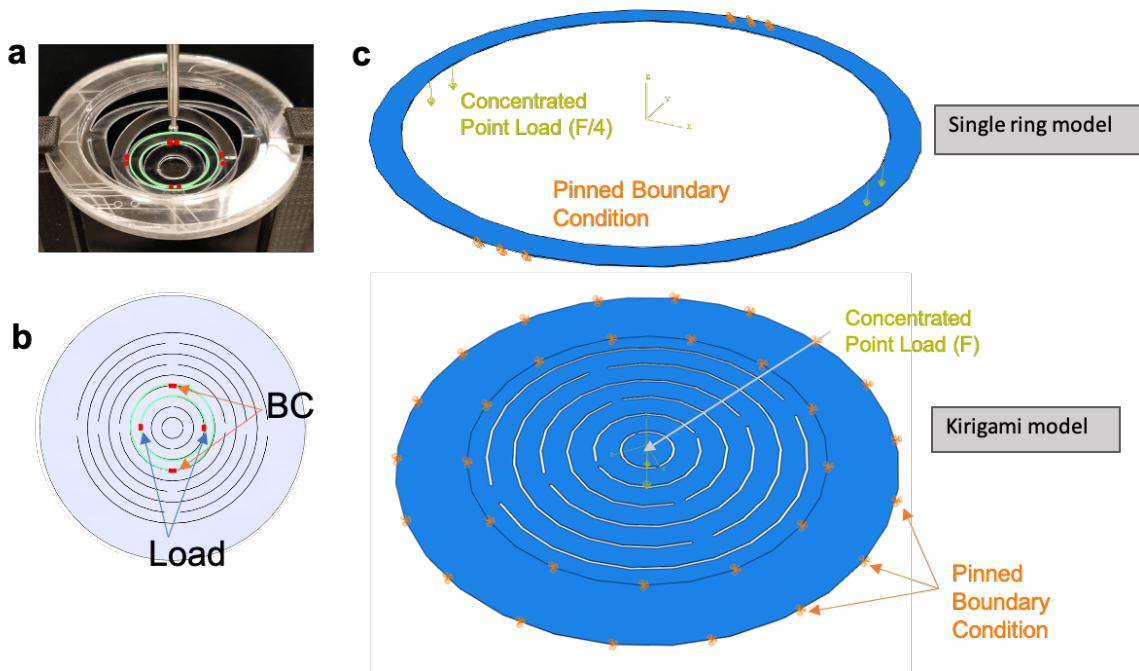


**Figure 2.12** Physical model and schematic representing the load and boundary conditions for the single ring model, as well as the FEA model showing the concentrating point load and pinned boundary condition for the single ring and full kirigami model.<sup>29</sup>

The resulting stress distribution and the displacement of PET corresponding to **Figure 2.6** is shown in **Figure 2.13**. The color bar in **Figure 2.13a** corresponds to the Von Mises stress criterion and the color bar in **Figure 2.13b** corresponds to the displacement in the y-axis.

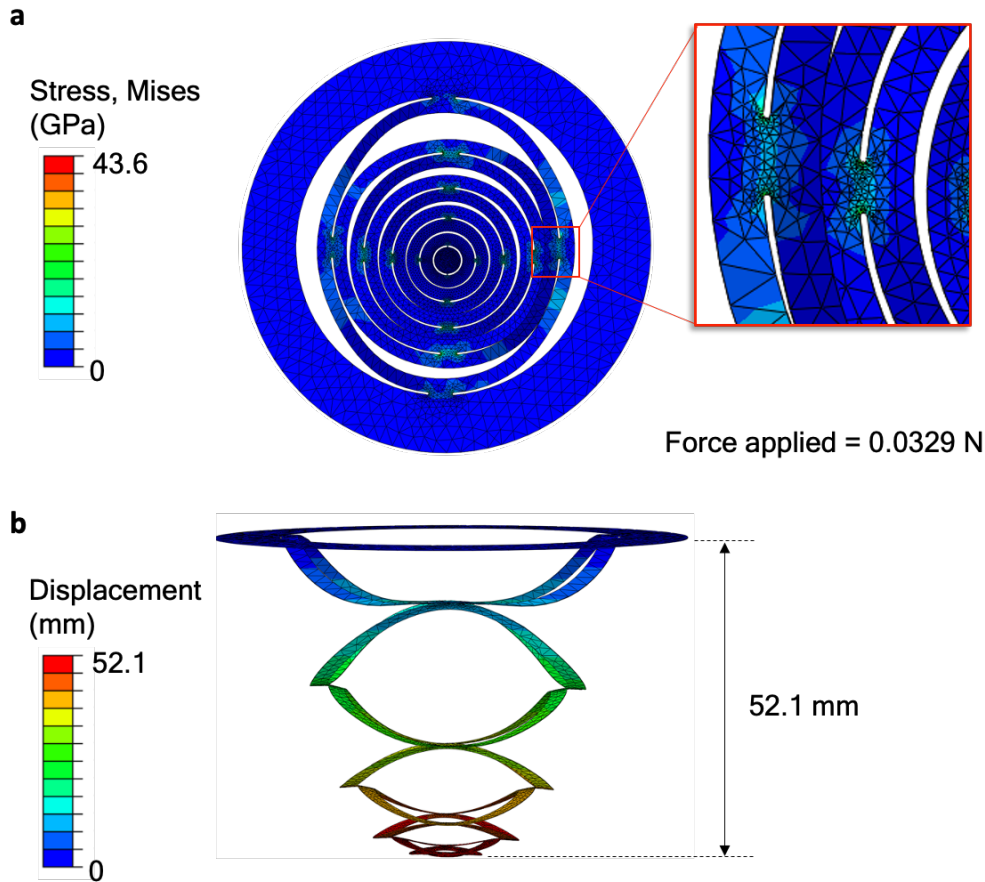


**Figure 2.13** Stress and displacement of FEA simulations. (a) Top view of deformed spring depicting the distribution of stress across the spring, based on Von Mises Criterion, where the scale bar is in GPa. The close-up is of the concentration of stress at the cut ends. (b) Side view of deformed spring, where the color bar indicates displacement in mm.<sup>29</sup>

In addition, other materials were experimentally tested and simulated to determine how the RSK pattern influences their mechanical properties. Polyimide (Dupont Kapton<sup>®</sup>), aluminum 1100 (McMaster Carr), and low-carbon steel 1010 (McMaster Carr) are experimentally tested and modeled. Because metals have a higher density and Young’s Modulus, a more durable experimental setup, than the previously used holder made of fused-deposition modeling (3D printed) plastic, is required to perform uniaxial tensile tests.

#### *2.4.1 Fabrication and testing of stiffer materials*

A 76  $\mu\text{m}$  thick Kapton® sheet is laser-cut using a 50W CO<sub>2</sub> laser cutter with 6% power, 4% speed, 1000 ppi, and 1.5” optics. The metal sheets, however, are very reflective and more power is required to laser-cut them; therefore, they were professionally laser-cut by Precise Metal Components (Ann Arbor, MI) with a 2,500W laser-cutter. Furthermore, instead of 3D printed holders made of ABS plastic used for previous experiments, thick steel rings were used. The sample is again sandwiched in between the rings as represented in the exploded CAD model view in **Figure 2.14**. Screws are used to clamp the material between the rings, as well as the bottom rectangular bar. The bar is then clamped into the bottom tensile grips. A force is applied to the center of the sample by attaching a screw with nut and washers to the center of the sample. The screw is attached to another rectangular bar which is attached to the top tensile grip. The instrument used is a TA.XT*Plus* Texture Analyzer (Texture Technologies, Hamilton, Massachusetts, USA) with a 30kgf load cell and the *Exponent* (Texture Technologies, Hamilton, Massachusetts, USA) software package.

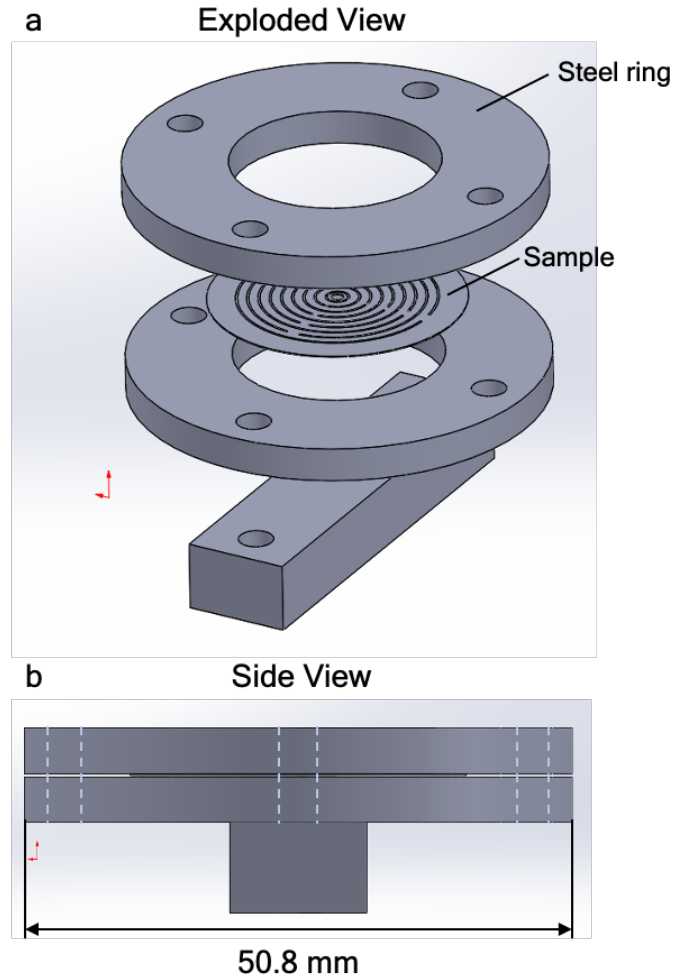


**Figure 2.14** Exploded isometric (a) and side view (b) of a CAD model of the steel parts to clamp the kirigami samples for tensile testing.

The cut parameters for the RSK springs used for the uniaxial tensile tests are  $w=2$  mm,  $\varphi=10^\circ$ , and  $N_{pc}=2$ . **Figure 2.15** shows the force as a function of displacement for 100  $\mu\text{m}$  steel (**Figure 2.15a**) and aluminum (**Figure 2.15b**) sheets, as well as 76  $\mu\text{m}$  thick Kapton<sup>®</sup> film (**Figure 2.15c**) at various displacement rates. Log force as a function of displacement for steel, aluminum, and Kapton<sup>®</sup> at a displacement rate of 0.25 mm/s are shown in **Figure 2.15d**.



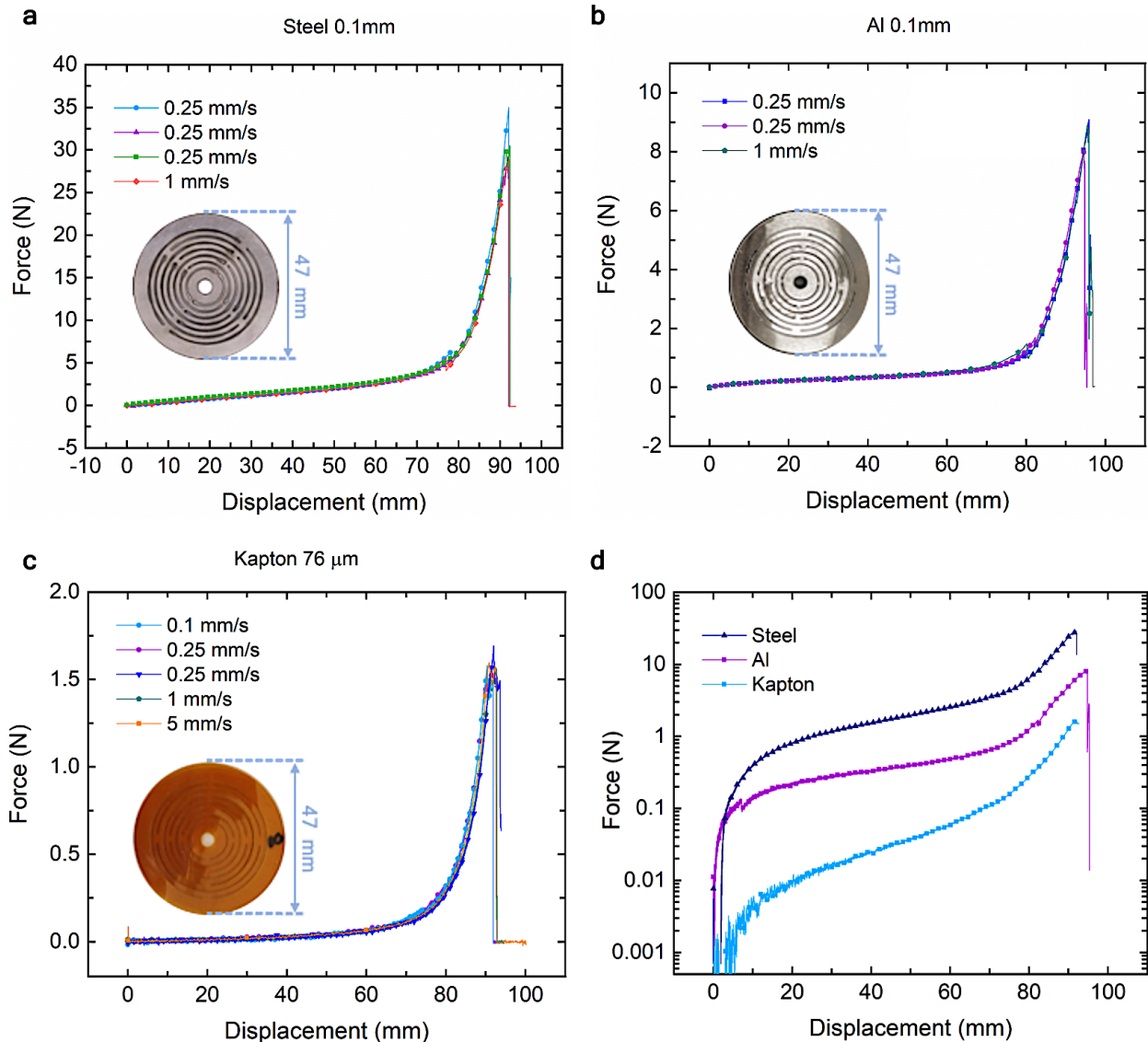


**Figure 2.15** Uniaxial tensile tests results of RSK springs made of (a) steel, (b) aluminum, and (c) kapton. (d) Log force versus displacement of steel, aluminum, and kapton at a displacement rate of 0.25 mm/s.

The FEA setup is similar to that previously delineated. The mesh consists of triangular prism elements as shown in **Figure 2.16a**. Similarly, the partitioned outer edge has the boundary condition, ENCASTRE, restricting any displacements or rotations, representing the region that is clamped during experimental tests. The inner partitioned circle represents the region clamped by the washer and nut and a concentrated force point load is applied to the center (**Figure 2.16b**).

Further refinement of the FEA model by taking into account plasticity is critical to accurately model the RSK springs. Stress-strain data of the bulk material is recorded under

“calibrations.” The data is then processed and converted to true stress-strain. Remaining under the calibrations tree, elastic plastic behavior is created from the true stress-strain data. Here, the ultimate point and yield point are chosen, and the material properties are updated based on the input data. **Table 2.2** shows the Young’s Modulus and density of the materials tested, used for the FEA models. Note, the Young’s Modulus for thin foils are different than that of bulk metals and are strain-rate dependent.<sup>30</sup> Uniaxial tensile tests were performed on steel and aluminum sheets according to ASTM E345-16, tension testing of metallic foils.<sup>31</sup>

**Table 2.2** Material properties used for FEA models and reference for input stress-strain data.

Material	Density (kg/m <sup>3</sup> )	Young’s Modulus (GPa)	Poisson’s Ratio
PET	1380	2.2	0.33
Kapton <sup>32</sup>	1420	2.55	0.34
1010 low carbon steel	7870	47	0.29
1100 aluminum	2710	23	0.33

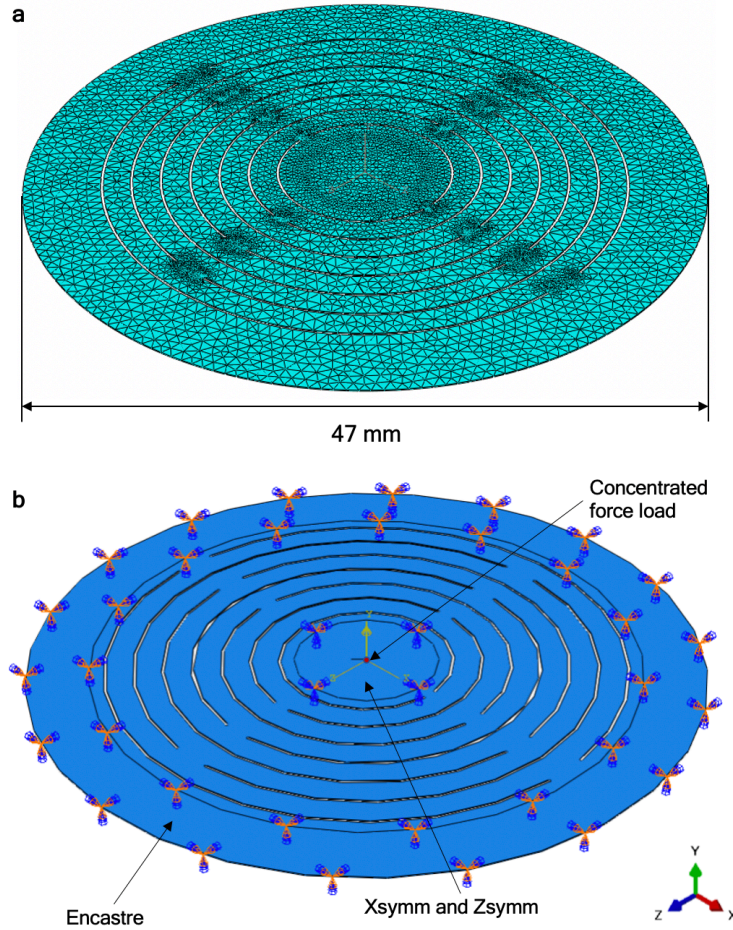


**Figure 2.16** FEA setup. (a) Mesh and (b) boundary conditions and applied load.

**Figure 2.17** shows the experimental and FEA results of Kapton<sup>®</sup> on a log force versus displacement plot. Results using two different displacement rates, 0.25 and 5 mm/s, were similar. The FEA results also match experimental results well including beyond the elastic regime as shown in **Figure 2.17a**. The inset shows the FEA and experimental results at approximately 80 mm displacement, where the color legend indicates displacement in millimeters. The displacement predicted by the FEA matches that measured experimentally very well. In **Figure 2.17b**, the stress distribution, in which the color bar represents Von Mises Stress in MPa, is highly localized to the cut ends.

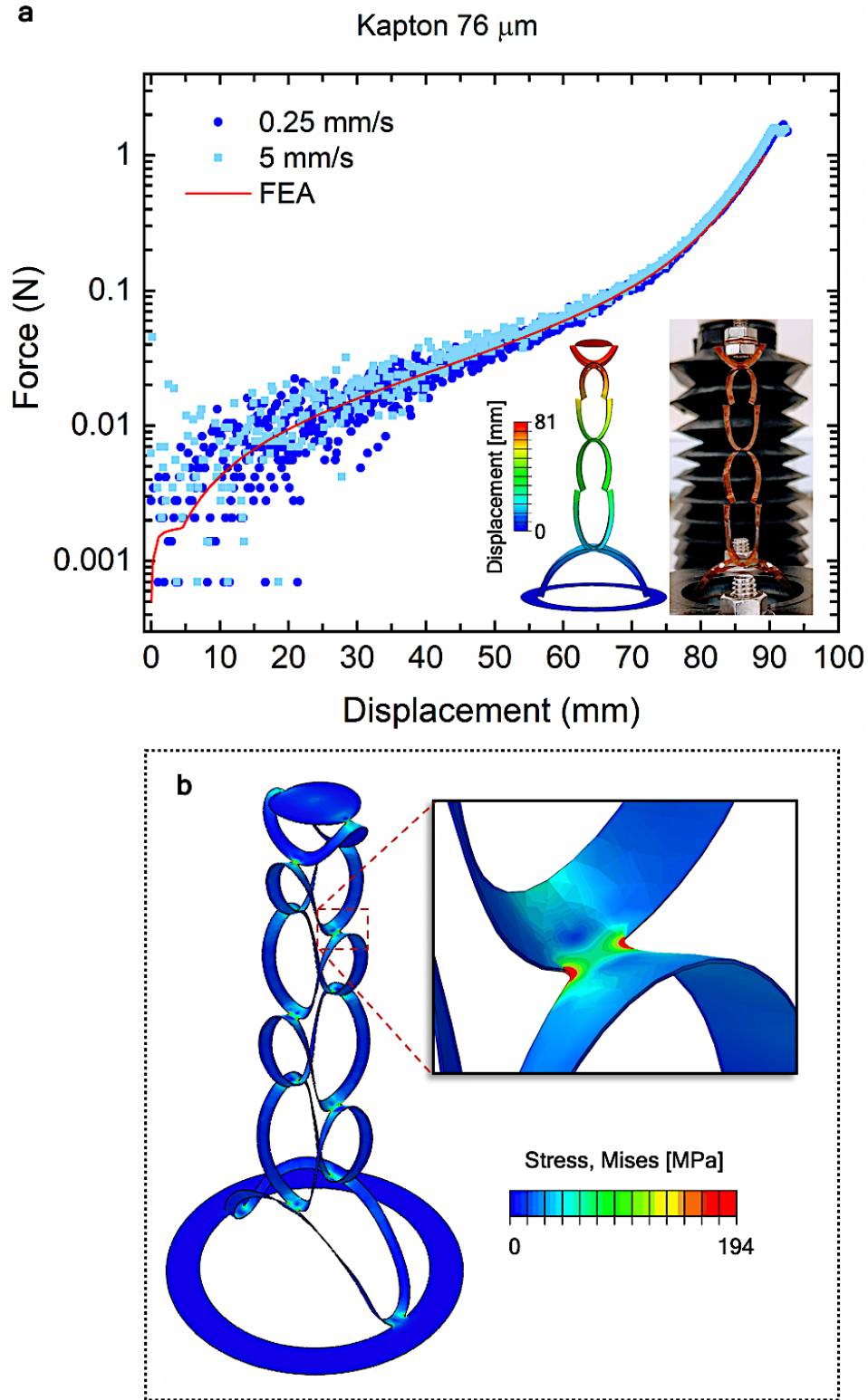


**Figure 2.17** Experimental and FEA results of kapton RSK spring. (a) Force versus displacement plot at 0.25 and 5 mm/s, as well as FEA results. Inset shows experimental and FEA models at a displacement of 81 mm. The color legend represents displacement in mm. (b) Corresponding FEA model representing the stress distribution with zoomed-in figure of cut ends. The color legend represents Von Mises Stress in MPa.

One way to determine if the material is undergoing plastic deformation is by examining the hysteresis in cyclic loading. If the force-displacement does not return to its original state, the material has been plastically deformed. **Figure 2.18** shows a plot of the force as a function of displacement as the aluminum RSK spring undergoes tension to a specified displacement and then compression back to its original state. The energy dissipation (quantified as a non-zero area between the stress-strain curves in the “out” and “back” directions) is greater at larger displacements. The images in the middle of **Figure 2.18a** correspond to 60-, 40-, and 20-mm displacement, from left to right. The images above those are taken post-test 60, 40, 20, 10, and 5 mm from left to right. Plastic deformation is most clearly seen even after compression from the sample taken to 60 mm displacement. A plot zoomed in to the elastic region is shown in **Figure 2.18b**. Plastic deformation occurs beyond 5 mm displacement.

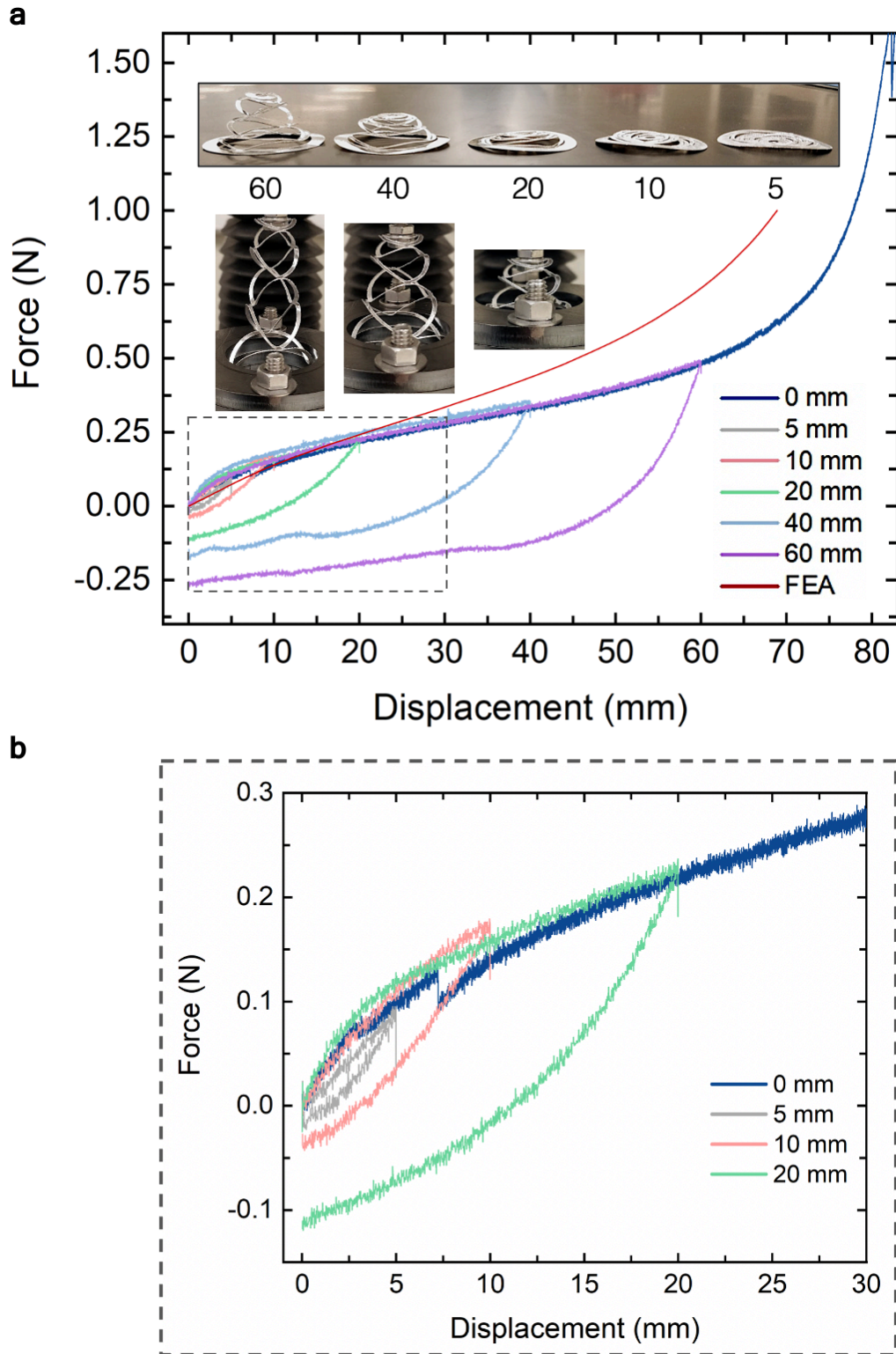


**Figure 2.18** Force vs. displacement of an aluminum RSK spring loaded to different displacements to examine the hysteresis. (a) shows overlaid images post testing on the top and during testing below at 60, 40, and 20 mm. (b) is a close-up indicated by the dash box in (a).



Steel is tested similarly, and the FEA results match well with the experimental results within the linear regime. Examining the hysteresis in **Figure 2.19** shows that above around 40 mm, plasticity begins. The force does not return to 0 after compressing the spring after displacing 60 mm displacement, indicating plasticity has occurred. It appears the FEA model deviates from experimental results past the elastic regime.

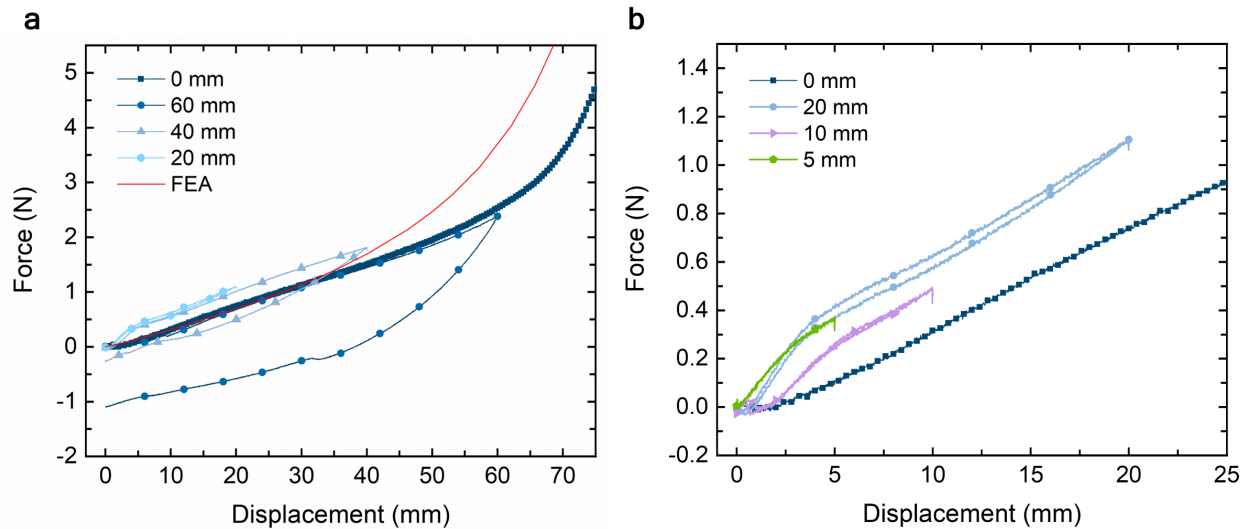


**Figure 2.19** Uniaxial tensile and compression tests performed on steel RSK springs, as well as FEA results (a) and experimental results at lower displacements (b).

Future work can further refine the FEA models to better account for plasticity and strain hardening, for example by augmenting the models with Johnson-Cook isotropic hardening. Also, inherent material property data should carefully and diligently be collected to ensure proper input stress-strain data is used. For instance, digital image correlation should be used to accurately determine strain during uniaxial tensile tests of metal foils. In addition, during the laser-cutting process, the material experiences local stress, which can be visually seen in **Figure 2.15b**. Reducing the amount of external force exerted on the sample before testing will yield more accurate results.

## 2.5 Summary

In this chapter, we conceptually introduced the concept of rotationally symmetric kirigami springs and created a classification system based on key cut parameters to differentiate RSK patterns. Experimentally, we demonstrated that changes in the radial spacing, angular spacing, and number of cuts along the perimeter influence the substrate's mechanical properties. Furthermore, an analytical model based on cantilever beam theory was developed to elucidate how beam geometry affects the mechanical properties in the elastic regime. By leveraging FEA—a powerful tool in accurately predicting the deformation of kirigami-based materials—we delineated the relationship between various cut parameters and stress and strain distributions within the material. Compared to experimental results, we found our FE models closely match polymer sheets such as Kapton® in both the elastic and plastic regimes. While FE model predictions approximate experimental results of metal foils—aluminum and steel—in the elastic regime, further refinement is necessary to capture deformation in the plastic regime. This may be accomplished by considering strain hardening and using more accurate testing methods to input stress-strain behaviors of thin foils.



# Chapter 3 Kirigami-Based Sensor Platform for Joint Motion Tracking

## 3.1 Introduction

Wearable activity and heart monitors have proliferated in the marketplace, creating an unprecedented data stream and opportunities for improving cardiovascular health and athletic performance. Joint movement, however, remains poorly quantified, while joint injuries dramatically impair function and raise the cost of healthcare. Nearly two million people in the U.S. enter the medical system just for rotator cuff injuries, with corresponding repair surgeries exceeding \$3 billion per year,<sup>33</sup> while the annual market for orthopedic braces exceeds \$5 billion. Over 120 million Americans (one in two adults) are affected by painful or disabling bone, joint or muscular conditions,<sup>34</sup> which often occur from improper positioning during active and/or passive activities, (e.g. weight-lifting, sitting, and sleeping with bad posture). The cost of treatment and lost wages is estimated at over \$200 billion.<sup>34,35</sup> Therefore, development of tools for *in situ* assessment and better understanding of joint movement could unlock a new frontier of using body kinematics to improve health span, athletic performance, gesture control of motion assistive devices, and enable many other applications.

Measurements of joint function typically involve the manual use of a goniometer to determine the range of motion.<sup>36</sup> Some joints (e.g. shoulder) exhibit complex motion that is poorly assessed by a simple goniometer, in which the accuracy can vary by as much as 45%.<sup>37,38</sup> In sports, exercise, common tasks, and post-injury recovery in particular, the process for achieving desired

range of motion requires professional assessment<sup>37</sup> and a strict rehabilitation regimen,<sup>39</sup> often hampered by poor adherence, resulting in poor patient outcomes. The ability to quantify movement of key joints *during activity* can dramatically improve outcomes for rehabilitation and boost athletic performance. However, directly monitoring and providing feedback on joint movement *during* an activity, unobtrusively and cost effectively, remain a major challenge.<sup>40–42</sup>

Currently, tracking motion or deducing impact stresses is performed using camera motion tracking systems<sup>43</sup> or inertial measurement units (IMUs) that consist of an accelerometer, gyroscope, and magnetometer, typically packaged in a rigid brace or integrated within a band or suit.<sup>44–46</sup> In an attempt to improve the wearable aspect of the sensors, collection of positional data has been shown using conductive textiles, where special fibers integrated into the textile are the sensing elements.<sup>47–52</sup> However, the sensing is based on stretching of the fibers, typically unidirectional and poorly suited for integration with substantially rigid electronic components that do not tolerate well repeated mechanical deformation. Furthermore, the integration of electronic function into textiles remains a non-standard, expensive process. Instead, an approach is needed where the device is flexible and curved, conforming to the body surface in use, yet is also flat and non-stretchable during fabrication to be compatible with dominant, scalable manufacturing and integration processes for electronics.

To resolve the conflicting design requirements stated above, macro- and mesoscale closed-shape, planar *kirigami* structures, nominally with rotational symmetry, are shown in **Figure 3.1**. As mentioned previously, kirigami has increasingly been used to engineer global elasticity in materials.<sup>7,24,53,54</sup> The addition of cutting allows for greater control over the geometric design and system behavior.<sup>55</sup> Recently, this has been leveraged to enable locomotion *via* soft actuators<sup>56</sup> and flexible electronics.<sup>17,25,57,58</sup> While technologies to generate patterns and functional coatings in two

dimensions are now highly evolved, the structures examined here are easily generated at the application-appropriate length scales using a laser or die cutter. As the structure is displaced normal to its original plane, concentric rings defined by the cut lengths bend to create a combination of saddles with alternating positive and negative Gaussian curvatures. A sufficiently dense and appropriately configured cut pattern enables the structure to achieve large deflections and to conform to an envelope shape of complex curvature. The alternating local curvature – and therefore strain – guides the strategic placement of strain sensors, which enable the quantification of joint movement.

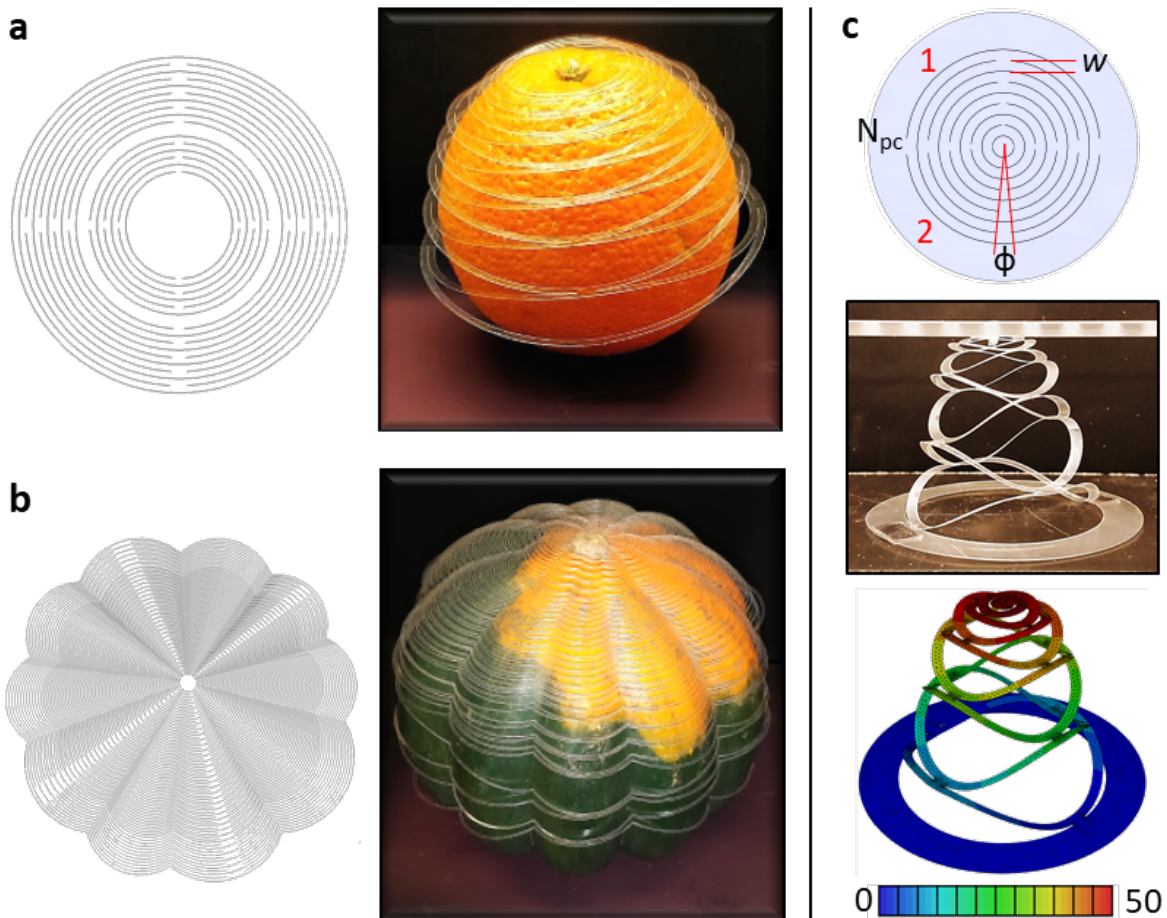


**Figure 3.1** RSK structures approximating different curved surfaces. a) RSK springs assume the shape of an orange and (b) an acorn squash; schematic of cut pattern on left and physical model on right. c) Baseline cut pattern delineating the cut parameters and deformation states of the physical and FEA model displaced to 50mm (color bar indicates displacement in mm).<sup>29</sup>

### 3.2 RSK structure as platform for sensing

We take advantage of the alternating curvatures exhibited by the structure and introduce electronic components in the regions suitable to their deformation requirements and tolerances. For example, rigid sensors can be placed between the cut ends on the kirigami sheet, where there is minimal curvature upon deflection. Strain gauges, on the other hand, can be placed at points of greater local curvature (e.g., near the start of the cut). This integration principle allows the RSK structures to act as a multi-functional platform for the placements of a variety of otherwise substantially rigid or flexible sensor components. As a proof-of-concept, simple strain gauges are embedded on the RSK platform, oriented off-axis to each other, located near the cut ends (see schematic in **Figure 3.2a**). The combined substrate and strain gauges are adhered onto the shoulder using a stretchy fabric adhesive used often in physical therapy; a cross-section is represented in **Figure 3.2b**. The placement of the sensors at the start and end of the cuts helps maximize the signal, as shown in **Figure 3.2c**, where a sub-unit ring is deformed using FEA, with force applied at the cut ends in the inner part of the ring; an orange box indicates the location of the sensors. A more detailed representation of the model is explained in **Section 2.4**. In **Figure 3.2d**, the platform is shown placed on the shoulder of a user, where SG# represents a linear strain gauge. The flexible adhesive was omitted in the images in **Figure 3.2d** to show how the RSK device assumes the topology of the subject's shoulder, and how the sensor platform is oriented along the top of the shoulder.

To capture shoulder joint motions, one strain gauge is positioned outside of the acromion, in the vicinity of the greater tubercle of humerus / deltoid to capture the significant change in elevation upon raising the arm. Another sensor is placed along the back of the shoulder (e.g., along or near the supraspinatus or infraspinatus) to capture arm movement across the body. The cut pattern used for this subject has a radial spacing of  $w = 1$  mm, (except for the spacing of the rings

that hold the strain sensors), an angular spacing of  $\phi = 5$  mm, and  $N_{pc} = 2$  (two cuts along the perimeter). Narrow yet long beams allow for the structure to be flexible enough to adapt to changes in the surface topology of the shoulder as the arm moves. The cut pattern can also be tuned to match variations in shoulder geometries – e.g., for broader shoulders an increase in the number of rings.

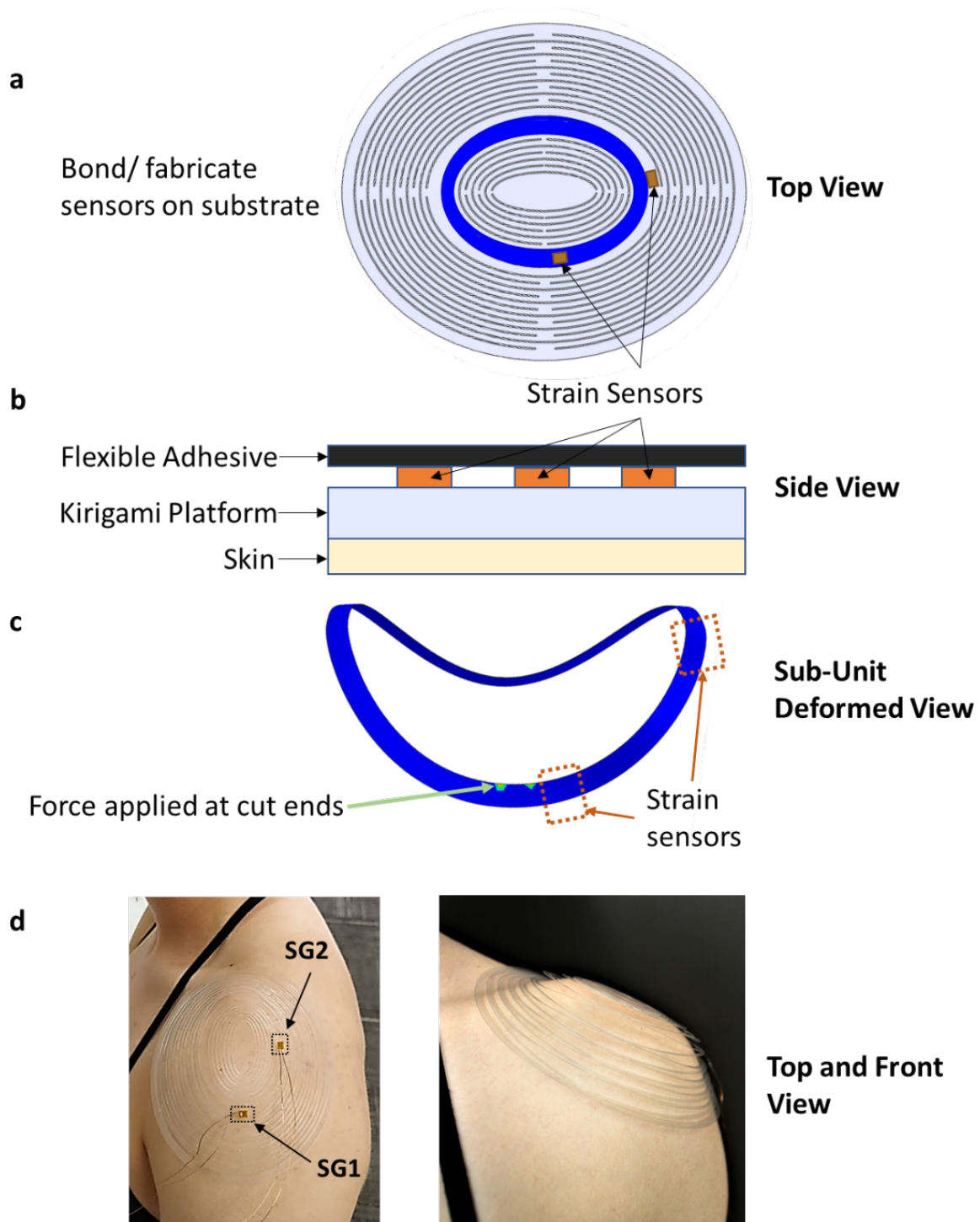


**Figure 3.2** Placement of strain sensors on RSK platform. a) top view of cut kirigami spring based on geometry of shoulder. b) Cross-sectional view of RSK-based device depicting the locations of sensing elements with respect to the kirigami platform, flexible adhesive, and skin. c) Sub-unit ring deformed shows the placement of strain sensors placed at the maximum degrees of curvature, which is at the start and ends of the cuts. d) Top and front view of device with bonded strain gauges placed on subject's shoulder without adhesive tape.<sup>29</sup>

The device shown in **Figure 3.2d** was placed on the shoulder, and the subject performed various motions. The strain gauges experience changes in the local strain, altering their electrical resistance, captured by a control unit. An example of the collected and processed data is shown in **Figure 5**, where the correlation is made between the position of the limbs (and joint), and signals from the sensor(s) as the subject raises her arm up and down following the humeral elevation plane.

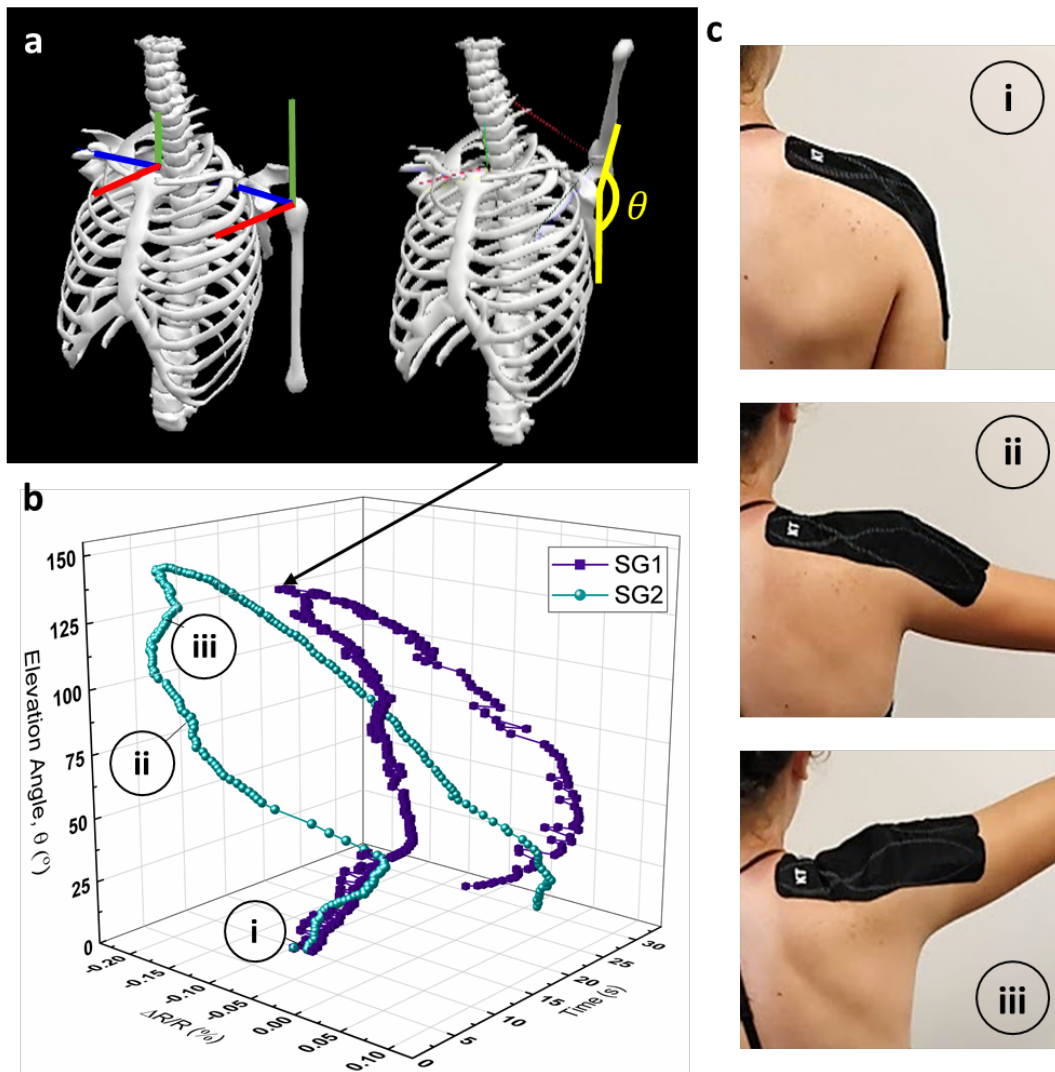


**Figure 3.3** Tracking motion of raising and lowering arm. a) Skeleton representation of body at neutral position and skeleton with arm raised up to 140o with coordinate system used by the image processing software and elevation angle,  $\theta$ . b) 3D plot representing elevation angle as a function of change of resistance and time in seconds. c) Kirigami sensing device at 0°, 79°, and 120°, represented in (i), (ii), and (iii), respectively.<sup>29</sup>

(For corroboration by conventional multi-point motion tracking, trackers were placed in specific locations on the user's body to accurately track the positions of the upper body *via* a 19-camera motion capturing system that surrounds the user.)<sup>59</sup> The coordinate system used to define the angular positions of the shoulder are depicted in the left skeleton diagram in **Figure 3.3a**. The humeral elevation angle is based on the plane parallel to the side of the body, humeral plane of elevation is the plane from the top view of the shoulder, and rotation of the shoulder joint, shown in **Figure 3.4** and described more fully in Ref. [43].

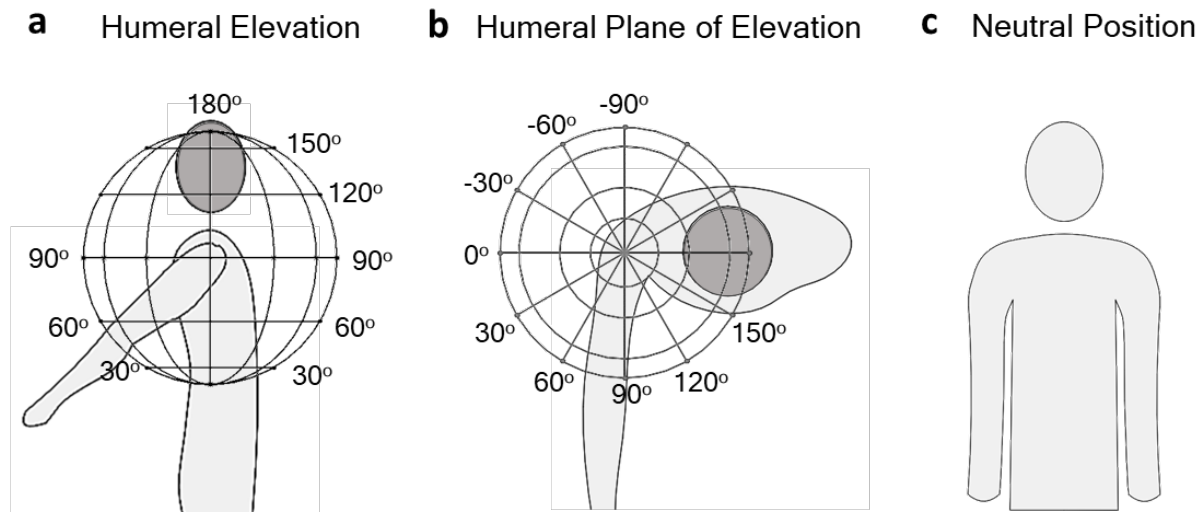


**Figure 3.4** Schematic of the planes of motion (a) humeral elevation angle, (b) humeral plane of elevation, and (c) neutral position of body.<sup>29</sup>

The skeletal representations of the user performing the raising arm motion, obtained by the camera tracking system, demonstrates the neutral position (left) and arm raised to 140° (right). A 3-dimensional plot of the elevation angle captured by the camera system is shown in **Figure 3.3b**, plotted against the resistance of two strain gauges, and versus time. The humeral plane of elevation angle and rotation remained relatively stable as the arm was raised and lowered along the humeral elevation angle ( $\theta$ ), with slight changes due to human error. The plateau sections in the beginning



and end of the motion correspond to the subject standing still in the neutral position, with the arm by the side against the body, as indicated in the top panel of **Figure 3.3c**. The device maintains good contact with the shoulder throughout the motion as shown when the arm is raised at 79° and 120° in the middle and bottom images of **Figure 3.3c**, respectively. Since the adhesive tape is applied when the arm is in the neutral state, at higher elevation angles the adhesive tape begins to fold in the areas not occupied by the sensor platform. Nevertheless, the device maintained conformability to the shoulder. Overall, the correspondence between the motion performed and the change in resistance is evident with respect to the elevation angle and permits the use of strain gauge signals to compute motion.

**Figure 3.5** captures the signals produced by other various shoulder motions, including circumduction and rotation. **Figure 3.5a** shows the subject circling the arm backwards (e.g., as in a backstroke) along the humeral elevation plane. SG1 more closely follows the motion corresponding to changes in the elevation angle, because it is located parallel to the beam bending in the direction of the performed motion. The angular velocity of the arm during these tests ranged from 0.16 to 1.7 rad/s. In addition to sensing relative changes in angular position, it also indicates acceleration as depicted in **Figure 3.5b**. The sequence starts with the user in a neutral position and then proceeds to run (in place), eventually slowing down to a walk and finishing back to the neutral position. (Refer to the supplemental video in Evke, E. *et al.*<sup>29</sup> to see the skeleton movement in real time synchronized to the  $\Delta R/R$  plots of **Figure 3.3b**, **Figure 3.5a**, and **Figure 3.5b**, which may help gain a better sense of the characteristics of the elevation change, circumduction, and running sequences.)

Intriguingly, the RSK sensing device can also detect muscle flexion and contraction associated with more subtle movements, including those of other joints in the arm. For example,

changes in resistance are prominent during wrist rotation, which is controlled by muscles surrounding the shoulder (**Figure 3.5c**). For the wrist rotation activity, the subject raised the arm forward 90° from the body, horizontal to the floor, and rotated the wrist back and forth, causing the muscles in the shoulder to flex and contract. Changes in resistance and the associated angular positions associated with the motion of shrugging shoulders at various speeds are depicted in **Figure 3.5d** and for moving the arm across the body in **Figure 3.5e**.

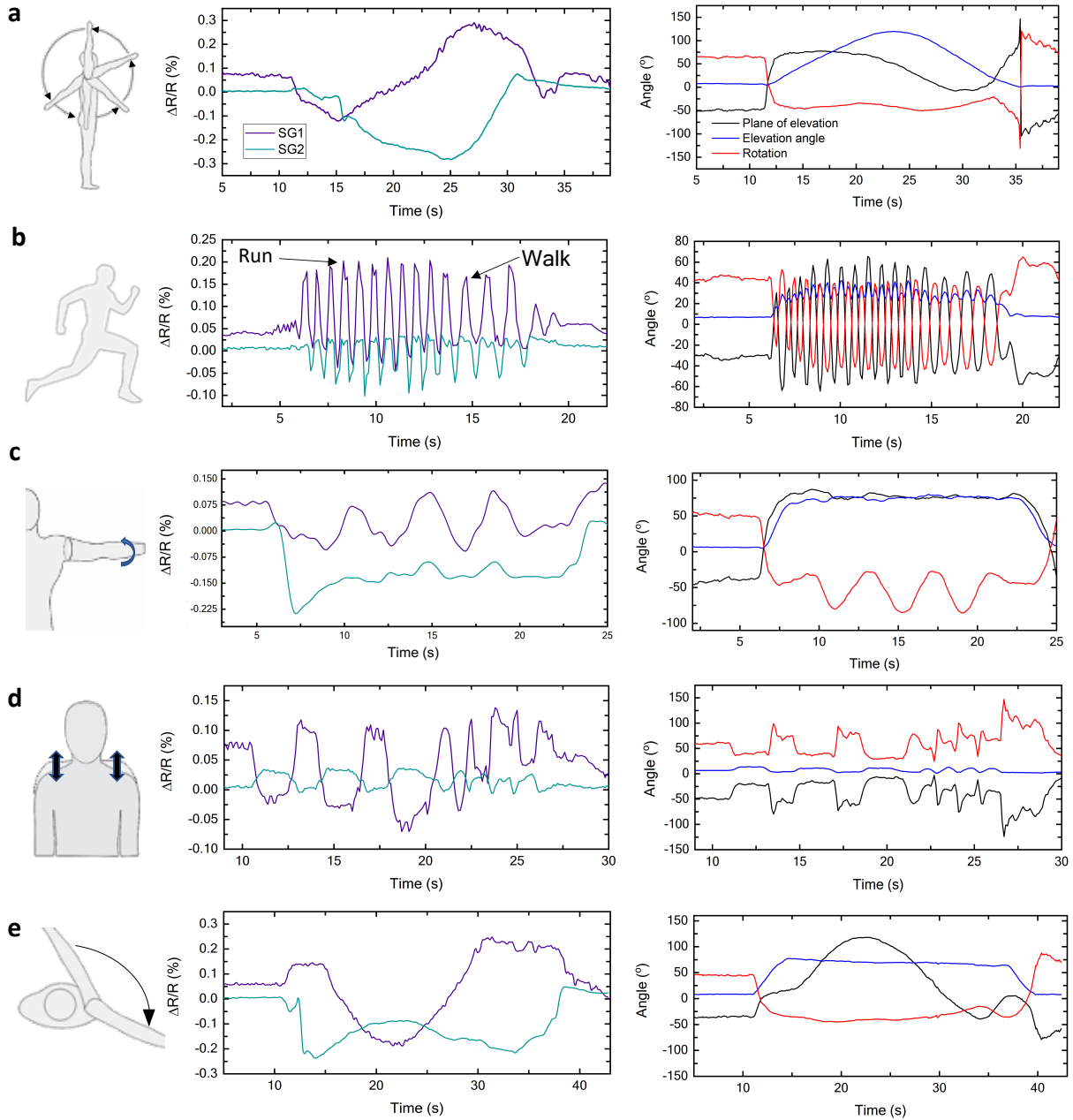


**Figure 3.5** Changes in resistance and corresponding angular positions as various motions are performed. From left to right: schematic of motion performed, plot of change of resistance versus time for two linear strain gauges placed on the RSK substrate, and a plot of the angular positions as a function of time. The three defining planes and axis of motion is plane of elevation, elevation angle, and rotation. a) Arm circle backwards, (b) running, (c) arm rotation, (d) shrugging shoulders, and (e) arm across body parallel to ground.<sup>29</sup>

### **3.3 Summary**

Planar, developable, rotationally symmetric kirigami structures were demonstrated to closely conform to surfaces with complex 3-dimensional curvature. The impact of cut geometry on the mechanical behavior of the cut structure was quantified using experiments and FEA. The alternating local Gaussian curvature – and therefore strain – between cuts was used to strategically place strain gauges on the RSK structure, permitting the direct monitoring of motion of a complex joint (shoulder) in a unique, marker-less motion tracking system. Simple, commercially available linear strain gauges were used to create a sensing device in a wired configuration, but scalable, monolithic integration using this platform can be cost-effective<sup>57</sup> and would facilitate the use of additional sensors, wireless communications and power transfer. These results indicate that the RSK structures constitute a highly promising platform for the integration of a variety of sensing technologies in a wearable form factor for highly modular and multi-functional health and movement monitoring devices, using well-established manufacturing processes.

### **3.4 Need for a fully wireless device**

Several improvements can be made to the prototype device described above. First, a wireless version of the device that is fully integrated with all of the necessary electronic components on the platform can help in collecting additional data across a more extensive set of movements, over longer time spans, different users, and multiple sensor applications for the same user. Additional work can also target improved integration of the device with garments and the donning / doffing procedure. The number of sensors used to quantify the motions can be optimized, as well as the interfacial layer between the device and skin. These additional tests and improvements would benefit the device's use by real patients to, e.g., facilitate rehabilitation, such as studied in the lab of Prof. David Lipps (Kinesiology) for patients who have undergone a mastectomy and suffer from

limited range of shoulder motion. Currently, there is no easy way to do this because patients are unable to move to studios who have camera motion tracking systems and using goniometers (type of protractor) are often inaccurate. Below, initial work on some of these improvements is described.

### 3.4.1 Circuit design

A fully wireless device is imperative to enable comfortable, convenient, and accurate real-time data collection. An example of the location of components on a wireless version of the device is shown in **Figure 3.6**. Electronic components such as operational amplifiers, microcontroller, and battery can be placed in the center. The red lines in **Figure 3.6** represent electrical traces, and the red squares indicate contact pads.

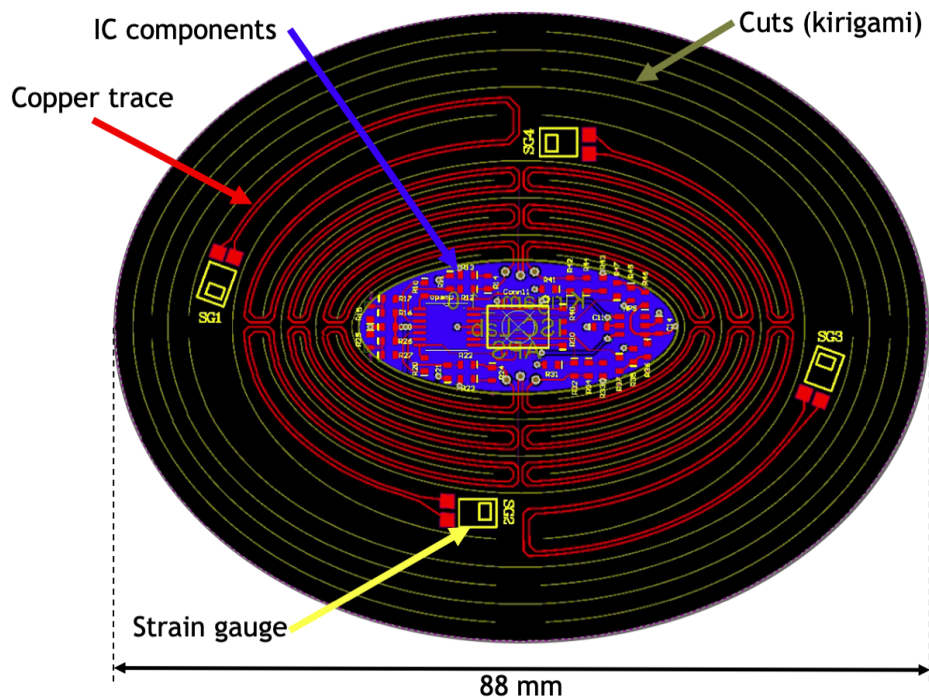


**Figure 3.6** Schematic of circuit design for embedding integrated circuit (IC) components to the kirigami sensor platform.

### 3.4.2 Fabrication method

A polyimide flexible printed circuit board (flex pcb) was fabricated by OSH Park. **Figure 3.7** shows a side view schematic of the kirigami device. The flex pcb was then placed back-side down onto the acrylic adhesive side of a double-sided adhesive from 3M (#2477P). While the liner on the other side of the adhesive is still intact, the flex pcb is placed face-down on a sacrificial acrylic sheet to prevent damage to the laser-cutter, as well as the traces. The flex pcb with the adhesive is laser-cut at 33% power, 8% speed, and 1000% ppi with a 50W CO<sub>2</sub> Universal Laser Systems 3.50 laser cutter.

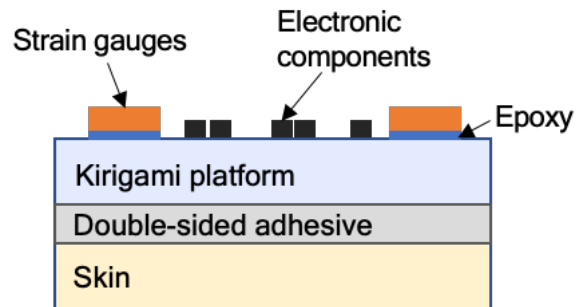


**Figure 3.7** Diagram of wireless kirigami device (not to scale).

After the substrate is laser-cut, strain gauges are adhered onto the substrate using five-minute two-part epoxy and cured for 24 hours, shown in **Figure 3.8**. Electronic components are then soldered onto the board. To adhere the device to the body the plastic linear is simply removed and the device is aligned to the shoulder.

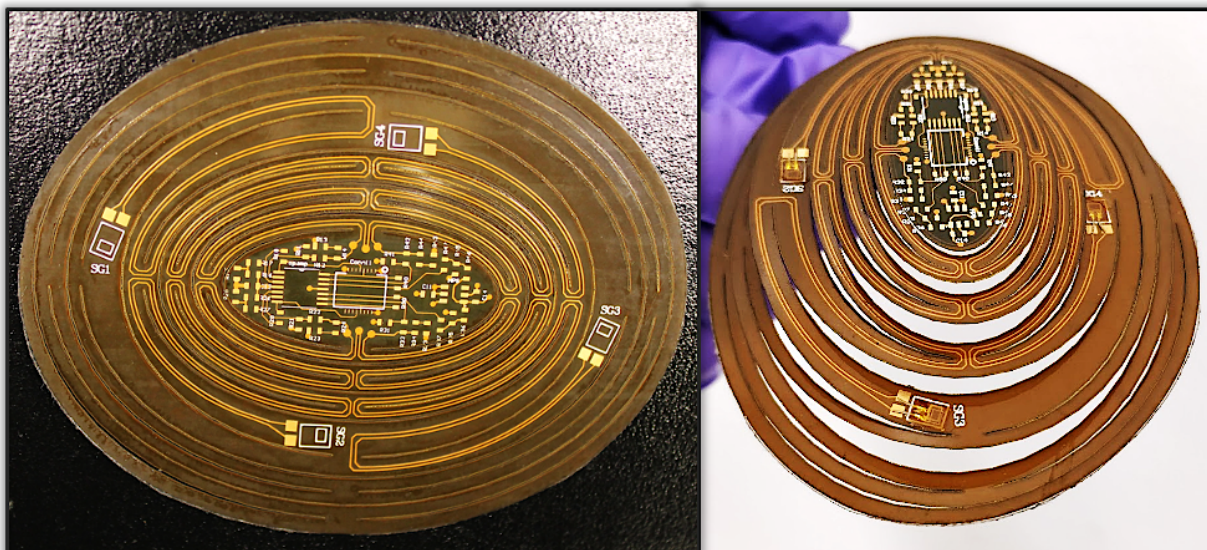


**Figure 3.8** Top (left) and iso view (right) of kirigami flex pcb after laser-cutting and bonding strain gauges.

### 3.4.3 Further work

Several aspects of the device should be further examined to characterize its accuracy for different users, for example, across different sizes and shapes of the shoulder, and whether modifications should be made to the cut pattern to accommodate these variations.

**Figure 3.9** describes various aspects important to the details of the sensor's design and options of different functionalities that can be integrated and/or coupled to the sensor. The versatility of the kirigami test platform is useful here, in that it can be easily customized to the particular use case and/or the user. Each user's shoulder shape, for example, can be determined using a three-dimensional scanning chamber, cameras having depth perceptibility, or measured traditionally using a tape measure. The platform can be configured in several standard sizes for various joints. Implementations of sensors on the kirigami platform include the use of strain gauges, accelerometers, gyroscopes, magnetometers, sweat, electrocardiographic, humidity, UV, pressure, optical, acoustic, and radiation sensors, as well as antennas. These sensors allow for the following functionalities: joint tracking/position monitoring, muscle tracking, heart rate

monitoring, temperature readings, UV monitoring, neuromuscular electrical stimulations, brace support, breath monitoring, sleep monitoring, haptic feedback, lactic acid sampling, local anesthetic dosing, pulse oximetry, vocal vibration detection, and sound amplification. From this, the module must communicate to the user in the form of mobile/portable devices, smart glasses, computer/laptops, watches, and virtual or augmented reality displays.

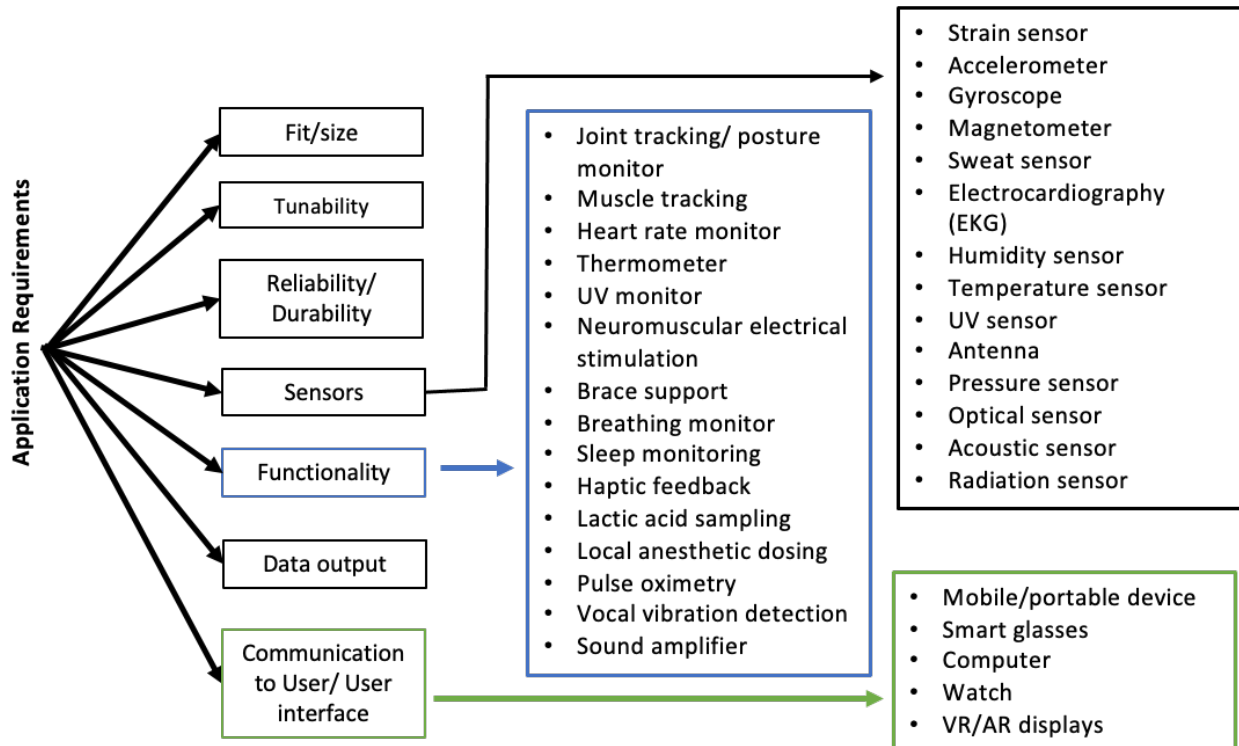


Figure 3.9 Application requirements and additional capabilities of the device.

### 3.4.3.1 Integrating virtual and augmented realities

Integrations with virtual and augmented realities (VR/AR) is a promising path to enhancing the benefits of this device, enabling real-time feedback through smartphone apps, for example, how the user moves their limbs and whether or not they are achieving a desired range of motion.<sup>60,61</sup> This would not only be useful for physical therapy but other applications where careful monitoring of form is essential such as during weightlifting, racquet sports, etc. Current AR/VR solutions have a number of limitations in that regard. For one, current smartphone apps lack sophistication of the



tracking itself and applicability to important joints (e.g., shoulder, hip). More sophisticated and higher fidelity optical tracking can be achieved using multiple cameras in a studio environment, but this typically involves expensive cameras with precise positioning needs, as well as separate optical tracking aids attached to joints. More sophisticated, wearable sensors could in principle be used to augment or supplement AR/VR motion tracking solutions.

An example utilization chain of integrating the kirigami module with handheld devices for augmented reality applications is shown in **Figure 3.10**. The mobile device is calibrated based on the room and direction of the phone held, to which an avatar is placed in the room and performs a motion (**Figure 3.10b**). The user then copies the avatar's motion, while the phone simultaneously gives feedback to the user on his/her performance (**Figure 3.10c**). After the full motion is performed, the phone displays the motion captured by the avatar, the ideal motion, overlaid with the motions performed by the user (**Figure 3.10d**). Real-time feedback and tracking history are provided to ensure proper performance (**Figure 3.10e**). This is essential to reap the full benefits of the activities or prevention of injuries, such as when performing physiotherapeutic exercises. It is important to note the existing implementation of using AR mobile devices to track positions are largely limited to the positions that are trackable based on where and how the phone is held and provides no other functionality.

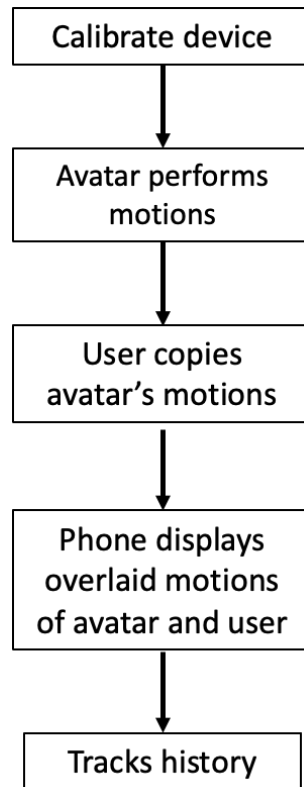


**Figure 3.10** Integration of kirigami platform with augmented reality used to track joint positions.

#### *3.4.3.2 Variations of the cut pattern to accommodate other body parts*

One of the biggest advantages for using RSK design methods is its versatility. While most of this chapter addressed the device performance and characteristics based on the shoulder joint, the device can also be used on other parts of the body by changing the shape and size of the pattern. For instance, the pattern can be modified to fit the lower back as shown in **Figure 3.1c**. This pattern is designed to track movement by bending forwards and backwards, as well as twisting. Furthermore, the pattern is not limited to one continuous pattern. Instead, multiple units can be placed in one to better accommodate intricate and nonsymmetric curvatures, such as the foot (**Figure 3.1a,b**).

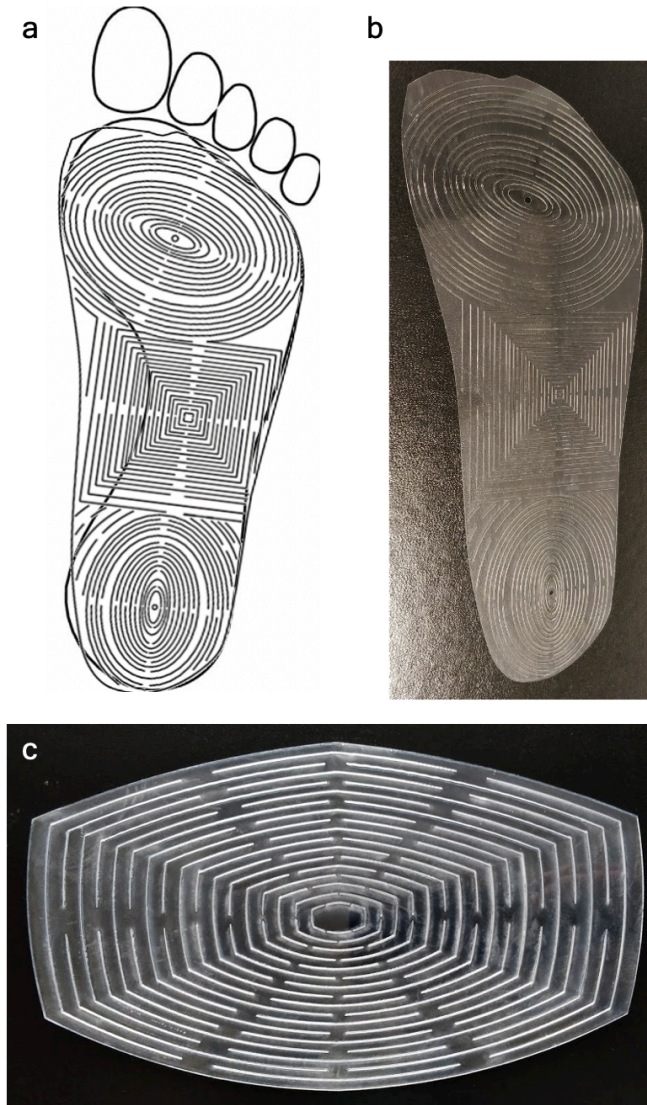


**Figure 3.11** Modification of RSK pattern to conform to foot and back. (a) CAD pattern and laser-cut substrate (b) to fit the shape of the foot. (c) Laser-cut plastic sheet designed to conform to the lower back.

## Chapter 4 Multi-Axis Optical Tracking System

### 4.1 Overview

As described in previous chapters, kirigami-based structures and materials have been developed with a variety of geometric transformation capabilities in applications such as flexible electronics, soft robotics, nano-photonics, energy-harvesting, and others. In this chapter, a 2-dimensional pattern of cuts (kirigami) is presented, capable of transforming into a 3-dimensional, one-piece compliant mechanism that allows for optical tracking over a solid angle sweep of over  $110^\circ$  in two axes. This structure can be scaled to an arbitrarily large (width x length) array, yet the actuation displacement required to achieve the angular sweep remains compact and independent of the number of elements and areal extent of the array, as does the height of the array. One of the applications of this mechanism is in solar concentration and dual-axis tracking. Using practical dimensions, 80-fold or greater concentration can be realized. Mutual shadowing of nearby concentrators is assessed along with thermal effects of optical concentration that limit photovoltaic cell efficiency. The significant reduction in semiconductor usage along with the multi-axis tracking ability will reduce the overall cost of solar photovoltaic panels. This is projected to make them competitive with stationary silicon panels capable of satisfying the household daily average energy requirement.

## 4.2 Introduction

Despite steady advances in the efficiency<sup>[24,25]</sup> of photovoltaic devices, widespread adoption of ultra-high efficiency materials remains limited due to the high cost of high-efficiency semiconductor photovoltaic (PV) cells.<sup>[26]</sup> Concentrated photovoltaic (CPV) systems reduce semiconductor requirements; however, most designs have a narrow acceptance angle and therefore require precise tracking.<sup>[27,28]</sup> Conventional trackers used to achieve the required tracking precision are large, heavy, complex, costly, and unsuitable for deployment in many desirable locations including residential rooftops.<sup>[27-29]</sup> Thus, a number of recent works have tried to address the limitations of narrow acceptance angle, tracking ability, and cost. Grede and Giebink proposed a concentrator shape that maintains over 90% optical efficiency over 140°,<sup>[30]</sup> and microcell arrays have been proposed to reduce concentrator cost and weight.<sup>[31,32]</sup> Origami and kirigami techniques have also been shown to overcome some limitations of existing trackers, including *miura-ori* and “flasher” origami patterns as deployable solar arrays.<sup>[23,33-35]</sup> However, many of these patterns require more semiconductor material than conventional panels, are not easily manufacturable due to the intricate folds required, and exhibit poor fatigue performance.

### 4.2.1 Previous kirigami solar tracker designs

As of Q2 2020, solar installations in the United States have the capacity to generate 85 GW, enough to power 16.1 million homes.<sup>62</sup> According to the National Energy Renewable Laboratory, rooftop solar photovoltaics have the potential to produce 40% of all U.S. electricity generation.<sup>63</sup> The report stated small building rooftops could produce 731 GW of PV capacity, or ~ 65% of the total potential of rooftop photovoltaics.<sup>63</sup> In addition, uniaxial solar tracking can further improve the amount generated by up to 40%. However, conventional solar tracking technology requires

complex mechanisms that are incompatible with rooftop installations, which comprise a significant portion of available solar energy capacity.

The simple linear kirigami pattern, as shown in **Figure 4.1**, was first used to demonstrate parity with conventional uniaxial solar tracking by incorporating gallium arsenide (GaAs) photovoltaic cells directly on a flexible substrate, laser-cut into a simple linear kirigami pattern that enabled “stretching” the solar cell, while progressively tilting the photovoltaic material toward the sun over the course of the day without damage.<sup>9</sup> **Figure 4.1(a)** depicts the rotational movement of the substrate induced by the cuts when stretched and in **Figure 4.1(b)** how this behavior is utilized for solar tracking. This approach achieved a 36% reduction in semiconductor needed relative to a stationary device and avoided complex folds and mitigated optical losses due to scattering (e.g., on overcast days).

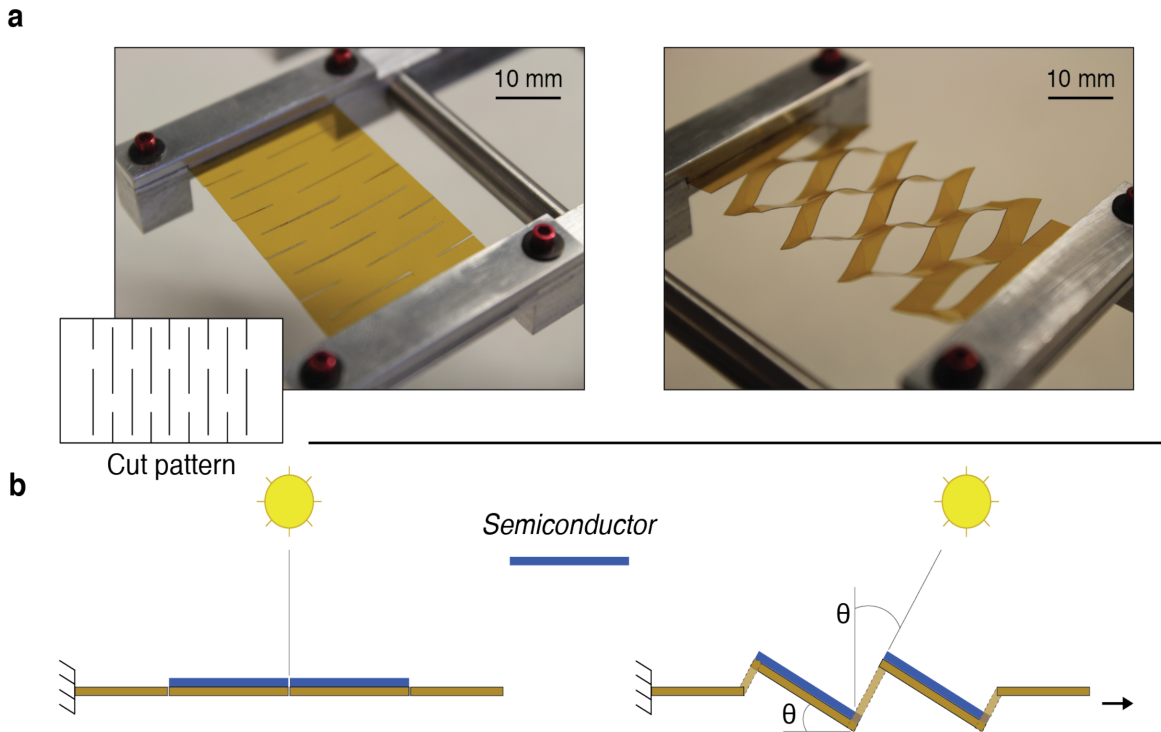


**Figure 4.1** Basic principle of how kirigami can be used as a solar-tracker. a Relaxed substrate (left) and b stretched substrate (right). b Planar tracker laid flat with sun directly above (left) and tracker tilted to track the position of the sun.<sup>9</sup>

To further improve the economics of solar energy collection, concentrated photovoltaic (CPV) systems that focus light onto very high efficiency solar cells are designed. While these are particularly attractive for their economic advantages over non-concentrated systems, provided an alternative approach is found to enable low profile solar tracking on rooftops. The narrow acceptance angle of concentration optics calls for very precise tracking and mutual alignment between the optical concentrator and the cell, while the rooftop mounting poses a challenge for achieving compactness and light weight. Therefore, an array of very lightweight, miniature parabolic concentrators integrated were with a single-axis planar tracking mechanism based on kirigami design principles. In this approach, the parabolic concentrator array is fabricated from a vacuum thermoformed plastic sheet, which is coated with a reflective metal coating, subsequently

cut and fused to a transparent sheet carrying small area gallium arsenide (GaAs) solar cells. The resulting structure comprises an integrated single-axis tracker/PV module that is scalable, and potentially low cost, eschewing complex, bulky support and tracking structures required by conventional concentrator designs. The concentrator array with a designed aperture-to-cell area ratio of 50x achieved a maximum concentration factor of 33x in optical flux and 22x in maximum power compared to a planar cell. Furthermore, combined with simple axial rotation, the kirigami array boosts the annually generated power by a factor of approximately 35x compared to a flat cell of the same area without tracking. This low-profile single axis solar tracker is demonstrated in **Figure 4.2**. A CAD pattern showing the kirigami pattern arranged in a honeycomb pattern with electrodes in gold and PV cell in blue is shown in **Figure 4.2a**. When one ends of the substrate are pulled apart from each other, this causes the concentrators to simultaneously tilt. The tilt angle,  $\theta$ , is highly dependent on the applied displacement. As the displacement increases, so too does the distance between concentrators,  $L$ , as depicted in **Figure 4.2b**. A top view of the physical array unstretched, a side view of the stretched array, and an isometric view of the stretched array is also shown in **Figure 4.2c**.



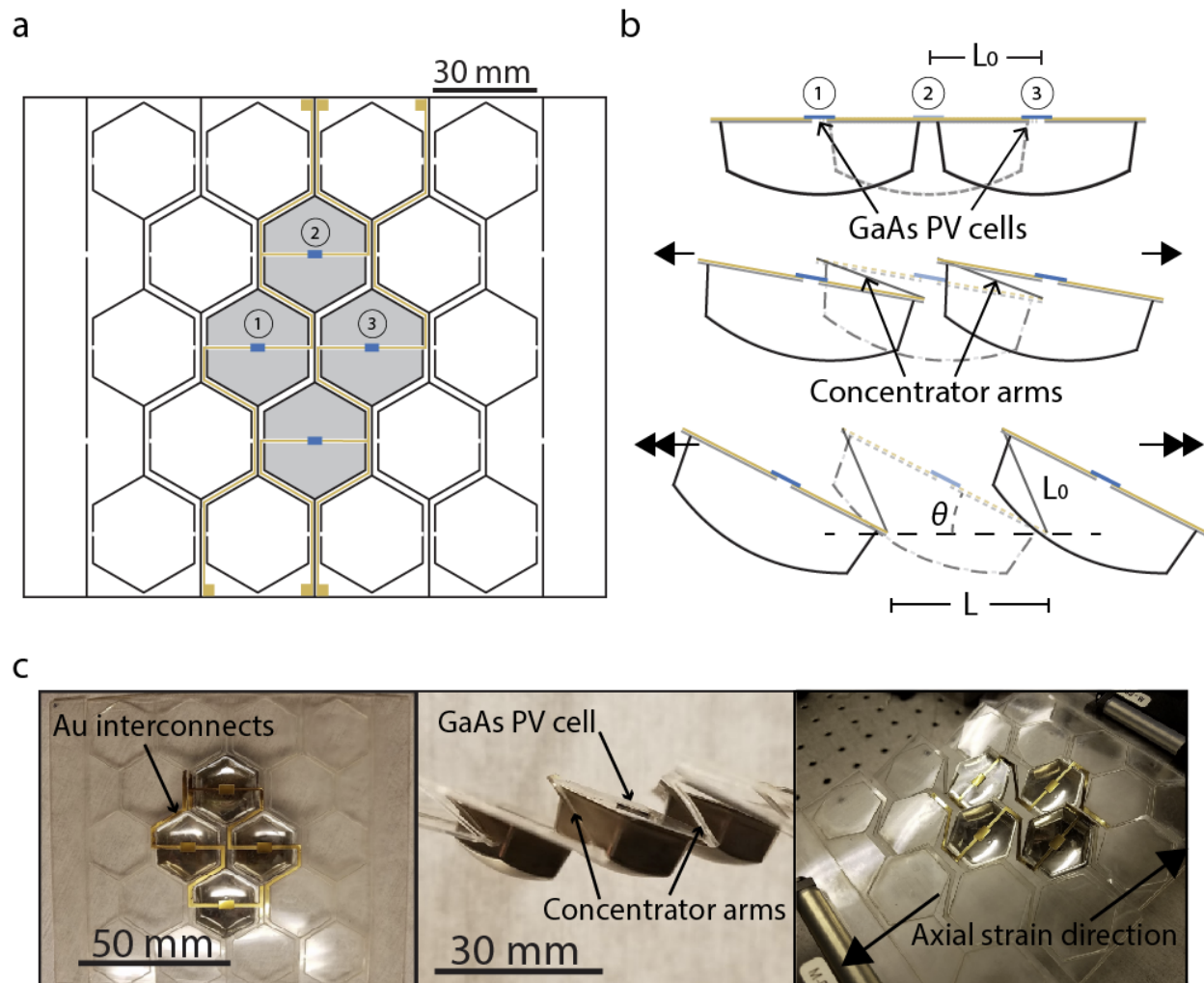


**Figure 4.2** Low-profile solar tracking system based on kirigami design principles. (a) represents a top view schematic of the tracking array module. (b) shows a side view of the tracker under different axial strains. (c) shows physical models of the Au interconnects (top view), location of the GaAs PV cell and concentrator arms that define the angle of rotation (side view) and the tracker under axial strain.

Although this design enables reduced size, weight, and cost solar tracking ability for rooftop mounted photovoltaic systems, there are several significant limitations. Initial cyclic tests seemed to indicate that the struts within the kirigami structure that define the angle of rotation, are sufficient for beyond 6,000 cycles, which is more than 10 years of use (**Figure 4.3a**). Nonetheless, the actuation energy still changes by 5% after 6,000 cycles. This is highly dependent on the strain rate and the amount of strain the tracker experiences. Furthermore, the response of the tracker array

was measured before and after multiple cycles, indicating its reliability as a tracker for at least 5,000 cycles (**Figure 4.3a**).

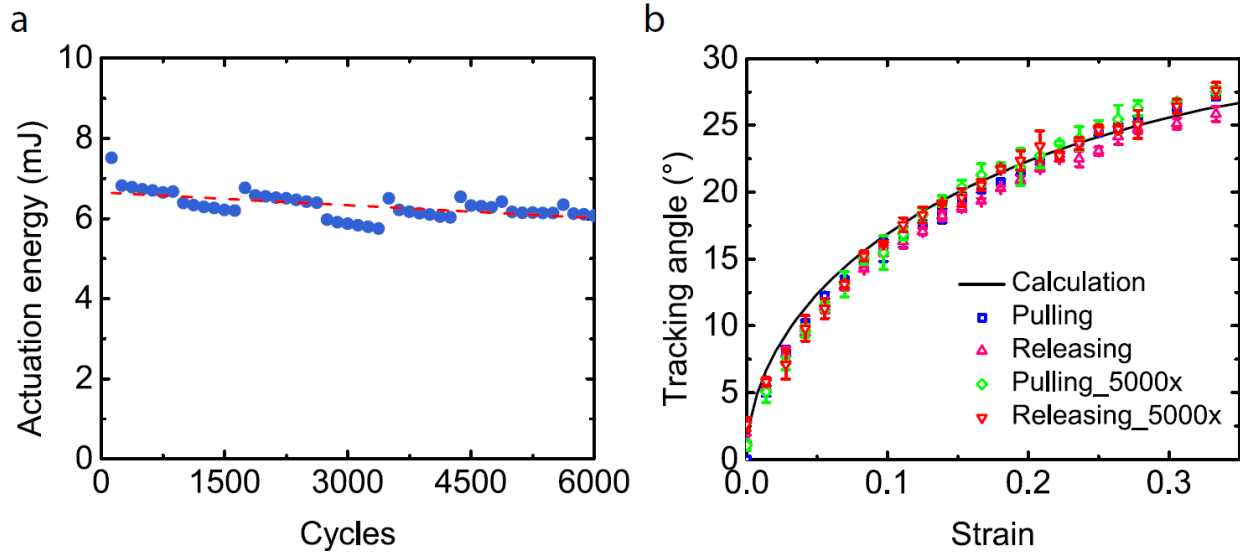


**Figure 4.3** Actuation energy of the concentrator every 125 cycles. Discontinuities are due to instrument limitations, which re-quired the resetting of the tracking mechanism after reaching 875 repeat cycles.

While the experiments conducted thus far indicate that the energy cost of actuation is negligible, and cycle life is very high, there is potential for plastic deformation and delamination between the top and bottom plastic sheets in the high local strain regions, as shown in **Figure 4.4a**. The type of plastic used is likely unsuitable for outdoor applications, due to the high UV exposure. Furthermore, because of the high concentration, the temperature of the PV cell increases, which significantly reduces the efficiency of the cell (**Figure 4.4b**).

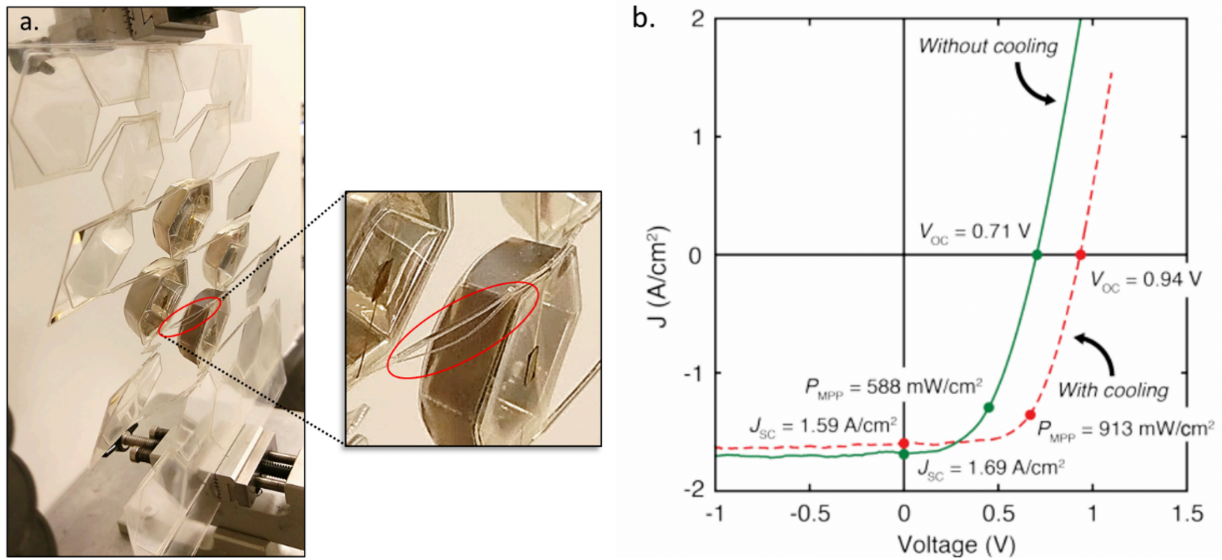


**Figure 4.4** Limitations of single-axis kirigami solar tracker. (a) Delamination of top and bottom sheets and limited angle of rotation. (b) Difference between fill factor with and without cooling, showing performance depends on temperature of the cell.<sup>64</sup>

With this design, as with any concentrator design, a tradeoff exists between the concentration factor and the efficiency of cell. Further, the hexagonally modified linear kirigami design limits the degree of rotation of the concentrators to  $\pm 27^\circ$ , meaning the sun is tracked only partially throughout the day. Therefore, maximum daily energy harvesting can be achieved by tracking the sun throughout the entire course of the day. Lastly, because the tracker only rotates in one axis it does not account for annual changes in the sun's position. However, even with these limitations stated, the kirigami approach can realize  $>10x$  reductions in the total exposed area of high efficiency photovoltaic solar cells relative to conventional planar and stationary configurations. NREL's projected cost models for non-destructive epitaxial lift-off (ND-ELO), GaAs based solar cells have the GaAs solar cell comprising  $>85\%$  of the module cost.<sup>65-67</sup> Consequently, a  $>10x$  reduction in the amount of GaAs solar cell needed to achieve the same energy harvest is likely to produce substantial economic benefit with an allowance for the increased cost of including a tracking mechanism and modified fabrication.

While this design achieved 6-fold optical concentration using non-imaging, folded, or molded optics mated to a kirigami substrate to enable diurnal tracking, it remains limited to single-axis and an angle sweep of  $\pm 54^\circ$ .<sup>64</sup> In this chapter, the kirigami pattern derived from the previous chapter is modified to enable dual-axis tracking. It is robust, easily scaled to large-area arrays, and can be integrated with a variety of optical elements. As proof of concept, the utility for a solar tracking mini-CPV application is explored and demonstrated how it dramatically reduces the amount of semiconductor material required. **Figure 4.5** demonstrates the progression of kirigami-based solar tracking systems, from left to right: v1 linear kirigami pattern, v2 modification of linear pattern to include concentrators, and v3 rotationally symmetric kirigami pattern with concentrators. The latter will be further discussed in this chapter; for more information on v1 and v2, please refer to [64].

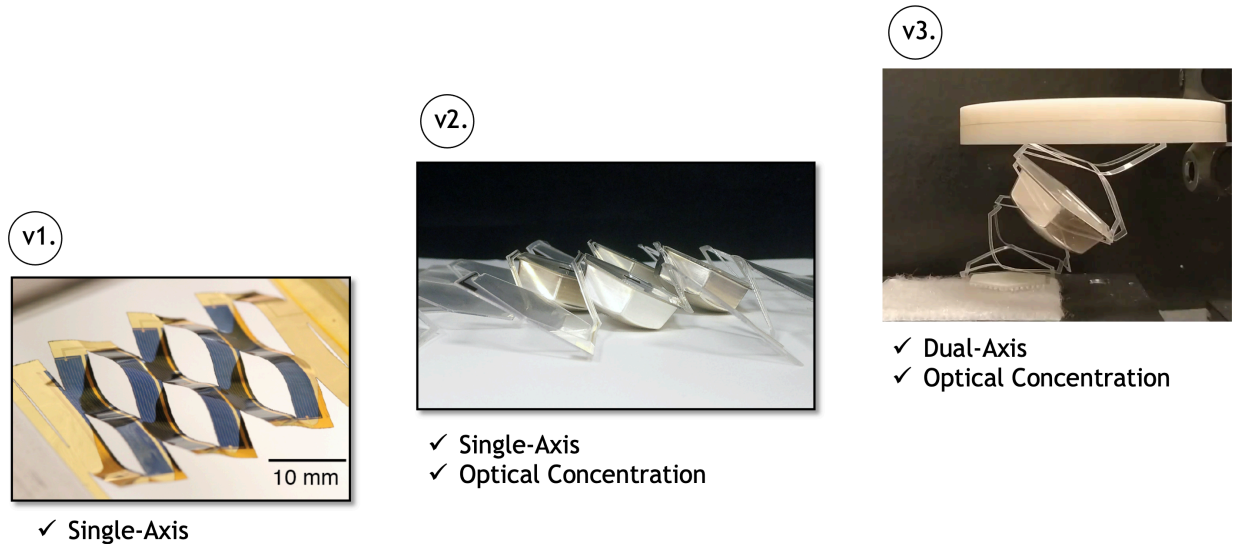


**Figure 4.5** Progression of kirigami-based solar tracking system designs.

## 4.3 Kirigami design, fabrication, and testing of the compliant mechanism

### 4.3.1 Baseline hexagonal kirigami spring

The baseline kirigami cut pattern consists of discontinuous concentric hexagonal cuts as shown in the inset of **Figure 4.6b**; each hexagonal “ring” has two diametrically opposed splits rotated by  $90^\circ$  between each concentric set. The hexagonal pattern has an overall three-fold rotational symmetry about the central axis. When a force is applied to the middle of the pattern along the rotational symmetry axis as depicted in **Figure 4.6a**, this creates a series of hexagonal rings. The rings can be segmented into S-shaped beams, which are connected *via* saddle-points formed by the uncut regions, similar to the structures shown in **Chapter 2**. This provides structural continuity between the outer- and inner-most hexagons. In the expanded structure, these become the “top”- and “bottom”-most horizontal members. When sliding them parallel to each other as depicted in **Figure 4.6a**, the symmetry is further broken, causing the connecting beams to tilt simultaneously. A close examination of the structure in the side view reveals that previously aligned saddle-points are located on the same cut perimeter in the middle ring. A red line connecting the two saddle points that results in tilt angle,  $\theta$ , is shown for clarity in **Figure 4.6a**. The relationship between the angle  $\theta$  and the lateral displacement,  $\delta$ , is controlled by the geometry of the cuts and cross-plane displacement,  $z$ . Also shown in **Figure 4.6a** is a top-view perspective, where the color bar indicates the normalized Von Mises stress. As previously discussed, FEA modeling clearly shows that stress is concentrated in the cut ends, informing the placement of other elements within the structure with minimal risk of structural damage.

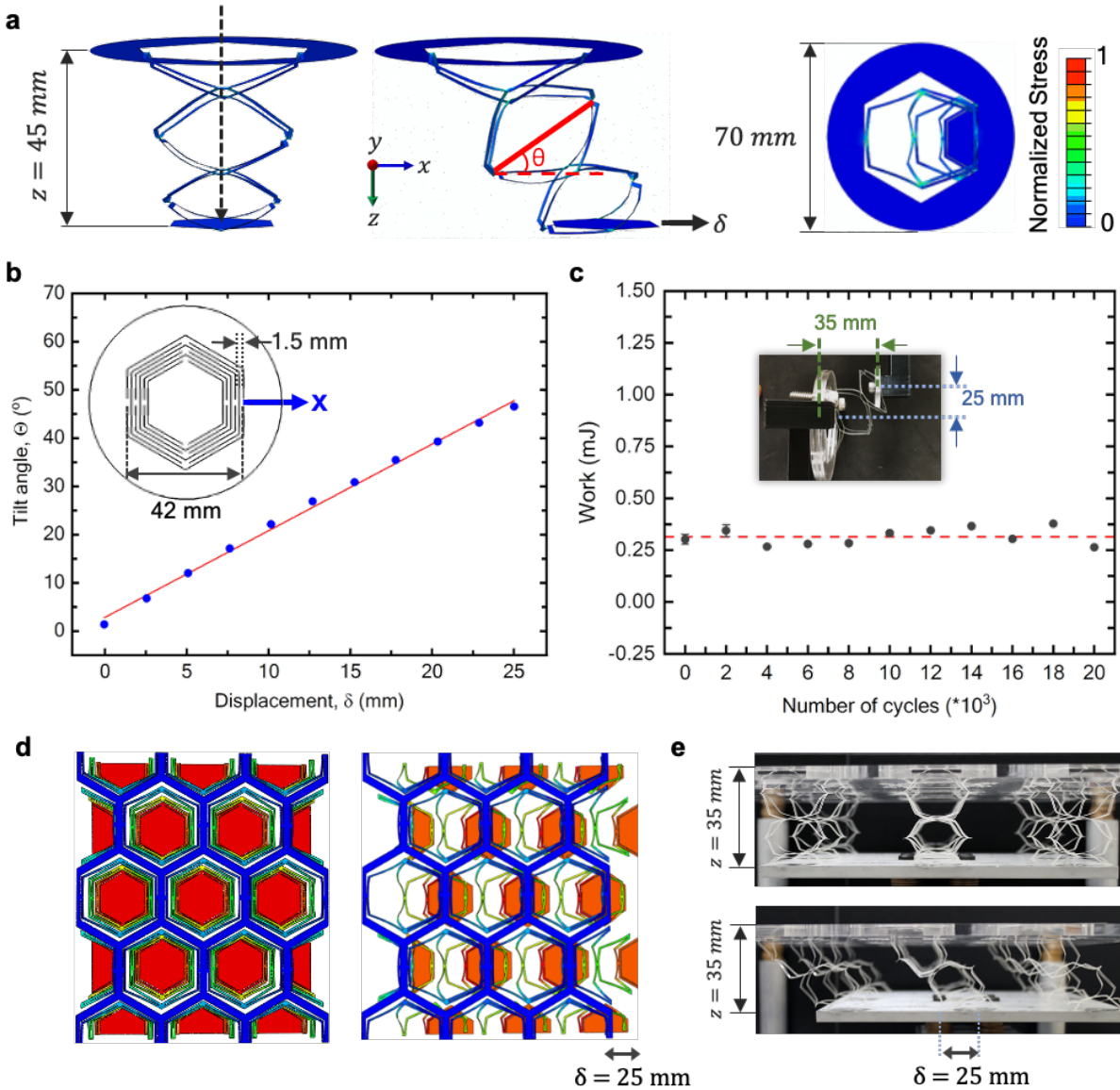


**Figure 4.6** Tilting mechanism of a hexagonal kirigami spring. a) Left: side view of FE model of a deformed spring displaced 45 mm in the  $z$ -direction, middle: side view and right: top view of model displaced 25 mm in the  $x$ -direction and 45 mm in the  $z$ -direction; color bar indicates normalized stress. b) Experimental measurement of tilt angle based on displacement in the  $x$ -direction maintaining a height of 35 mm with linear fit. c) Work required to shear the spring in the  $x$ -direction by 25 mm for up to 20,000 cycles, maintaining a height of 35 mm. d) FE model of deformed array arranged in a honeycomb pattern in the  $x$ -direction at  $\delta=0$  mm (left) and  $\delta=25$  mm (right) where  $z=35$  mm. e) Side view of deformed physical array arranged in a rectangular pattern for visual clarity at  $\delta=0$  mm (top) and  $\delta=25$  mm (bottom) in the  $x$ -direction where  $z=35$  mm.<sup>68</sup>

The structure described above and shown in **Figure 4.6** is simple to fabricate using a number of scalable methods; for the purposes of this demonstration, 100  $\mu\text{m}$  thick polyethylene

terephthalate (PET) sheets are laser-cut. Tilt angle,  $\theta$  as a function of  $\delta$  was measured (**Figure 4.6b**) showing a monotonic, approximately linear dependence, having an  $R^2$  value of 0.99:

$$\theta = 1.8\delta + 2.9 \quad (4.1)$$

This dependence is applicable for the cut pattern shown in the inset of **Figure 4.6b** in which there are two cuts per “ring”,  $z = 45$  mm, the radial spacing between cuts ( $w$ ) is 1.5 mm, the angular spacing ( $\varphi$ ) formed by the cut ends from the center is  $6^\circ$ , and the phase shift ( $\gamma$ ) referring to the central angle of the placement of the hinges, non-cut regions, with respect to the side is  $0^\circ$ . Note the slight offset could be attributed to the camera rotation during data collection.

For a variety of tracking applications, repeated displacement is expected, and it is important to know the force and work required to perform the movement, as well as the fatigue life of the structure. **Figure 4.6c** shows that to induce tilting, an average of 0.3 mJ are required over a lateral displacement from 0 to 25 mm for  $z = 35$  mm. Despite large global deformations, this range of  $\delta$  is well within the linear elastic regime of the structure as shown in **Figure 4.7**.



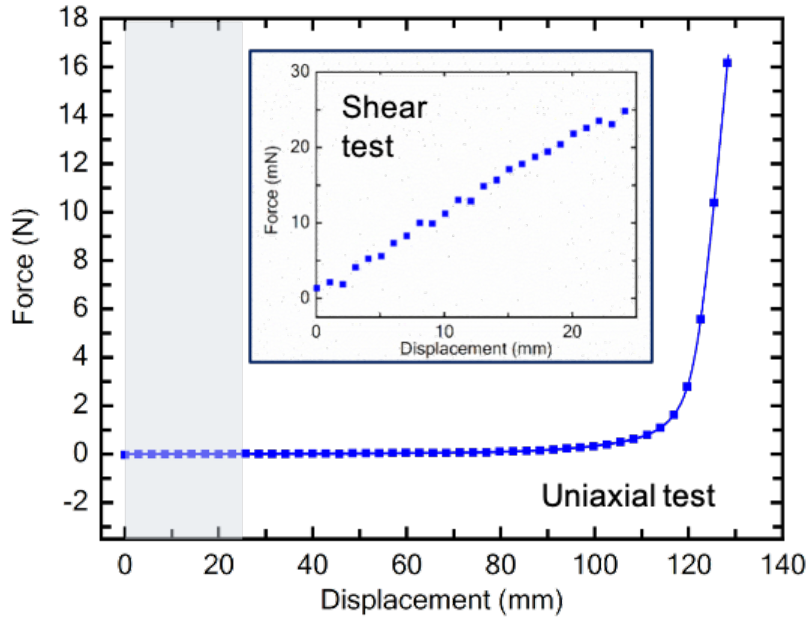


**Figure 4.7** Uniaxial and shear tests of unit cell. a) Force vs displacement plot of unit cell undergoing uniaxial tensile test and (b) undergoing shear test along the x-direction.<sup>68</sup>

**Figure 4.6d** shows the  $\delta$  behavior as a function of  $\theta$  incurs no hysteresis in the work required for a cycle after performing 20,000 cycles at a displacement rate of 1 mm/s. This number of test cycles correspond to 20 years of operation and indicates there is minimal perceptible plastic deformation of the structure. One cycle is performed to follow the sun throughout the day and another cycle to return to the original position before sunrise the next day. Error bars are included for the control and 2,000 cycle cases; deviations are attributed due to human error in re-aligning the substrate in 3D printed holders attached to tensile grips during shear tests, due to test apparatus limitations.

The individual-concentrator tracker assembly lends itself to creating a low-profile array in which the motion of the individual actuators is intrinsically synchronized. **Figure 4.6d** shows the top view of hexagonal concentrators arranged in a honeycomb pattern and deformed such that  $z = 35 \text{ mm}$  at displacements of  $\delta = 0 \text{ mm}$  and  $\delta = 25 \text{ mm}$ . The side view of a physical array at  $\delta = 0 \text{ mm}$  and  $\delta = 25 \text{ mm}$  when  $z = 35 \text{ mm}$  are also shown in **Figure 4.6e**. Translating the



top (or bottom) plane by 25 mm induces the same maximum tilt angle for each of the concentrators. That is, the same amount of lateral translation is required independent of array size. In addition, the lightweight hexagonal kirigami pattern requires significantly less work to induce a desired tilt response compared to standard trackers. A major drawback of many mechanical trackers and actuators is the parasitic energy loss due to the use of large mechanical motors, hinged joints, and moving mass required to tilt a photovoltaic panel or optical array.<sup>[28]</sup> Standard trackers that rely on rotating the entire panel at once require more work and occupy a larger tracking region when increasing the size of the panel. They also often need heavy and bulky supports. For instance, if the kirigami-based tracker panel is 180 m<sup>2</sup>, a total of approximately 0.04 kJ would be required to tilt all of the concentrators to 55° at  $z = 35$  mm; in contrast, >128 kJ would be required by a 10x18-m rectangular silicon solar panel with a mass density of 15.13 kg/m<sup>2</sup><sup>[37]</sup> at a height of 8.2 m at a tilt angle of 55°.

#### *4.3.2 Mechanical testing setup*

For mechanical testing, polyethylene terephthalate (PET), 901 Highland Laser Printer Film (3M, 90 μm) is cut with a 50 W Universal Laser Systems CO<sub>2</sub> laser cutter (5% power, 10% speed, 1000 ppi, 1.5” optics). The Young’s Modulus and Poisson’s ratio of the film is 2.2 GPa and 0.37, respectively. Two rings were cut from Optically Clear Cast Acrylic Sheets (McMaster-Carr, 7/64” thick) with the laser cutter (100% power, 5% speed, 2.0” optics) to hold and align the RSK springs during tensile tests. To conduct uniaxial and shear tests, acrylic rings sandwiched the substrate and placed in holders that were 3D printed (Monoprice Maker Select, Brea, CA, USA) out of polylactic acid (PLA). The holders were then clamped into tensile grips, and both tests were conducted at a strain rate of 1 mm/s. The force versus displacement curves were obtained via a TA.XTPlus Texture Analyzer (Texture Technologies, Hamilton, Massachusetts, USA) with a 30kgf load cell

and the *Exponent* (Texture Technologies, Hamilton, Massachusetts, USA) software package. Work was obtained by integrating the force versus displacement data using OriginPro. Motorized lead screws attached to stages are used to translate the spring in the  $x$ - and  $y$ -directions; the CAD of the setup is shown in **Figure 4.8**. The noise within the experimental data at lower forces is due to the resolution of the equipment and the plotted data is smoothed by adjacent averaging in OriginPro.

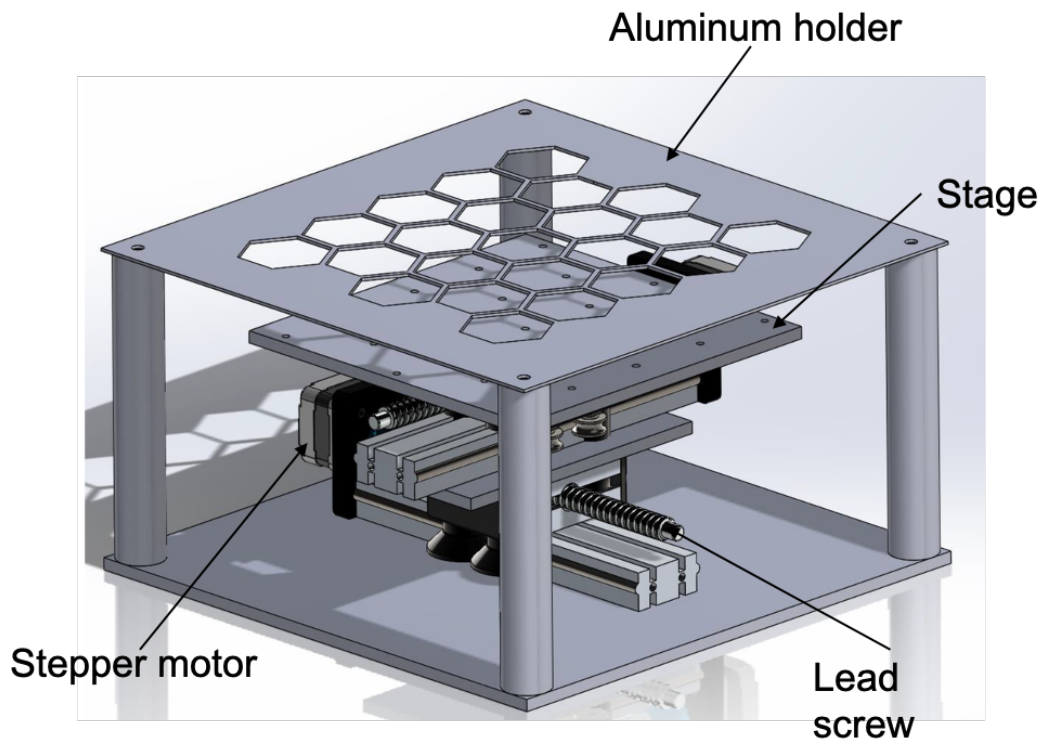


**Figure 4.8** CAD model of cyclic tester, consisting of DC steppers powering lead screws, aluminum frames to hold unit cells and stage connected to motors.<sup>68</sup>

### 4.3.3 Influence of varying cut parameters

**Figure 4.9** gives an overview of the influence of varying cut parameters based on directionality of displacement,  $\delta$ . The cut parameters,  $w$  and  $\varphi$ , are similar to those discussed in **Chapter 2** with the addition of the cut phase shift,  $\gamma$  (**Figure 4.9a-d**). For each of the cut parameters, displacement

in the  $x$ -direction, indicated as  $0^\circ$  on a polar plot, results in a higher tilt angle per displacement than displacement in the  $y$ -direction for each cut parameter (**Figure 4.9e-g**). Also, as the deformation height increases, the lower  $\theta_{max}$  as a function of  $\delta$  (**Figure 4.9h**). While many of the experiments are completed for two directions, it is possible for the pattern to be displaced as a resultant of the  $x$ - and  $y$ -directions. In **Figure 4.9i**, it is again shown that  $\theta_{max}$  decreases as the displacement direction approaches  $90^\circ$ . Precise control of the simultaneous displacement in the  $x$ - and  $y$ -direction yields a specific offset angle. For instance, the substrate when displaced 25 mm at  $50^\circ$  translates to 18.7 mm in the  $x$ -direction ( $0^\circ$ ) and 22.3 mm in the  $y$ -direction ( $90^\circ$ ), see **Table 4.1** for the corresponding displacement coordinates. The differences in the obtained  $\theta_{max}$  between the cut parameters and displacement direction is due to the beam geometry and location of the pivot point within the ring, which is further discussed later.

**Table 4.1** Example displacement coordinates corresponding to Figure 4.9i.

Rotation, $\omega$ (deg)	X Displacement (mm)	Y Displacement (mm)
0	25.40	0.00
10	25.01	4.41
20	23.87	8.69
30	22.00	12.70
40	19.46	16.33
50	16.33	19.46
60	12.70	22.00
70	8.69	23.87
80	4.41	25.01
90	0.00	25.40

$$x = \cos(\omega) \delta \quad (4.2)$$

$$y = \sin(\omega) \delta \quad (4.3)$$

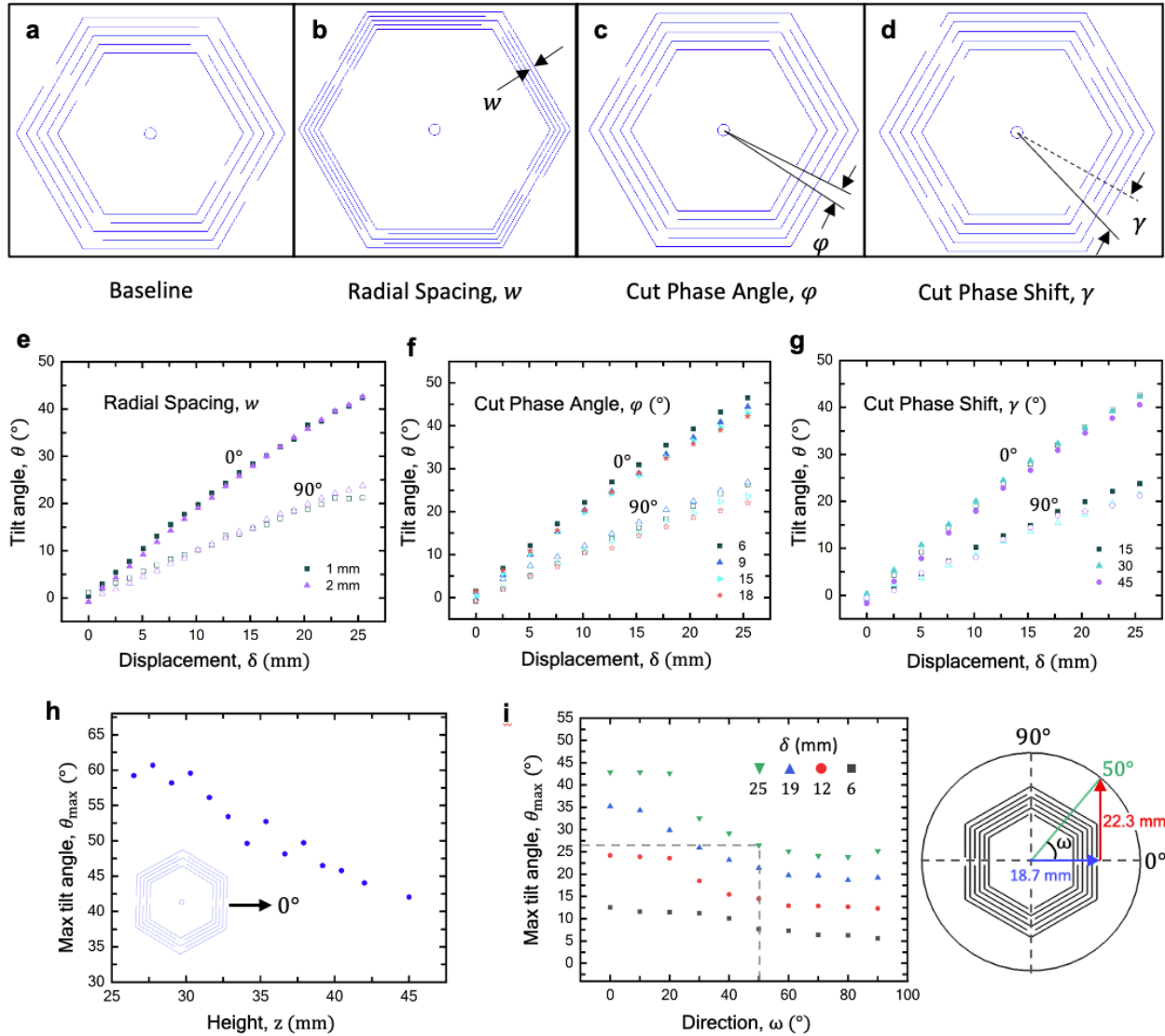


**Figure 4.9** Key cut parameters dictating cut pattern: radial spacing ( $w$ ), the cut phase angle ( $\Phi$ ), the cut phase shift ( $\gamma$ ), and number of cuts along the perimeter. (a) Represents the baseline pattern having a radial spacing of 0.75 mm, cut phase angle of  $6^\circ$ , and cut phase shift of  $0^\circ$ . (b) Differs from the baseline pattern by decreasing the radial spacing to 0.5 mm. (c) Decreased cut phase angle by  $3^\circ$ , and (d) cut phase shift of  $12^\circ$ . The shape of the pattern can also be altered to form shapes other than a hexagon, such as a rectangle or circle.  $\theta$  as a function of  $\delta$  varying  $w$  (e),  $\phi$  (f), and  $\gamma$  (g) when displaced in the x- and y-directions.  $\theta_{max}$  as a function of  $z$  (h) in the x-direction and  $\theta_{max}$  as a function of  $\delta$  of the base along the polar coordinate direction (i). The legend refers to the amount of displacement (mm).<sup>68</sup>

#### 4.3.4 Assembly of kirigami tracking system and methods

The imaginary segment previously highlighted in red in **Figure 4.6a** connecting two saddle points on a given perimeter of the cuts. To realize a solar tracking, micro-concentrator device, we insert

a hexagonal parabolic mirror in this location and adhere it along its outer edge to the kirigami spring. The kirigami patterns were fabricated by cutting PET as mentioned earlier. The cuts form a hexagonal shape, spacing between cuts is 1.5 mm, and two cuts along the perimeter are made. The overall diameter of the patterns was 70 mm with the largest cut radius at 27 mm.

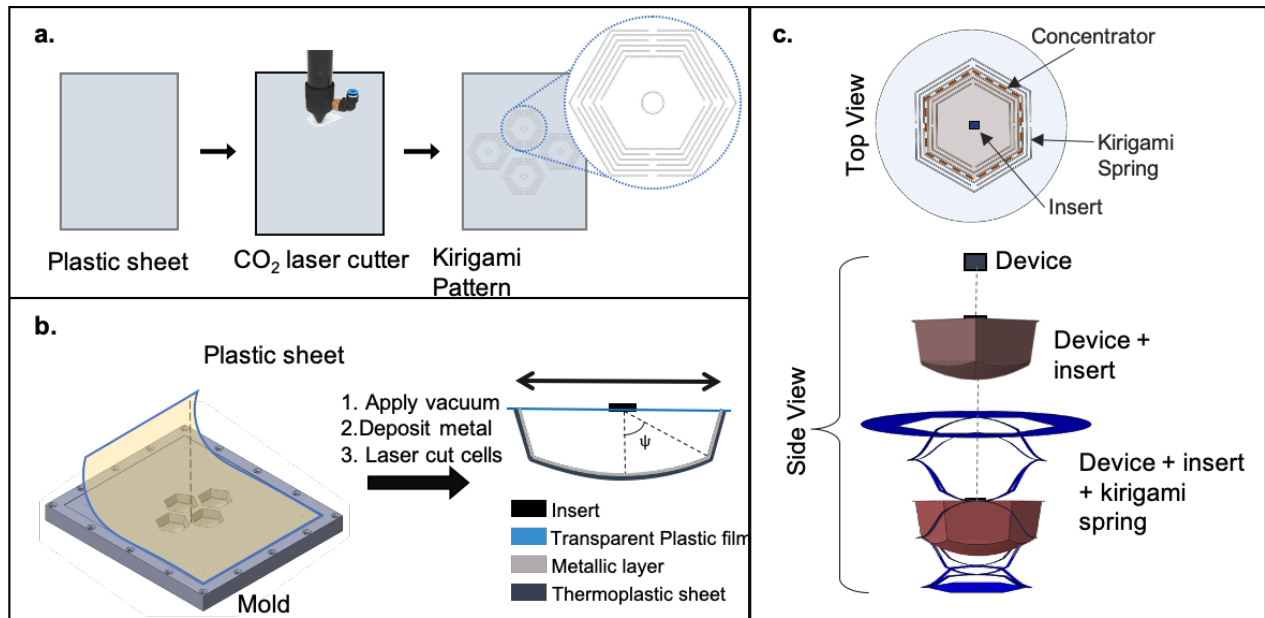


**Figure 4.10** Assembly of kirigami tracking system. (a) Laser-cutting sheet to kirigami pattern. (b) Fabricate concentrator array via vacuum thermoforming where a plastic sheet is placed on mold and then a metal coating is deposited, and the concentrators are laser-cut into the individual concentrator. (c) Top view of kirigami cut pattern with outline showing location of concentrator and insert, and side view of FE model depicting the assembly of the tracker with a concentrator.<sup>68</sup>

The concentrator is fabricated by vacuum thermoforming a 250  $\mu\text{m}$  polyethylene terephthalate glycol (PETG) sheet at 105°C for 10 min. This is followed by 0.5  $\mu\text{m}$  of Ag deposited by vacuum thermal evaporation, as depicted in **Figure 4.10b**. The front-facing side of the hexagonal paraboloid is then attached to a sheet of transparent material (here PET is used for convenience). The PET sheet has a hole in its center, which is at the focal point of the parabolic mirror. A small photodiode is then aligned in the hole facing down towards the mirror. This assembly is inserted

and affixed to the kirigami structure as indicated in **Figure 4.11a**. Sliding the bottom portion of the kirigami unit cell in a manner depicted in **Figure 4.11b** produces a tilt of the concentrator-spring assembly in accordance with Equation (1). The neutral position of the kirigami solar tracking system is represented in the left image of **Figure 4.11b**, where  $z$  is the height of the spring, and the cut pattern is represented in the inset of **Figure 4.11c**; (A) are the pivot points when the innermost ring is laterally displaced in the  $y$ -direction, and (B) are the pivot points when displaced in the  $x$ -direction. The right-side image in **Figure 4.11b** shows the structure with deflection  $\delta$  in the  $y$ -direction, the outermost hexagonal ring being fixed in place. **Figure 4.11c** plots the experimentally measured  $\theta$  vs.  $\delta$  of the concentrator-spring assembly. The inset of **Figure 4.11c** shows the cut pattern and directions of  $\delta$ ; the pink shaded region represents the concentrator area. The height of the spring is set at 33 and 45 mm, and the innermost hexagon is displaced in the  $x$ - and  $y$ -directions to determine the effects of changing the  $z$  and directions of  $\delta$ . The 33 mm height is chosen such that the corner of the concentrator does not contact the base plate at the maximum tilt angle, and also keeps the height of the array reasonably small. A greater height was also tested for comparison. We find that the mechanism performs better when the height of the expanded spring remains smaller than the displacement at which plastic deformation occurs. At each specified displacement, an image of the system was taken using a camera, and the tilt angle of the concentrator was determined using Image J. A displacement of  $\delta = 25$  mm in the  $x$ -direction results in a larger maximum tilt angle compared to the same displacement in the  $y$ -direction. Furthermore, increasing the height of the spring decreases the maximum tilt angle  $\theta_{max}$  as expected for an equivalent hinged mechanism.

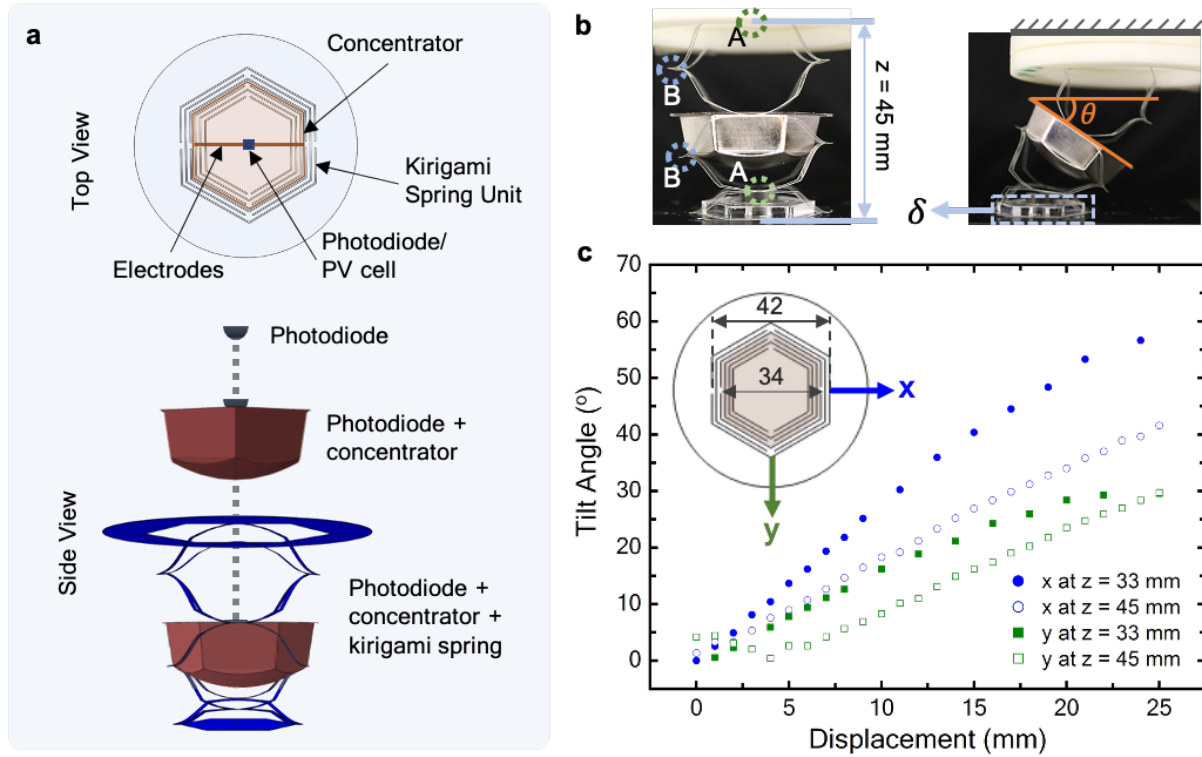


**Figure 4.11** Tilting mechanism of a kirigami hexagonal spring with concentrators embedded in the middle ring. (a) Top view and side view of the tracker with kirigami cut pattern and locations of the concentrator, photodiode or photovoltaic cell, and electrodes. (b) Images of kirigami spring deformed at  $z = 45$  mm with concentrator placed in middle ring (left) and displaced  $\delta = 25$  mm in the y-direction, prompting the concentrator to tilt  $\theta = 37^\circ$  (right). A and B represent pivot points at the edge and corner of the pattern, respectively. (c) Experimental measurements of the tracker displaced in the x- or y-direction at deformed lengths of 33 and 45 mm. Inset represents cut pattern.<sup>68</sup>

The relationship between displacement and tilt depends on the cut parameters (as described earlier and shown in **Figure 4.9**) and is approximately predictable using cantilever beam theory.<sup>[9,22,38]</sup> When increasing the radial spacing and phase angle, the beams become wider and shorter, respectively, increasing their stiffness. Shortening the length of the beam decreases the distance between the two pivot points, which increases the tilt angle. If the height of the spring is too short, the concentrator will encounter the base that restricts further tilting. The rate of increase in  $\theta$  vs.  $\delta$  differs for this system when the concentrator is facing up *versus* down due to gravity (**Figure 4.12** and **Figure 4.13**).

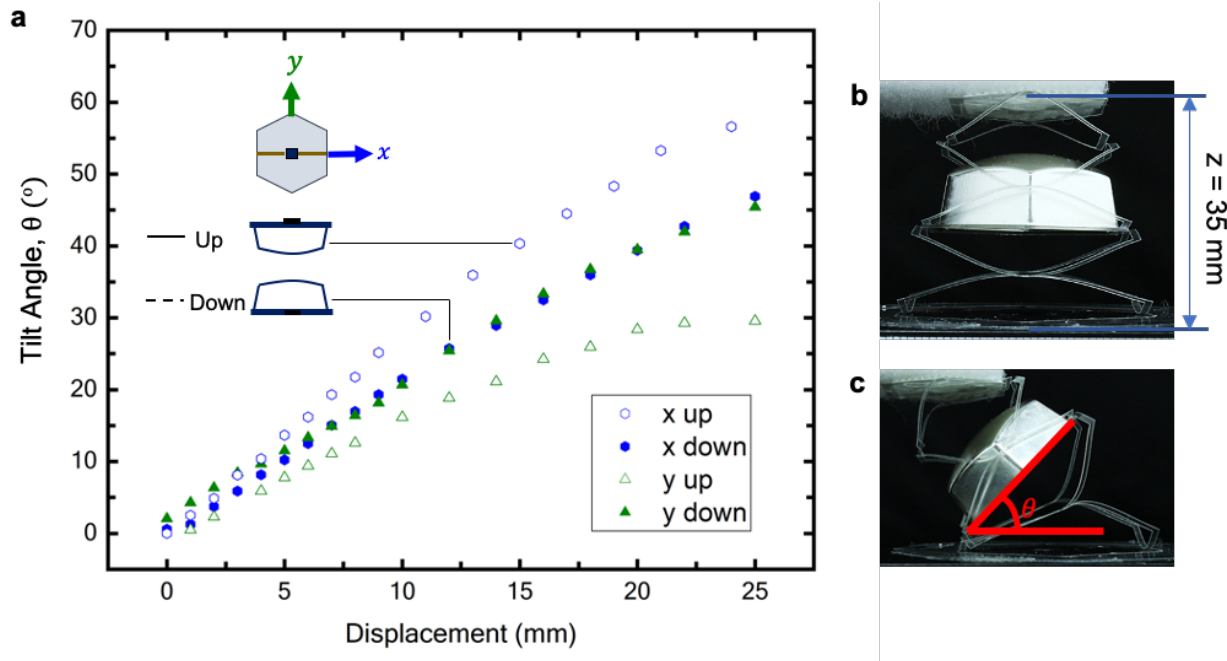


**Figure 4.12** Tilt angle vs displacement of concentrator facing up or down. (a) Solid symbols represent the concentrator facing down and the open points represent the concentrator facing up ( $z = 35 \text{ mm}$ ). The circle symbol represents translation in the  $x$ -direction and the triangular symbol represents translation in the  $y$ -direction. (b)  $\delta = 0$  (c)  $\delta = 25 \text{ mm}$  in  $x$ -direction, resulting in tilt angle of  $40^{\circ}$ .<sup>68</sup>

When the system is facing up, the concentrator is located closer to the innermost hexagonal ring, as compared to the concentrator facing down, which is due to the force of gravity. For the concentrator facing up, longer beams are used to hold the concentrator in place. Longer beams are more flexible than shorter beams, as determined based on the cantilever beam theory. Therefore, less force is required to deflect the beams, thus the effect of gravity on the concentrator is more significant when the concentrator faces upward.



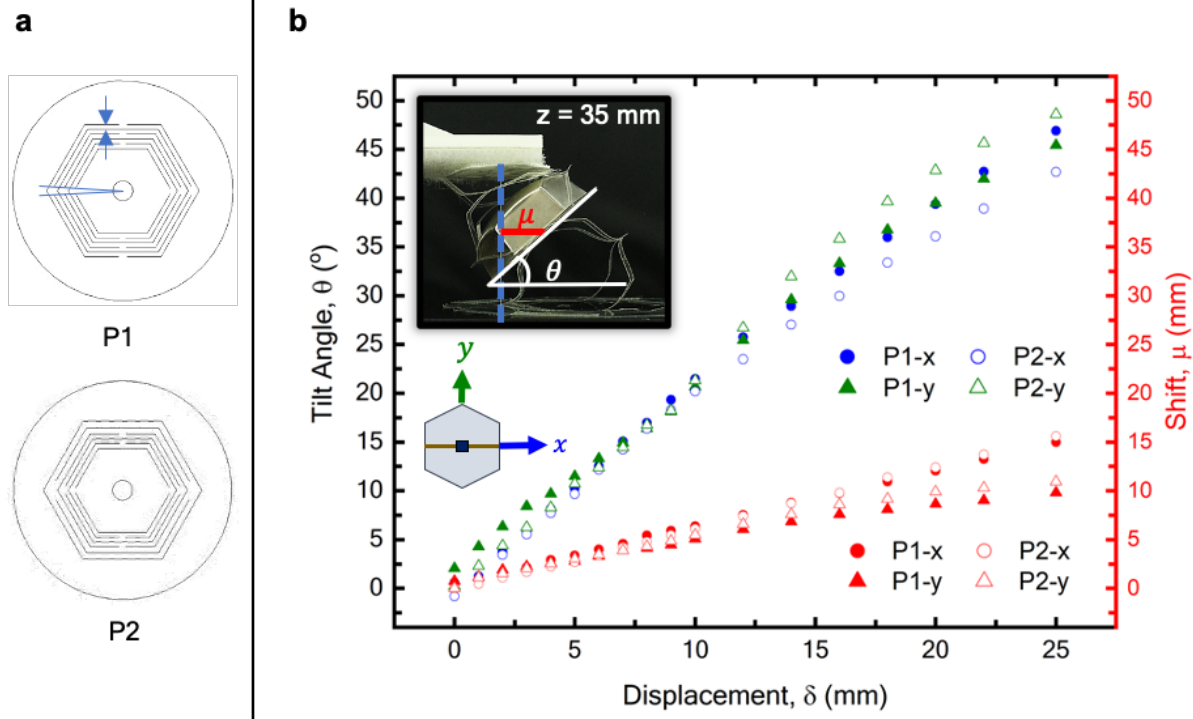


**Figure 4.13** Varying cut parameters affect maximum tilt angle and shift. (a) Schematics of cut pattern 1 (P1) and cut pattern 2 (P2). (b) Experimental measurements of the tilt angle as a function of displacement for P1 (solid symbols) and P2 (open symbols) and the shift from the median on the right y-axis in red. Inset of the spring with concentrator facing down, showing shift  $\mu = 15$  mm and tilt angle  $\theta = 47^\circ$  in the y-direction at  $z = 35$  mm.<sup>68</sup>

There is also an accompanying shift,  $\mu$ , of the concentrator in the  $\delta$  direction, which increases with  $\delta$  (**Figure 4.13**). The maximum tilt angle  $\theta_{max}$  varies depending on the cut pattern when the concentrator is facing down. P1 refers to the baseline pattern, in which the spacings between the rings are equal (**Figure 4.13a**). P2 refers to another cut pattern, in which the radial and angular spacing of the outermost rings are increased by 50% and 60%, respectively. In P2,  $\delta$  in the y-direction surpasses the maximum tilt angle achieved by  $\delta$  in the x-direction, as well as P1 in both directions (**Figure 4.13b**). There is an accompanying shift,  $\mu$ , of the concentrator in the  $\delta$  direction, which increases with  $\delta$ . **Figure 4.13** shows that  $\mu$  is linearly proportional to  $\delta$  of the innermost hexagon. Increasing beam width and shortening the length of the beam (i.e., increasing the stiffness), increases  $\theta_{max}$  in the y-direction. Through optimization of the cut pattern, sheet

thickness, and composition, these phenomena can be controlled and minimized, and greater tilt angles may be achievable.

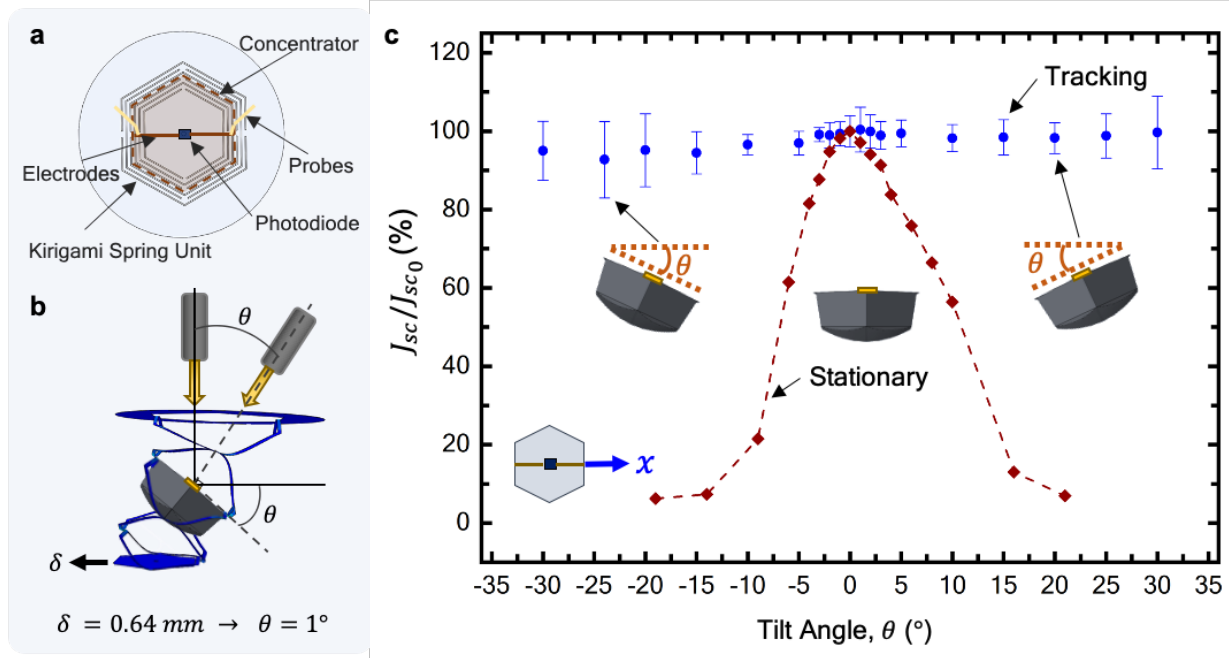


**Figure 4.14** Tracking performance of the kirigami spring integrated with mini concentrators in x-direction. (a) Top view of tracker, depicting cut pattern of kirigami spring; the concentrator, photodiode, and electrodes locations; and placement of probes for measuring the electrical current. (b) Side view of electrical measurement setup, in which the spring tilts to maintain its position with the light source at various angles. (c) Experimental measurements of the short circuit current to the initial short circuit current at various tilt angles of the tracker and stationary systems. Blue circles with error bars represent tracking system, and red diamonds represent stationary system with schematics represent  $\theta=0^\circ$  and  $\theta=\pm 22^\circ$ .<sup>68</sup>

**Figure 4.14a** shows how an individual kirigami-spring concentrator assembly tracks a moving light source using a photodiode in the focal point of the concentrator. The top view of the system is depicted in **Figure 4.14a**, which shows the kirigami spring, the placement of the concentrator with respect to the spring, and the centered photodiode; a side view is shown in **Figure 4.14b**. As the light source positioned on a goniometer rotated by  $\theta$  in one-degree increments, the concentrator matched  $\theta$  through  $\delta$  of the innermost hexagon, while the outermost portion of the spring remained fixed. For experimental convenience, the light source faced upward

in the laboratory reference frame, and the tracker was positioned such that the concentrator faced the light source. For the baseline pattern, when  $z = 35$  mm,  $\delta = 0.64$  mm correlates to  $\theta = 1^\circ$ .

In **Figure 4.14c**, the normalized short circuit current density,  $J_{sc}$ , is plotted versus  $\theta$ . The circular symbols with error bars correspond to the system when tracking in the  $x$ -direction while the diamond symbols represent the system without tracking. This demonstrates how  $J_{sc}$  remains virtually unchanged when varying the tracking angle in contrast to the stationary system. Deviations are attributed mainly to human error of aligning the individual spring to the stage, slight misalignment of the concentrator in the spring, and imperfect reflectivity of the concentrator (issues easily mitigated by automation during array production). A misalignment between the light source angle and photodiode drops the performance more rapidly than the cosine loss, as expected for concentration optics, and can be mitigated by using lower concentrations.<sup>[39]</sup>

**Figure 4.15** shows the analogous measurements for translation in the  $y$ -direction.

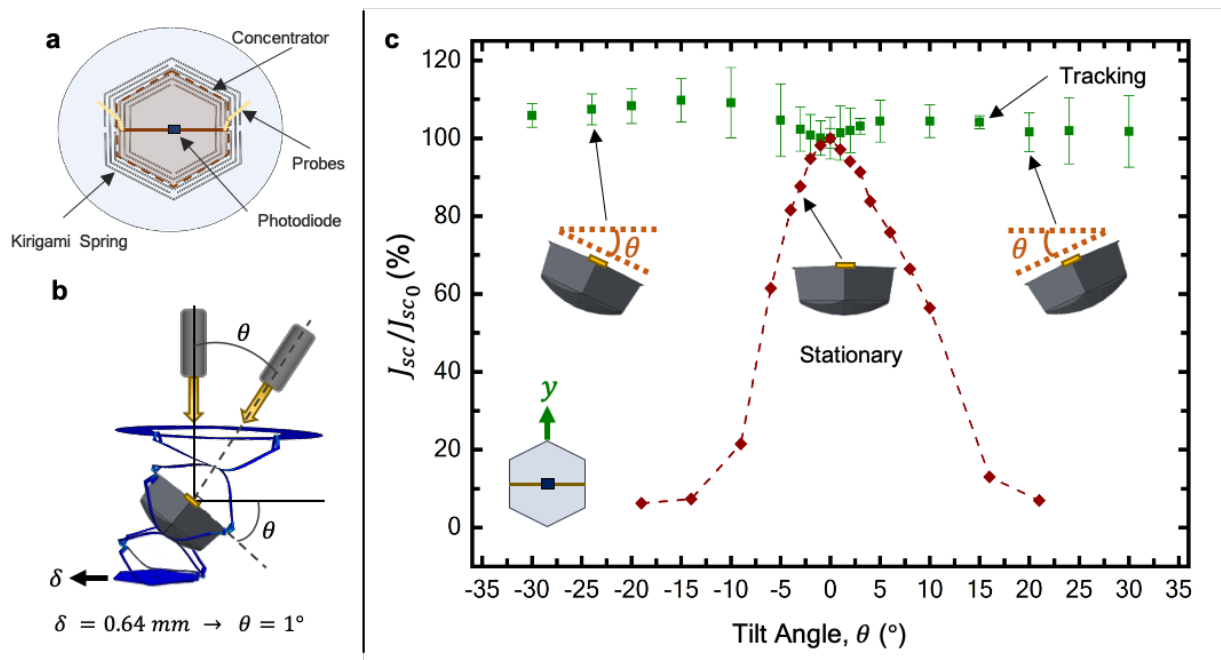


**Figure 4.15** Tracking performance of the kirigami spring integrated with mini concentrators in  $y$ -direction. (a) Top view of tracker depicting cut pattern of kirigami spring, concentrator, photodiode, and electrodes, as well as placement of probes for measuring the electrical current. (b) Side view of electrical measurement setup, in which the spring tilts to maintain its position with the light source at various angles. (c) Experimental measurements of the short circuit

current to the initial short circuit current at various tilt angles of the tracker and stationary systems. Green squares with error bars represent tracking system, and red diamonds represent stationary system with schematics represent  $\theta = 0^\circ$  and  $\theta = \pm 22^\circ$ . Deviations from 100% normalized current density are attributed to PV cell misalignment with the focal spot of the concentrator due to manual assembly for the test.<sup>68</sup>

#### *4.3.5 Electrode pattern and physical demonstration of kirigami solar tracking array*

The hexagonal unit cells combined in a honeycomb arrangement gives the highest packing density. The connection between unit cells is an important design consideration that must carefully be engineered. **Figure 4.16** shows an example array with an example electrode pattern that mazes between and within unit cells, connecting the pattern in series. One sheet carries the entire array, and even though the laser cutter cuts each of the unit cells, they remain intact so they can simultaneously be displaced. The red circles indicate the placement of the photovoltaic cell, the blue lines represent the kirigami cut pattern, and the green lines represent the electrode trail which connects the cells. An example of the fabrication of the electrodes consists of depositing 7 nm thick iridium (IR) adhesion layer, followed by 700 nm thick gold (Au). In this example, a GaAs solar cell is used, fabricated as described by Lamoureux, A.,<sup>9</sup> can attach to the electrodes using silver conductive paste, wire bonding, or other electrically conductive adhesive methods. The closeup shows more clearly the kirigami pattern and electrodes that maze through the pattern and connect adjacent cells. It should be noted, this is not an ideal arrangement because if one PV cell is shaded or not working, the rest of the cells will not work. Therefore, other measures should be taken to avoid this issue, such as the use of bypass diodes.

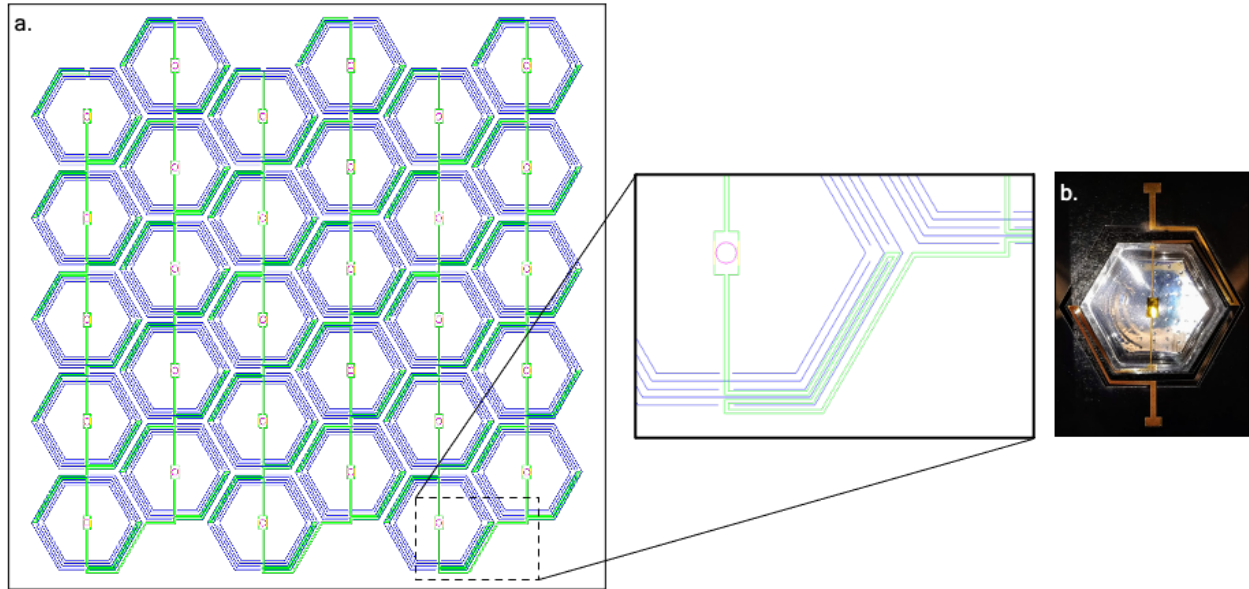


**Figure 4.16** Example honeycomb arrangement of cells with embedded electrodes. (a) CAD drawing of electrode pattern within the hexagonal cells and (b) physical model of one-unit cell.

#### 4.4 Thermal considerations and impact on efficiency of a unit cell

The design of the insert for solar energy harvesting applications should be engineered to balance the concentration factor for economy of costly semiconductor material, required tolerances in alignment and tracking accuracy, and potential for excessive heating of the solar cell that would adversely impact the power conversion efficiency. Focusing on heat dissipation, we expect thermal radiation and convection from the PV cell surface as well as thermal conduction by the electrodes as illustrated in **Figure 4.17a**.

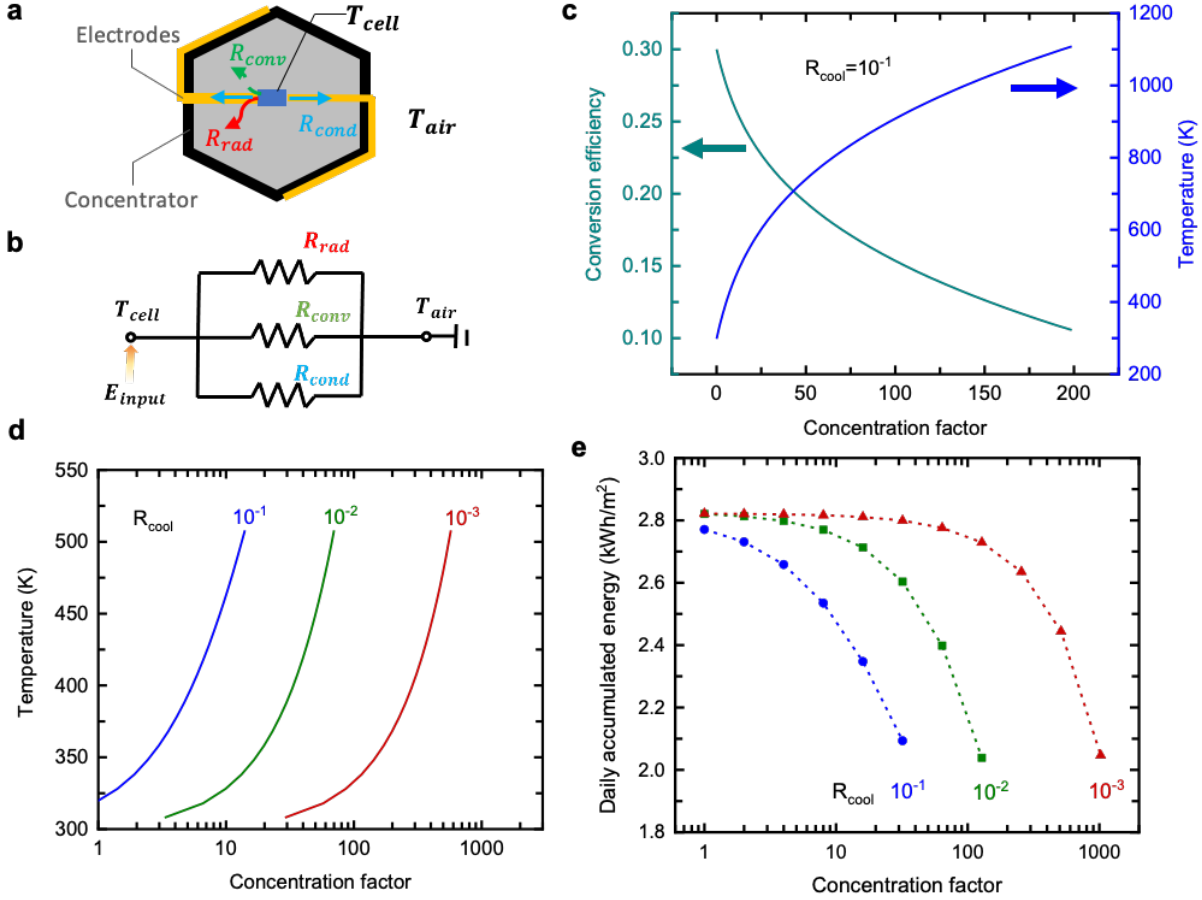


**Figure 4.17** Theoretical thermal effects of the cell on conversion efficiency and energy. (a) Schematic illustration of the types of heat dissipation in the solar cell. (b) Respective thermal circuit diagram with radiation, convection and conduction load. (c) Temperature and efficiency as a function of concentration factor where  $R_{cool} = 10^{-1} \text{ K}\cdot\text{m}^2/\text{W}$ . (d) Temperature and (e) daily accumulated energy versus logarithmic CF with cooling resistance equal to  $10^{-1}, 10^{-2}, 10^{-3} \text{ K}\cdot\text{m}^2/\text{W}$ .<sup>68</sup>

To first order, the energy balance is governed by the Equations (4.4) and (4.5):

$$\Phi \cdot A_{conc} = \varepsilon\sigma(T_{cell}^4 - T_{air}^4) \cdot 2A_{cell} + 2\Delta T \cdot \frac{1}{R_{cool}} \cdot A_{cell} + \eta \cdot \Phi \cdot A_{conc} \quad (4.4)$$

$$\frac{1}{R_{cool}} = \frac{1}{R_{conv}} + \frac{1}{R_{wire}} \quad (4.5)$$

where  $\Phi$ ,  $A_{conc}$ ,  $A_{cell}$ ,  $\eta$ ,  $\varepsilon$  denote the solar intensity, the area of the parabolic concentrator and solar cell, power conversion efficiency, and hemispherical emissivity, respectively. The

corresponding thermal circuit diagram is shown in **Figure 4.17b** depicting the radiation, convection and conduction load. When the cooling resistance is equal to  $10^{-1} K \cdot m^2/W$ , the dominant dissipation methods are radiation and natural convection. As the concentration factor, CF, increases the cell temperature increases. CF is defined as the ratio  $A_{conc}/A_{cell}$ , where  $A_{conc}$  is the area of the concentrator and  $A_{cell}$  is the area of the photodiode/photovoltaic cell.

Studies have shown that power conversion efficiency drops linearly with operating cell temperature, and the temperature coefficient of GaAs is  $-0.08\% K^{-1}$ .<sup>[40]</sup> This behavior is reflected in the prediction in **Figure 4.17c**. If the cooling resistance is reduced to  $10^{-2} Km^2W^{-1}$ , the solar cell can maintain a lower operating temperature, as shown by the parametric curves in **Figure 4.17d**, and produce a higher daily accumulated energy as indicated in **Figure 4.17e**. An order-of-magnitude increase in CF leads to an approximately 14% drop in the daily accumulated energy value, which can be countered by an order-of-magnitude decrease in thermal resistance, physically consistent with the energy balance. The practical maximum operating temperature is determined jointly by the material selection as well as by the economics of diminishing efficiency with high CF. For instance, at  $R_{cool}=10^{-3} Km^2W^{-1}$  and  $CF = 50$  the cell temperature exceeds  $42^{\circ}C$ , while when  $CF = 182$  the temperature reaches  $89^{\circ}C$ .

#### **4.5 Shadowing effects in the kirigami tracking array**

While arranging the concentrators in a hexagonal array allows a large collection area to be covered without increasing the vertical profile of the array, as with any solar tracking system, there exists a trade-off between area utilization and shadowing caused by nearby concentrators as determined by Chao Huang in Evke, E. *et al.*<sup>68</sup>

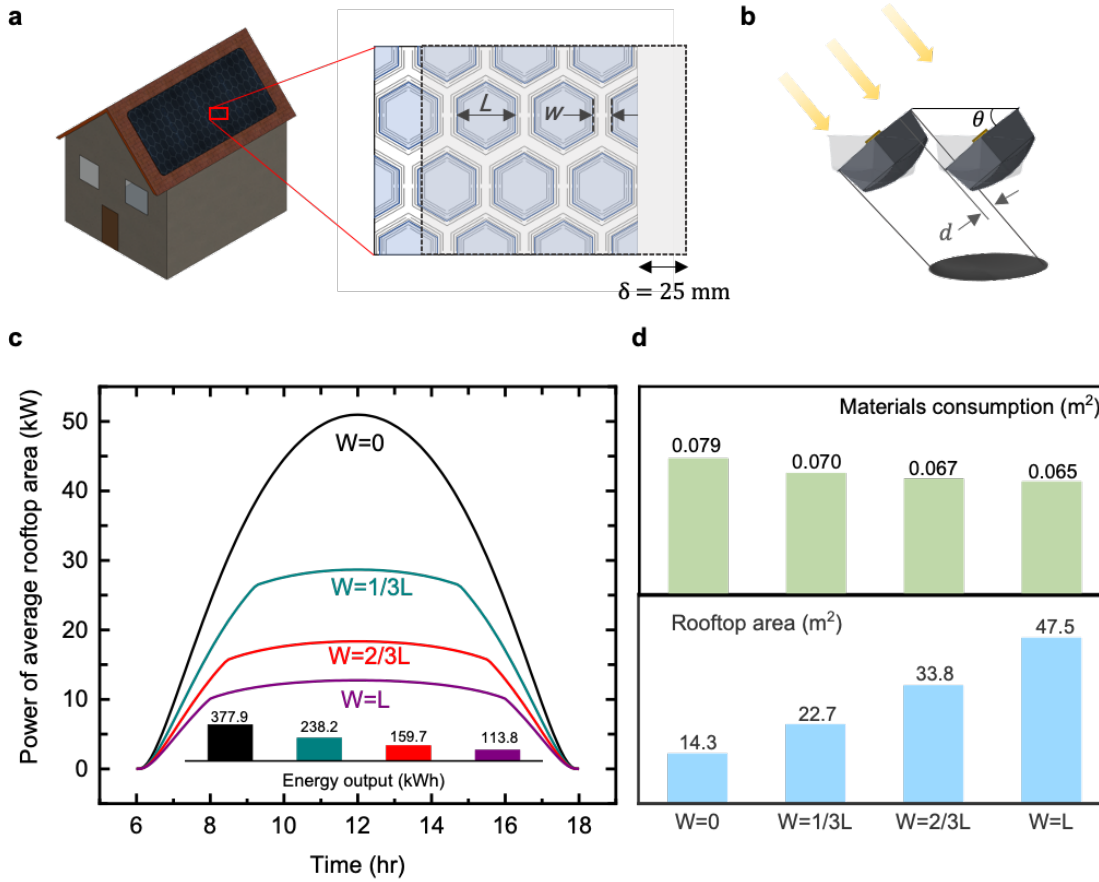


**Figure 4.18** Effect of shadowing on the performance of solar trackers. (a) Schematic of solar array on the roof of a house and close-up of the cut pattern array with shaded area representing the area extent of displacing the tracker by 25 mm;  $L$  represents the length and  $W$  represents the width between concentrators. (b) Side view of packed neighbor concentrators, where  $\theta$  is the tilt angle and  $d$  is the shadowing area. (c) Total instantaneous power output produced by average 180 m<sup>2</sup> rooftop area versus time of a day. Assuming 30% conversion efficiency and cooling resistance equal to  $10^{-3}$  K·m<sup>2</sup>/W. Inset: energy accumulated over the day. (d) Comparison of materials consumption and rooftop area needed to meet daily energy requirement at CF = 182 with different  $W$ , assuming daily energy requirement equal to 30 kWh.<sup>68</sup>

In **Figure 4.18a**,  $L$  indicates the length of the concentrator and  $W$  indicates the width between concentrators. A schematic of the side view of two nearby concentrators that shadow each other are represented in **Figure 4.18b**. Here,  $d$  is the shadowed area and  $\theta_0$  is the critical angle when a shadow appears. The effective area, which is the concentrating light area, changes based on the extent of the shadowing area and when  $\theta_0 < \theta < \theta_{max}$ . The governing equations below assume a



to be the side of the concentrator,  $A_{effect}$  the effective area,  $A_{shad}$  the shadowing area, and  $A_{total}$  the total area. We thus obtain:

$$A_{effect} = A_{total} - A_{shadow} \quad (4.6)$$

$$A_{effect} = \frac{\sqrt{3}}{2}L^2 - \frac{\sqrt{3}}{3}L \cdot [L - (L + W) \cdot \cos\theta] - \frac{\sqrt{3}}{6}[L - (L + W) \cdot \cos\theta]^2 \quad (4.7)$$

#### 4.5.1 Shadowing of nearby concentrators calculations

According to Equation (4.7), increasing the spacing  $W$  between two concentrators reduces shadowing at the expense of area utilization. **Figure 4.18c** illustrates this trade-off, assuming the average rooftop area is  $180 \text{ m}^2$ ,  $CF = 182$ , and a fixed area for each concentrator ( $7.8 \text{ cm}^2$  if  $L \approx 30 \text{ mm}$ ).<sup>[41]</sup> For a fixed panel area, increasing  $W$  decreases the total daily harvested energy. To avoiding shadowing, the separation distance between concentrators must increase, reducing their number (and thus, sunlight collection area) in a fixed panel area. **Figure 4.18d** depicts the area of semiconductor material and rooftop area needed to meet the average daily electricity requirement of  $30 \text{ kWh}$ .<sup>[42]</sup> As a benchmark, a 20%-efficient, stationary silicon panel requires  $22 \text{ m}^2$  of semiconductor. Using higher-efficiency (e.g., 29%) GaAs semiconductor PV cells reduces the semiconductor illuminated area requirement. This effect is multiplied by the use of the micro-concentrator arrangement, provided tracking and shadowing errors are mitigated. The latter is accomplished by increasing  $W$ , albeit increasing the total area occupied by the panel. Because for high efficiency PV panels the cost of semiconductor PV cells dominates the panel's bill of materials, increasing  $W$  is beneficial to lowering the levelized cost of electricity, as the projections below suggest.

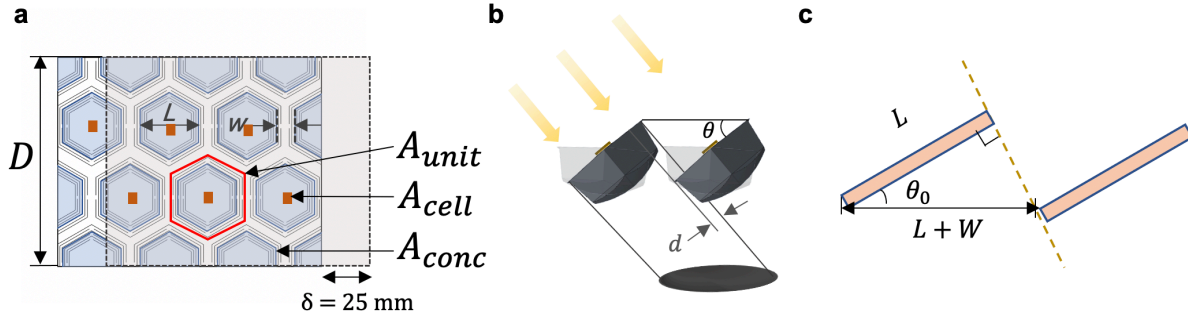


**Figure 4.19** Schematics showing shadowing of nearby concentrators. (a) Cut pattern array with shaded area representing the area extent of displacing the tracker by 25 mm;  $L$  represents the length,  $W$  represents the width between concentrators,  $D$  represents the length of the array, and  $a$  represents the edge length of the concentrator.  $A_{unit}$ ,  $A_{cell}$ , and  $A_{conc}$  represent the area of the unit, the photovoltaic cell, and concentrator, respectively. (b) Side view of packed neighbor concentrators, where  $\theta$  is the tilt angle and  $d$  is the shadowing area. (c) Side view of two nearby concentrators represented as rectangles, where  $\theta_0$  represents the critical angle when a shadow appears.<sup>68</sup>

The onset of shadowing at the critical angle  $\theta_0$  occurs when  $\theta_0 = \theta_{max} = 55^\circ, W = 0.74L$ .

$$\theta_0 = \arccos\left(\frac{L}{L+W}\right) \tag{4.8}$$

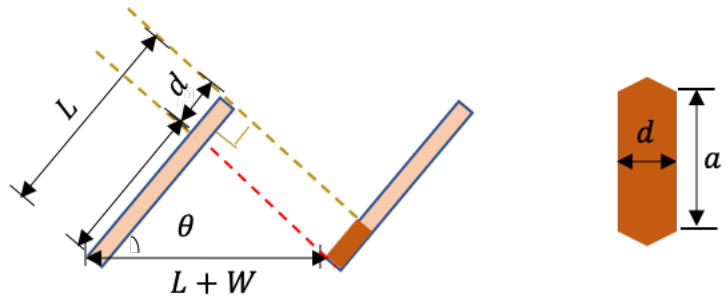
To calculate the effective area,  $A_{effect}$ , that can receive the solar flux, there are two cases:  $W < 0.74L$  and  $W > 0.74L$ .

**Case I:**  $W$  is very small ( $W < 0.74L$ ),  $\theta_0 < \theta_{max}$ , shadow appears before reaching maximum tilt angle

When  $0 < \theta < \theta_0$ , no shadow and cosine loss

$$A_{effect} = A_{total} = \frac{\sqrt{3}}{2} L^2 \tag{4.9}$$

When  $\theta_0 < \theta < \theta_{max}$ , shadow appears



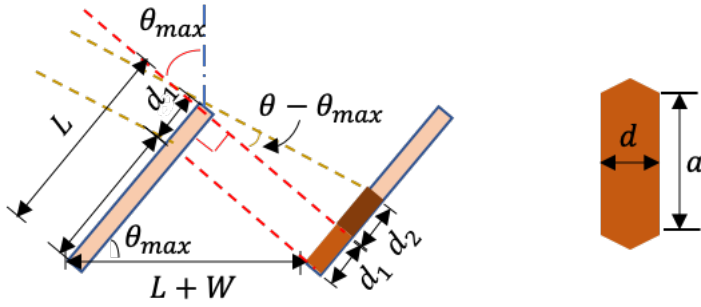
$$d = L - (L + W) \cdot \cos\theta \quad (4.10)$$

$$A_{shad} = a \cdot d + \frac{\sqrt{3}}{6} d^2 \quad (4.11)$$

$$A_{effect} = A_{total} - A_{shad} = \frac{\sqrt{3}}{2} L^2 - a \cdot d - \frac{\sqrt{3}}{6} d^2 \quad (4.12)$$

$$A_{effect} = \frac{\sqrt{3}}{2} L^2 - \frac{\sqrt{3}}{3} L \cdot [L - (L + W) \cdot \cos\theta] - \frac{\sqrt{3}}{6} [L - (L + W) \cdot \cos\theta]^2 \quad (4.13)$$

When  $\theta_{max} < \theta < 90$  shadowing increases and cosine loss starts



$$d_1 = L - (L + W) \cdot \cos\theta_{max} \quad (4.14)$$

$$d_2 = (L + W) \cdot \sin\theta_{max} \cdot \tan(\theta - \theta_{max}) \quad (4.15)$$

$$d = d_1 + d_2 \quad (4.16)$$

$$A_{shad} = a \cdot d + \frac{\sqrt{3}}{6} d^2 \quad (4.17)$$

$$A_{effect} = (A_{total} - A_{shad}) \cdot \cos(\theta - \theta_{max}) \quad (4.18)$$

$$= \left( \frac{\sqrt{3}}{2} L^2 - a \cdot d - \frac{\sqrt{3}}{6} d^2 \right) \cdot \cos(\theta - \theta_{max})$$

$$= \left[ \frac{\sqrt{3}}{2} L^2 - \frac{\sqrt{3}}{3} L \cdot (d_1 + d_2) - \frac{\sqrt{3}}{6} (d_1 + d_2)^2 \right] \cdot \cos(\theta - \theta_{max})$$

$$A_{effect} = \left\{ \frac{\sqrt{3}}{2} L^2 - \frac{\sqrt{3}}{3} L \cdot [(L - (L + W) \cdot \cos\theta_{max} + (L + W) \cdot \sin\theta_{max} \cdot \tan(\theta - \theta_{max})] - \frac{\sqrt{3}}{6} [L - (L + W) \cdot \cos\theta_{max} + (L + W) \cdot \sin\theta_{max} \cdot \tan(\theta - \theta_{max})]^2 \right\} \cdot \cos(\theta - \theta_{max}) \quad (4.19)$$

**Case II:**  $W > 0.74L$ ,  $\theta_0 > \theta_{max}$ , shadow appears after reaching maximum tilt angle

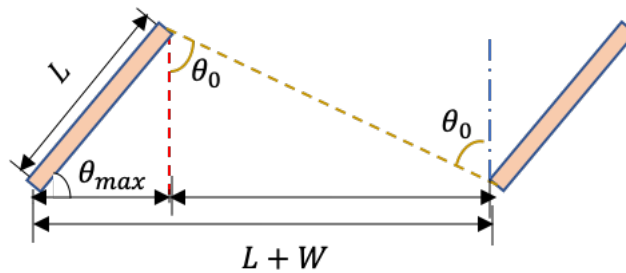
When  $0 < \theta < \theta_{max}$ , no shadow and cosine loss

$$A_{effect} = A_{total} = \frac{\sqrt{3}}{2} L^2 \quad (4.20)$$

When  $\theta_{max} < \theta < \theta_0$ , cosine loss starts

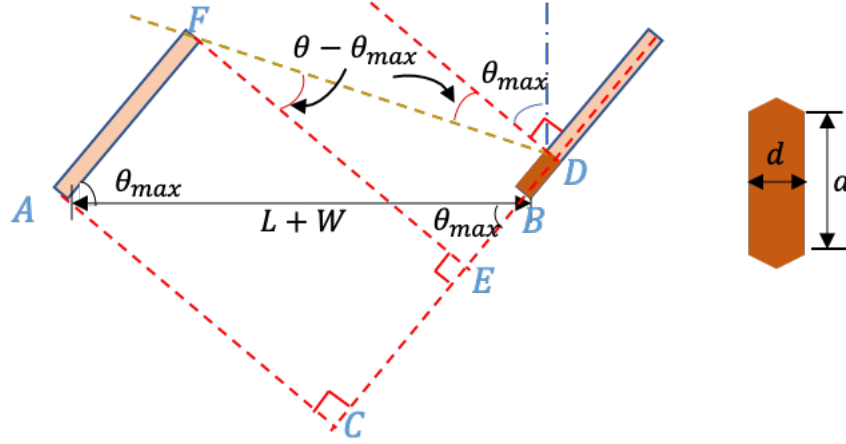
$$A_{effect} = A_{total} \cdot \cos(\theta - \theta_{max}) = \frac{\sqrt{3}}{2} L^2 \cdot \cos(\theta - \theta_{max}) \quad (4.21)$$

When  $\theta = \theta_0$  (calculate the critical angle  $\theta_0$ )



$$\tan\theta_0 = \frac{(L + W) - L\cos\theta_{max}}{L\sin\theta_{max}} \quad (4.22)$$

- i. When  $\theta_0 < \theta < 90$ , shadow appears, cosine loss continues



$$d = BD = ED - EB \quad (4.23)$$

$$ED = EF \cdot \tan(\theta - \theta_{max}) \quad (4.24)$$

$$= AC \cdot \tan(\theta - \theta_{max})$$

$$= (L + W) \cdot \sin\theta_{max} \cdot \tan(\theta - \theta_{max})$$

$$EB = CB - CE = (L + W) \cdot \cos\theta_{max} - L \quad (4.25)$$

$$d = [(L + W) \cdot \sin\theta_{max} \cdot \tan(\theta - \theta_{max})] - [(L + W) \cdot \cos\theta_{max} - L] \quad (4.26)$$

$$A_{effect} = (A_{total} - A_{shad}) \cdot \cos(\theta - \theta_{max}) \quad (4.27)$$

$$= \left( \frac{\sqrt{3}}{2} L^2 - \frac{\sqrt{3}}{3} L \cdot d - \frac{\sqrt{3}}{6} d^2 \right) \cdot \cos(\theta - \theta_{max})$$

To calculate the energy produced by one-unit cell over the whole day,  $\rho_e$ , the following equations are used, where  $E_e$  represents the energy produced by one GaAs cell and  $GF$  represents the geometric fill factor.

$$GF \triangleq \frac{A_{conc}}{A_{unit}} = \left( \frac{L}{L + W} \right)^2 \quad (4.28)$$

$$\rho_e = \frac{E_e}{A_{unit}} = \frac{E_e}{A_{conc}} \cdot \frac{A_{conc}}{A_{cell}} \cdot \frac{A_{cell}}{A_{unit}} = \frac{E_e}{A_{conc}} \cdot CF \cdot GF \quad (4.29)$$

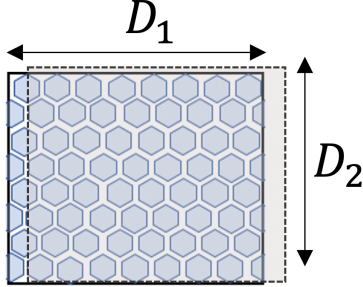
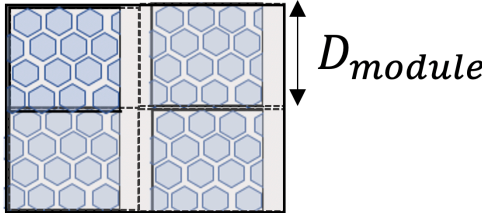
To meet daily requirement ( $E_{tot}$ ), which is 30 kWh per day. The total GaAs consumption

( $A_{tot mat}$ ) is obtained by

$$A_{tot\ mat} = \frac{E_{tot}}{E_e} \cdot A_{cell} \quad (4.30)$$

The total rooftop area can be calculated by two different cases. Figure 6 is calculated by the first scenario. The first assumes the whole panel is devised of an array of unit cells. The second scenario assumes the whole panel is devised of an array of modules where each module consists of a set number of unit cells. **Table 4.2** summarizes these equations.

**Table 4.2** Breakdown of calculating the energy density and rooftop area for two scenarios.<sup>68</sup>

	Scenario 1	Scenario 2
<b>Assumption</b>	The whole panel is made of unit cell array	The whole panel is made of modules. Each module consists of several unit cells
<b>Diagram</b>		
<b>Energy density</b> $\rho$	Per unit cell $\rho_{unit} = \frac{E_e}{A_{unit}} = \frac{E_e}{A_{conc}} \cdot CF \cdot GF$	Per module $\rho_{module} = \frac{E_e}{A_{module}}$
<b>Materials consumption</b> $A_{tot\ mat}$	$A_{tot\ mat} = \frac{E_{tot}}{E_e} \cdot A_{cell}$	$A_{tot\ mat} = \frac{E_{tot}}{E_e} \cdot A_{cell}$
<b>Number of unit cells (or modules) to meet daily requirement</b> $N$	$N_{unit} = \frac{E_{tot}}{\rho_{unit}}$	$N_{module} = \frac{E_{tot}}{\rho_{module}}$
<b>Extra area for lateral displacement</b> $A_{extra}$	$A_{extra} = 2\delta \cdot D_2$	$A_{extra} = 2\delta \cdot D_{module} \cdot N_{module}$
<b>Total rooftop area needed</b> $A_r$	$A_{r,1} = N_{unit} \cdot A_{unit} + A_{extra}$	$A_{r,2} = N_{module} \cdot A_{module} + A_{extra}$

### Scenario 1

$$A_{r,1} = N_{unit} \cdot A_{unit} + A_{extra} \approx D_1 \cdot D_2 + 2\delta \cdot D_2 = D_2 \cdot (D_1 + 2\delta) \quad (4.31)$$

Assuming  $\delta = 2.5 \text{ cm}$  and is negligible compared to  $D_1$

$$A_{r,1} \approx N_{unit} \cdot A_{unit} \quad (4.32)$$

### Scenario 2

$$A_{r,2} = N_{module} \cdot A_{module} + A_{extra} = N_{module} \cdot (A_{module} + 2\delta \cdot D_{module}) \quad (4.33)$$

Considering  $\delta$  is very small compared with the total dimension of the solar tracker,  $2D\delta$  is neglected in these calculations. This is appropriate based on the following calculations. If we assume each tracking module is a square such that  $A_{module} = D * D = D^2 \text{ m}^2$ , the extra area for lateral displacement is

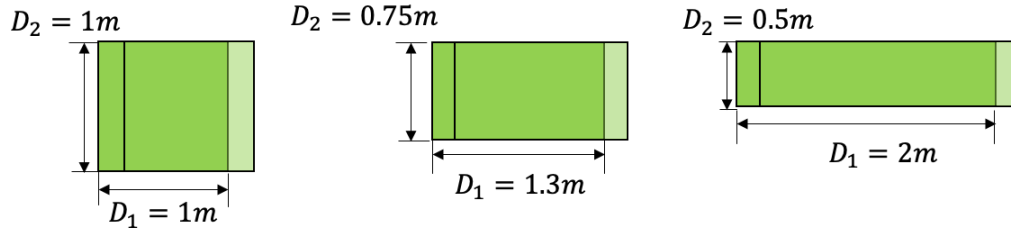
$$A_{extra} = 2\delta \cdot D = 2 * 0.025 * D = 0.05D \text{ m}^2 \quad (4.34)$$

$$\frac{A_{extra}}{A_{module}} = \frac{0.05D}{D^2} = \frac{0.05}{D} \quad (4.35)$$

If the module is larger than  $1 \text{ m}^2$ ,

$$\frac{A_{extra}}{A_{module}} = \frac{0.05}{D} \leq 5\% \quad (4.36)$$

The relationship  $\frac{A_{extra}}{A_{module}}$  can also be minimized by altering the dimensions of the array. If the module is a rectangle instead of square, such that  $D_1$  is greater than  $D_2$ , the area for lateral displacement can be minimized. As an example, the relationship between  $\frac{A_{extra}}{A_{module}}$  and area of module (square) is 5%, 3.75%, and 2.5% respectively based on the variations in dimensions as shown below.



#### 4.5.2 Calculating the total rooftop area for a silicon stationary panel to meet the daily energy requirement

For comparison with the GaAs solar tracking concentrators, we considered the silicon stationary system is comprised of a large panel, as opposed to several modules. Based on the previous calculations and knowing the energy produced per area of silicon panel,  $E_{Si}$ , the total materials consumption equal to the rooftop area is calculated as followed:

$$A_r = A_{tot\ mat} = \frac{E_{tot}}{E_{Si}} \quad (32)$$

Another design trade-off exists between the economy of semiconductor at higher CF values and increasing tracking and cell alignment precision requirements; therefore, the feasibility of lower concentration factors is considered. **Figure 4.20a** depicts the daily energy harvested per unit area of panel for varying CF and  $\mathcal{W}$ , assuming  $R_{cool} = 10^{-3} \text{ Km}^2\text{W}^{-1}$ .



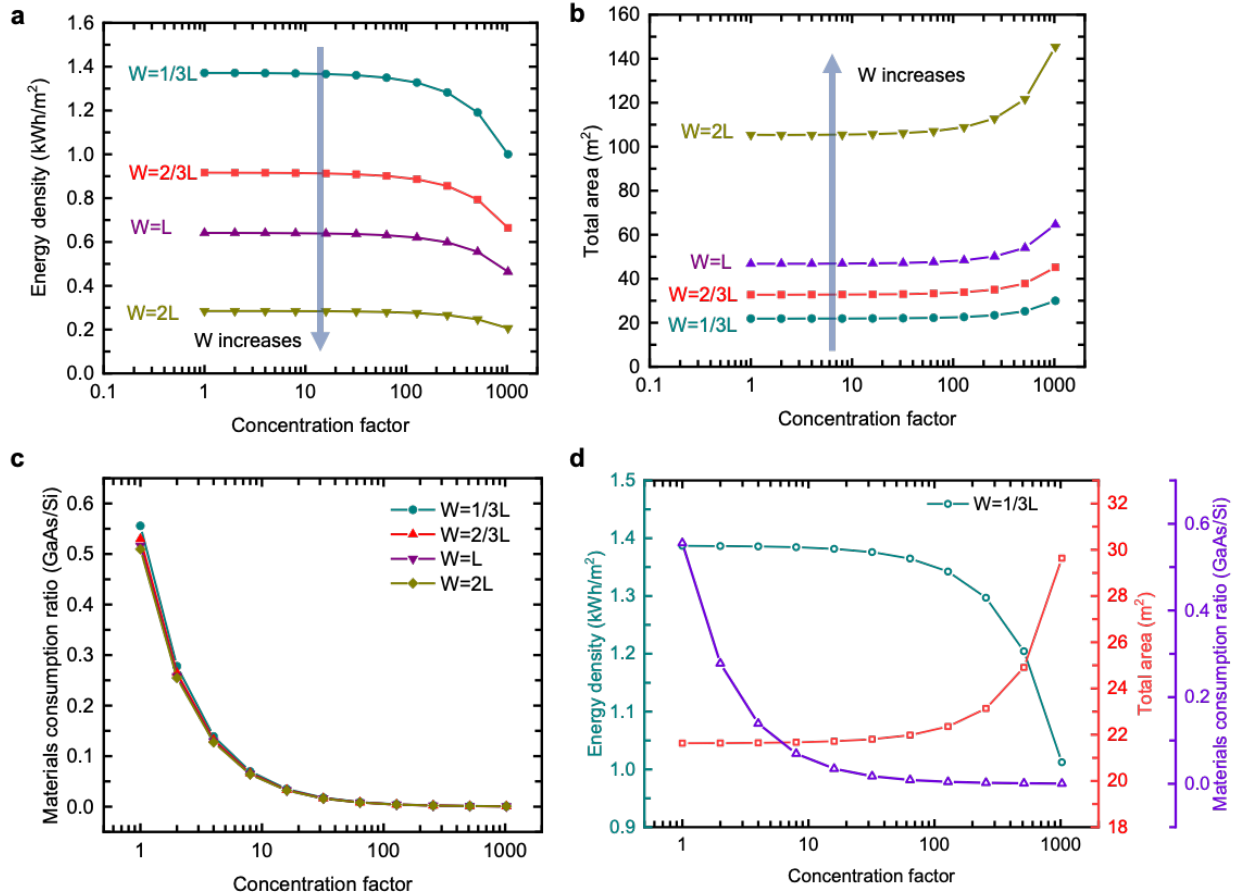


**Figure 4.20** Shadowing of concentrators and cell temperature influences on energy density, area, and cost, having a maximum tilt angle  $\theta=55^\circ$ . (a) Energy density as a function of CF with varying  $W$ . (b) Total rooftop area and (c) materials consumption ratio needed to meet daily average energy requirement. (d) Comparison of energy density, required rooftop area, and materials consumption ratio as a function of CF when  $W=L$ .<sup>68</sup>

For a given CF, increasing  $W$  to reduce shadowing increases the amount of area needed to achieve the same energy output as shown in **Figure 4.20b**. Nevertheless, the amount of semiconductor material needed to produce the daily output requirement decreases rapidly with CF, and diminishing returns occur beyond  $CF > 20$  (**Figure 4.20c**). If space is the most limiting factor for designing a tracker, minimizing  $W$  is the preferred approach. For example, taking the minimum  $W = 1/3L$  at  $CF = 50$  (**Figure 4.20d**), the required area for the panel fits well within the typical available rooftop area. Only  $0.246 \text{ m}^2$  of GaAs PV cells or  $0.368 \text{ m}^2$  of Si PV cells are required as opposed to the total  $22 \text{ m}^2$ -area of stationary silicon PV panels needed to achieve the

aforementioned daily electricity requirement. Given that the fraction of high efficiency PV panel cost attributed to the semiconductor can exceed 85%, these projected cost reductions are highly encouraging. Comparisons between dual-axis GaAs, single-axis GaAs, stationary GaAs, and stationary Si systems are shown in **Figure 4.21**. Here, GaAs is assumed to be 30% efficient, whereas silicon is assumed to be 20% efficient. In **Figure 4.21a**, the dual axis GaAs solar tracker has a higher annual energy density than the silicon stationary panel by 84%, focusing on the unit cell area. In **Figure 4.21b**, the dual axis GaAs solar tracker has a higher annual energy density than the silicon stationary panel by ~4%, focusing on the occupied panel area. The decrease in annual energy density improvement from the silicon panel occupying the same area is due to the concentrator area and empty space between neighboring concentrators accounting for the kirigami pattern.

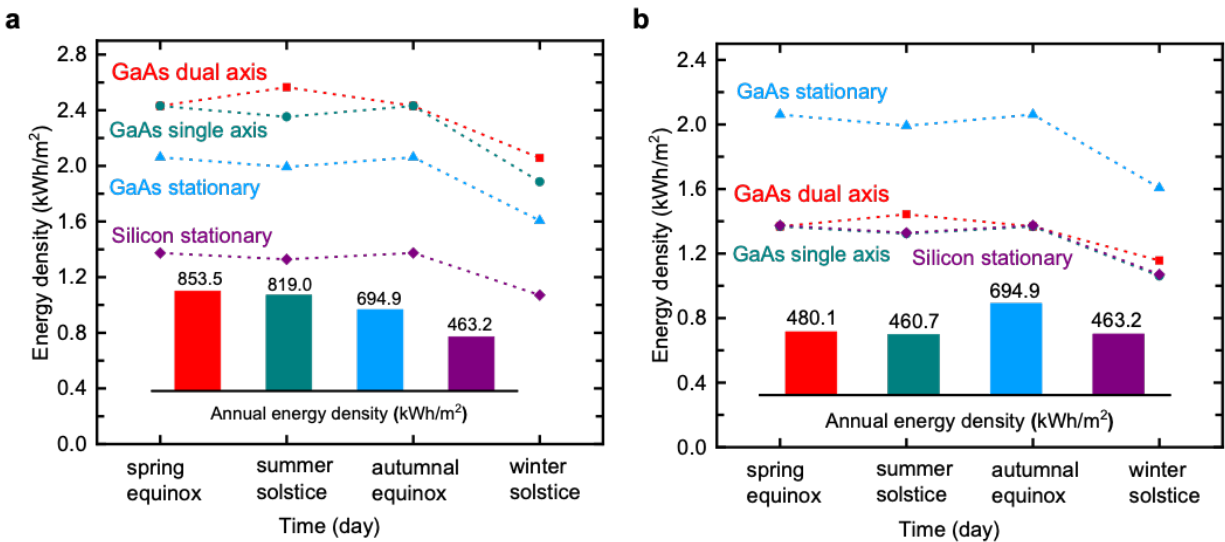


**Figure 4.21** Comparison of energy harvesting between four systems: GaAs dual axis trackers, GaAs single axis trackers, GaAs stationary system and Silicon stationary system. (a) Energy accumulated by per area of unit cell on four typical days in one year where the inset depicts the energy density produced over the year. Assuming energy conversion efficiency of GaAs and Si equal to 30% and 20%, respectively. (b) Energy accumulated per area of 1 m<sup>2</sup> panel where the inset depicts the energy density produced over the year.<sup>68</sup>

## 4.6 Summary and conclusions

A novel kirigami-based, multi-axis tracking mechanism and its application as a scalable solar tracking array were presented. The design parameters for achieving the desired tracking application requirements are summarized in **Figure 4.22**. To demonstrate tracking ability, a mini concentrator combined with a photodiode is placed within a deformed kirigami spring, and the concentrator tilts according to the displacement vector. High optical performance was maintained upon variations in the light-source angle whereby the concentrator matches the tilt angle through a corresponding lateral  $\delta$ .

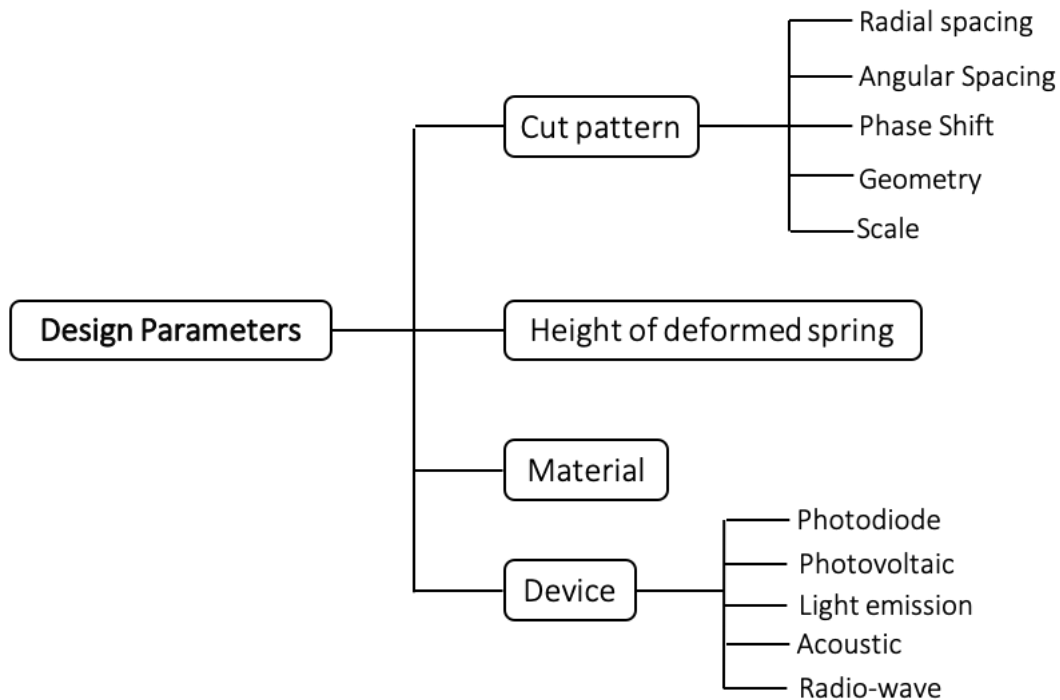


**Figure 4.22** List of key design parameters used for modifying the kirigami tracking mechanism. This includes variations in the cut pattern, height of the deformed spring, material, and device application.

Thermal dissipation and shadowing of nearby concentrators were calculated to influence the efficiency of solar electricity production and help guide the optimization of the concentrator and tracker design for solar energy harvesting applications. This mechanism provides an alternative tracking method where the semiconductor consumption is an important factor, and a small lateral

displacement is necessary to uniformly induce tilting for a scaled array. The combination of the kirigami tracking mechanism and wide-angle microcell concentrators with high-efficiency solar cells and sufficient cooling may help enable widespread adoption of rooftop solar systems. The mechanical behavior described above enables a number of other applications, both purely mechanical in nature (e.g., a suspension or positioner design), as well as multi-functional via integration with other components and materials.

#### **4.7 Future work on modifying system design to reduce thermal effects**

A limitation to using parabolic reflectors is the PV cell may experience high temperatures that decrease its efficiency. One way to overcome this is to move the PV cell to the bottom, innermost ring. This can then sit on a heat sink used to extract heat from cell and keep it cool. Reducing the concentration factor would also decrease the temperature the cell experiences. Because of this, a Fresnel lens can be placed in the center of the kirigami spring where the parabolic reflector was. **Figure 4.23** shows a CAD model of the Fresnel lens attached to the kirigami spring and resulting FEA models showing the displacement at a height of 35 mm and corresponding stress distribution.

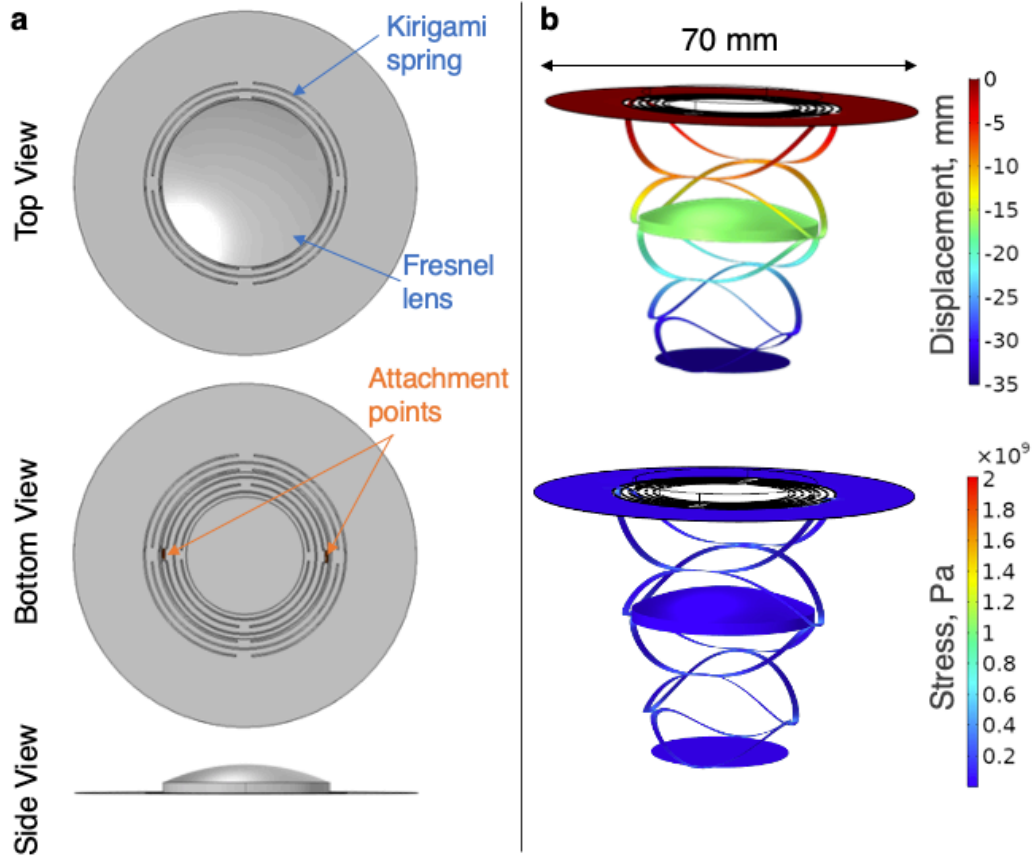


**Figure 4.23** CAD model (a) and FEA results (b) of the kirigami spring-fresnel lens assembly.

COMSOL is used to simulate light focusing and the operating temperature of a cell when mounted on an aluminum plate. The kirigami spring-lens assembly shown in **Figure 4.24** is simulated using the solid mechanics and ray heating modules. Chao Huang showed thermal convection, radiation, and conduction all contribute to the cell's operating temperature as illustrated by the schematic in **Figure 4.24a**. In this case, GaAs is used as the PV cell and aluminum is used as the base plate. An example of the simulation results is shown in the side view of **Figure 4.24a** and top view (**Figure 4.24b**).

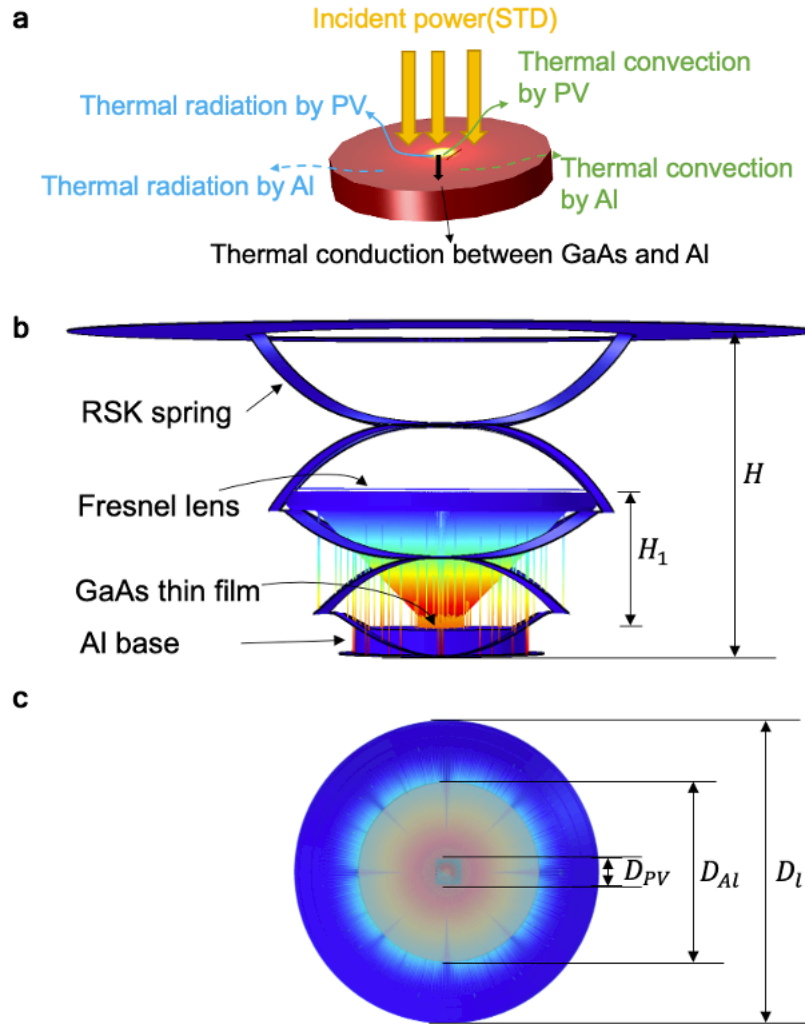


**Figure 4.24** Schematics of heat transfer when PV cell is placed on a heat sink. (a) Diagram of the components of heat transfer between GaAs and Al. Side (b) and top (c) views of an FEA model of the RSK spring with embedded Fresnel lens and GaAs PV cell on an Al heat sink.

**Table 4.3** lists the numerical values corresponding to **Figure 4.24**, where  $H$  is the height from the top of the deformed spring to the bottom,  $H_1$  is the height from the Fresnel lens to the PV cell,  $FL$  is the focal length,  $D_l$  is the diameter of the Fresnel lens,  $D_{Al}$  is the diameter of the aluminum heat sink,  $D_{PV}$  is the diameter of the PV cell,  $h_{conv}$  is the convective heat transfer coefficient,  $\varepsilon$  is the emissivity,  $k_{cond,PV}$  is the thermal conductivity of the PV cell, and  $k_{cond,Al}$  is the thermal conductivity of aluminum. The ray power is assumed to be one sun at  $1000 \text{ W/m}^2$ .

**Table 4.3** Numerical values corresponding to Figure 4.24.

$H$	24mm
$H_1$	9.5mm
$FL$	10mm
$D_l$	25mm
$D_{Al}$	14mm
$D_{PV}$	2mm
$h_{conv}$	10
$\varepsilon$	0.5
$k_{cond,PV}$	46W/(m*K)
$k_{cond,Al}$	155W/(m*K)

**Figure 4.25** shows how the operating temperature can be reduced substantially when the mounting plate acts as a heat sink. The temperature of the cell without heat dissipation reaches 342°C, but with a 1 mm thick aluminum plate the temperature of the cell is only 72°C. However, future work is required to accurately show how the focus of the lens changes as the spring is displaced laterally.

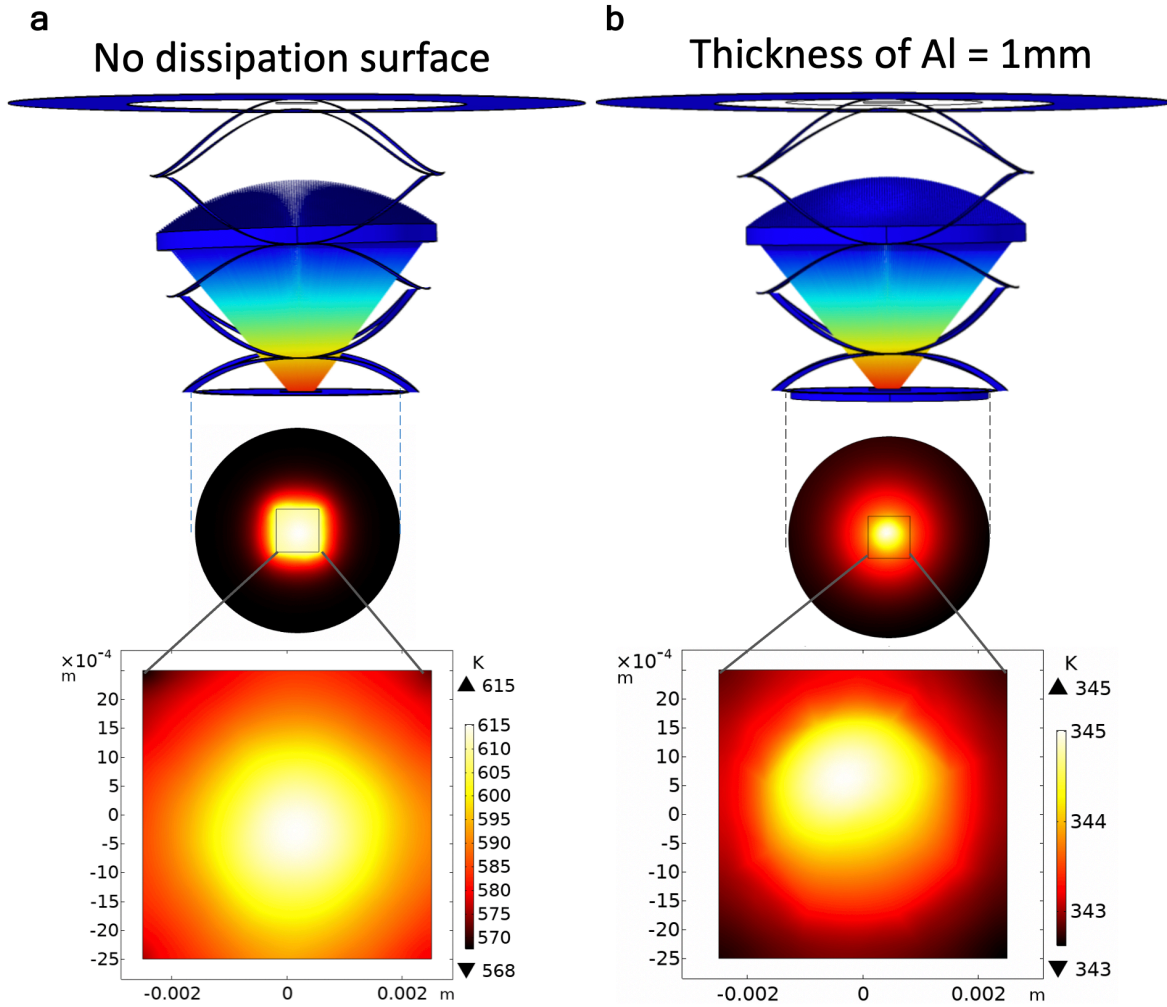


**Figure 4.25** Heat dissipation surface effects of a kirigami spring with lens insert. (a) Cell temperature with no heat dissipation surface and (b) heat sink with a thickness of 1 mm.



# Chapter 5 Tunable Periodic Arrays for High Electromagnetic Absorption

## 5.1 Overview

As the number, density, and power requirements of wireless communications components increases, interference and stray radiation can adversely impact component and system performance. Novel materials have been developed to mitigate this arising problem by absorbing radiation across different portions of the EM spectrum. Previously foams with ferroelectric, dielectric, and other fillers were used. However, the process of creating foams is expensive and frequently involves toxic chemicals and residues. Furthermore, it is difficult to control the pore size and filler distribution, resulting in sub-optimal radiation blocking performance.

Here, modification of the linear kirigami pattern is used such that upon stretching of the sheet results in uniform voids. The size and shape of the voids depend on the cut geometry and degree of stretching. The sheets can be stacked, before and/or after cutting, creating a 3-dimensional distribution of voids, surrounded by the material comprising the sheets. Because the cut pattern is precisely definable, the void size, shape, and distribution in shape are precisely controllable. Resonance between edges of the voids allow a high degree of propagation attenuation (e.g., absorption) across a narrow or broad bandwidth. Since cutting is accomplished on an industrial scale using a wide variety of precise and highly scalable methods (e.g., laser, die, etch, etc.), large areas and quantities of sheets are easily manufacturable. Varying the sheet material's

complex permittivity and permeability, enables another method of optimizing the blocking of electromagnetic radiation through composites and coatings.

We demonstrate a honeycomb-like structure created in a graphene-based sheet, sandwiched between two graphene-based composites with a thickness of 1 mm, achieving a higher reflection loss than the bulk material, exceeding the -30 dB requirement for defense applications in the X-band, as an example. Experiments characterizing the scattering parameters of kirigami-structured composites, comprising graphene nanoplatelets blended with a flexible polymer, demonstrate a greater than three-fold improvement of the shielding efficiency over bulk film. The influence of pore geometry on the total shielding efficiency and reflection loss is further illustrated using numerical simulations of electromagnetic propagation.

## 5.2 Introduction

Modern telecommunications and sensors equipment are increasingly adopted in a variety of applications.<sup>69–71</sup> The EM spectrum shown in **Figure 5.1** depicts example applications for different ranges of frequencies and corresponding wavelengths, ranging from extremely low frequency used in power lines to extremely high frequency gamma rays. Because of all the applications that require network connectivity, such as stealth aircraft, autonomous vehicles, 5G networks, and wearable electronics, electromagnetic pollution has become a major concern.<sup>72–74</sup> It is a concern not only for electronic devices, but also detrimental to human health.<sup>73,75,76</sup> This has led to EM compatibility standards and regulations, as well as significant research to address the concern from both a device interference and a public health standpoint.

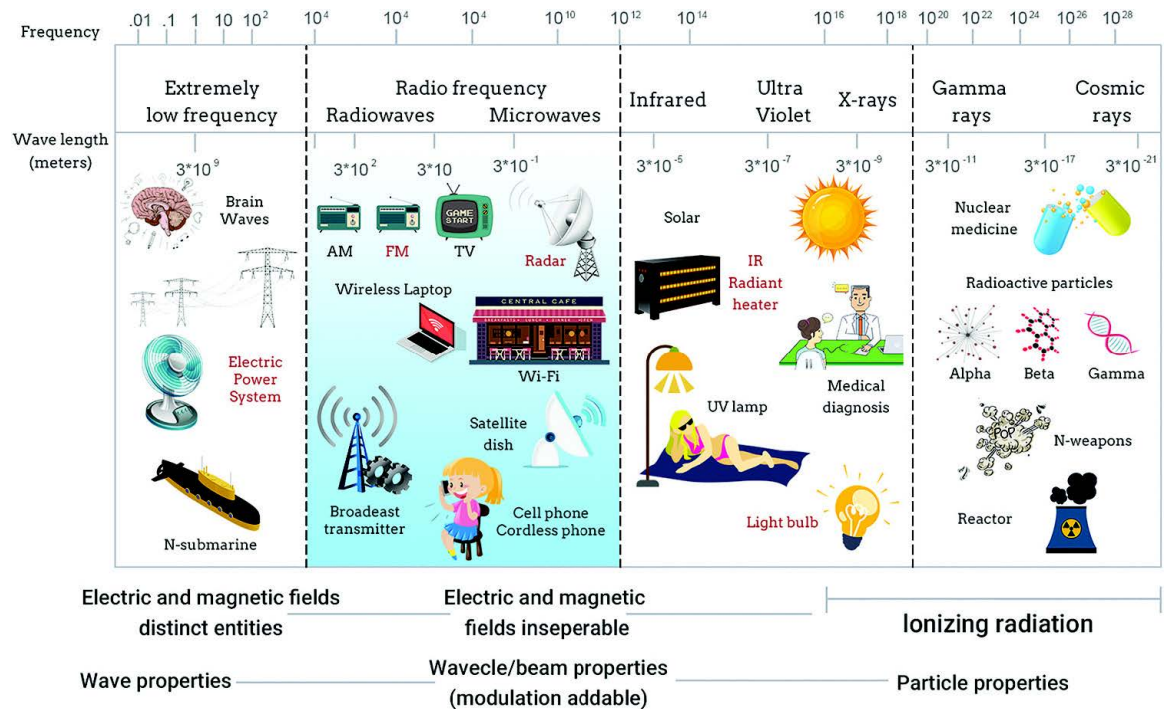


**Figure 5.1** Electromagnetic spectrum representing a broad frequency range including examples of applications in each range.<sup>72</sup>

The ability to reduce electromagnetic waves passing through a barrier refers to electromagnetic interface (EMI) shielding. This is often accomplished using electrically conductive and/or magnetic materials. There are multiple components that contribute to the material’s ability to shield electromagnetic waves: incident, reflected, and transmitted waves. Waves that are not reflected or transmitted are absorbed by the material. The amount of absorption can be enhanced through internal reflections and secondary effects.

### 5.2.1 Shielding efficiency and reflection loss

The shielding efficiency (SE) is a figure of merit used to depict the material’s effectiveness to restrict incident waves from passing through and is denoted on the decibel scale (e.g., -20 dB equates to a power ratio of 0.01, -30 dB equates to 0.001, and so on). SE is equated by the Equation below, where  $P_i$  is the incident power and  $P_o$  is the output power.

$$SE = 10 \log \left( \frac{P_i}{P_o} \right) \quad (5.1)$$

The total shielding efficiency,  $SE_{total}$ , is therefore the summation of the shielding efficiency for each of the contributions from surface reflection ( $SE_{reflection}$ ), absorption ( $SE_{absorption}$ ), and multiple reflections ( $SE_{multiple\ reflections}$ ), as shown in **Figure 5.2**.

$$SE_{total} = SE_{reflection} + SE_{absorption} + SE_{multiple\ reflections} \quad (5.2)$$

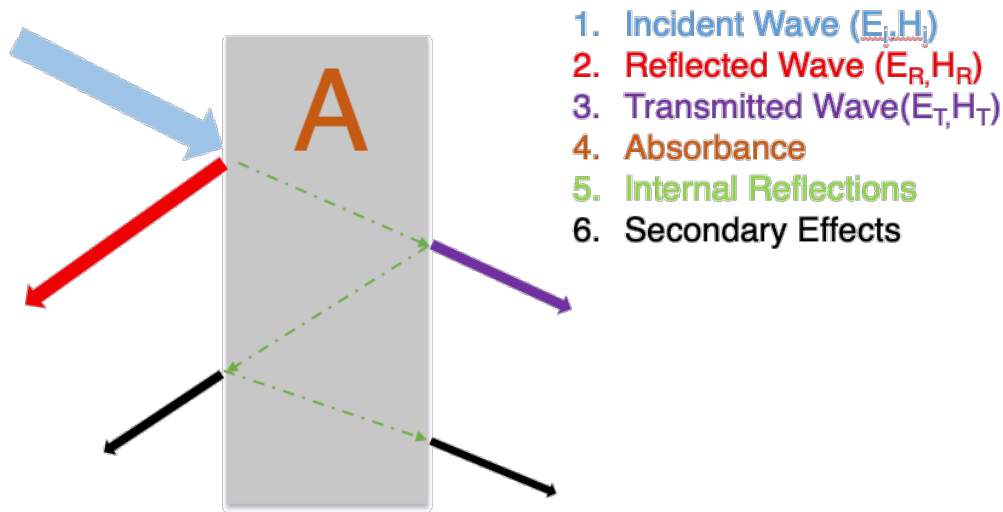


**Figure 5.2** Schematic of EM wave components interacting with a material.

Multiple reflections happen when a portion of the internal reflected wave is re-reflected within the shielding material. They are a result of scattering inhomogeneity within the material, which can be realized by adjusting the materials structure.<sup>77</sup>

Reporting the SE, however, does not give a holistic insight to the material's ability to prevent both shielding from other devices as well as itself. Therefore, it is important to decouple the incident power into three parts: reflection, absorption, and transmission power. Maximizing EM absorption protects the device itself and others, but keep in mind this absorption converts EM waves into thermal energy. EM absorption, which is represented by the reflection loss ( $R_L$ ), is

highly dependent on the material's relative complex permittivity, Equation (5.3), and relative complex permeability, Equation (5.4).

$$\varepsilon_r = \varepsilon' - j\varepsilon'' \quad (5.3)$$

$$\mu_r = \mu' - j\mu'' \quad (5.4)$$

The real parts  $\varepsilon'$  and  $\mu'$  represent the storage capability and the imaginary parts  $\varepsilon''$  and  $\mu''$  represent the dissipation of the EM wave energy.<sup>74,78</sup> From  $\varepsilon_r$  and  $\mu_r$ ,  $R_L$  can be determined using transmission line theory, where  $Z_{in}$  and  $Z_0$  are the input impedance and free-space impedance, respectively,  $Z'$  is the wave impedance,  $Z$  is the impedance matching.<sup>73,74,79</sup>

$$R_L = 20 \log \left| \frac{(Z_{in} - Z_0)}{(Z_{in} + Z_0)} \right| \quad (5.5)$$

$$Z_{in} = Z_0 \sqrt{\frac{\mu_r}{\varepsilon_r}} \tanh \left[ j \left( \frac{2\pi f d}{c} \right) \sqrt{\frac{\mu_r}{\varepsilon_r}} \right] \quad (5.6)$$

$$Z_0 = \sqrt{\frac{\mu_0}{\varepsilon_0}} \quad (5.7)$$

$$Z' = \frac{|E|}{|H|} = \sqrt{\frac{j\omega\mu}{\sigma + j\omega\varepsilon}} \quad (5.8)$$

$$Z = \left| \frac{Z_{in}}{Z_0} \right| \quad (5.9)$$

$f$  is the frequency of EM wave,  $d$  is the absorber thickness,  $c$  is the speed of light ( $\sim 3.0 \times 10^8$  m/s),  $E$  is the electric field,  $H$  is the magnetic field, and  $\sigma$  is the electrical conductivity. When  $Z$  is unity, EM waves are fully absorbed meaning they are not reflected off the surface. A good absorber, i.e., high  $R_L$  absolute value, has high impedance matching and internal attenuation. These characteristics are highly dependent on the frequency of the incident wave, material properties, and thickness. The EM field drops exponentially with increasing skin depth ( $\delta$ ), and  $\delta$  decreases

with increasing frequency, electric conductivity, and magnetic permeability. The skin depth is the distance at which the incident wave can penetrate through a material (**Figure 5.3**); it is when the field drops to  $1/e$  of the incident value further defined by Equation (5.10).

$$\delta = \frac{1}{\sqrt{\pi f \mu \sigma}} \quad (5.10)$$

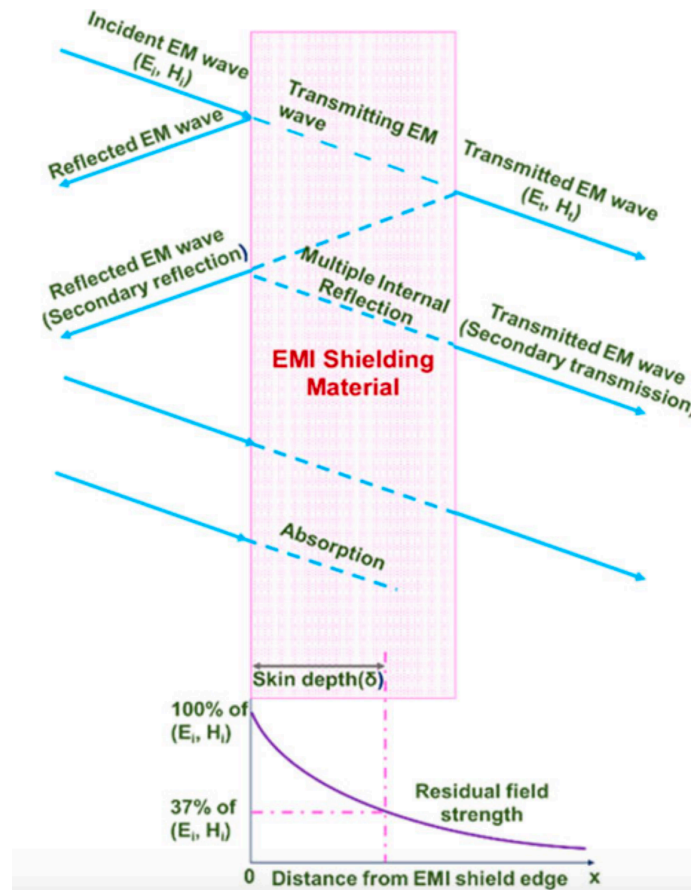


**Figure 5.3** EM wave interactions with EMI shielding material and skin depth representation as a function of distance from the edge of the shielding material.<sup>79</sup>

The minimum SE and  $R_L$  requirements are based on the target application. At least 20 dB attenuation is required for commercial applications like mobile electronics for human safety, whereas at least 30 dB attenuation is required for military applications.<sup>80</sup> These performance metrics are obtained through careful selection of materials and their electrical and mechanical

properties. For certain applications, it is more advantageous to have a sharp peak at a specific frequency, while in others it is more advantageous to have a broad peak spanning a wide frequency range, i.e., a high bandwidth. **Figure 5.4** shows example reflection curves to depict two different scenarios, as well as a list of the key factors that are influential to achieving the desired performance. Our goal is to achieve high broadband absorption, similar to the green curve, with similar levels of attenuation.

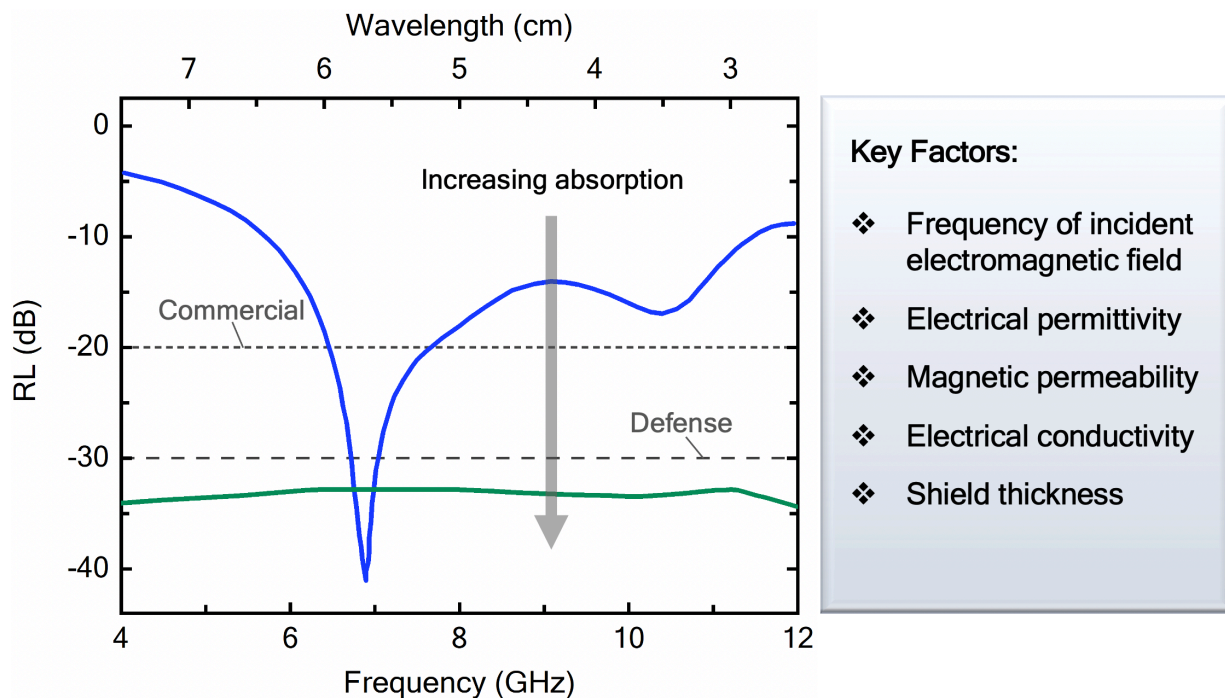


**Figure 5.4** Example reflection loss broad and peak curves, as well as key factors influencing shielding performance.

Traditionally, metallic films or meshes were used to obtain high shielding efficiencies; however, it mainly shields EM waves through reflection and not absorption.<sup>81,82</sup> This is because incident waves are easily reflected from the surface of the metal having a sea of free electrons. This protects the device itself but at the expense of potentially damaging other nearby devices or objects. They are also heavy, expensive, corrosive, and rigid. Therefore, there are many researchers exploring the use of polymer composites to achieve high electromagnetic absorption.<sup>83-97</sup> Many of

the polymer composites developed consist of conductive fillers whose physical or chemical properties differ from the base material. While the base polymer is insulative, the fillers are conductive to allow current to flow through their network. The filler content should be above the percolation threshold, so they are able to form a conductive network.<sup>72</sup> Percolation threshold refers to the minimum filler content in the polymer matrix at which the concentration of fillers causes the electrical conductivity to significantly increase. To achieve high electromagnetic absorption, there is a narrow range of electrical conductivities needed: too high and many of the waves are reflected, too low and they are transmitted. The conductivity range we need is between  $10^{-2}$ - $10^{-4}$  S/m.<sup>82</sup> Carbon-based composites can yield conductivity values in the appropriate range and thus have gained significant traction in the EMI shielding field. This is due to the ability to create flexible shields, tune their performance *via* filler fraction and type, be cost-effective, and use existing infrastructure for fabrication.<sup>73,98,99</sup> Several articles thoroughly review various types of polymer composites that have been explored using a variety of fillers including carbon-based and magnetic particles.<sup>73,79,82,100-106</sup> Magnetic particles have consistently shown to improve absorption as they contribute to wave attenuation and allow for a higher impedance match.<sup>78,82,85,107-115</sup>

### *5.2.2 Prior implementations for modulating internal reflections*

In addition, a compelling strategy to increase the absorption is to introduce pores into the structure that increase the attenuation through multiple reflections.<sup>82,106</sup> It also improves the impedance matching between the material and free-space *via* gradual increases in the permittivity and permeability relative to fully solid materials of the same composition. Reducing front-face reflection allows the EM wave to penetrate into the shielding material, enhancing absorption.<sup>82</sup> This can be achieved in a variety of ways; one of which is through foaming.<sup>72,82,116-124</sup> During the foaming process, the average pore size and filler material can be tuned. When the geometry, size,



and position of the periodic pores meet certain conditions, the interaction between the pores and incidence EM wave induces an internal resonance. Resonance causes the electric field to concentrate at the cell wall, causing EM energy loss inside the shield, thereby enhancing absorption. However, it has shown to be difficult to control the distribution and homogeneity of the pores.<sup>82</sup> The inability to precisely control the pore sizes can be overcome using 3D printing.<sup>117,125–129</sup> This allows for more intricate structures with periodic pores to be created, thereby enabling precise tunability of the frequency range and bandwidth. Although, some of the limitations for 3D printing are the lack of scalability, cost (due to the time it takes to print the structures), poor surface finish, and limited feature resolution.

### *5.2.3 Applying kirigami for EM absorption*

To overcome the manufacturing challenges with foaming and the scalability and resolution, kirigami design principles can be applied. The use of kirigami has shown to be advantageous for its ability to create a controlled array of pores and its facile fabrication. The kirigami pattern can also be precisely tuned based on the desired wavelength. Previous studies have shown the usefulness of origami and kirigami for EMI applications.<sup>130–134</sup> However, they focused on enhancing the shielding efficiency through reflection by coating polymer films with metal. Here, the linear kirigami design (shown in **Figure 5.5**) is patterned onto a polymer composite and then stretched to transform the sheet into the 3D shape where the material in between the cuts rotates out of plane, creating periodic voids. (Note that the void shape, size and distribution is, optionally, randomizable, broadening the structure's frequency response range.) The kirigami substrate is then placed in between two polymer composites with magnetic particles. We simulated the EM behavior of the multi-layer stack using a multi-physics simulation tool and optimized the pore geometry in the X-band. We then fabricated and tested the composites experimentally.

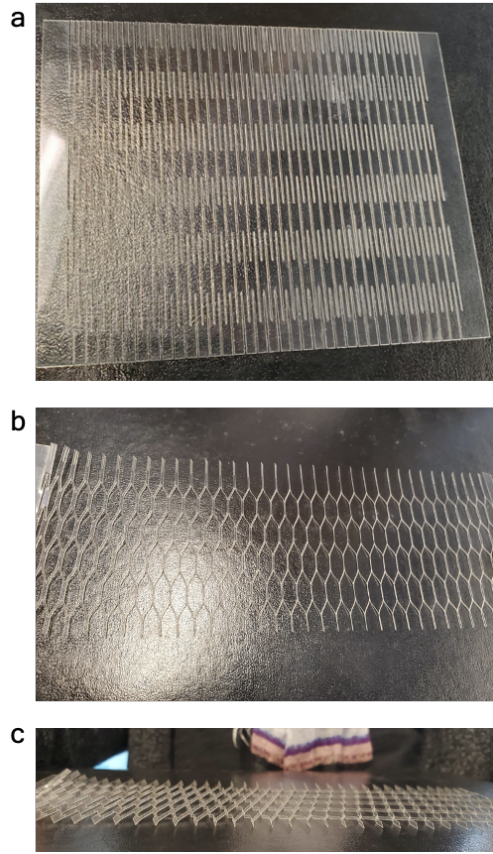


**Figure 5.5** Linear kirigami pattern unstretched (a), stretched top view (b), and stretched side view (c).

## **5.3 Modeling the kirigami-based polymer composites**

### *5.3.1 COMSOL setup*

EM waves are simulated using COMSOL to help determine what the reflection loss is when a kirigami layer is inserted between bulk carbon-based composites. The required size and shape of the pores are highly dependent on the incoming EM frequency. In this chapter, we will primarily focus on frequencies of 4–12 GHz or wavelengths of 7.5 – 2.4 cm. The electromagnetic waves, frequency domain module is used to simulate the scattering parameters and reflection loss.

The real and complex electrical permittivity and magnetic permeability as a function of frequency are inputted parameters. For this example, electromagnetic properties of a Fe<sub>3</sub>O<sub>4</sub>/graphene heterostructure developed by Song, W. *et al.* are used.<sup>88</sup> The permittivity and

permeability values across the frequencies of interest used for the simulations are shown in **Figure 5.6**.

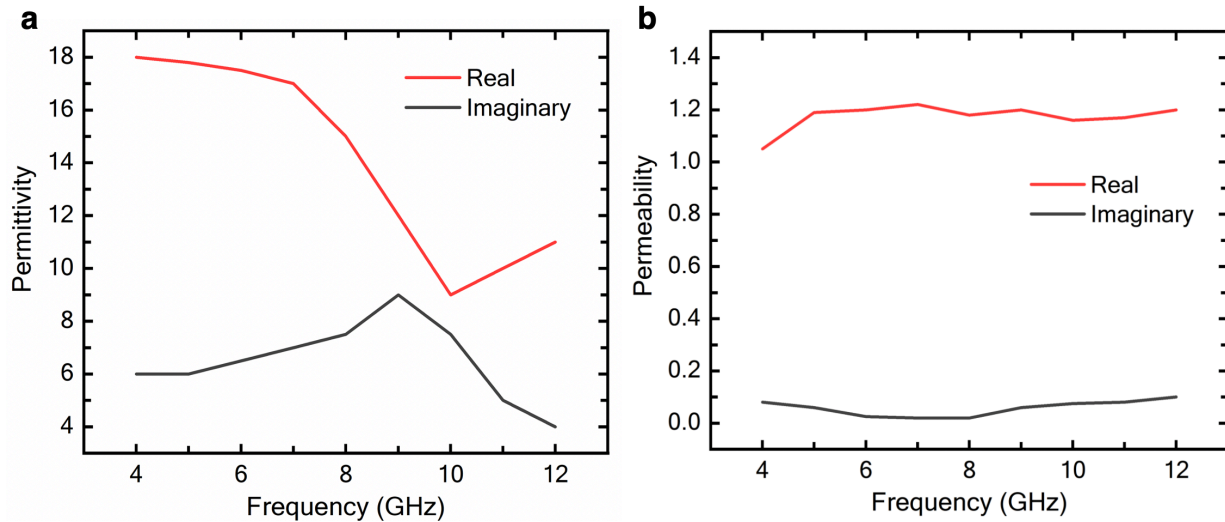


**Figure 5.6** Electrical permittivity (a) and magnetic permeability (b) used to carry out the electromagnetic wave simulations.

The kirigami unit cell used for modeling and testing is sandwiched between two composites and surrounded by air as shown in **Figure 5.7**. For simplicity, the walls of the linear kirigami pattern were assumed to be  $90^\circ$ . Therefore, the thickness of the wall corresponds to the thickness of the kirigami sheet and the pore size corresponds to the displacement of the sheet. A periodic condition was also applied to the sides of the assembly. A perfectly matched layer is applied to the top surface to prevent secondary reflections and the perfect electrical conductor condition is applied to the bottom surface to prevent transmission past the material. COMSOL simulates the scattering parameters and the reflection loss (RL) is calculated using Equation (5.11).

$$RL = -20 \log_{10} |S_{11}| \quad (5.11)$$

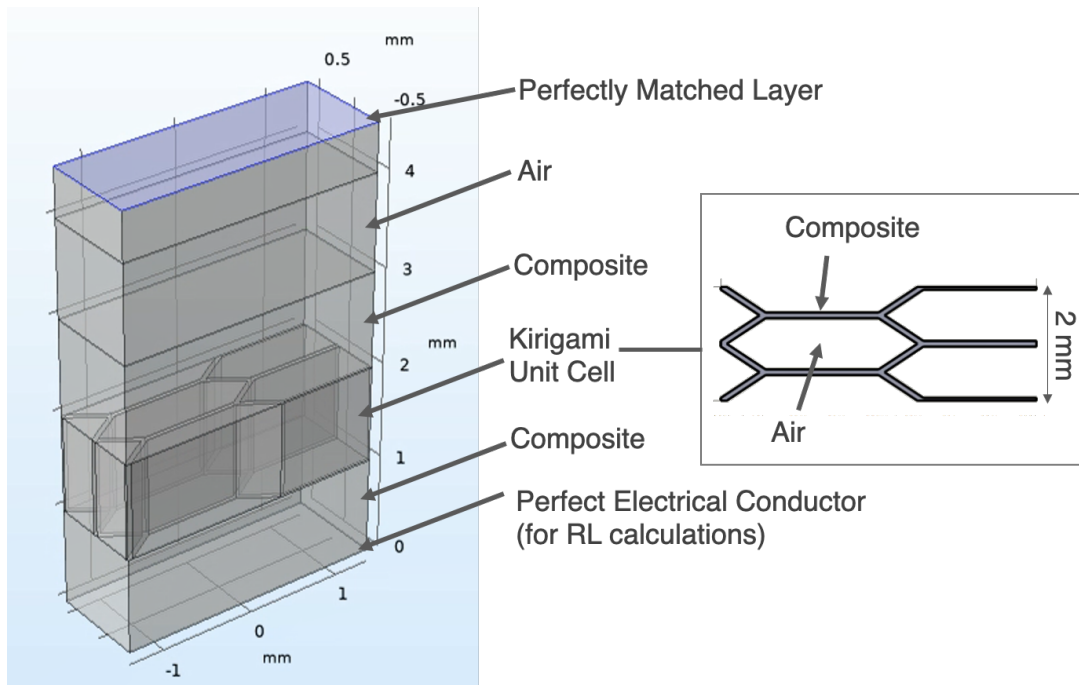


**Figure 5.7** Diagram of COMSOL setup for simulating EM waves through a multi-layer stack.

### 5.3.2 Modeling results

**Figure 5.8** shows changing the thickness of the honeycomb significantly changes the reflection loss. The legend in **Figure 5.8a** represents the thickness of the unit cell and the geometry is shown in **Figure 5.8b**. Compared to the bulk, without the kirigami honeycomb structure, the kirigami unit cell shows a greater absolute reflection loss beyond the -30 dB requirement for defense applications for the 1 mm thick cell. As the thickness of the cell increased, so did the absolute reflection loss up to a certain size is reached. Beyond this, the performance starts to diminish. This can be seen with the 2 mm thick sample underperforming the bulk sample. The exact mechanism for the behavior of multiple internal reflections is unknown. A 3D visualization of the electric and magnetic fields of the composite-kirigami cell assembly at the peak RL at 6.7 GHz at 1 mm thickness is shown in **Figure 5.8c** and **Figure 5.8d**. It is apparent the fields are most concentrated

at the edges of the unit cell. Coatings can thus be used to effectively interact with electromagnetic fields using the kirigami structure as a platform.

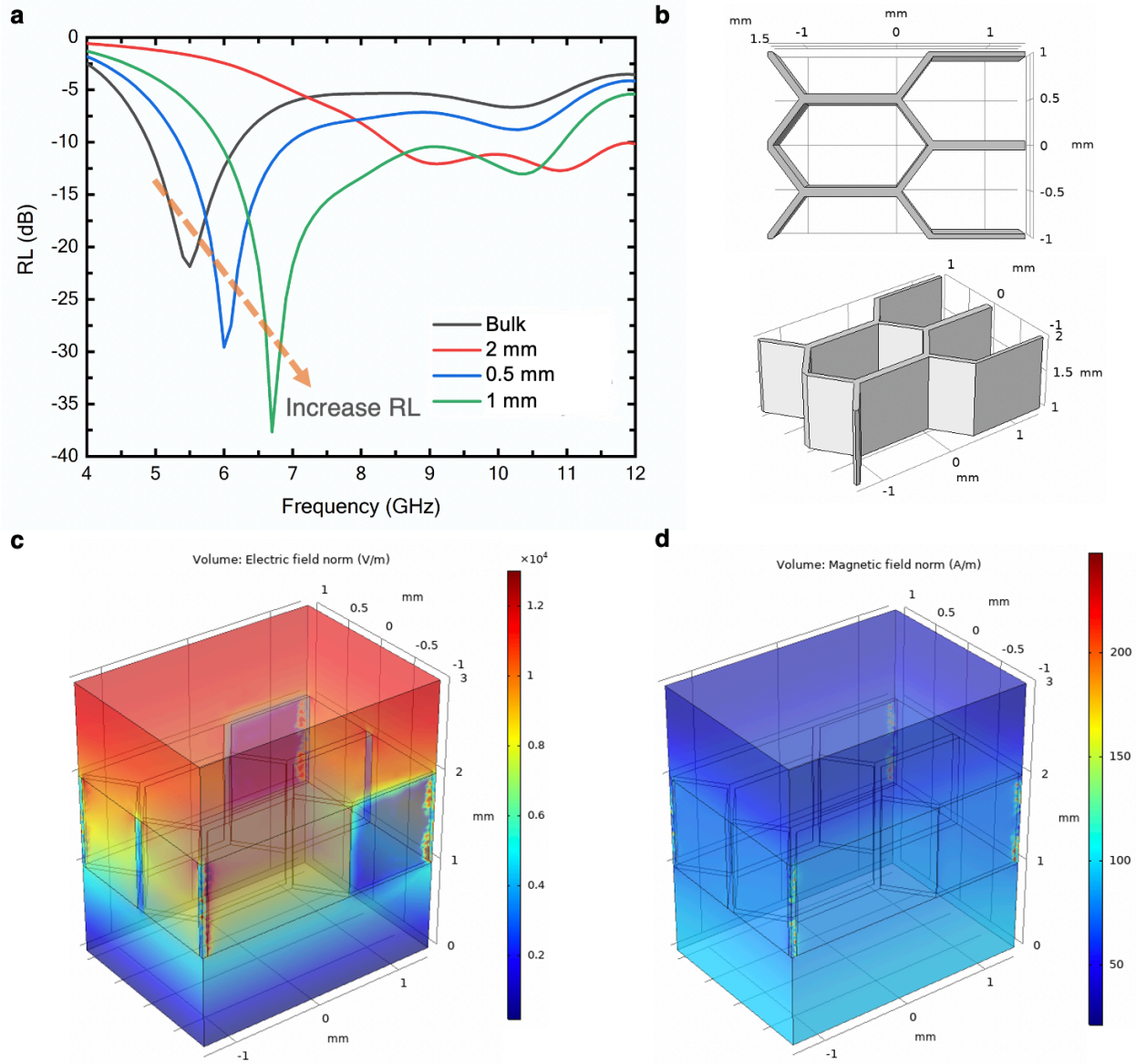


**Figure 5.8** Comsol results of kirigami-based graphene composite. (a) Reflection loss as a function of frequency varying pore geometry. (b) Top and iso view of kirigami honeycomb unit cell. 3D visualization of the electric (c) and magnetic (d) fields at 6.7 GHz corresponding to the geometry in (b).

## 5.4 Methods

### 5.4.1 Fabrication of solution

For this study, graphene nanoplates with the size of 5–15  $\mu\text{m}$  were produced by XG Science. Dopamine hydrochloride, levodopa, Tris, and Poly vinyl alcohol ( $M_w$  89,000~98,000) are supplied by Sigma Aldrich. Graphene nanoplatelets (GnPs) were functionalized with polydopamine (PDA). The reaction was carried out in a 500 ml flask equipped with a magnetic stirring in room temperature. Tris (0.3 g) were added to 250 ml of deionized water. GnPs (0.5 g) was dispersed in the above buffer solution under ultrasound for 30 min. Then, dopamine (0.25 g) was added under gentle magnetic stirring. Finally, the mixture was continuously stirred for 24 h. Subsequently, the suspension was filtered through a 0.22  $\mu\text{m}$  polytetrafluoroethylene membranes and washed several times with deionized water and ethanol until the filtrate became colorless and neutral. Finally, the resulting product was dried in a vacuum at 40°C for 24 h to a constant weight. The composite mixture was prepared by dissolving PVA (0.95g) powders in deionized water (8 mg) at 80°C. Then GnPs/Polydopamine (0.53g) or GnPs/Poly(levodopa) (0.53g) was added and dispersed by applying the ultrasonic wave for 30 min at room temperature.

### 5.4.2 Fabrication of film

**Figure 5.9** shows the fabrication process of making a kirigami-based composite film. A rectangular mask with a thickness of 0.25 mm is laser cut three times at 100% power, 60% speed, 1000 ppi, 1.5” optics, and then placed on top of a clean silicon wafer and adhered with tape. The carbon-based composite solution is sonicated for at least 30 min at room temperature and then drop casted onto the wafer. A glass rod is then slowly moved across the mask taking caution to apply even pressure. It is then baked at a temperature solvent evaporates for 30-45 min until all of it evaporates. The film is then removed from the wafer and then laser-cut with the same laser-

cutter stated previously. The cut parameters will vary depending on the thickness. For example, PVA functionalizing 5 wt% GnP in PDA having a thickness of 100  $\mu\text{m}$  will have cut parameters (20% power, 20% speed, 1000 ppi with 1.5" optics). Note, the thickness of the mask is greater than the resulting film thickness because of the amount of solvent that evaporated.

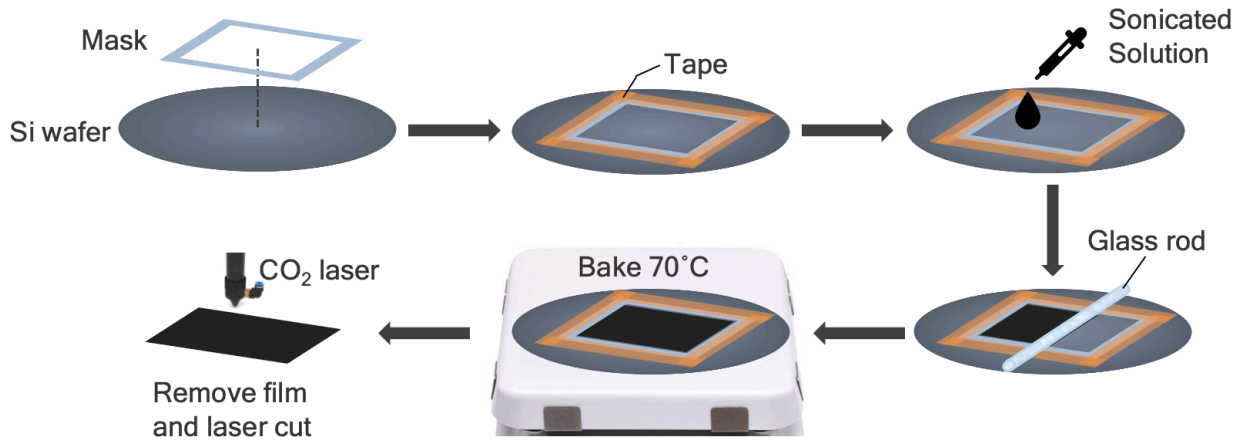


**Figure 5.9** Fabrication method of a thin, kirigami-based carbon composite film using a drop-cast, doctor-blade method.

In **Figure 5.10a**, the film fabricated from the above method is laser-cut to the dimensions of the waveguide for testing. The film is also laser-cut into the linear kirigami pattern (**Figure 5.10b**) and **Figure 5.10c** shows the kirigami substrate when displaced 4 mm. Here, the length of the cuts is and the spacing between cuts is mm. There are small bubbles that formed in the film, which may impact the shielding performance. Therefore, future work must address this issue to achieve a more homogeneous, bubble-free film. Also, for thicker bulk samples used to sandwich the kirigami film, a different fabrication process should be used such as a hot press.



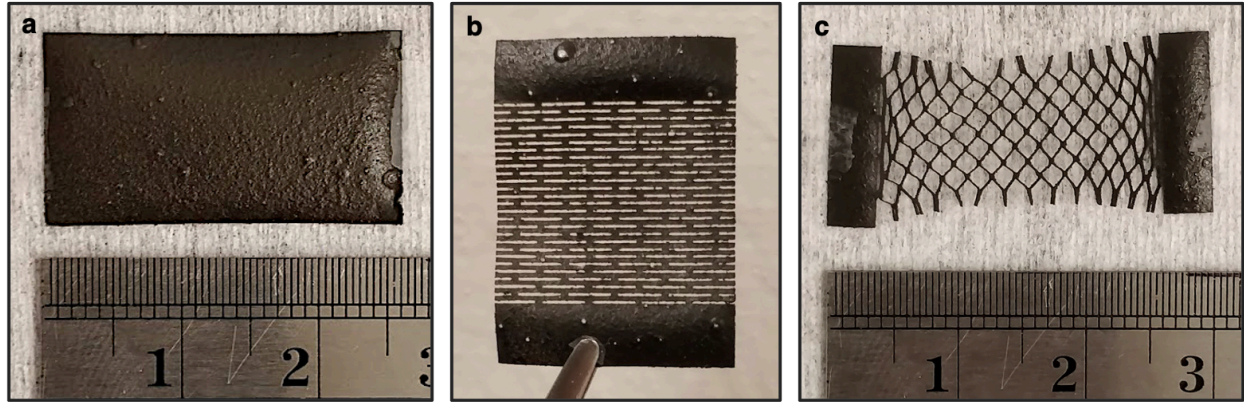


**Figure 5.10** GNP/PDA-PVA film after drop-cast, doctor-blade method. (a) solid film, (b) laser-cut film unstretched, and (c) laser-cut film stretched.

#### 5.4.3 Measurement setup

The scattering parameters used to determine the complex electrical permittivity and complex magnetic permeability are obtained using a 2-port vector network analyzer (VNA). A rectangular waveguide (22.86 mm x 10.16 mm x 3 mm) was used to perform the measurements in the X-band (8-12 GHz frequency range). The VNA generates a signal that measures amplitude and phase properties. The Nicholson-Ross-Weir method can then be used to calculate the permittivity and permeability from the scattering parameters.<sup>82,135</sup>

### 5.5 Experimental results

An example of how kirigami can enhance the shielding performance is shown in **Figure 5.11**. Here, the shielding efficiency of the kirigami-based substrate is normalized with the neat (without cuts) shielding efficiency for a GnP/PDA-PVA film. The thickness of this substrate is around 50  $\mu\text{m}$ . For some frequencies in the X-band, the kirigami-based composite has a higher shielding efficiency than the sample without cuts.



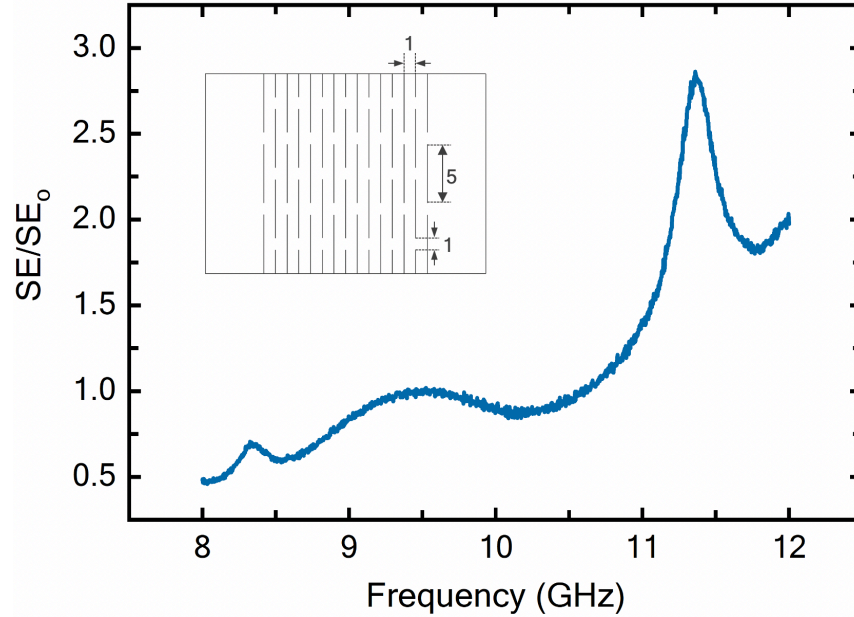


**Figure 5.11** Shielding efficiency of the kirigami-based GnP/PDA-PVA composite normalized with the neat shielding efficiency. The inset shows a schematic of the kirigami cut pattern and its dimensions are shown in mm.

## 5.6 Summary and conclusions

We have shown how the linear kirigami pattern can be utilized in electromagnetic shielding applications. The displacement of the kirigami substrate and its cut parameters dictate the pore geometry. We found through simulations that using a honeycomb structure achieves a higher reflection loss compared to the bulk material. For instance, a unit cell with a length of 2.25 mm, a width of 2 mm, and a thickness of 1 mm achieved a peak reflection loss of around -37 dB at 6.7 GHz. We also showed through experiments of a GnP/PDA-PVA film that the shielding efficiency is increased when a kirigami-based film is used as opposed to a neat film. Leveraging kirigami design techniques shows great promise for achieving a more scalable fabrication method, enhanced shielding performance, and increased flexibility of carbon composite films.

## **5.7 Future work**

Future work related to incorporating kirigami into effective electromagnetic absorbers involves two main research thrusts: the improvement of intrinsic material properties and the optimization of kirigami cut parameters. Ultimately, practical designs may incorporate multiple stacked kirigami layers of varied pore sizes. Combining layers of various resonant units at different frequencies inside a single unit may help achieve a broadband, high reflection loss material. To predict performance and guide this design optimization process, finite difference time domain (FDTD) simulations in conjunction with COMSOL solid mechanics modeling could be used. FDTD simulations allow visualization of electromagnetic wave propagation through the structure, which may help better understand the internal reflections affected by the kirigami structure.

## Chapter 6 Additional Applications and Future Work

### 6.1 Design space of kirigami-based shape memory materials

There has been growing interest in space exploration, where devices and structures must be transported long distances in confined spaces, as well as operate in harsh conditions. These applications call for the ability to compactly stow the devices and then deploy them, while also minimizing weight. Thus, a variety of folding and deploying mechanisms have been developed,<sup>136-138</sup> as well as novel materials that enable actuation without the weight or energy penalty.<sup>139</sup> One class of such materials are so-called smart materials, capable of sensing, controlling, and actuating in response to environmental stimuli. Shape memory alloys (SMAs) are one type of smart materials that has shape-adaptive capabilities upon changes in temperature or applied stress. SMAs are advantageous for their high actuation stress and fatigue life but are limited by their poor actuation strain (8-10%).<sup>140</sup> Although other high-actuation strain material systems exist, such as shape memory polymers (50-300%), they all possess inherent limitations that preclude their widespread use.<sup>141</sup> The foremost of these limitations is a low actuation force and poor fatigue life.<sup>142,143</sup> Evidently, there exists a trade-off between a high actuation stress and low actuation strain.<sup>144</sup> We are interested in combining SMAs with advanced actuation mechanisms to circumvent existing trade-offs between actuation strength, stowed volume, actuation stroke, and energy requirements. Specifically, we want to combine SMAs with novel kirigami shapes. Since the cut pattern dictates the shape and spacing of the beams and their mechanical interactions, we can apply kirigami

designs to SMAs to develop a “smarter” structure. This is because it can act as a control algorithm that allows the actuator to function properly after sensing changes.

New functionalities and properties of transformable shape memory alloys are discoverable through a systematic design of experiments focused on understanding the capabilities and limitations of applying kirigami techniques to smart materials. Initial thermomechanical tests were conducted on shape memory polymers and shape memory alloys to determine the extent to which introducing cuts affects its mechanical properties. In collaboration with Prof. Arvind Agarwal at Florida International University, we laser-cut and tested novel SMPs fabricated by Idowu, A.<sup>145</sup>

### *6.1.1 Shape memory polymers*

**Figure 6.1** shows the storage modulus and  $\tan\delta$  as a function of temperature measured by a TA Instruments Q800 dynamic mechanical analyzer (DMA). The frequency is 1 Hz, initial strain is 0.1%, preload force is 0.01 N, and the temperature rate is 3°C/min. The storage modulus measures the sample’s elastic behavior and  $\tan\delta$ , also known as damping, measures the material’s energy dissipation and is the ratio of the loss to the storage modulus. When the  $\tan\delta$  is less than 1, the material behaves like a solid or gel. When it is equal to 1, the material shows viscoelastic behavior, and when it is greater than 1, the material behaves as a liquid or sol and there is significant loss of elastic energy in the form of heat. This SMP shows optimum performance as the drop in modulus is large and sharp, followed by an extended rubbery plateau. The glass transition temperature of the SMP is 58.9°C, and since we are interested in the elastic response a temperature above 70°C, below  $\tan\delta$  of 0.5, and above its  $T_g$  is used.

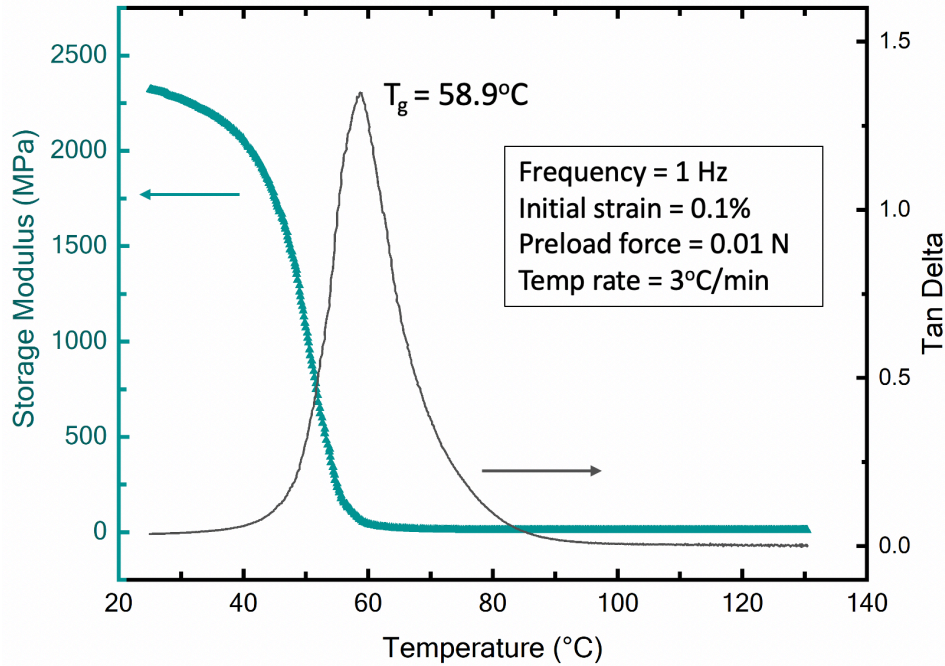


**Figure 6.1** Storage modulus and tan delta as a function of temperature of epoxy-based shape memory polymer obtained via DMA.

**Table 6.1** summarizes the key cut parameters for designing the linear kirigami pattern, as well as the inherent material properties. It also includes testing variables such as the blocking force and recovery ratio.

**Table 6.1** Variables for kirigami-based SMP design and testing, including cut parameters and material properties.

Kirigami cut parameters	Sample size	Inherent material properties	Testing variables
Length of cut ( $L_c$ )	Length ( $L$ )	Density	Strain %
Transverse spacing ( $x$ )	Width ( $W$ )	Poisson's ratio	Strain rate
Longitudinal spacing ( $y$ )	Thickness ( $t$ )	Young's modulus	Temperature delay before test
		Composite wt%	Number of temp ramp cycles
		Transformation temperature ( $T_f$ )	Number of cycles at $T_f$
		Storage & loss modulus	Blocking force
		$\tan \delta$	Recovery ratio
		Creep compliance	
		Relaxation modulus	

Thermomechanical tests were conducted on the linear kirigami pattern (**Figure 6.2**) via TA Instruments Ares Rheometer. The length of the cut is 5 mm, the hinge length is 1.5 mm, and the spacing between cuts is 0.75 mm. A force-gap test was conducted after the sample equilibrated at the desired temperature, having a heating rate of 10°C/min.

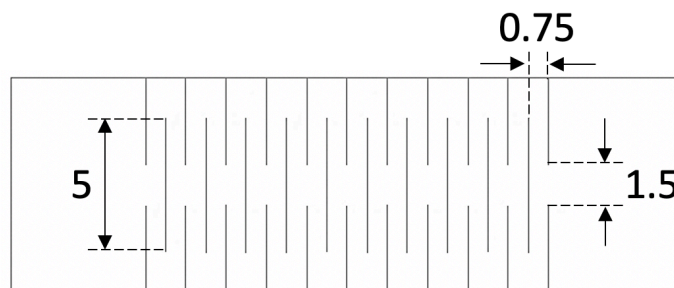


**Figure 6.2** Linear kirigami pattern schematic, in which the dimensions are in mm.

To define testing parameters, a temperature study, displacement-rate study, and dwell time study were conducted (**Figure 6.3**). The baseline for these tests were 70°C, 1 mm/s displacement rate, and 1 min dwell time after reaching equilibrium, which took around 10 min. 70°C was chosen as it is above the glass transition temperature of the polymer. The stress and strain refer to the cross-sectional area of the global film and the global strain, respectively. These should not be mistaken for the actual stress and strain experienced by the sample. This is because the kirigami sheet acts as a series of beams that bend out of plane, so the traditionally calculated stress-strain is not accurate. However, these samples were fabricated using a hot press and there were variations in the thicknesses of the samples. Therefore, the global stress is used to normalize the samples.

More work must be done to determine the variations amongst samples with the same testing conditions. Thermomechanical tests on different cut parameters must also be conducted to determine how they influence the SMP's actuation stress and strain behaviors, as well as how cyclic tests affect their fatigue.

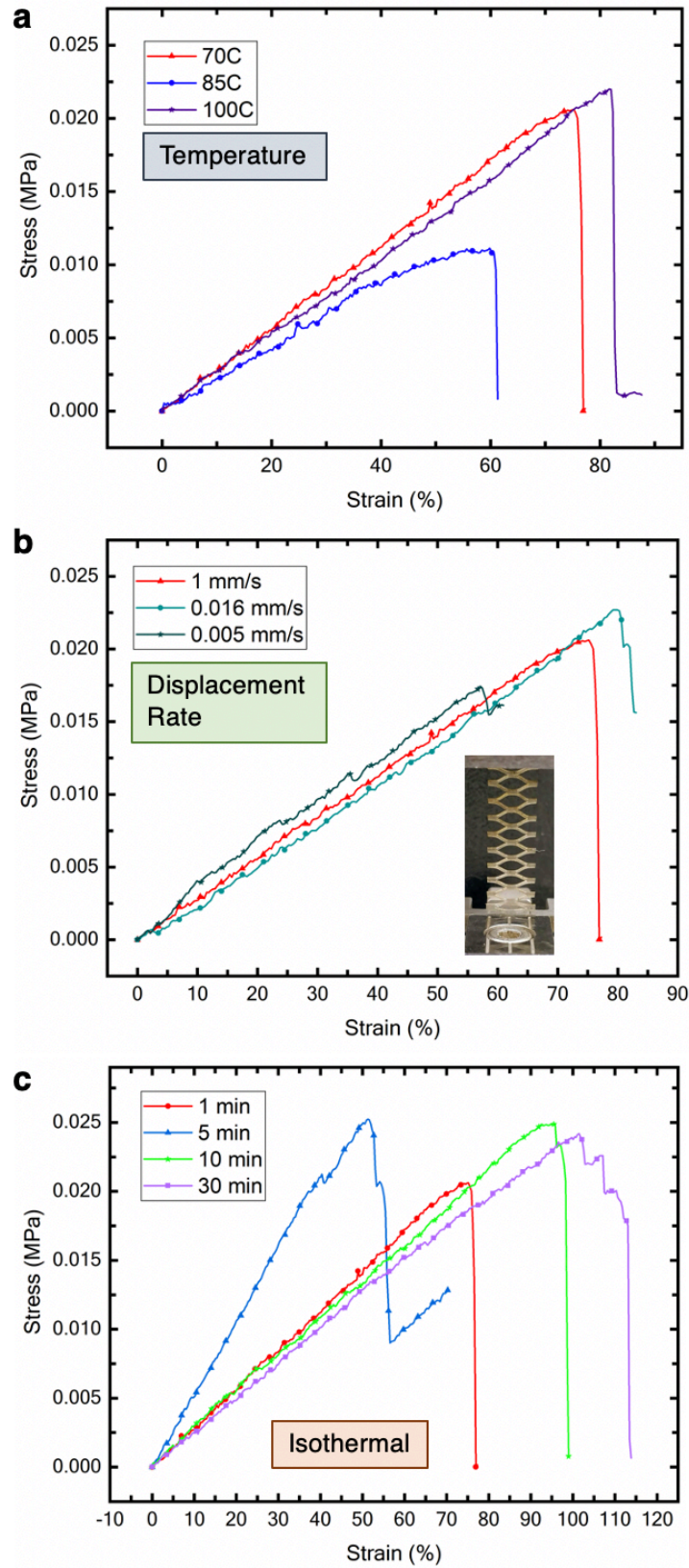


**Figure 6.3** Thermomechanical test results of kirigami SMPs. (a) Varying temperature, (b) varying displacement rate where the inset shows the stretched SMP, and (c) varying dwell temperatures.

### 6.1.2 Shape memory alloys

Nickel-titanium (NiTi) or Nitinol sheets with a transition temperature of 45°C and a thickness of 100  $\mu\text{m}$  (Kellogg's Research Labs, Salem, NH) was used. They were tested using differential scanning calorimetry (DSC), TA Instruments TRIOS DSC 2500, to determine the phase transformation temperatures. **Figure 6.4** shows the normalized heat flow as a function of temperature, where  $M$  represents the martensite phase and  $A$  represents the austenite phase.  $f$  represents finish,  $p$  represents peak, and  $s$  represents start. The sample was first heated and equilibrated to 100°C, then cooled to -75°C, then reheated to 100°C at a heating and cooling rate of 10°C/min.

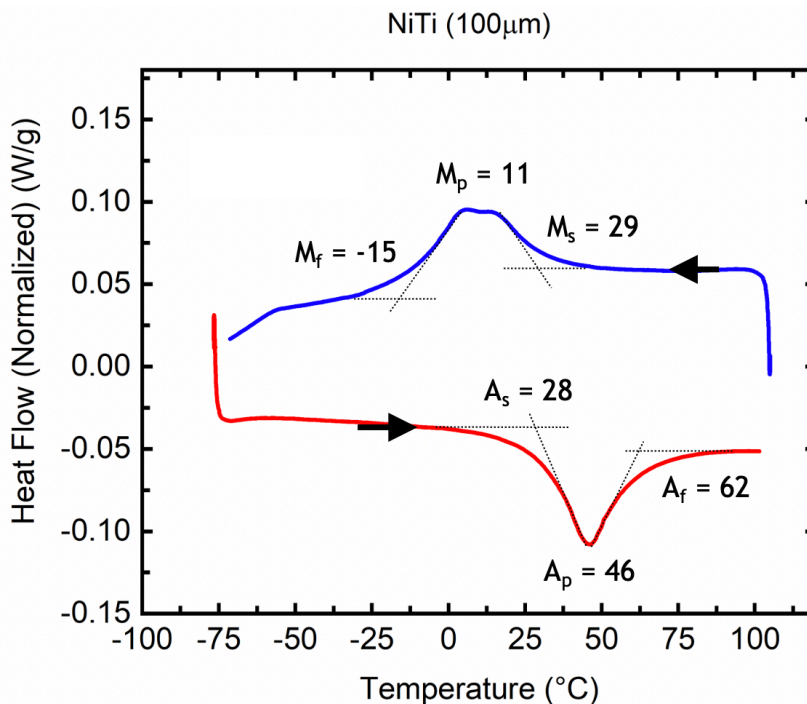


**Figure 6.4** Heat flow as a function of temperature of nitinol obtained via DSC.

Previously, structures were laser-cut into the kirigami pattern with a CO<sub>2</sub> laser. However, SMAs are reflective and notoriously hard to machine. Many laser cutters do not have the appropriate wattage or do not have high enough pulse rates, and therefore cause local heating.



Local heating is detrimental to the sample as it may change the phases and therefore its thermomechanical properties. Therefore, untreated nitinol was micromachined (Arctos, Dayton, OH) with a pulse width of 45 ns, pulse energy of 420  $\mu\text{J}$ , 17.1 W, pulse rate of 40 kHz, and 150 passes. Scanning electron microscopy (SEM) was used to visualize the cuts after micromachined and energy dispersive x-ray analysis (EDX) was used to determine the percentage of nickel and titanium in the bulk and near the cut ends as shown in **Figure 6.5**. SEM images were taken at 20.0 kV at a working distance of 12.9 mm in high vacuum. In the bulk, the sample has a composition of 48% nickel, 40% titanium, 12% oxygen, and 0.14% aluminum, while near the cut ends it is 42% nickel, 34% titanium, 24% oxygen, and 0.14% aluminum. The cut width averages 33  $\mu\text{m}$ . From the images, there are significant deposits around the edges and an apparent heat affected zone.

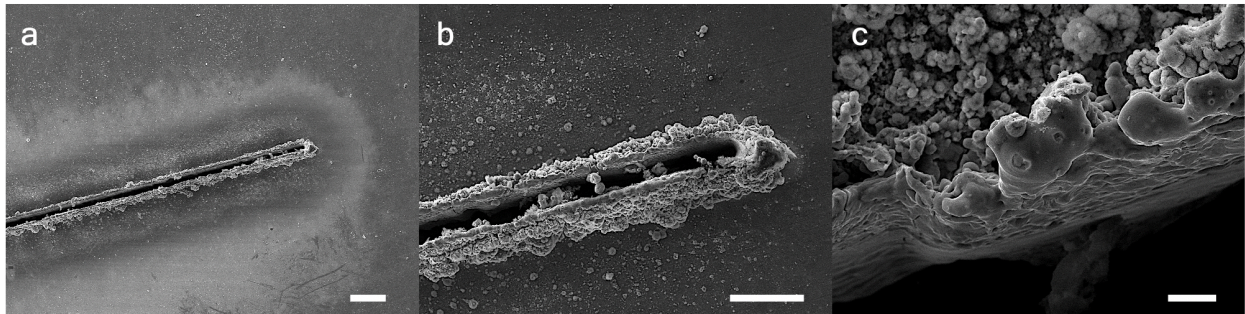


**Figure 6.5** SEM images of micromachined NiTi at (a) 40x, (b) 230x, and (c) 1,500x. Scale bars represent 200  $\mu\text{m}$ , 100  $\mu\text{m}$ , and 10  $\mu\text{m}$ , respectively.

Thermomechanical tests were conducted with an Instron with a 100 kN load cell with a thermal chamber. **Figure 6.6a** shows uniaxial tensile tests of NiTi samples taken to failure at 25°C around  $A_s$ , 45°C around  $A_p$ , and 60°C around  $A_f$ . As the temperature increased, so too does the amount of force required to displace it, because the alloy experiences martensitic hardening. For each of the samples, after the peak, the force decreases and does so abruptly as beams simultaneously bend out of plane. **Figure 6.6b** shows the dissipation of energy in the SMA after

two cycles. The kirigami nitinol samples were displaced 1 mm, which is beyond the linear elastic region, and then compressed back to the original state at a displacement rate of 0.1 mm/s. At 1 mm displacement, unloading occurred with residual strain at all temperatures tested. However, upon annealing, the residual strain is recoverable.

Further research is required to test the variability amongst samples at various temperatures. Also, other cut parameters must be explored to determine how the actuation stress and strain vary based on beam stiffness. To more accurately determine the strain particularly at the cut ends, digital image correlation should be used. Thermomechanical modeling using finite-element software could also be used to predict the smart kirigami material's performance. Lastly, cyclic tests should also be performed to determine fatigue when cuts are introduced to the material and how that affects the actuation stress and blocking force.

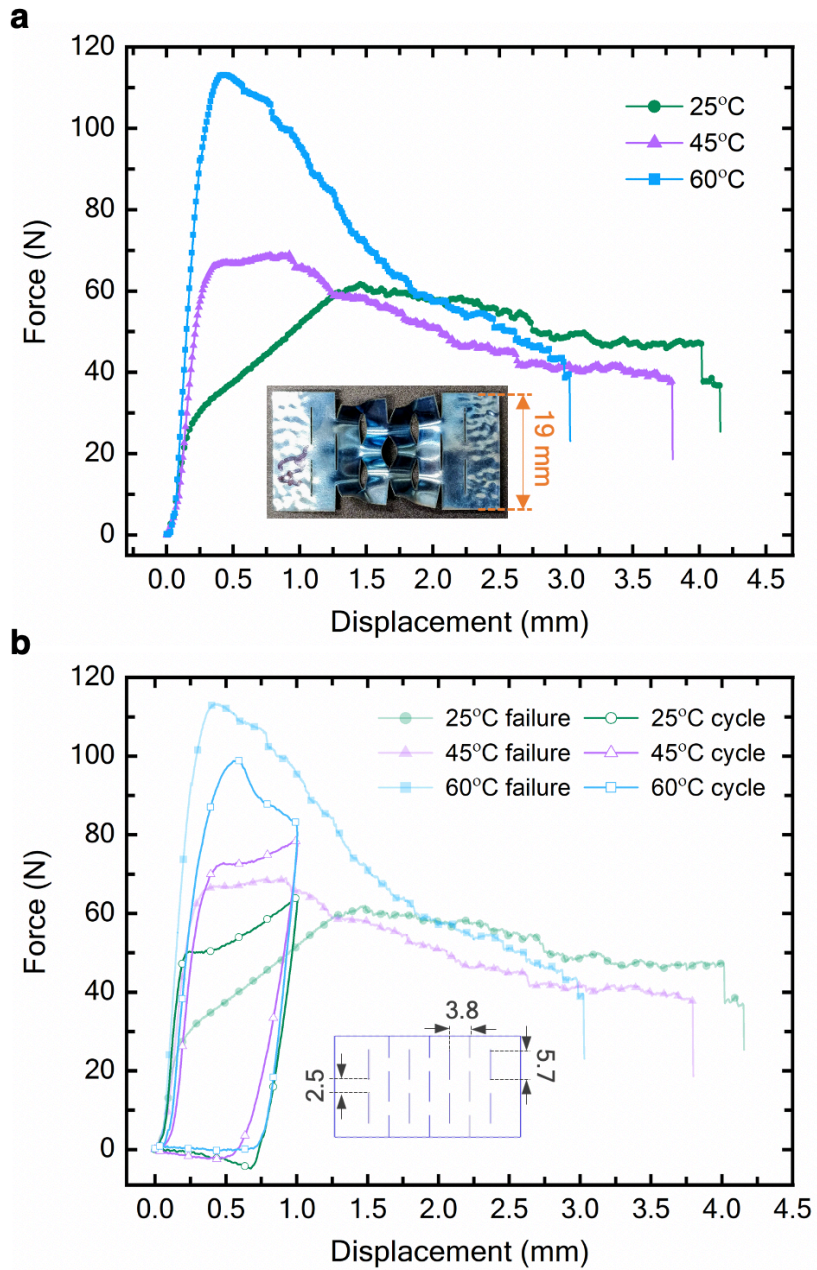


**Figure 6.6** Uniaxial tensile test results of kirigami-based NiTi samples at a displacement rate of 0.1 mm/s. (a) Tensile tests to failure; inset shows a kirigami SMA sample deformed to around 3 mm. (b) Thermomechanical test after two cycles to 1 mm at 25°C, 45°C, and 60°C. The inset is a schematic of the cut pattern in mm.

## 6.2 Mechanotransduction platform to promote cardiomyocyte maturation

Another promising application that can benefit from using kirigami design principles is for the creation of mini pillars that induce mechanical forces on cells. Researchers found a mechanical stimulus has significant influence on the cellular behavior, which motivated the creation of 3D culture models.<sup>146–149</sup> They found for human induced pluripotent stem cell-derived cardiomyocytes to reach maturation *in vitro*, the cellular environment must undergo dynamic changes in loading similar to that *in vivo*.<sup>148</sup> Previously, micro-tug platforms, consisting of an array of posts, were used to apply tunable loadings to cells, which the cells used to impart contractile forces.<sup>146–149</sup> In one study, the distance between the pillars oscillate closer and farther apart magnetically via Ni microspheres.<sup>147</sup> However, these platforms are challenging to fabricate and hard to scale.

Therefore, we are working on an easy-to-use and fabricate kirigami-based cellular platform that resembles the pulsing of a heartbeat to help promote cardiac tissue maturation. A modification of the linear kirigami pattern is created such that pairs of pillars pop out upon stretching. The posts move closer or farther apart depending on how much the substrate's ends are displaced.

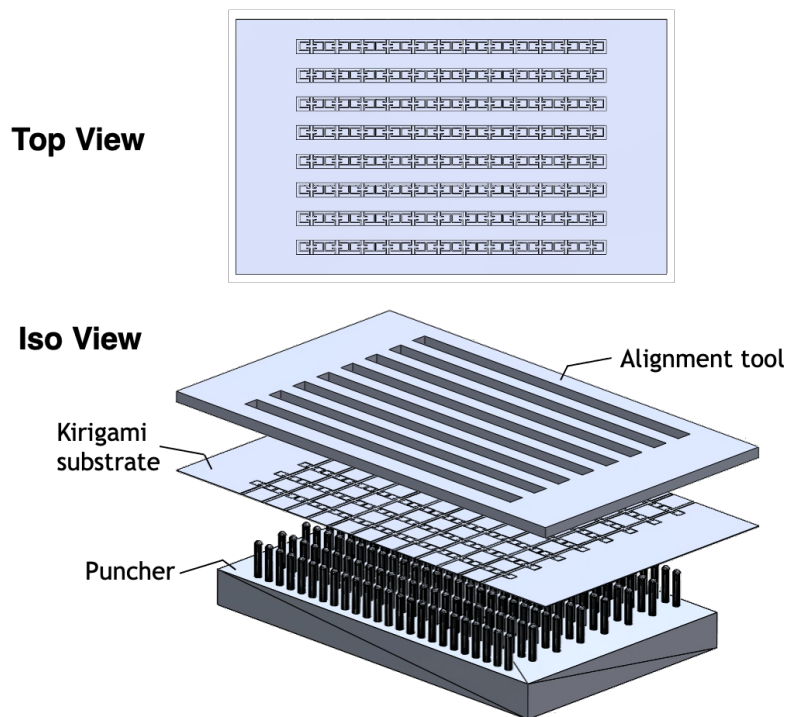


**Figure 6.7** Top and iso exploded view of CAD models of the kirigami substrate between a puncher and alignment tool.

Two pillars, when in the upright position (pillars stand  $90^\circ$  from the base), fit inside one well of a 96-well plate. The kirigami PET substrate can achieve close to  $90^\circ$  by stretching the sheet alone. However, not all the pillars are at the same tilt angle. To overcome the nonuniformity, the posts are folded over  $180^\circ$  after stretching forming a crease. In addition, the substrate is heat-treated after laser-cutting to remove residual stress, fixing it in the upright position. The substrate is heat treated either in a 3D printed or CNC-milled puncher-topper assembly (**Figure 6.7**) slightly above its glass transition temperature for 20 min. After cooling at room temperature, the kirigami substrate is removed and the resulting structure is shown in **Figure 6.8a** (iso view) and **c** (side view). An FEA model of a pair of pillars is shown in **Figure 6.8b** displaced 3mm to show the stress distribution. The amount of displacement is dependent on the inherent material properties and the thickness of the sheet.

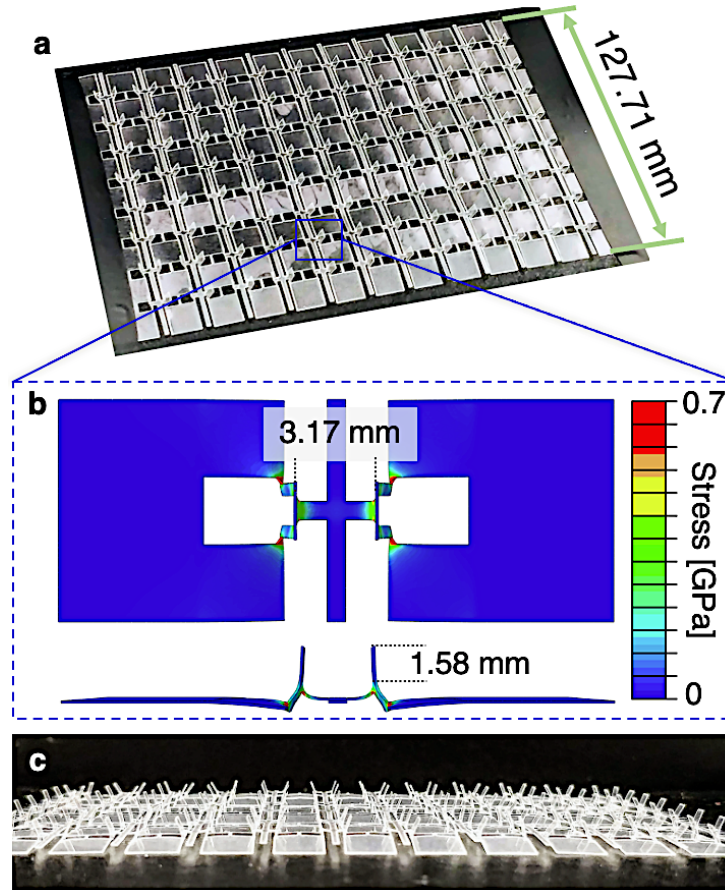


**Figure 6.8** Experimental and FEA models of kirigami platform. Iso view (a) and side view (c) of 96-well plate platform. (b) FEA model top and side view of a single unit cell. The color legend refers to the Von Mises stress in GPa.

Uniaxial tensile tests are performed on a PET substrate 0.1 mm thick. Acrylic bars sandwich the substrate and adhered with double sided stick tape to ensure the force is equally distributed across the edges of the substrate. In **Figure 6.9**, three different pre-stresses were applied to the substrate to determine how biasing the flaps to pop open in a certain direction influences the overall mechanical properties. No bias refers to testing the substrate as is after laser-cutting, bias 1 refers to using the puncher-topper assembly to bias the posts to pop out in the same direction taking caution to not apply too much stress on the material, and bias 2 refers to the combination of using the puncher-topper assembly and folding. Bias 2 results in a higher yield rate of pillars facing upward, followed by bias 1, then the no bias.



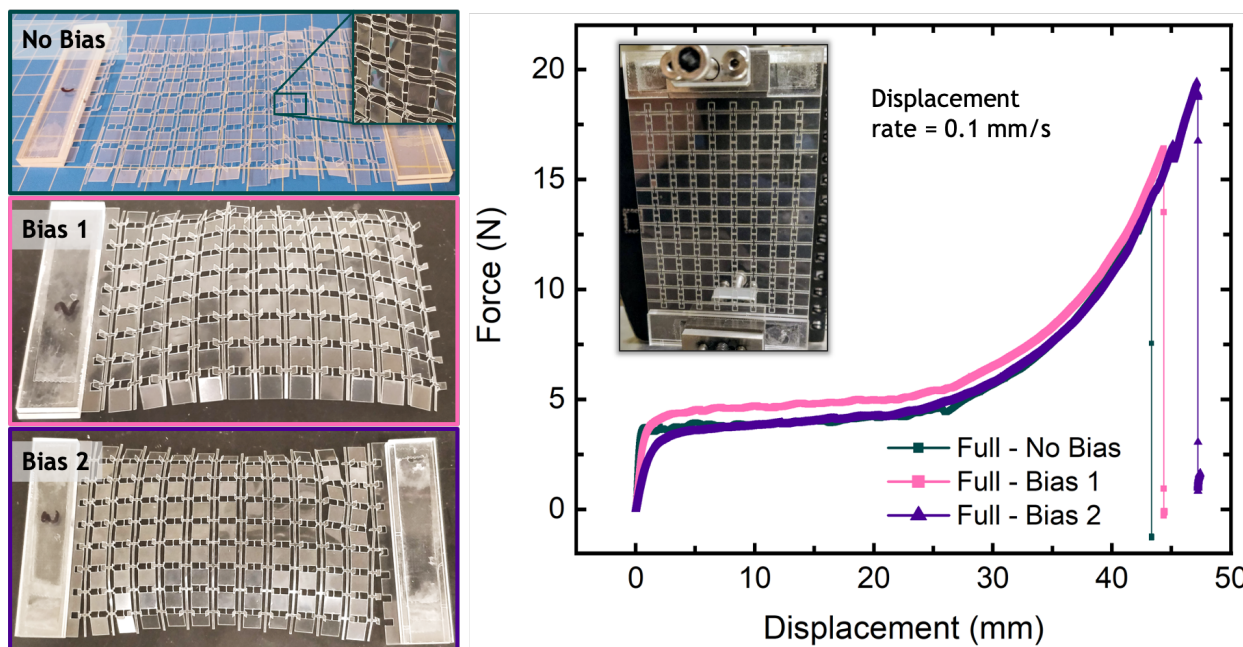


**Figure 6.9** Uniaxial force versus displacement plot of 96-well plate substrates experiencing different pre-stress treatments.

Similarly, a smaller, 18-well plate pattern was fabricated and tested (**Figure 6.10**). The inset shows the multi-stable states occurring as the posts flap open and get pulled apart. Each of these samples failed towards the end of the substrate. The displacement rate for this test is the same as the 96-well plate at 0.1 mm/s.

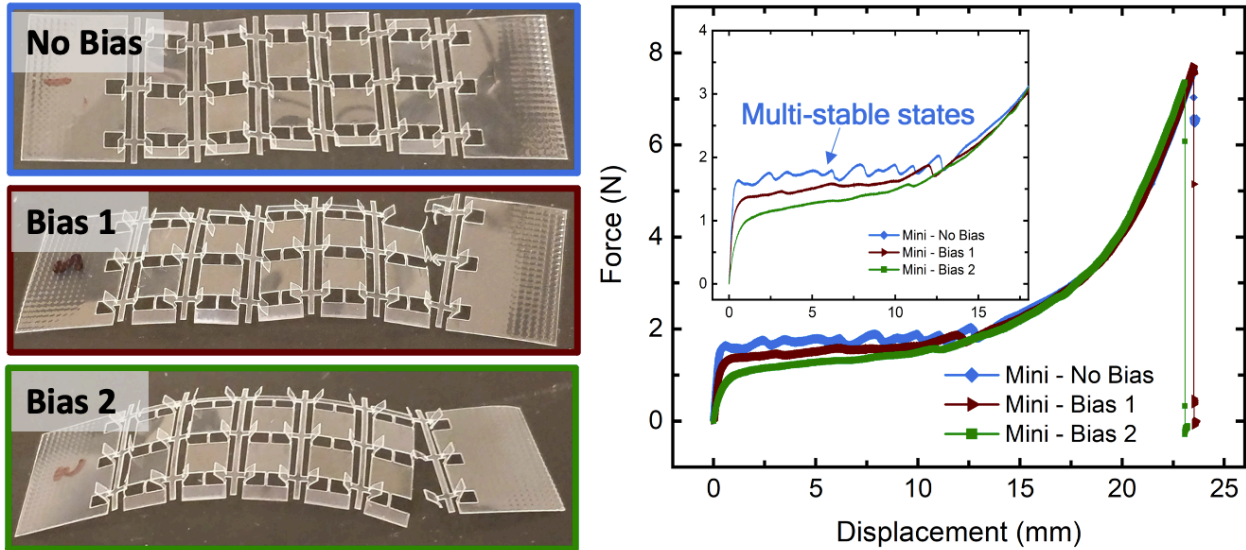


**Figure 6.10** Uniaxial force versus displacement plot of 18-well plate substrates experiencing different pre-stress treatments and the inset is a close up showing multi-stable states.

The full (96-well plate) and the mini (18-well plate) are plotted together in **Figure 6.11** to compare the force required to fail the substrate and at what displacement. It is interesting to note that despite the 96-well plate having over 5.3x the number of pillars as the 18-well plate, the uniaxial force does not scale to 5.3x. This is because the pattern is more intricate and therefore, the simple summation of beams in series may not apply for this pattern. The reason being is that the hinges rotate simultaneously as the posts rotate upward, making the calculations not as straightforward.



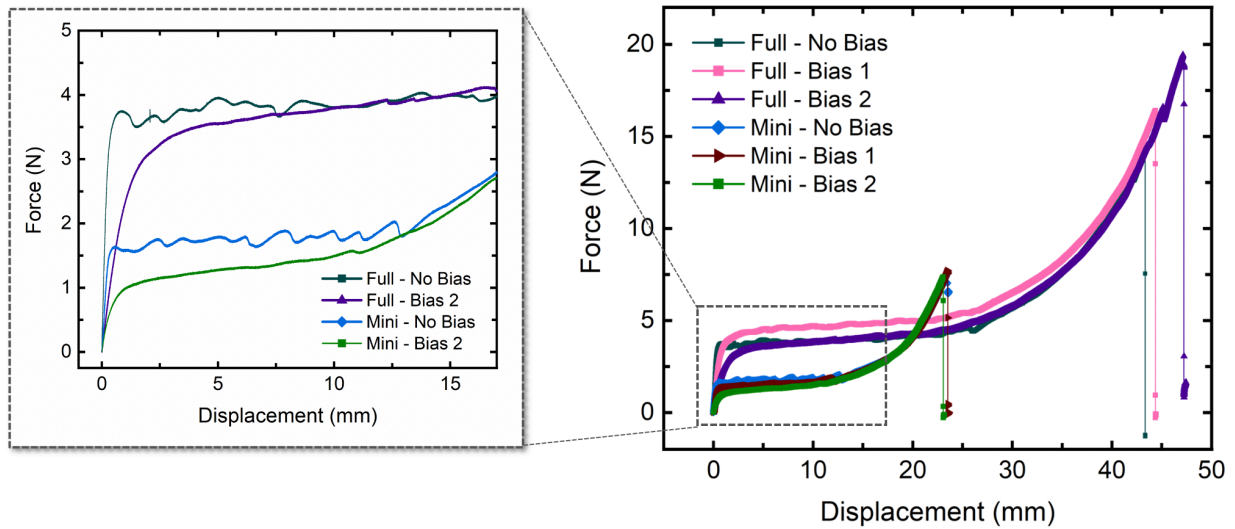


**Figure 6.11** Full and mini arrays with and without an initial bias before testing. Inset is a close-up of the force versus displacement without bias and with bias 2.

Another important parameter to determine is the stiffness of each post. A post bending stiffness range of 0.1-1 N/m is recommended to form good contracting cardiomyocyte tissues. A similar study found  $\sim 1.0$  N/m seems to be an appropriate stiffness for creating mature cardiomyocyte tissue and above 9.0 N/m induces a diseased tissue phenotype.<sup>148</sup> Two mechanisms that contribute to the tissue architecture are cell-generated contractile forces that drive tissue compaction and the alignment between the cell and its extracellular matrix.<sup>146</sup>

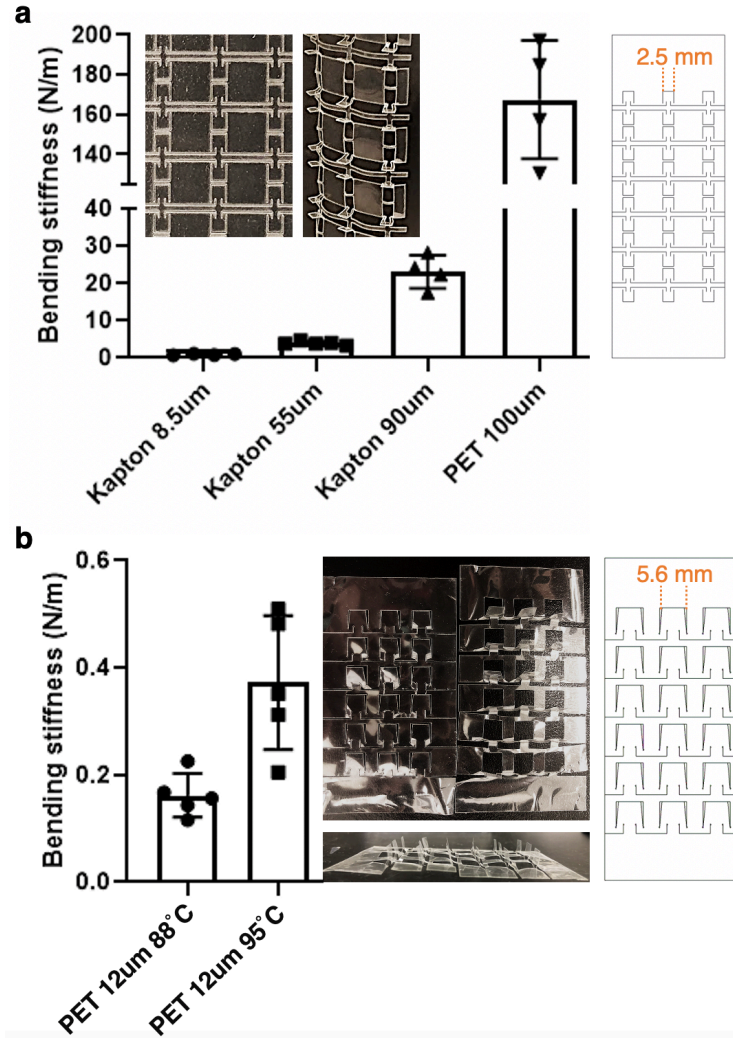


**Figure 6.12** Bending stiffness of one post for the kirigami pattern with two posts per well (a) and one post per well (b).

A cantilever is used to apply a small force of  $24 \mu\text{N}$  and the resulting deflection is measured. Based on the geometry and resulting deflection, the stiffness can be determined using the following equations and shown in **Figure 6.12**.

$$I = \frac{wt^3}{12} \tag{6.1}$$

$$F = \frac{6EI}{a^2(3L - a)} \delta \tag{6.2}$$

The pattern in **Figure 6.12a** consists of two pillars that fit into one standard well, whereas in **Figure 6.12b**, the length of the posts are longer and therefore, only one post fits inside the well. Therefore, two layers nested inside one another is required to achieve the two-post per well requirement needed to mature cardiomyocyte tissues. The average stiffness for PET 100  $\mu\text{m}$  is 162 N/m for the smaller post and for 12  $\mu\text{m}$  is 0.1-0.5 N/m for the larger post. For Kapton, having a thickness of 8.5  $\mu\text{m}$ , the bending stiffness was 0.885 N/m. Both films are biocompatible, but Kapton is more advantageous because its higher glass transition temperature allows electrodes to be patterned onto the film. This allows an electrical pulse to be driven from the posts, driving tissue development. More work is required to ensure the tilt angle is uniform across the substrate and the kirigami platform with cardiomyocytes on it must be tested. The pattern must also be modified to include holes at the tip of the posts to enhance adhesion of the cells to the posts.

### 6.3 Redesigning N95 masks

The COVID-19 pandemic created an unprecedented demand for N95 class respirators, which are desperately needed to help protect against the life-threatening virus. N95 masks (**Figure 6.13a**) made of thermoformed polypropylene have the ability to filter aerosols to 95% efficiency. However, these medical-grade masks are one-time use, uncomfortable to wear for long hours and some find it hard to breathe.<sup>150,151</sup> Moreover, tests to determine fit are subjective and many do not sustain proper fit for the duration of wear.<sup>152,153</sup> Alongside collaborators in the School of Architecture, Prof. Sean Ahlquist, and Dept. of Electrical Engineering and Computer Science, Prof. Alanson Sample, we set out to design a reusable textile mask, similar to that shown in **Figure 6.13b**. This mask also consists of a kirigami-based insert embedded with sensing elements to ensure proper fit, comfort, and filtration efficiency. The inclusion of weak magnets and health-monitoring sensors, paired with a device such as a smartwatch, may enable real-time sensing.

Magnets can be used to determine how well a mask fits the user's face and detect when the person is touching their face or mask. This detection prompts the user's smartwatch to alert the user and hopefully stops the user from touching their face.

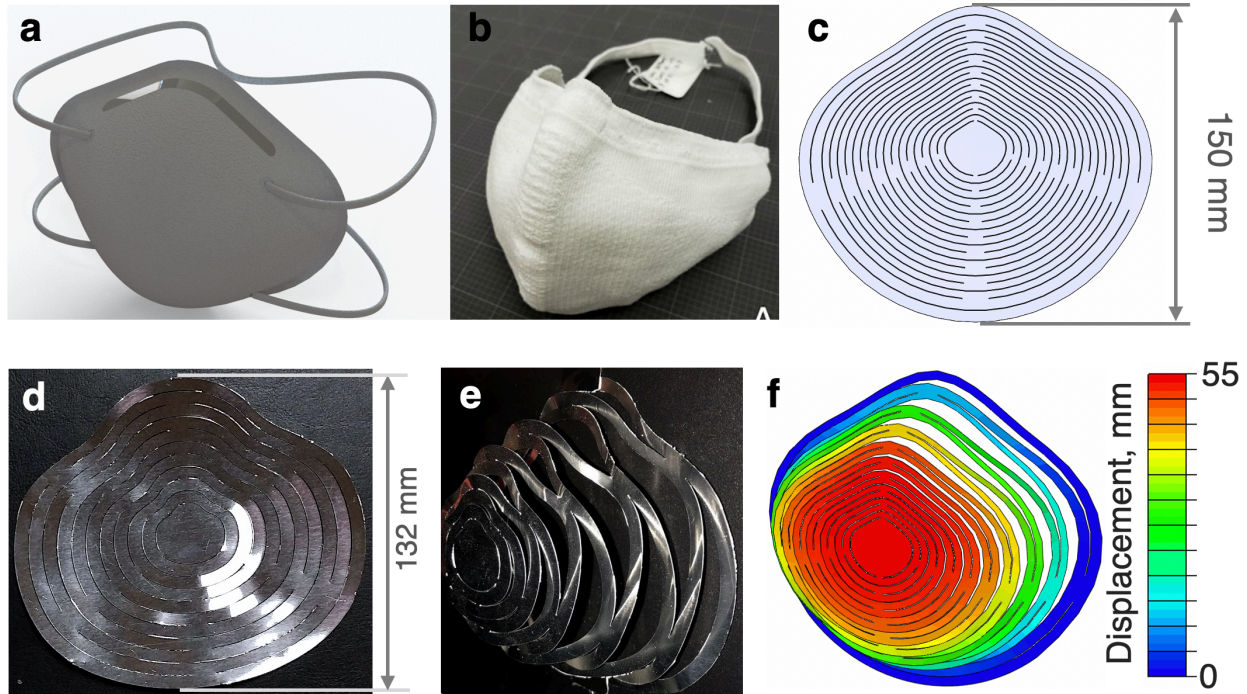


**Figure 6.13** RSK-based mask. (a) N95 mask CAD model, (b) knitted fabric mask, (c) CAD pattern of RSK-based mask, (d) top view and (e) iso view of pattern cut out of Al, as well as FEA model (f). The color legend indicates displacement in mm.

One way to increase breathability is to increase the mask area, increasing the flow rate. Studies have shown a flow rate of at least 30 L/min is required for normal breathing and 85 L/min for heavier breathing.<sup>154</sup> An issue with many conventional cloth masks is that breathing in causes the mask to collapse, decreasing flow rate, making the user uncomfortable. To overcome this, a kirigami pattern can be plastically deformed, forming a rib-like structure, and inserted into a cloth mask. As a proof-of-concept, a modification of the pattern shown in **Figure 6.13c** with larger radial spacing is laser-cut from an aluminum sheet and deformed by applying force to the center, making the structure protrude outwards, depicted in **Figure 6.13d-e**. An FEA model (**Figure 6.13f**)

demonstrates the deformed structure, displaced by 55 mm from the center, which is roughly the distance from cheek to the tip of the nose.

## 6.4 Additional applications

Figure 6.14 shows a mind map of applications kirigami design principles can be leveraged.

Categories include healthcare, electronic, defense, and energy sectors.

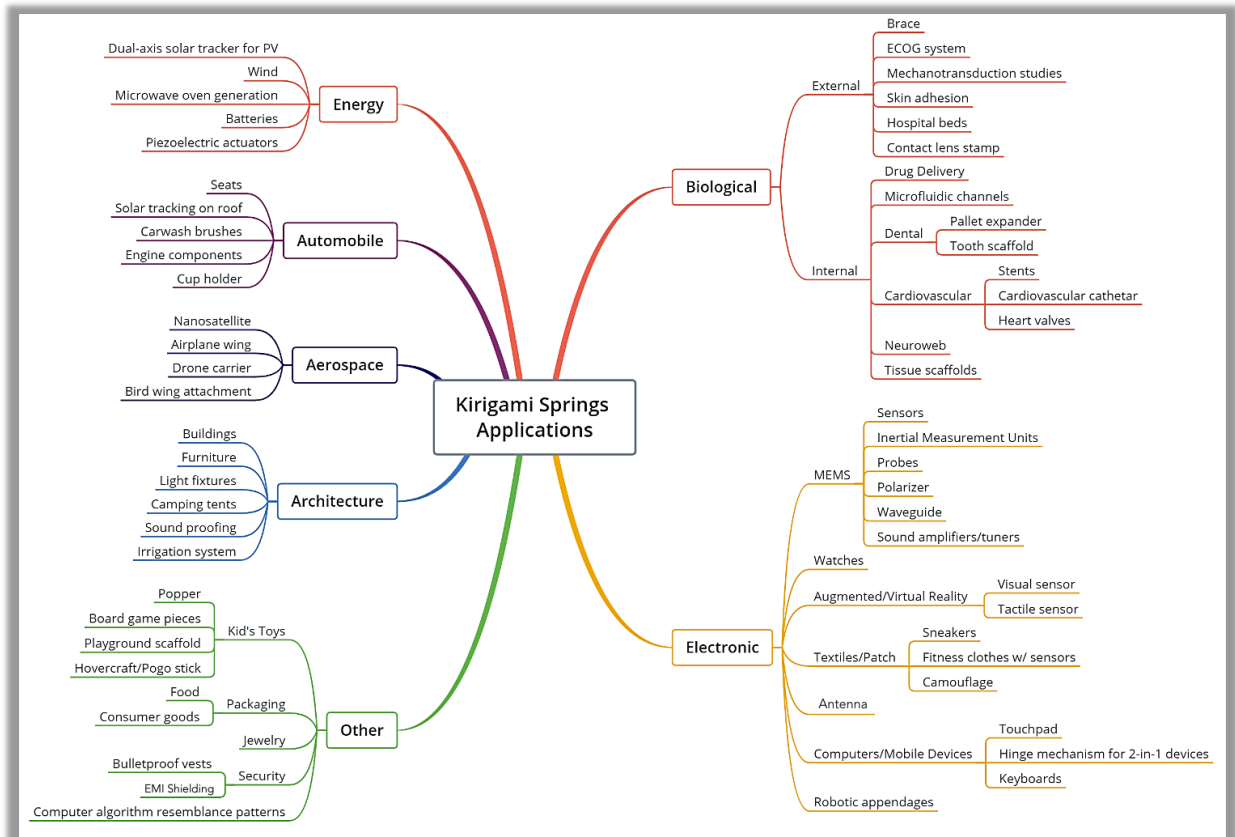


Figure 6.14 Kirigami springs applications.

## Appendix

**Table A.1** Database of kirigami-based engineering solutions, sorted by application.

Material	Scale	Kirigami Shape	Application	Year
PS (Shrinky-Dink) <sup>21</sup>	Macro	saddle/box-hinge	Actuators	2016
PET, Fe-PDMS, eutectic indium-gallium and Cu <sup>155</sup>	Macro	linear cross	Actuators	2018
FEP/PTFE, PET, Kapton and Cu paper <sup>12</sup>	Macro	linear interlock	Actuators, energy harvesting	2016
PVDF <sup>11</sup>	Macro	linear	Actuators, energy harvesting	2018
Graphene, MoS2, mylar BoPET <sup>156</sup>	Meso	linear and radial	Actuators, Soft robotics	2017
PET, PDMS <sup>157</sup>	Macro	linear	Adhesion	2018
SMA wires, PDMS <sup>14</sup>	Macro	linear wave	Aerospace, satellite deployable	2017
SMP, styrene and butyl acrylate, divinylbenzene SMA strips (NiTiCu) <sup>143</sup>	Macro	honeycomb	Aerospace, satellite deployable	2017
Paper <sup>28</sup>	Macro	honeycomb	Aerospace, satellite deployable	2017
PEEK (Victrex) <sup>158</sup>	Macro	honeycomb	Aerospace, satellite deployable	2016
Woven Kevlar <sup>159,160</sup>	Macro	honeycomb	Aerospace-Morphing Wing	2011
lithium-ion batteries-graphite (electrodes), Cu and Al (collectors), PP (separator), LiPF6 (electrolyte), aluminized PE (packaging), PVDF <sup>161</sup>	Macro	linear-zigzag	Batteries	2015
Graphite, carbon black, PVDF-HFP <sup>162</sup>	Macro	Radially symmetric square	Batteries	2017
Graphene <sup>24</sup>	Nano	Radial/linear/square	Flexible electronics	2015
Ag/ANF (aramid nanofiber) <sup>19</sup>	Micro	linear	Flexible electronics	2017
CNT and PDMS <sup>163</sup>	Meso	linear	Flexible electronics	2017
Silicone rubber and PDMS <sup>26</sup>	Meso	fractal	Flexible electronics	2018
Al2O3, titanium isopropoxide, silicone elastomer, PET <sup>164</sup>	Micro	linear wrist	Flexible electronics, energy harvesting	2017
GO-PVA nanocomposite <sup>7</sup>	Nano	linear	Flexible electronics, optoelectronics	2015
Boron nitride <sup>165</sup>	Nano	linear	Flexible electronics, optoelectronics, sensors	2017

PET, Ag, CNT ink, AgNP ink, silicone rubber, PEDOT:PSS with CNT, ZnO nanowires, polyimide, CNT-TFT <sup>25</sup>	Nano-Micro	linear	Flexible Electronics, Sensors	2016
PDMS <sup>8</sup>	Macro	linear	Flexible Electronics, Sensors	2017
cellulose fiber, graphene ink, PU <sup>58</sup>	Micro	linear fish	Flexible Electronics, Sensors	2017
Si-epoxy SU8, Cu, PDMS and Cu/PET <sup>17</sup>	Nano-Macro	precursor random	Flexible Electronics, Sensors, Near field communications	2016
GO sheets, PDMS, Ag/AgCl electrodes <sup>166</sup>	Nano	linear	Nanofluidics	2018
Cr/parylene C on PMMA and CNT/PVA/Parylene C <sup>15</sup>	Micro	linear	Optics	2016
Mylar sheet <sup>167</sup>	Macro	slit k-cone	Optics	2016
SU8 with Au <sup>23</sup>	Meso	Radial/serpentine	Optics	2015
PZT (lead zirconate titanate) <sup>131</sup>	Micro	Cell block	Optics	2018
Kapton <sup>9</sup>	Macro	linear	Optoelectronic	2015
Pyrrrole monomer, Li, propylene carbonate, PVDF <sup>168</sup>	Macro	radial cuts	Soft Robotics	2016
IPMC: Nafion 112 (gold plated) <sup>18</sup>	Macro	Burstbot (radial)	Soft Robotics, artificial muscles	2013
SMA wires (flexinol by Dynalloy) <sup>169</sup>	Macro	Worm robot	Soft Robotics, artificial muscles	2015
Carbon fiber, polyimide, Cu (piezoceramic), parylene C <sup>170</sup>	Meso	linear	Soft Robotics, artificial muscles, energy harvesting	2017

## Bibliography

- (1) Koshiro, Hatori. History of Origami <https://origami.ousaan.com/library/historye.html> (accessed Sep 27, 2020).
- (2) Mitani, J.; Igarashi, T. Interactive Design of Planar Curved Folding by Reflection. *Pacific Graphics* **2011**.
- (3) Petzall, G. *Ullagami: Geometric Kirigami Pop-Ups*; Tarquin Publications, 2015.
- (4) One “origami Engineer” Is Giving the Ancient Art a Modern Twist. *Create*, 2019.
- (5) Merali, Z. “Origami Engineer” Flexes to Create Stronger, More Agile Materials. *Science* **2011**, 332 (6036), 1376–1377. <https://doi.org/10.1126/science.332.6036.1376>.
- (6) Zirbel, S. A.; Lang, R. J.; Thomson, M. W.; Sigel, D. A.; Walkemeyer, P. E.; Trease, B. P.; Magleby, S. P.; Howell, L. L. Accommodating Thickness in Origami-Based Deployable Arrays. *Journal of Mechanical Design* **2013**, 135 (11). <https://doi.org/10.1115/1.4025372>.
- (7) Shyu, T. C.; Damasceno, P. F.; Dodd, P. M.; Lamoureux, A.; Xu, L.; Shlian, M.; Shtein, M.; Glotzer, S. C.; Kotov, N. A. A Kirigami Approach to Engineering Elasticity in Nanocomposites through Patterned Defects. *Nature Materials* **2015**, 14 (8), 785–789. <https://doi.org/10.1038/nmat4327>.
- (8) Tang, Y.; Lin, G.; Yang, S.; Yi, Y. K.; Kamien, R. D.; Yin, J. Programmable Kiri-Kirigami Metamaterials. *Advanced Materials* **2017**, 29 (10), 1604262. <https://doi.org/10.1002/adma.201604262>.
- (9) Lamoureux, A.; Lee, K.; Shlian, M.; Forrest, S. R.; Shtein, M. Dynamic Kirigami Structures for Integrated Solar Tracking. *Nature Communications* **2015**, 6 (1), 1–6. <https://doi.org/10.1038/ncomms9092>.
- (10) Lee, K.; Chien, C.-W.; Lee, B.; Lamoureux, A.; Shlian, M.; Shtein, M.; Ku, P. C.; Forrest, S. Origami Solar-Tracking Concentrator Array for Planar Photovoltaics. *ACS Photonics* **2016**, 3 (11), 2134–2140. <https://doi.org/10.1021/acsphotonics.6b00592>.
- (11) Hu, N.; Chen, D.; Wang, D.; Huang, S.; Trase, I.; Grover, H. M.; Yu, X.; Zhang, J. X. J.; Chen, Z. Stretchable Kirigami Polyvinylidene Difluoride Thin Films for Energy Harvesting: Design, Analysis, and Performance. *Physical Review Applied* **2018**, 9 (2), 021002. <https://doi.org/10.1103/PhysRevApplied.9.021002>.
- (12) Wu, C.; Wang, X.; Lin, L.; Guo, H.; Wang, Z. L. Paper-Based Triboelectric Nanogenerators Made of Stretchable Interlocking Kirigami Patterns. *ACS Nano* **2016**, 10 (4), 4652–4659. <https://doi.org/10.1021/acsnano.6b00949>.
- (13) Zhang, K.; Jung, Y. H.; Mikael, S.; Seo, J.-H.; Kim, M.; Mi, H.; Zhou, H.; Xia, Z.; Zhou, W.; Gong, S.; Ma, Z. Origami Silicon Optoelectronics for Hemispherical Electronic Eye Systems. *Nature Communications* **2017**, 8 (1), 1–8. <https://doi.org/10.1038/s41467-017-01926-1>.
- (14) Wang, W.; Li, C.; Rodrigue, H.; Yuan, F.; Han, M.-W.; Cho, M.; Ahn, S.-H. Kirigami/Origami-Based Soft Deployable Reflector for Optical Beam Steering. *Advanced Functional Materials* **2017**, 27 (7), 1604214. <https://doi.org/10.1002/adfm.201604214>.



- (15) Xu, L.; Wang, X.; Kim, Y.; Shyu, T. C.; Lyu, J.; Kotov, N. A. Kirigami Nanocomposites as Wide-Angle Diffraction Gratings. *ACS Nano* **2016**, *10* (6), 6156–6162. <https://doi.org/10.1021/acsnano.6b02096>.
- (16) Fu, H.; Nan, K.; Bai, W.; Huang, W.; Bai, K.; Lu, L.; Zhou, C.; Liu, Y.; Liu, F.; Wang, J.; Han, M.; Yan, Z.; Luan, H.; Zhang, Y.; Zhang, Y.; Zhao, J.; Cheng, X.; Li, M.; Lee, J. W.; Liu, Y.; Fang, D.; Li, X.; Huang, Y.; Zhang, Y.; Rogers, J. A. Morphable 3D Mesostructures and Microelectronic Devices by Multistable Buckling Mechanics. *Nature Materials* **2018**, *17* (3), 268–276. <https://doi.org/10.1038/s41563-017-0011-3>.
- (17) Yan, Z.; Zhang, F.; Liu, F.; Han, M.; Ou, D.; Liu, Y.; Lin, Q.; Guo, X.; Fu, H.; Xie, Z.; Gao, M.; Huang, Y.; Kim, J. H.; Qiu, Y.; Nan, K.; Kim, J.; Gutruf, P.; Luo, H.; Zhao, A.; Hwang, K. C.; Huang, Y.; Zhang, Y.; Rogers, J. A. Mechanical Assembly of Complex, 3D Mesostructures from Releasable Multilayers of Advanced Materials. *Science Advances* **2016**, *2* (9). <https://doi.org/10.1126/sciadv.1601014>.
- (18) Sareh, S.; Rossiter, J. Kirigami Artificial Muscles with Complex Biologically Inspired Morphologies. *Smart Materials and Structures* **2013**, *22*, 14004–14013. <https://doi.org/10.1088/0964-1726/22/1/014004>.
- (19) Lyu, J.; Hammig, M. D.; Liu, L.; Xu, L.; Chi, H.; Uher, C.; Li, T.; Kotov, N. A. Stretchable Conductors by Kirigami Patterning of Aramid-Silver Nanocomposites with Zero Conductance Gradient. *Applied Physics Letters* **2017**, *111* (16). <https://doi.org/10.1063/1.5001094>.
- (20) Ko, H.; Javey, A. Smart Actuators and Adhesives for Reconfigurable Matter. *Accounts of Chemical Research* **2017**. <https://doi.org/10.1021/acs.accounts.6b00612>.
- (21) Zhang, Q.; Wommer, J.; O'Rourke, C.; Teitelman, J.; Tang, Y.; Robison, J.; Lin, G.; Yin, J. Origami and Kirigami Inspired Self-Folding for Programming Three-Dimensional Shape Shifting of Polymer Sheets with Light. *Extreme Mechanics Letters (in press)* **2016**. <https://doi.org/10.1016/j.eml.2016.08.004>.
- (22) Huang, G.; Mei, Y. Assembly and Self-Assembly of Nanomembrane Materials—From 2D to 3D. *Small* **2018**, *14* (14), 1–23. <https://doi.org/10.1002/sml.201703665>.
- (23) Zhang, Y.; Yan, Z.; Nan, K.; Xiao, D.; Liu, Y.; Luan, H.; Fu, H.; Wang, X.; Yang, Q.; Wang, J.; Ren, W.; Si, H.; Liu, F.; Yang, L.; Li, H.; Wang, J.; Guo, X.; Luo, H.; Wang, L.; Huang, Y.; Rogers, J. A. A Mechanically Driven Form of Kirigami as a Route to 3D Mesostructures in Micro/Nanomembranes. *Proceedings of the National Academy of Sciences* **2015**. <https://doi.org/10.1073/pnas.1515602112>.
- (24) Blees, M. K.; Barnard, A. W.; Rose, P. A.; Roberts, S. P.; McGill, K. L.; Huang, P. Y.; Ruyack, A. R.; Kevek, J. W.; Kobrin, B.; Muller, D. A.; McEuen, P. L. Graphene Kirigami. *Nature* **2015**, *524* (7564), 204–207. <https://doi.org/10.1038/nature14588>.
- (25) Yamamoto, Y.; Harada, S.; Yamamoto, D.; Honda, W.; Arie, T.; Akita, S.; Takei, K. Printed Multifunctional Flexible Device with an Integrated Motion Sensor for Health Care Monitoring. *Science Advances* **2016**, *2* (11), e1601473. <https://doi.org/10.1126/sciadv.1601473>.
- (26) Cho, Y.; Shin, J.-H.; Costa, A.; Kim, T. A.; Kunin, V.; Li, J.; Lee, S. Y.; Yang, S.; Han, H. N.; Choi, I.-S.; Srolovitz, D. J. Engineering the Shape and Structure of Materials by Fractal Cut. *Proceedings of the National Academy of Sciences* **2014**, *111* (49), 17390–17395. <https://doi.org/10.1073/pnas.1417276111>.

- (27) Sussman, D. M.; Cho, Y.; Castle, T.; Gong, X.; Jung, E.; Yang, S.; Kamien, R. D. Algorithmic Lattice Kirigami: A Route to Pluripotent Materials. *Proceedings of the National Academy of Sciences* **2015**. <https://doi.org/10.1073/pnas.1506048112>.
- (28) Wang, F.; Guo, X.; Xu, J.; Zhang, Y.; Chen, C. Q. Patterning Curved Three- Dimensional Structures With Programmable Kirigami Designs. *Journal of Applied Mechanics* **2017**, *84*, 061007. <https://doi.org/10.1115/1.4036476>.
- (29) Evke, E. E.; Meli, D.; Shtein, M. Developable Rotationally Symmetric Kirigami-Based Structures as Sensor Platforms. *Advanced Materials Technologies* **2019**, *4* (12), 1900563. <https://doi.org/10.1002/admt.201900563>.
- (30) Zhixin Pan, Puying Zhao, Yong Xia, Xinqi Wei, Huili Yu. Characterization of Metal Foil in Anisotropic Fracture Behavior with Dynamic Tests. *SAE International Journal of Materials and Manufacturing* **2018**, *11* (4), 563–573. <https://doi.org/doi:10.4271/2018-01-0108>.
- (31) E28 Committee. *Test Methods of Tension Testing of Metallic Foil*; E345-16; ASTM International. <https://doi.org/10.1520/E0345-16>.
- (32) Edward Hughes, John Rutherford. *Determination of Mechanical Properties of Polymer Film Materials*; KD 75-9; The Singer Company: Singer Co., Little Falss, NJ, 1975.
- (33) Mather, R. C.; Koenig, L.; Acevedo, D.; Dall, T. M.; Gallo, P.; Romeo, A.; Tongue, J.; Williams, G. The Societal and Economic Value of Rotator Cuff Repair. *J Bone Joint Surg Am* **2013**, *95* (22), 1993–2000. <https://doi.org/10.2106/JBJS.L.01495>.
- (34) *United States Bone and Joint Initiative: The Burden of Musculoskeletal Diseases in the United States (BMUS)*, Third.; Rosemont, IL, 2014.
- (35) Gedalia, U.; Solomonow, M.; Zhou, B. H.; Baratta, R. V.; Lu, Y.; Harris, M. Biomechanics of Increased Exposure to Lumbar Injury Caused by Cyclic Loading. Part 2. Recovery of Reflexive Muscular Stability with Rest. *Spine* **1999**, *24* (23), 2461–2467. <https://doi.org/10.1097/00007632-199912010-00007>.
- (36) Gajdosik, R. L.; Bohannon, R. W. Clinical Measurement of Range of Motion. Review of Goniometry Emphasizing Reliability and Validity. *Physical Therapy* **1987**, *67* (12), 1867–1872. <https://doi.org/10.1093/ptj/67.12.1867>.
- (37) Glynn, A.; Fiddler, H. *The Physiotherapist's Pocket Guide to Exercise: Assessment, Prescription and Training*, First.; Churchill Livingstone, 2009.
- (38) McVeigh, K. H.; Murray, P. M.; Heckman, M. G.; Rawal, B.; Peterson, J. J. Accuracy and Validity of Goniometer and Visual Assessments of Angular Joint Positions of the Hand and Wrist. *The Journal of Hand Surgery* **2016**, *41* (4), e21-35. <https://doi.org/10.1016/j.jhsa.2015.12.014>.
- (39) Sluijs, E. M.; Kok, G. J.; van der Zee, J. Correlates of Exercise Compliance in Physical Therapy. *Physical Therapy* **1993**, *73* (11), 771–782. <https://doi.org/10.1093/ptj/73.11.771>.
- (40) Heikenfeld, J.; Jajack, A.; Rogers, J.; Gutruf, P.; Tian, L.; Pan, T.; Li, R.; Khine, M.; Kim, J.; Wang, J.; Kim, J. Wearable Sensors: Modalities, Challenges, and Prospects. *Lab Chip* **2018**, *18* (2), 217–248. <https://doi.org/10.1039/c7lc00914c>.
- (41) Subramanian, S. K.; Massie, C. L.; Malcolm, M. P.; Levin, M. F. Does Provision of Extrinsic Feedback Result in Improved Motor Learning in the Upper Limb Poststroke? A Systematic Review of the Evidence. *Neurorehabilitation and Neural Repair* **2010**, *24* (2), 113–124. <https://doi.org/10.1177/1545968309349941>.
- (42) Wang, Q.; Markopoulos, P.; Yu, B.; Chen, W.; Timmermans, A. Interactive Wearable Systems for Upper Body Rehabilitation: A Systematic Review. *Journal of*

- Neuroengineering and Rehabilitation* **2017**, *14* (1), 20. <https://doi.org/10.1186/s12984-017-0229-y>.
- (43) Gates, D. H.; Walters, L. S.; Cowley, J.; Wilken, J. M.; Resnik, L. Range of Motion Requirements for Upper-Limb Activities of Daily Living. *American Journal of Occupational Therapy* **2016**, *70* (1). <https://doi.org/10.5014/ajot.2016.015487>.
- (44) Menguc, Y.; Park, Y.-L.; Martinez-Villalpando, E.; Aubin, P.; Zisook, M.; Stirling, L.; Wood, R. J.; Walsh, C. J. Soft Wearable Motion Sensing Suit for Lower Limb Biomechanics Measurements. In *2013 IEEE International Conference on Robotics and Automation*; IEEE, 2013; pp 5309–5316. <https://doi.org/10.1109/ICRA.2013.6631337>.
- (45) Chen, Y. C.; Lee, H. J.; Lin, K. H. Measurement of Body Joint Angles for Physical Therapy Based on Mean Shift Tracking Using Two Low Cost Kinect Images. In *2015 37th Annual International Conference of the IEEE Engineering in Medicine and Biology Society (EMBC)*; 2015; pp 703–706. <https://doi.org/10.1109/EMBC.2015.7318459>.
- (46) Robert-Lachaine, X.; Mecheri, H.; Larue, C.; Plamondon, A. Validation of Inertial Measurement Units with an Optoelectronic System for Whole-Body Motion Analysis. *Medical & Biological Engineering & Computing* **2017**, *55* (4), 609–619. <https://doi.org/10.1007/s11517-016-1537-2>.
- (47) Tao, X.; Wang, G.; Wang, Y.; Zhang, H. Method for Manufacturing Fabric Strain Sensors. US20090282671A1, November 19, 2009.
- (48) Wang, Q.; De Baets, L.; Timmermans, A.; Chen, W.; Giacolini, L.; Matheve, T.; Markopoulos, P. Motor Control Training for the Shoulder with Smart Garments. *Sensors* **2017**, *17* (7). <https://doi.org/10.3390/s17071687>.
- (49) Ma, S.; Ye, T.; Zhang, T.; Wang, Z.; Li, K.; Chen, M.; Zhang, J.; Wang, Z.; Ramakrishna, S.; Wei, L. Highly Oriented Electrospun P(VDF-TrFE) Fibers via Mechanical Stretching for Wearable Motion Sensing. *Advanced Materials Technologies* **2018**, *3* (7), 1800033. <https://doi.org/10.1002/admt.201800033>.
- (50) Gholami, M.; Ejupi, A.; Rezaei, A.; Ferrone, A.; Menon, C. Estimation of Knee Joint Angle Using a Fabric-Based Strain Sensor and Machine Learning: A Preliminary Investigation. In *2018 7th IEEE International Conference on Biomedical Robotics and Biomechatronics (Biorob)*; 2018; pp 589–594. <https://doi.org/10.1109/BIOROB.2018.8487199>.
- (51) Seyedin, S.; Razal, J. M.; Innis, P. C.; Jeiranikhameneh, A.; Beirne, S.; Wallace, G. G. Knitted Strain Sensor Textiles of Highly Conductive All-Polymeric Fibers. *ACS Applied Materials & Interfaces* **2015**, *7* (38), 21150–21158. <https://doi.org/10.1021/acsami.5b04892>.
- (52) Lorussi, F.; Carbonaro, N.; De Rossi, D.; Paradiso, R.; Veltink, P.; Tognetti, A. Wearable Textile Platform for Assessing Stroke Patient Treatment in Daily Life Conditions. *Frontiers in Bioengineering and Biotechnology* **2016**, *4*. <https://doi.org/10.3389/fbioe.2016.00028>.
- (53) Xu, L.; Shyu, T. C.; Kotov, N. A. Origami and Kirigami Nanocomposites. *ACS Nano* **2017**, *11* (8), 7587–7599. <https://doi.org/10.1021/acsnano.7b03287>.
- (54) Guan, Y.-S.; Li, H.; Ren, F.; Ren, S. Kirigami-Inspired Conducting Polymer Thermoelectrics from Electrostatic Recognition Driven Assembly. *ACS Nano* **2018**, *12* (8), 7967–7973. <https://doi.org/10.1021/acsnano.8b02489>.
- (55) Isobe, M.; Okumura, K. Initial Rigid Response and Softening Transition of Highly Stretchable Kirigami Sheet Materials. *Scientific Reports* **2016**, *6* (1), 1–6. <https://doi.org/10.1038/srep24758>.

- (56) Rafsanjani, A.; Zhang, Y.; Liu, B.; Rubinstein, S. M.; Bertoldi, K. Kirigami Skins Make a Simple Soft Actuator Crawl. *Science Robotics* **2018**, *3* (15).  
<https://doi.org/10.1126/scirobotics.aar7555>.
- (57) Kim, B. H.; Liu, F.; Yu, Y.; Jang, H.; Xie, Z.; Li, K.; Lee, J.; Jeong, J. Y.; Ryu, A.; Lee, Y.; Kim, D. H.; Wang, X.; Lee, K.; Lee, J. Y.; Won, S. M.; Oh, N.; Kim, J.; Kim, J. Y.; Jeong, S.-J.; Jang, K.-I.; Lee, S.; Huang, Y.; Zhang, Y.; Rogers, J. A. Mechanically Guided Post-Assembly of 3D Electronic Systems. *Advanced Functional Materials* **2018**, *28* (48), 1803149. <https://doi.org/10.1002/adfm.201803149>.
- (58) Gao, B.; Elbaz, A.; He, Z.; Xie, Z.; Xu, H.; Liu, S.; Su, E.; Liu, H.; Gu, Z. Bioinspired Kirigami Fish-Based Highly Stretched Wearable Biosensor for Human Biochemical–Physiological Hybrid Monitoring. *Advanced Materials Technologies* **2018**, *3* (4), 1700308. <https://doi.org/10.1002/admt.201700308>.
- (59) Engdahl, S. M.; Gates, D. H. Reliability of Upper Limb and Trunk Joint Angles in Healthy Adults during Activities of Daily Living. *Gait Posture* **2018**, *60*, 41–47.  
<https://doi.org/10.1016/j.gaitpost.2017.11.001>.
- (60) Vito, L. D.; Postolache, O.; Rapuano, S. Measurements and Sensors for Motion Tracking in Motor Rehabilitation. *IEEE Instrumentation Measurement Magazine* **2014**, *17* (3), 30–38.  
<https://doi.org/10.1109/MIM.2014.6825386>.
- (61) Baldominos, A.; Saez, Y.; Pozo, C. G. del. An Approach to Physical Rehabilitation Using State-of-the-Art Virtual Reality and Motion Tracking Technologies. *Procedia Computer Science* **2015**, *64*, 10–16. <https://doi.org/10.1016/j.procs.2015.08.457>.
- (62) Perea, Austin; Smith, Colin; Davis, Michelle; Sun, Xiaojing; White, Bryan; Cox, Molly; Curtin, Gregson; Rumery, Shawn; Goldstein, Rachel; Silver, Colin; Baca, Justin. U.S. Solar Market Insight Executive Summary: Q3 2020. Solar Energy Industries Association September 2020.
- (63) Gagnon, P.; Margolis, R.; Melius, J.; Phillips, C.; Elmore, R. *Rooftop Solar Photovoltaic Technical Potential in the United States. A Detailed Assessment*; NREL/TP--6A20-65298, 1236153; 2016; p NREL/TP--6A20-65298, 1236153. <https://doi.org/10.2172/1236153>.
- (64) Lamoureux, Aaron. *Origami and Kirigami Design Principles for Optical Tracking, Energy Harvesting, and Other Applications*, University of Michigan, Ann Arbor, MI, 2017.
- (65) Konagai, M.; Sugimoto, M.; Takahashi, Kiyoshi. High Efficiency GaAs Thin Film Solar Cells by Peeled Film Technology. *Journal of Crystal Growth* **1978**, *45*, 277–280.
- (66) Lee, K.; Shiu, K.-T.; Zimmerman, J. D.; Renshaw, C. K.; Forrest, S. R. Multiple Growths of Epitaxial Lift-off Solar Cells from a Single InP Substrate. *Applied Physics Letters* **2010**, *97* (10), 101107. <https://doi.org/10.1063/1.3479906>.
- (67) Lee, K.; Zimmerman, J. D.; Hughes, T. W.; Forrest, S. R. Non-Destructive Wafer Recycling for Low-Cost Thin-Film Flexible Optoelectronics. *Advanced Functional Materials* **2014**, *24* (27), 4284–4291. <https://doi.org/10.1002/adfm.201400453>.
- (68) Evke, E. E.; Huang, C.; Wu, Y.-W.; Arwashan, M.; Lee, B.; Forrest, S. R.; Shtein, M. Kirigami-Based Compliant Mechanism for Multi-axis Optical Tracking and Energy-Harvesting Applications. *Advanced Engineering Materials* **2020**, 2001079.  
<https://doi.org/10.1002/adem.202001079>.
- (69) Almobaideen, W.; Krayshan, R.; Allan, M.; Saadeh, M. Internet of Things: Geographical Routing Based on Healthcare Centers Vicinity for Mobile Smart Tourism Destination. *Technological Forecasting and Social Change* **2017**, *123*, 342–350.  
<https://doi.org/10.1016/j.techfore.2017.04.016>.

- (70) Bresciani, S.; Ferraris, A.; Del Giudice, M. The Management of Organizational Ambidexterity through Alliances in a New Context of Analysis: Internet of Things (IoT) Smart City Projects. *Technological Forecasting and Social Change* **2018**, *136*, 331–338. <https://doi.org/10.1016/j.techfore.2017.03.002>.
- (71) Oughton, E.; Frias, Z.; Russell, T.; Sicker, D.; Cleevly, D. D. Towards 5G: Scenario-Based Assessment of the Future Supply and Demand for Mobile Telecommunications Infrastructure. *Technological Forecasting and Social Change* **2018**, *133*, 141–155. <https://doi.org/10.1016/j.techfore.2018.03.016>.
- (72) Zhang, L.; Bi, S.; Liu, M. Lightweight Electromagnetic Interference Shielding Materials and Their Mechanisms. *Electromagnetic Materials and Devices* **2018**. <https://doi.org/10.5772/intechopen.82270>.
- (73) Gupta, S.; Tai, N.-H. Carbon Materials and Their Composites for Electromagnetic Interference Shielding Effectiveness in X-Band. *Carbon* **2019**, *152*, 159–187. <https://doi.org/10.1016/j.carbon.2019.06.002>.
- (74) Zeng, X.; Cheng, X.; Yu, R.; Stucky, G. D. Electromagnetic Microwave Absorption Theory and Recent Achievements in Microwave Absorbers. *Carbon* **2020**, *168*, 606–623. <https://doi.org/10.1016/j.carbon.2020.07.028>.
- (75) Kacprzyk, A.; Kanclerz, G.; Rokita, E.; Tatoń, G. Which Sources of Electromagnetic Field Are of the Highest Concern for Electrosensitive Individuals? – Questionnaire Study with a Literature Review. *Electromagnetic Biology and Medicine* **2020**, *0* (0), 1–8. <https://doi.org/10.1080/15368378.2020.1839489>.
- (76) Kasevich, R. S. Cellphones, Radars, and Health [Speakout]. *IEEE Spectrum* **2002**, *39* (8), 15–16. <https://doi.org/10.1109/MSPEC.2002.1021945>.
- (77) Cao, M.-S.; Song, W.-L.; Hou, Z.-L.; Wen, B.; Yuan, J. The Effects of Temperature and Frequency on the Dielectric Properties, Electromagnetic Interference Shielding and Microwave-Absorption of Short Carbon Fiber/Silica Composites. *Carbon* **2010**, *48* (3), 788–796. <https://doi.org/10.1016/j.carbon.2009.10.028>.
- (78) Zeng, X.; Yang, B.; Zhu, L.; Yang, H.; Yu, R. Structure Evolution of Prussian Blue Analogues to CoFe@C Core–Shell Nanocomposites with Good Microwave Absorbing Performances. *RSC Adv.* **2016**, *6* (107), 105644–105652. <https://doi.org/10.1039/C6RA18928H>.
- (79) Jiang, D.; Murugadoss, V.; Wang, Y.; Lin, J.; Ding, T.; Wang, Z.; Shao, Q.; Wang, C.; Liu, H.; Lu, N.; Wei, R.; Subramania, A.; Guo, Z. Electromagnetic Interference Shielding Polymers and Nanocomposites - A Review. *Polymer Reviews* **2019**, *59* (2), 280–337. <https://doi.org/10.1080/15583724.2018.1546737>.
- (80) Markham, D. Shielding: Quantifying the Shielding Requirements for Portable Electronic Design and Providing New Solutions by Using a Combination of Materials and Design. *Materials & Design* **1999**, *21* (1), 45–50. [https://doi.org/10.1016/S0261-3069\(99\)00049-7](https://doi.org/10.1016/S0261-3069(99)00049-7).
- (81) Casey, K. F. Electromagnetic Shielding Behavior of Wire-Mesh Screens. *IEEE Transactions on Electromagnetic Compatibility* **1988**, *30* (3), 298–306. <https://doi.org/10.1109/15.3309>.
- (82) Avi Bregman. Morphology Control of Polymer Composites for Enhanced Microwave Absorption. PhD Thesis, 2019.
- (83) Wei, Q.; Pei, S.; Qian, X.; Liu, H.; Liu, Z.; Zhang, W.; Zhou, T.; Zhang, Z.; Zhang, X.; Cheng, H.-M.; Ren, W. Superhigh Electromagnetic Interference Shielding of Ultrathin

- Aligned Pristine Graphene Nanosheets Film. *Advanced Materials* **2020**, 32 (14), 1907411. <https://doi.org/10.1002/adma.201907411>.
- (84) Yao, B.; Hong, W.; Chen, T.; Han, Z.; Xu, X.; Hu, R.; Hao, J.; Li, C.; Li, H.; Perini, S. E.; Lanagan, M. T.; Zhang, S.; Wang, Q.; Wang, H. Highly Stretchable Polymer Composite with Strain-Enhanced Electromagnetic Interference Shielding Effectiveness. *Advanced Materials* **2020**, 32 (14), 1907499. <https://doi.org/10.1002/adma.201907499>.
- (85) Ding, Y.; Liao, Q.; Liu, S.; Guo, H.; Sun, Y.; Zhang, G.; Zhang, Y. Reduced Graphene Oxide Functionalized with Cobalt Ferrite Nanocomposites for Enhanced Efficient and Lightweight Electromagnetic Wave Absorption. *Scientific Reports* **2016**, 6 (April), 1–9. <https://doi.org/10.1038/srep32381>.
- (86) Bai, X.; Zhai, Y.; Zhang, Y. Green Approach to Prepare Graphene-Based Composites with High Microwave Absorption Capacity. *Journal of Physical Chemistry C* **2011**, 115 (23), 11673–11677. <https://doi.org/10.1021/jp202475m>.
- (87) Yan, J.; Huang, Y.; Wei, C.; Zhang, N.; Liu, P. Covalently Bonded Polyaniline/Graphene Composites as High-Performance Electromagnetic (EM) Wave Absorption Materials. *Composites Part A: Applied Science and Manufacturing* **2017**, 99, 121–128. <https://doi.org/10.1016/j.compositesa.2017.04.016>.
- (88) Song, W.-L.; Guan, X.-T.; Fan, L.-Z.; Cao, W.-Q.; Zhao, Q.-L.; Wang, C.-Y.; Cao, M.-S. Tuning Broadband Microwave Absorption via Highly Conductive Fe<sub>3</sub>O<sub>4</sub>/Graphene Heterostructural Nanofillers. *Materials Research Bulletin* **2015**, 72, 316–323. <https://doi.org/10.1016/j.materresbull.2015.07.028>.
- (89) Shen, W.; Ren, B.; Cai, K.; fei Song, Y.; Wang, W. Synthesis of Nonstoichiometric Co<sub>0.8</sub>Fe<sub>2.2</sub>O<sub>4</sub>/Reduced Graphene Oxide (RGO) Nanocomposites and Their Excellent Electromagnetic Wave Absorption Property. *Journal of Alloys and Compounds* **2019**, 774, 997–1008. <https://doi.org/10.1016/j.jallcom.2018.09.361>.
- (90) Das, C. K.; Bhattacharya, P.; Kalra, S. S. Graphene and MWCNT: Potential Candidate for Microwave Absorbing Materials. *Journal of Materials Science Research* **2012**, 1 (2), 126–132. <https://doi.org/10.5539/jmsr.v1n2p126>.
- (91) Kong, L.; Yin, X.; Yuan, X.; Zhang, Y.; Liu, X.; Cheng, L. Electromagnetic Wave Absorption Properties of Graphene Modified with Carbon Nanotube / Poly ( Dimethyl Siloxane ) Composites. *Carbon* **2014**, 73, 185–193. <https://doi.org/10.1016/j.carbon.2014.02.054>.
- (92) Guo, Z.; Park, S.; Hahn, H. T.; Wei, S.; Moldovan, M.; Karki, A. B.; Young, D. P. Magnetic and Electromagnetic Evaluation of the Magnetic Nanoparticle Filled Polyurethane Nanocomposites. *Journal of Applied Physics* **2007**, 101 (9). <https://doi.org/10.1063/1.2711074>.
- (93) Zong, M.; Huang, Y.; Zhang, N.; Wu, H. Influence of (RGO)/(Ferrite) Ratios and Graphene Reduction Degree on Microwave Absorption Properties of Graphene Composites. *Journal of Alloys and Compounds* **2015**, 644, 491–501. <https://doi.org/10.1016/j.jallcom.2015.05.073>.
- (94) Meng, X. M.; Zhang, X. J.; Lu, C.; Pan, Y. F.; Wang, G. S. Enhanced Absorbing Properties of Three-Phase Composites Based on a Thermoplastic-Ceramic Matrix (BaTiO<sub>3</sub> + PVDF) and Carbon Black Nanoparticles. *Journal of Materials Chemistry A* **2014**, 2 (44), 18725–18730. <https://doi.org/10.1039/c4ta04493b>.
- (95) Zhang, X. J.; Wang, G. S.; Cao, W. Q.; Wei, Y. Z.; Liang, J. F.; Guo, L.; Cao, M. S. Enhanced Microwave Absorption Property of Reduced Graphene Oxide (RGO)-MnFe<sub>2</sub>O<sub>4</sub>

- Nanocomposites and Polyvinylidene Fluoride. *ACS Applied Materials and Interfaces* **2014**, *6* (10), 7471–7478. <https://doi.org/10.1021/am500862g>.
- (96) Tirkey, M. M.; Gupta, N. Electromagnetic Absorber Design Challenges. *IEEE Electromagnetic Compatibility Magazine* **2019**, *8* (1), 59–65. <https://doi.org/10.1109/MEMC.2019.8681370>.
- (97) Wang, J.; Wang, J.; Xu, R.; Sun, Y.; Zhang, B.; Chen, W.; Wang, T. Enhanced Microwave Absorption Properties of Epoxy Composites Reinforced with Fe<sub>50</sub>Ni<sub>50</sub>-Functionalized Graphene. *Journal of Alloys and Compounds* **2015**, *653*, 14–21.
- (98) Al-Saleh, M. H.; Sundararaj, U. A Review of Vapor Grown Carbon Nanofiber/Polymer Conductive Composites. *Carbon* **2009**, *47* (1), 2–22. <https://doi.org/10.1016/j.carbon.2008.09.039>.
- (99) Al-saleh, M. H.; Sundararaj, U. Electromagnetic Interference Shielding Mechanisms of CNT / Polymer Composites. *Carbon* **2009**, *47* (7), 1738–1746. <https://doi.org/10.1016/j.carbon.2009.02.030>.
- (100) Tirkey, M. M.; Gupta, N. The Quest for Perfect Electromagnetic Absorber: A Review. *International Journal of Microwave and Wireless Technologies* **2019**, *11* (2), 151–167. <https://doi.org/10.1017/S1759078718001472>.
- (101) Shukla, V. Review of Electromagnetic Interference Shielding Materials Fabricated by Iron Ingredients. *Nanoscale Advances* **2019**, *1* (5), 1640–1671. <https://doi.org/10.1039/C9NA00108E>.
- (102) Saini, P.; Arora, M. Microwave Absorption and EMI Shielding Behavior of Nanocomposites Based on Intrinsically Conducting Polymers, Graphene and Carbon Nanotubes. *New Polymers for Special Applications* **2012**. <https://doi.org/10.5772/48779>.
- (103) Meng, F.; Wang, H.; Huang, F.; Guo, Y.; Wang, Z.; Hui, D.; Zhou, Z. Graphene-Based Microwave Absorbing Composites : A Review and Prospective. *Composites Part B* **2018**, *137*, 260–277. <https://doi.org/10.1016/j.compositesb.2017.11.023>.
- (104) Kong, L. B.; Li, Z. W.; Liu, L.; Huang, R.; Abshinova, M.; Yang, Z. H.; Tang, C. B.; Tan, P. K.; Deng, C. R.; Matitsine, S. Recent Progress in Some Composite Materials and Structures for Specific Electromagnetic Applications. *International Materials Reviews* **2013**, *58* (4), 203–259. <https://doi.org/10.1179/1743280412Y.0000000011>.
- (105) Qin, F.; Brosseau, C. A Review and Analysis of Microwave Absorption in Polymer Composites Filled with Carbonaceous Particles. *Journal of Applied Physics* **2012**, *111*, 061301. <https://doi.org/10.1063/1.3688435>.
- (106) Sankaran, S.; Deshmukh, K.; Ahamed, M. B.; Khadheer Pasha, S. K. Recent Advances in Electromagnetic Interference Shielding Properties of Metal and Carbon Filler Reinforced Flexible Polymer Composites: A Review. *Composites Part A: Applied Science and Manufacturing* **2018**, *114*, 49–71. <https://doi.org/10.1016/j.compositesa.2018.08.006>.
- (107) Quan, L.; Qin, F. X.; Estevez, D.; Wang, H.; Peng, H. X. Magnetic Graphene for Microwave Absorbing Application : Towards the Lightest Graphene-Based Absorber. *Carbon* **2017**, *125*, 630–639. <https://doi.org/10.1016/j.carbon.2017.09.101>.
- (108) Gass, J.; Poddar, P.; Almand, J.; Srinath, S.; Srikanth, H. Superparamagnetic Polymer Nanocomposites with Uniform Fe<sub>3</sub>O<sub>4</sub> Nanoparticle Dispersions. *Advanced Functional Materials* **2006**, *16* (1), 71–75. <https://doi.org/10.1002/adfm.200500335>.
- (109) Jiang, W.; Liu, Y.; Li, F.; Chu, J.; Chen, K. Superparamagnetic Cobalt-Ferrite-Modified Carbon Nanotubes Using a Facile Method. *Materials Science and Engineering B* **2010**, *166*, 132–134. <https://doi.org/10.1016/j.mseb.2009.10.013>.

- (110) Chen, Y.; Wang, Y.; Zhang, H. B.; Li, X.; Gui, C. X.; Yu, Z. Z. Enhanced Electromagnetic Interference Shielding Efficiency of Polystyrene/Graphene Composites with Magnetic Fe<sub>3</sub>O<sub>4</sub> Nanoparticles. *Carbon* **2015**, *82* (C), 67–76. <https://doi.org/10.1016/j.carbon.2014.10.031>.
- (111) Liu, Y.; Lu, M.; Wu, K.; Yao, S.; Du, X.; Chen, G.; Zhang, Q.; Liang, L.; Lu, M. Anisotropic Thermal Conductivity and Electromagnetic Interference Shielding of Epoxy Nanocomposites Based on Magnetic Driving Reduced Graphene Oxide@Fe<sub>3</sub>O<sub>4</sub>. *Composites Science and Technology* **2019**, *174*, 1–10. <https://doi.org/10.1016/j.compscitech.2019.02.005>.
- (112) Liao, H.; Li, D.; Zhou, C.; Liu, T. Microporous Co/RGO Nanocomposites: Strong and Broadband Microwave Absorber with Well-Matched Dielectric and Magnetic Loss. *Journal of Alloys and Compounds* **2019**, *782*, 556–565.
- (113) Li, J.; Wei, J.; Pu, Z.; Xu, M.; Jia, K.; Liu, X. Influence of Fe<sub>3</sub>O<sub>4</sub>/Fe-Phthalocyanine Decorated Graphene Oxide on the Microwave Absorbing Performance. *Journal of Magnetism and Magnetic Materials* **2016**, *399*, 81–87. <https://doi.org/10.1016/j.jmmm.2015.09.072>.
- (114) Shi, Y.; Yin, Y.; Zhang, Y.; Hu, Y.; Liu, W. Preparation and Microwave Absorption Properties of C@Fe<sub>3</sub>O<sub>4</sub> Magnetic Composite Microspheres. *Materials* **2019**, *12* (15). <https://doi.org/10.3390/ma12152404>.
- (115) Li, C.-Q.; Xu, W.; Ding, R.-C.; Shen, X.; Chen, Z.; Li, M.-D.; Wang, G.-S. Tunable High-Performance Microwave Absorption and Shielding by Three Constituent Phases Between RGO and Fe<sub>3</sub>O<sub>4</sub>@SiO<sub>2</sub> Nanochains. *Frontiers in Chemistry* **2019**, *7*. <https://doi.org/10.3389/fchem.2019.00711>.
- (116) Bregman, A.; Michielssen, E.; Taub, A. Comparison of Experimental and Modeled EMI Shielding Properties of Periodic Porous XGNP/PLA Composites. *Polymers* **2019**, *11* (8). <https://doi.org/10.3390/polym11081233>.
- (117) Bregman, A.; Taub, A.; Michielssen, E. Computational Design of Composite EMI Shields through the Control of Pore Morphology. *MRS Communications* **2018**, *8* (3), 1153–1157. <https://doi.org/10.1557/mrc.2018.171>.
- (118) Lai, D.; Chen, X.; Wang, Y. Controllable Fabrication of Elastomeric and Porous Graphene Films with Superior Foldable Behavior and Excellent Electromagnetic Interference Shielding Performance. *Carbon* **2020**, *158*, 728–737. <https://doi.org/10.1016/j.carbon.2019.11.047>.
- (119) Yuan, Y.; Liu, L.; Yang, M.; Zhang, T.; Xu, F.; Lin, Z.; Ding, Y.; Wang, C.; Li, J.; Yin, W.; Peng, Q.; He, X.; Li, Y. Lightweight, Thermally Insulating and Stiff Carbon Honeycomb-Induced Graphene Composite Foams with a Horizontal Laminated Structure for Electromagnetic Interference Shielding. *Carbon* **2017**, *123*, 223–232. <https://doi.org/10.1016/j.carbon.2017.07.060>.
- (120) Shen, B.; Li, Y.; Zhai, W.; Zheng, W. Compressible Graphene-Coated Polymer Foams with Ultralow Density for Adjustable Electromagnetic Interference (EMI) Shielding. *ACS Applied Materials and Interfaces* **2016**, *8* (12), 8050–8057. <https://doi.org/10.1021/acsami.5b11715>.
- (121) Fletcher, A.; Gupta, M. C.; Dudley, K. L.; Vedeler, E. Elastomer Foam Nanocomposites for Electromagnetic Dissipation and Shielding Applications. *Composites Science and Technology* **2010**, *70*, 953–958. <https://doi.org/10.1016/j.compscitech.2010.02.011>.



- (122) Thomassin, J. M.; Jérôme, C.; Pardoën, T.; Bailly, C.; Huynen, I.; Detrembleur, C. Polymer/Carbon Based Composites as Electromagnetic Interference (EMI) Shielding Materials. *Materials Science and Engineering R: Reports* **2013**, *74* (7), 211–232. <https://doi.org/10.1016/j.mser.2013.06.001>.
- (123) Dhakate, S. R. Â.; Subhedar, K. M. Â.; Singh, B. P. Polymer Nanocomposite Foam Filled with Carbon Nanomaterials as an Efficient Electromagnetic Interference Shielding Material. *RSC Advances* **2015**, *5* (54), 43036–43057. <https://doi.org/10.1039/C5RA03409D>.
- (124) Xu, H.; Yin, X.; Li, M.; Li, X.; Li, X.; Dang, X.; Zhang, L.; Cheng, L. Ultralight Cellular Foam from Cellulose Nanofiber/Carbon Nanotube Self-Assemblies for Ultrabroad-Band Microwave Absorption. *ACS Applied Materials and Interfaces* **2019**. <https://doi.org/10.1021/acsami.9b03731>.
- (125) Shi, S.; Peng, Z.; Jing, J.; Yang, L.; Chen, Y. 3D Printing of Delicately Controllable Cellular Nanocomposites Based on Polylactic Acid Incorporating Graphene/Carbon Nanotube Hybrids for Efficient Electromagnetic Interference Shielding. *ACS Sustainable Chemistry and Engineering* **2020**, *8* (21), 7962–7972. <https://doi.org/10.1021/acssuschemeng.0c01877>.
- (126) Ren, J.; Yin, J. Y. 3D-Printed Low-Cost Dielectric-Resonator-Based Ultra-Broadband Microwave Absorber Using Carbon-Loaded Acrylonitrile Butadiene Styrene Polymer. *Materials* **2018**, *10* (7). <https://doi.org/10.3390/ma11071249>.
- (127) Wei, X.; Li, D.; Jiang, W.; Gu, Z.; Wang, X.; Zhang, Z.; Sun, Z. 3D Printable Graphene Composite. *Scientific Reports* **2015**, *5*, 1–7. <https://doi.org/10.1038/srep11181>.
- (128) Yin, L.; Tian, X.; Shang, Z.; Li, D. Ultra-Broadband Metamaterial Absorber with Graphene Composites Fabricated by 3D Printing. *Materials Letters* **2019**, *239*, 132–135. <https://doi.org/10.1016/j.matlet.2018.12.087>.
- (129) Chizari, K.; Arjmand, M.; Liu, Z.; Sundararaj, U.; Therriault, D. Three-Dimensional Printing of Highly Conductive Polymer Nanocomposites for EMI Shielding Applications. *Materials Today Communications* **2017**, *11*, 112–118. <https://doi.org/10.1016/j.mtcomm.2017.02.006>.
- (130) Hayes, G. J.; Liu, Y.; Genzer, J.; Lazzi, G.; Dickey, M. D. Self-Folding Origami Microstrip Antennas. *IEEE Transactions on Antennas and Propagation* **2014**, *62* (10), 5416–5419. <https://doi.org/10.1109/TAP.2014.2346188>.
- (131) Zhu, R.; Yasuda, H.; Huang, G. L.; Yang, J. K. Kirigami-Based Elastic Metamaterials with Anisotropic Mass Density for Subwavelength Flexural Wave Control. *Scientific Reports* **2018**, *8* (1), 1–11. <https://doi.org/10.1038/s41598-017-18864-z>.
- (132) Dijvejin, Z. A.; Kazemi, K. K.; Alasvand Zarasvand, K.; Zarifi, M. H.; Golovin, K. Kirigami-Enabled Microwave Resonator Arrays for Wireless, Flexible, Passive Strain Sensing. *ACS Applied Materials & Interfaces* **2020**, *12* (39), 44256–44264. <https://doi.org/10.1021/acsami.0c10384>.
- (133) Jeong, H. Y.; Lim, Y.; An, S.-C.; Nguyen, T. H.-Y.; Byun, G.; Jun, Y. C. Tunable Resonance and Phase Vortices in Kirigami Fano-Resonant Metamaterials. *Advanced Materials Technologies* **2020**, *5* (8), 2000234. <https://doi.org/10.1002/admt.202000234>.
- (134) Jing, L.; Wang, Z.; Zheng, B.; Wang, H.; Yang, Y.; Shen, L.; Yin, W.; Li, E.; Chen, H. Kirigami Metamaterials for Reconfigurable Toroidal Circular Dichroism. *NPG Asia Mater* **2018**, *10* (9), 888–898. <https://doi.org/10.1038/s41427-018-0082-x>.

- (135) Vicente, A. N.; Dip, G. M.; Junqueira, C. The Step by Step Development of NRW Method. In *2011 SBMO/IEEE MTT-S International Microwave and Optoelectronics Conference (IMOC 2011)*; 2011; pp 738–742. <https://doi.org/10.1109/IMOC.2011.6169318>.
- (136) Hartl, D.; Lane, K.; Malak, R. Computational Design of a Reconfigurable Origami Space Structure Incorporating Shape Memory Alloy Thin Films; American Society of Mechanical Engineers Digital Collection, 2013; pp 277–285. <https://doi.org/10.1115/SMASIS2012-8219>.
- (137) Sakovsky, M.; Pellegrino, S. Closed Cross-Section Dual-Matrix Composite Hinge for Deployable Structures. *Composite Structures* **2019**, *208*, 784–795. <https://doi.org/10.1016/j.compstruct.2018.10.040>.
- (138) Dao, T. D.; Goo, N. S.; Yu, W. R. Blocking Force Measurement of Shape Memory Polymer Composite Hinges for Space Deployable Structures. *Journal of Intelligent Material Systems and Structures* **2018**, *29* (18), 3667–3678. <https://doi.org/10.1177/1045389X18798950>.
- (139) Paton, B. E.; Lobanov, L. M.; Volkov, V. S. Metal Transformable-Volume Structures for Space Engineering. *Acta Astronautica* **2015**, *110*, 50–57. <https://doi.org/10.1016/j.actaastro.2015.01.005>.
- (140) Mohd Jani, J.; Leary, M.; Subic, A.; Gibson, M. A. A Review of Shape Memory Alloy Research, Applications and Opportunities. *Materials & Design (1980-2015)* **2014**, *56*, 1078–1113. <https://doi.org/10.1016/j.matdes.2013.11.084>.
- (141) Leng, J.; Lan, X.; Liu, Y.; Du, S. Shape-Memory Polymers and Their Composites: Stimulus Methods and Applications. *Progress in Materials Science* **2011**, *56* (7), 1077–1135. <https://doi.org/10.1016/j.pmatsci.2011.03.001>.
- (142) Huber, J. E.; Fleck, N. A.; Ashby, M. F. The Selection of Mechanical Actuators Based on Performance Indices. *Proceedings of the Royal Society of London. Series A: Mathematical, Physical and Engineering Sciences* **1997**, *453* (1965), 2185–2205. <https://doi.org/10.1098/rspa.1997.0117>.
- (143) Neville, R. M.; Chen, J.; Guo, X.; Zhang, F.; Wang, W.; Dobah, Y.; Scarpa, F.; Leng, J.; Peng, H.-X. A Kirigami Shape Memory Polymer Honeycomb Concept for Deployment. *Smart Materials and Structures* **2017**, *26* (5), 05LT03. <https://doi.org/10.1088/1361-665X/aa6b6d>.
- (144) P.K. Kumar, D. C. Lagoudas. Introduction to Shape Memory Alloys. *Springer Science+Business Media, LLC* **2008**. <https://doi.org/DOI:10.1007/978-0-387-47685-81>.
- (145) Idowu, A. Graphene Foam Reinforced Shape Memory Polymer Epoxy Composites. PhD Thesis, Florida International University, Miami, FL, 2019.
- (146) Eyckmans, J.; Chen, C. S. 3D Culture Models of Tissues under Tension. *Journal of Cell Science* **2017**, *130* (1), 63–70. <https://doi.org/10.1242/jcs.198630>.
- (147) Liu, A. S.; Wang, H.; Copeland, C. R.; Chen, C. S.; Shenoy, V. B.; Reich, D. H. Matrix Viscoplasticity and Its Shielding by Active Mechanics in Microtissue Models: Experiments and Mathematical Modeling. *Scientific Reports* **2016**, *6* (1), 33919. <https://doi.org/10.1038/srep33919>.
- (148) Leonard, A.; Bertero, A.; Powers, J. D.; Beussman, K. M.; Bhandari, S.; Regnier, M.; Murry, C. E.; Sniadecki, N. J. Afterload Promotes Maturation of Human Induced Pluripotent Stem Cell Derived Cardiomyocytes in Engineered Heart Tissues. *Journal of*

- Molecular and Cellular Cardiology* **2018**, *118*, 147–158.  
<https://doi.org/10.1016/j.yjmcc.2018.03.016>.
- (149) McGarry, J. P.; Fu, J.; Yang, M. T.; Chen, C. S.; McMeeking, R. M.; Evans, A. G.; Deshpande, V. S. Simulation of the Contractile Response of Cells on an Array of Micro-Posts. *Philos Trans A Math Phys Eng Sci* **2009**, *367* (1902), 3477–3497.  
<https://doi.org/10.1098/rsta.2009.0097>.
- (150) Leung, W. W.-F.; Sun, Q. Charged PVDF Multilayer Nanofiber Filter in Filtering Simulated Airborne Novel Coronavirus (COVID-19) Using Ambient Nano-Aerosols. *Separation and Purification Technology* **2020**, *245*, 116887.  
<https://doi.org/10.1016/j.seppur.2020.116887>.
- (151) Or, P. P.; Chung, J. W.; Wong, T. K. A Study of Environmental Factors Affecting Nurses' Comfort and Protection in Wearing N95 Respirators during Bedside Procedures. *Journal of Clinical Nursing* **2018**, *27* (7–8), e1477–e1484. <https://doi.org/10.1111/jocn.14268>.
- (152) Suen, L. K. P.; Guo, Y. P.; Ho, S. S. K.; Au-Yeung, C. H.; Lam, S. C. Comparing Mask Fit and Usability of Traditional and Nanofibre N95 Filtering Facepiece Respirators before and after Nursing Procedures. *Journal of Hospital Infection* **2020**, *104* (3), 336–343.  
<https://doi.org/10.1016/j.jhin.2019.09.014>.
- (153) Oberg, T.; Brosseau, L. M. Surgical Mask Filter and Fit Performance. *American Journal of Infection Control* **2008**, *36* (4), 276–282. <https://doi.org/10.1016/j.ajic.2007.07.008>.
- (154) Grinshpun, S. A.; Yermakov, M.; Khodoun, M. Autoclave Sterilization and Ethanol Treatment of Re-Used Surgical Masks and N95 Respirators during COVID-19: Impact on Their Performance and Integrity. *Journal of Hospital Infection* **2020**, *105* (4), 608–614.  
<https://doi.org/10.1016/j.jhin.2020.06.030>.
- (155) Hwang, D.-G.; Bartlett, M. D. Tunable Mechanical Metamaterials through Hybrid Kirigami Structures. *Scientific Reports* **2018**, *8* (1), 1–8. <https://doi.org/10.1038/s41598-018-21479-7>.
- (156) Dias, M. A.; McCarron, M. P.; Rayneau-Kirkhope, D.; Hanakata, P. Z.; Campbell, D. K.; Park, H. S.; Holmes, D. P. Kirigami Actuators. *Soft Matter* **2017**, *13* (48), 9087–9092.  
<https://doi.org/10.1039/c7sm01693j>.
- (157) Hwang, D. G.; Trent, K.; Bartlett, M. D. Kirigami-Inspired Structures for Smart Adhesion. *ACS Applied Materials and Interfaces* **2018**, *10* (7), 6747–6754.  
<https://doi.org/10.1021/acsami.7b18594>.
- (158) Neville, R. M.; Scarpa, F.; Pirrera, A. Shape Morphing Kirigami Mechanical Metamaterials. *Scientific Reports* **2016**, *6* (August 2015), 31067.  
<https://doi.org/10.1038/srep31067>.
- (159) Saito, K.; Agnese, F.; Scarpa, F. A Cellular Kirigami Morphing Wingbox Concept. *Journal of Intelligent Material Systems and Structures* **2011**, *22* (9), 935–944.  
<https://doi.org/10.1177/1045389X11416030>.
- (160) Hou, Y.; Neville, R.; Scarpa, F.; Remillat, C.; Gu, B.; Ruzzene, M. Graded Conventional-Auxetic Kirigami Sandwich Structures: Flatwise Compression and Edgewise Loading. *Composites Part B: Engineering* **2014**, *59*, 33–42.  
<https://doi.org/10.1016/j.compositesb.2013.10.084>.
- (161) Song, Z.; Wang, X.; Lv, C.; An, Y.; Liang, M.; Ma, T.; He, D.; Zheng, Y.-J.; Huang, S.-Q.; Yu, H.; Jiang, H. Kirigami-Based Stretchable Lithium-Ion Batteries. *Scientific Reports* **2015**. <https://doi.org/10.1038/srep10988>.

- (162) Choi, S.; Lee, D.; Kim, G.; Lee, Y. Y.; Kim, B.; Moon, J.; Shim, W. Shape-Reconfigurable Aluminum–Air Batteries. *Advanced Functional Materials* **2017**, *27* (35), 1–9. <https://doi.org/10.1002/adfm.201702244>.
- (163) Wang, Z.; Zhang, L.; Duan, S.; Jiang, H.; Shen, J.; Li, C. Kirigami-Patterned Highly Stretchable Conductors from Flexible Carbon Nanotube-Embedded Polymer Films. *Journal of Materials Chemistry C* **2017**, *5*, 8714–8722. <https://doi.org/10.1039/c7tc01727h>.
- (164) Jang, N. S.; Kim, K. H.; Ha, S. H.; Jung, S. H.; Lee, H. M.; Kim, J. M. Simple Approach to High-Performance Stretchable Heaters Based on Kirigami Patterning of Conductive Paper for Wearable Thermotherapy Applications. *ACS Applied Materials and Interfaces* **2017**, *9* (23), 19612–19621. <https://doi.org/10.1021/acsami.7b03474>.
- (165) Han, T.; Scarpa, F.; Allan, N. L. Super Stretchable Hexagonal Boron Nitride Kirigami. *Thin Solid Films* **2017**. <https://doi.org/10.1016/j.tsf.2017.03.059>.
- (166) Gao, J.; Koltonow, A. R.; Raidongia, K.; Beckerman, B.; Boon, N.; Luijten, E.; Olvera De La Cruz Abc, M.; Huang, J. Kirigami Nanofluidics. *Materials Chemistry* **2018**, *2*, 475–482. [https://doi.org/DOI: 10.1039/c7qm00620a](https://doi.org/DOI:10.1039/c7qm00620a).
- (167) Seffen, K. A. K-Cones and Kirigami Metamaterials. *Physical Review E* **2016**, *94* (3), 033003. <https://doi.org/10.1103/PhysRevE.94.033003>.
- (168) Mutlu, R.; Alici, G.; Li, W. A Soft Mechatronic Microstage Mechanism Based on Electroactive Polymer Actuators. *IEEE/ASME Transactions on Mechatronics* **2016**, *21* (3), 1467–1478. <https://doi.org/10.1109/TMECH.2015.2502597>.
- (169) Zhang, K.; Qiu, C.; Dai, J. S. Helical Kirigami-Enabled Centimeter-Scale Worm Robot With Shape-Memory-Alloy Linear Actuators. *Journal of Mechanisms and Robotics* **2015**, *7* (2), 021014. <https://doi.org/10.1115/1.4029494>.
- (170) York, P. A.; Jafferis, N. T.; Wood, R. J. Meso Scale Flextensional Piezoelectric Actuators. *Smart Materials and Structures* **2018**, *27*, 015008. <https://doi.org/doi.org/10.1088/1361-665X/aa9366>.